

Imperial College London
Department of Earth Science and Engineering

Sensitivity analysis, uncertainty quantification and parameter estimation for a numerical tide and storm surge model

Simon Charles Warder

Supervised by
Prof. Matthew D. Piggott
Prof. Kevin J. Horsburgh
Prof. Colin J. Cotter
Dr David A. Ham

Submitted in part fulfilment of the requirements for the degree of
Doctor of Philosophy in Computational Physics

April 2020

Declaration of Originality

I herewith certify that all material in this thesis which is not my own work has been properly acknowledged.

Simon Charles Warder

Copyright Declaration

The copyright of this thesis rests with the author. Unless otherwise indicated, its contents are licensed under a Creative Commons Attribution-Non Commercial 4.0 International Licence (CC BY-NC).

Under this licence, you may copy and redistribute the material in any medium or format. You may also create and distribute modified versions of the work. This is on the condition that: you credit the author and do not use it, or any derivative works, for a commercial purpose.

When reusing or sharing this work, ensure you make the licence terms clear to others by naming the licence and linking to the licence text. Where a work has been adapted, you should indicate that the work has been changed and describe those changes.

Please seek permission from the copyright holder for uses of this work that are not included in this licence or permitted under UK Copyright Law.

Abstract

Storm surges pose a significant hazard to coastal communities worldwide. Accurate and reliable storm surge numerical models, combined with an understanding of model uncertainties, are therefore vital. In this work, an adjoint-capable numerical coastal ocean model, *Thetis*, is extended and used to perform a sensitivity analysis for a hindcast case study in the North Sea, revealing the spatial patterns of the sensitivity of modelled surges to three model inputs. These sensitivities are used to gain physical insight, and to perform uncertainty quantification for each of the model inputs. The results indicate that, while the greatest contribution to uncertainty is made by meteorological inputs, uncertain bottom friction is nevertheless significant.

This motivates a comparison of parameter estimation methods for a spatially varying bottom friction coefficient. This is performed for a tide-only case study consisting of the Bristol Channel and Severn Estuary. Here, a gradient-based optimisation method via the adjoint model is compared with Bayesian inference via a Markov Chain Monte Carlo algorithm, utilising a Gaussian process emulator as a surrogate for the full numerical model. Three friction parameters, based on the distribution of sediment types within the model domain, are estimated, with the results from each calibration method consistent within the estimated parameter uncertainties. Furthermore, the estimated parameters are found to reduce model-observation misfit for a second numerical model, TELEMAC-2D, suggesting that the calibration process has identified physically meaningful parameters.

Since such a model calibration relies on the availability of observation data, this work considers a framework for the identification of observation locations which will perform best in a parameter estimation exercise. In addition to an application within the Bristol Channel case study, this work takes steps towards guiding new observations in the Maldives, where present datasets are severely limited and the development of well-calibrated numerical models would be highly valuable.

Acknowledgements

I would like to thank my supervisors, in particular Matthew Piggott for ideas, discussions and opportunities, and Kevin Horsburgh for valuable input on all things storm surge. I am also grateful for input from friends and colleagues within the Applied Modelling & Computation Group, not only for scientific discussions, but for their ever-helpful responses to variations on ‘my code has stopped working again’.

I also wish to acknowledge the National Oceanography Centre for hosting me for an enjoyable month working on the storm surge aspects of this thesis. This work would not have been feasible without the support of the Research Computing Service at Imperial, or the CDT in Fluid Dynamics Across Scales.

Finally, thanks to my family and friends for making the last few years so enjoyable, and for all those tea breaks and lunchtimes.

Contents

List of Tables	13
List of Figures	15
1 Introduction	21
1.1 Motivation & objectives	21
1.2 Contributions	22
1.3 Publications	23
1.4 Thesis outline	23
2 Literature review	25
2.1 Tide-surge models in context	25
2.2 Tide-surge numerical modelling choices	28
2.3 Uncertainty in tide-surge modelling	31
2.3.1 Sources of uncertainty	31
2.3.2 Sensitivity analysis	32
2.3.3 Uncertainty quantification	34
2.3.4 Model calibration and data assimilation	34
2.3.5 Implications for new observations	37

3 Background	39
3.1 Shallow water equations	39
3.2 The finite element method	45
3.3 Adjoint modelling	47
3.4 Thetis	50
3.5 Gaussian process emulation	50
4 Adjoint-based sensitivity analysis and uncertainty quantification for a storm surge model	54
4.1 Introduction	54
4.2 Background	56
4.2.1 Definitions	56
4.2.2 Case study event: Storm Xaver	56
4.2.3 The UK operational storm surge model	57
4.3 Implementation of atmospheric pressure forcing within Thetis	58
4.4 Forward storm surge modelling	61
4.4.1 Model setup	61
4.4.2 Model calibration & validation	63
4.5 Sensitivity analysis & uncertainty quantification	67
4.5.1 Method	70
4.5.2 Results	73
4.5.3 Aside: analytic adjoint approach	79
4.6 Connection to ensemble methods	83
4.7 Model-free hazard assessment	88
4.8 Discussion	93
4.9 Summary	96

5 Bottom friction parameter estimation in the Bristol Channel	97
5.1 Introduction	97
5.2 Data, models and inputs	98
5.2.1 Data sources	98
5.2.2 Thetis model setup	99
5.2.3 TELEMAC-2D	99
5.2.4 Choices of calibration parameter space	100
5.3 Methods	101
5.3.1 Gradient-based optimisation via the adjoint	101
5.3.2 Bayesian inference	105
5.3.3 Assessment of calibrated parameters	110
5.4 Results: freely varying friction parameter	112
5.4.1 Results without regularisation	112
5.4.2 Results with regularisation	114
5.5 Results: sediment-based friction parameter	115
5.5.1 Synthetic experiment	115
5.5.2 Assimilation of real data	120
5.6 Discussion	125
5.6.1 Comparison of freely varying and sediment-based friction parameters	125
5.6.2 Comparison of calibration methods for sediment-based friction pa- rameter	126
5.7 Summary	129
6 Guiding new tidal observations	131
6.1 Introduction	131

6.2	The parameter estimation problem	132
6.3	Methods	133
6.3.1	Skewness method	133
6.3.2	Volume method	137
6.4	Application to the Bristol Channel	140
6.4.1	Background	140
6.4.2	Selection of locations from within existing data	142
6.4.3	Proposal of new observation locations	146
6.4.4	Characterising ‘good’ observation locations	152
6.5	Application to the Maldives	156
6.5.1	Background & model setup	156
6.5.2	Selection of bottom friction parameter space	158
6.5.3	Selection of optimal observation sites	159
6.5.4	Assimilation test: synthetic data	163
6.5.5	Response to observation uncertainty	165
6.6	Discussion	166
6.7	Summary	169
7	Conclusions	171
7.1	Summary of thesis achievements	171
7.2	Potential for future work	173
7.2.1	Application of adjoint methods to storm surge modelling	173
7.2.2	Model calibration	174
7.2.3	Proposal of new observations	174
References		176

List of Tables

6.1	Summary of values for each metric, for the optimal maps from each metric, selected from within existing observation locations. Note that optimal skewness corresponds to the minimum value, while optimal volume corresponds to the maximum value.	143
6.2	Summary of estimated parameters for the synthetic experiment, using optimal maps selected from within existing observation locations. Units: $s m^{-1/3}$	144
6.3	Summary of estimated parameters for the assimilation of real data, using optimal maps selected from within existing observation locations. Units: $s m^{-1/3}$	145
6.4	Summary of values for each metric, for the optimal maps from each metric, selected from the proposed observation locations.	149
6.5	Summary of estimated parameters for the synthetic experiment, using optimal maps selected from within proposed observation locations. Units: $s m^{-1/3}$	150

List of Figures

2.1	Schematic diagram of typical storm surge hazard modelling framework.	26
3.1	Definition of variables for the shallow water equations.	40
3.2	Original (left) and modified (right) shallow water variables, for the wetting-drying scheme by Kärnä et al. (2011).	43
4.1	Definitions of surge residual and skew surge.	57
4.2	Example mesh used for pseudo-1D atmospheric pressure test case.	59
4.3	Comparison of two spatial resolutions for the pseudo-1D atmospheric pressure test case, along the $y = 500$ m transect. Top: $\Delta x = 2500$ m. Bottom: $\Delta x = 625$ m.	60
4.4	Convergence test for pseudo-1D atmospheric pressure test case. Second order convergence is achieved.	60
4.5	Example mesh used for 2D atmospheric pressure test case.	61
4.6	Convergence test for 2D atmospheric pressure test case. Second order convergence is achieved.	62
4.7	Mesh used for North Sea tide-surge simulations. Tide gauge locations are labelled.	64
4.8	Two key physical features within the model domain. Blue region in north-east: Norwegian Trench, extracted from 200 m contour. Orange region, below centre: Dogger Bank, extracted from 20 m contour.	65
4.9	Calibration of the tide-only model with respect to the Manning coefficient n . The optimal choice is $n = 0.025 \text{ s m}^{-1/3}$.	66

4.10 Calibration of the surge model, with respect to the Charnock parameter α . The optimal choice is $\alpha = 0.028$	67
4.11 Comparison between Thetis model and observations for the Xaver surge event, at the eight tide gauge locations used for the calibration of the Charnock parameter. Solid line: observed residuals. Dashed line: modelled residuals using Thetis. The overall RMSE is 15.9 cm.	68
4.12 Comparison between CS3X model and observations for the Xaver surge event, at the eight tide gauge locations used for the calibration of the Charnock parameter within Thetis. Solid line: observed residuals. Dotted line: modelled residuals using CS3X. The overall RMSE is 16.4 cm.	69
4.13 Selected target locations for sensitivity analysis and uncertainty quantification. Three tide gauge locations are selected, along with an integrated measure along the section of coastline indicated by the red line.	71
4.14 Sensitivity of modelled skew surges to bottom friction coefficient. Units: $\text{m s}^{-1} \text{m}^{1/3} \text{m}^{-2}$ (metres of surge, per unit Manning coefficient, per unit area). Top left: North Shields. Top right: Immingham. Bottom left: Lowestoft. Bottom right: mean along coastline section.	75
4.15 Sensitivity of modelled skew surges to bathymetry. Units: $\text{m m}^{-1} \text{m}^{-2}$ (metres of surge, per metre of bathymetry, per unit area). Top left: North Shields. Top right: Immingham. Bottom left: Lowestoft. Bottom right: mean along coastline section.	77
4.16 Snapshots of the magnitude of the skew surge sensitivity at Immingham to wind stress at previous times, as labelled. Units: $\text{m Pa}^{-1} \text{m}^{-2} \text{s}^{-1}$ (metres of surge, per Pa wind stress, per unit area, per second).	78
4.17 Magnitude of the time-integrated sensitivity of modelled skew surges to wind stress. Units: $\text{m Pa}^{-1} \text{m}^{-2}$ (metres of surge, per Pa wind stress, per unit area). Top left: North Shields. Top right: Immingham. Bottom left: Lowestoft. Bottom right: coastline section. Note the logarithmic scale. . . .	80
4.18 Comparison of linearised response to wind stress and full model outputs for the surge residuals at North Shields, Immingham and Lowestoft.	86
4.19 Errors in the linearised response to wind stress, compared with full model outputs, for the surge residuals at North Shields, Immingham and Lowestoft. .	87

4.20 Schematic diagram of two approaches to the use of Taylor expansions to evaluate approximations to model outputs. Top: expansion about a deterministic forecast. Bottom: expansion about zero forcing. Solid lines show the response curve of the full numerical model. Dotted lines show the linearised response, via a Taylor expansion.	89
4.21 Comparison of approximated residual timeseries (dashed line) with results from the full numerical model (solid line).	92
5.1 Mesh used for all simulations within this chapter. Locations where tidal harmonic data are available are shown as green squares. Red circles indicate BODC tide gauges, where timeseries surface elevation data is available.	100
5.2 Distribution of sediment types: rock (black), gravel (grey), sand (white). Locations where tidal harmonic data are available are shown as green squares. Red circles indicate BODC tide gauges, where timeseries surface elevation data is available.	102
5.3 Histograms showing the errors between GPE outputs and full Thetis model runs for the 11 gauge locations, and across 10 random samples of the input parameters. The superimposed normal distributions have zero mean and variances estimated by the GPE.	108
5.4 Results from adjoint-based assimilation of timeseries data using L-BFGS-B algorithm, for a freely spatially varying Manning coefficient. Top: Evolution of misfit functional. Middle: RMS change in Manning coefficient from initial guess ($n = 0.02 \text{ s m}^{-1/3}$). Bottom: Convergence. Left: without regularisation. Right: with regularisation, $\gamma = 10^{-10}$	113
5.5 Optimised Manning coefficient field, without regularisation.	114
5.6 Results from the cross-validation method for selection of the regularisation parameter γ	115
5.7 Optimised Manning coefficient field, with regularisation term with $\gamma = 10^{-10}$	116
5.8 Posterior joint probability density function (PDF) obtained from MCMC sampling, based on assimilation of M2 harmonic amplitudes, using ‘synthetic’ observations and using a fixed $\sigma_C^2 = 0.0025 \text{ m}^2$. Black points/lines show original synthetic friction values.	118

5.9 Posterior joint PDF obtained from MCMC sampling, based on assimilation of M2, S2, N2 and K2 harmonic amplitudes, using ‘synthetic’ observations and using a fixed $\sigma_C^2 = 0.0025 \text{ m}^2$. Black points/lines show original synthetic friction values.	119
5.10 Posterior joint PDF obtained from MCMC sampling, based on assimilation of M2 harmonic amplitudes, using real observations.	122
5.11 Posterior joint PDF obtained from MCMC sampling, based on assimilation of M2, S2, K2 and N2 harmonic amplitudes, using real observations.	123
5.12 Results from adjoint-based assimilation of M2 harmonic data (left) and timeseries data (right) using L-BFGS-B algorithm. Top: Evolution of misfit functional. Middle: Evolution of estimated parameter values. Bottom: Convergence.	124
6.1 Examples of sensitivity vectors for well-conditioned (top) and poorly-conditioned (bottom) inverse problems, using a simple two-dimensional example. The skewness is low in the well-conditioned case, and high in the poorly-conditioned case.	136
6.2 Top: sensitivity vectors for an inverse problem exhibiting low skewness, but small sensitivity magnitudes. Bottom: sensitivity vectors exhibiting moderate skewness, but large sensitivity magnitudes.	138
6.3 The area between two sensitivity vectors.	139
6.4 Segment areas can be summed, generalising the volume-based measure to a greater number of model outputs.	140
6.5 Bristol Channel model domain, showing locations of existing data, labelled by an index for identification purposes. Background colours show sediment type: rock (black), gravel (grey) and sand (white).	141
6.6 Posterior PDF from the assimilation of synthetic data at the locations specified by the optimal-skewness map, selected from within existing observations. The prescribed friction coefficients (shown as black points/lines) are well recovered.	144
6.7 Posterior PDF from the assimilation of real data at the locations specified by the optimal-skewness map, selected from within existing observations.	145

6.8 Posterior PDF from the assimilation of synthetic data at the locations specified by the optimal-volume map, selected from within existing observations. The prescribed friction coefficients (shown as black points/lines) are well recovered.	147
6.9 Posterior PDF from the assimilation of real data at the locations specified by the optimal-volume map, selected from within existing observations. . .	148
6.10 Existing (numbered 0–15) and proposed (16–81) observation locations. . .	149
6.11 Posterior PDF from the assimilation of synthetic data at the locations specified by the optimal-skewness map, selected from the proposed observation locations. The prescribed friction coefficients (shown as black points/lines) are poorly recovered.	150
6.12 Posterior PDF from the assimilation of synthetic data at the locations specified by the optimal-volume map, selected from the proposed observation locations. The prescribed friction coefficients (shown as black points/lines) are well recovered.	151
6.13 Posterior PDF from the assimilation of synthetic data at the locations specified by the optimal-skewness map, selected from a filtered subset of the proposed observation locations. The prescribed friction coefficients (shown as black points/lines) are well recovered.	153
6.14 A negative correlation is observed between sensitivity magnitude and bathymetry.	154
6.15 Distributions of $\frac{\partial Q}{\partial n_1}$, $\frac{\partial Q}{\partial n_2}$ and $\frac{\partial Q}{\partial n_3}$ for observations Q made in rock regions. The greatest sensitivity magnitudes are shown with respect to n_1 , which is the Manning coefficient corresponding to rock.	155
6.16 Distributions of sensitivity to the sand coefficient (n_3) for each of the sets of observation points (rock locations, gravel locations, sand locations). The greatest sensitivities to the sand coefficient are exhibited by observations made in sand regions.	155
6.17 Bathymetry of the North Malé Atoll region.	157
6.18 Mesh used for tidal modelling of the North Malé Atoll.	158

6.19 Example of the peak velocity magnitude throughout the model domain. The greatest velocity magnitudes are found within the channels around the atoll rim.	159
6.20 Distribution of friction coefficients within the North Malé Atoll model do- main. Light blue: Deep water, n_1 . Darker blue: atoll interior, n_2 . Purple: coral reefs, n_3	160
6.21 Candidate observation locations within the North Malé Atoll domain. Most locations are within channels in the atoll rim, where velocities are greatest.	162
6.22 Optimal set of two observation locations within the North Malé Atoll do- main, selected via the maximum-volume method.	163
6.23 Optimal set of three observation locations within the North Malé Atoll domain, selected via the maximum-volume method.	164
6.24 Posterior PDFs from four synthetic experiments using optimal set of two locations, with $\sigma = 0.01 \text{ m s}^{-1}$. Black points indicate true parameters. . . .	165
6.25 Posterior PDFs from four synthetic experiments using optimal set of three locations, with $\sigma = 0.01 \text{ m s}^{-1}$. Black points indicate true parameters. . . .	166
6.26 Posterior PDFs from four synthetic experiments using optimal set of two locations, with $\sigma = 0.05 \text{ m s}^{-1}$. Black points indicate true parameters. . . .	167
6.27 Posterior PDFs from four synthetic experiments using optimal set of three locations, with $\sigma = 0.05 \text{ m s}^{-1}$. Black points indicate true parameters. . . .	168

Chapter 1

Introduction

1.1 Motivation & objectives

A storm surge is an increase in sea level due to a severe storm, caused by high winds and atmospheric pressure gradients which act to force water against coastlines. Allowing for investment in adaptation measures (e.g. flood defences), global flood losses in 136 of the world's largest coastal cities have been estimated to rise from US\$6 bn per year in 2005 to US\$60–63 bn per year in 2050 (Hallegatte et al., 2013). Globally, the future increase in extreme sea levels (Stocker et al., 2013) will result in critical flood defence thresholds being reached more frequently and therefore the risk of flooding will increase. The UK is vulnerable to storm surges, particularly along its North Sea coast; a large number of severe storms have impacted the UK in the last century (Haigh et al., 2016), with the two most severe of those events occurring in the North Sea in 1953 and 2013. The approximate economic impacts of the coastal flooding resulting from these events (using 2014 figures) were £1.2 bn and £0.25 bn respectively; the impact of the latter event was reduced through mitigation action taken after the 1953 event (Wadey et al., 2015). With continued development of the coastal zone in flood risk areas (ASC, 2014), the role of storm surge modelling remains vital.

The challenges in modelling storm surges stem from their multi-scale nature, and the variety of physical effects which must be included. The area of the North Sea, for example, is 575,000 km², and the wavelength of the tides is $\mathcal{O}(1000 \text{ km})$. A storm surge model must therefore operate on these large scales, while also adequately resolving coastlines, which are a well-known example of naturally-occurring fractals (Mandelbrot, 1983). Since wind-generated waves with wavelengths of order 10 m are key to the surge-generating atmosphere-ocean interaction (Brown and Wolf, 2009), they must also be represented

within a surge model. These waves are typically accounted for either by coupling to a (spectral) wave model, or the use of an adequate parameterisation (Brown et al., 2013). Inherently three-dimensional processes such as loss of momentum due to friction at the sea floor are also typically unresolved, even by three-dimensional models, and are therefore parameterised.

The introduction of each of these physical effects introduces assumptions and model parameters which induce uncertainty in surge model outputs. This is compounded by the coupling between multiple models for atmosphere, ocean and waves, and the need to propagate uncertainty throughout this framework. Uncertainty in meteorological inputs dominates surge forecast uncertainty (Flowerdew et al., 2013), with uncertainties in peak surge heights in excess of 1 m commonplace, depending on the surge event and the forecast lead time. While uncertainties induced by other sources (including bottom friction parameterisation and other input data such as bathymetry and boundary conditions) tend to be smaller, it is nevertheless important to quantify their contribution to overall model uncertainty. Furthermore, since these sources are not specific to a particular surge event, their effects can be minimised by model calibration methods, using previous storm surge case studies or tide-only modelling.

The first objective of this thesis is to create a storm surge model of the North Sea using the novel numerical coastal ocean model *Thetis*, and to utilise the model's adjoint to perform sensitivity analysis and uncertainty quantification for a storm surge hindcast case study. Following the results of this uncertainty quantification exercise, the second objective is to compare methods and datasets for model calibration, estimating a spatially varying bottom friction parameter within a smaller scale tide-only case study, via the assimilation of sea surface level observations. The final objective is to test frameworks for the selection of new observation locations, motivated by the parameter estimation problem.

1.2 Contributions

The previous use of adjoint methods for storm surge sensitivity analysis and uncertainty quantification is limited. The first objective of this thesis builds on previous work by Wilson et al. (2013), who considered only one storm surge model output, and investigated sensitivity to only one model input, namely wind stress due to meteorological forcing. In the work presented in this thesis, three model inputs are considered (wind stress, bottom friction, bathymetry), and the sensitivity analysis and uncertainty quantification are carried out for multiple model output locations. This provides additional physical

insight, and facilitates a comparison of different sources of uncertainty. This work also represents the first application of *Thetis* to storm surge modelling.

The problem of assimilating data in order to estimate a spatially varying bottom friction parameter is well studied in the literature. However, the work of this thesis constitutes the first direct comparison of gradient-based optimisation via the adjoint and Bayesian inversion via a Markov Chain Monte Carlo (MCMC) algorithm.

Finally, the proposal of observation locations utilises an existing framework by Butler et al. (2015), testing its applicability outside of its original context in a specific model inversion algorithm. This work further proposes a modified framework for observation location selection, and compares the two methods.

1.3 Publications

Parts of the work presented in this thesis have been submitted for publication.

Chapter 4 is an amalgamation of a conference article (Warder et al., 2019) and a journal article (in review) (Warder et al., 2020b), with sections 4.3 and 4.7 additional material for this thesis.

Much of chapter 5 has also been submitted for publication (Warder et al., 2020a), with the consideration of a freely spatially varying friction parameter (sections 5.4 and 5.6.1) added for this thesis.

1.4 Thesis outline

Chapter 2 reviews the relevant literature, placing tide-surge models in a broader forecast/hazard assessment context and addressing the numerical modelling choices available. Particular attention is given to uncertainty in tide-surge modelling, including the sources of uncertainty, approaches to sensitivity analysis and uncertainty quantification, and how uncertainty can be reduced using model calibration and data assimilation methods.

Chapter 3 presents the relevant background to the work undertaken within this thesis, including the choice of underlying model equations and the numerical methods used for their approximate solution, and the principles of adjoint methods. This includes a description of the modelling software used. Since Gaussian process emulation is used in both chapters 5 and 6, it is also described in chapter 3.

Chapter 4 presents the implementation and testing of atmospheric pressure forcing within Thetis, and the application of Thetis (and its adjoint) to perform a hindcast, sensitivity analysis and uncertainty quantification for Storm Xaver (from December 2013) in the North Sea. Based on a simple estimate of the uncertainty in the model's bottom friction coefficient, the results of this chapter indicate that uncertain bottom friction induces an uncertainty of around 20 cm in modelled surge heights, which is significant in the context of surge hazard, and motivates the remainder of the thesis. Chapter 4 also draws a connection to ensemble uncertainty quantification methods and presents a novel model-free scheme for approximating storm surges.

Motivated by the results from the uncertainty quantification of chapter 4, chapter 5 approaches the problem of bottom friction parameter estimation, taking the Bristol Channel and Severn Estuary as a case study. In particular, this chapter compares two methods for the estimation of a spatially varying bottom friction parameter, with the objective of establishing parameters which are physically meaningful and therefore applicable across multiple numerical models. This is achieved via the assimilation of observations of sea surface levels, in the form of timeseries and harmonic analysis data.

Following this application of model calibration methods in a data-rich region, chapter 6 addresses the issue of how to identify optimal locations for new observations. This is motivated in part by the results of chapter 5, where the available observation data is insufficient to independently constrain all of the considered input parameters, and also by tidal modelling of the Maldives, where observation data is severely lacking, and model validation and calibration are not currently possible.

Finally, chapter 7 summarises the findings of this thesis, and discusses possible avenues for future work.

Chapter 2

Literature review

The focus of this thesis is on the numerical modelling of tides and storm surges, with an emphasis on dealing with uncertainty. Section 2.1 first places tide-surge modelling within a broader modelling framework, and section 2.2 reviews the choices available for regional tide-surge modelling, in terms of model equations and numerical discretisations. Section 2.3 reviews approaches to treating uncertainty in tide-surge models, including the application of techniques for sensitivity analysis, uncertainty quantification and parameter estimation.

2.1 Tide-surge models in context

Figure 2.1 outlines a typical modelling framework, motivated by the forecasting and hazard assessment of storm surges. The diagram indicates the use of four models, although in practice two or more models may be combined, and roughly follows the framework of operational flood forecasting in the UK (Stansby et al., 2013). Each block in the diagram includes different physical processes and/or spatial scales, which are described here.

Atmospheric models

In calm atmospheric conditions, the dynamics of shallow coastal seas are dominated by the astronomical tide. The accurate prediction of tides (on a single-locations basis) long pre-dates numerical methods (from Kepler's initial ideas (Kepler, 1609) to Doodson's work on harmonic analysis (Doodson, 1921)). Storm surges, however, are generated by forces exerted on the ocean by the atmosphere, specifically surface stress due to wind,

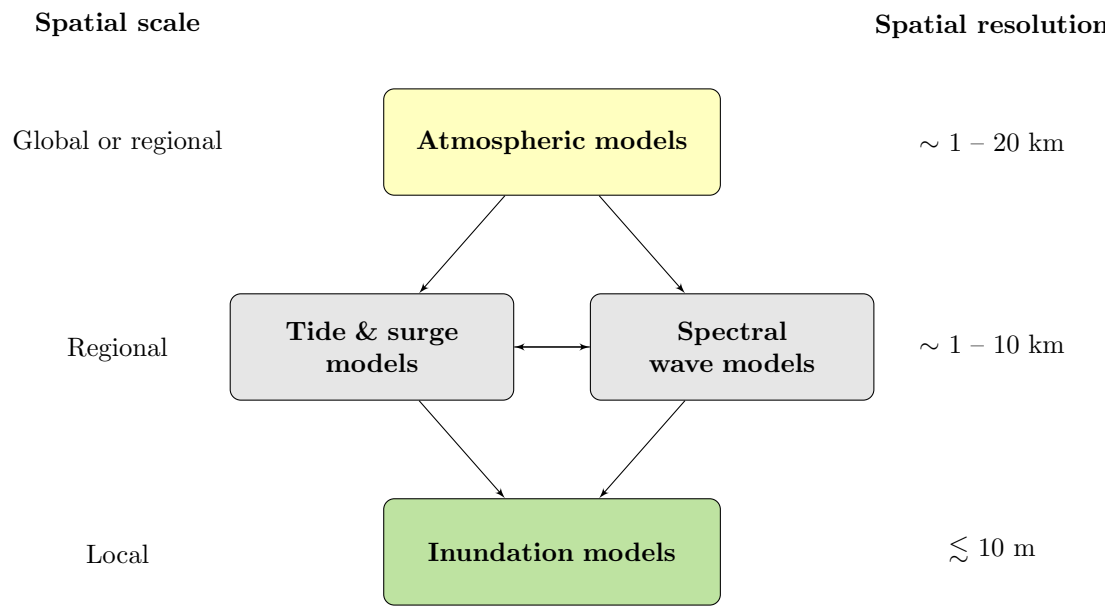


Figure 2.1: Schematic diagram of typical storm surge hazard modelling framework.

and horizontal gradients in atmospheric pressure (Gill, 1982). In the modelling of storm surges, therefore, atmospheric input is vital, and is typically provided by an atmospheric numerical model, from which wind velocities at a fixed height (often 10 m) above sea level, and the atmospheric pressure, are obtained. Alternatively, a parametric hurricane model, such as that by Holland (1980), may be utilised to synthesise storm surge events; this is common in probabilistic studies of storm surge impact, often motivated by climate change (Lin et al., 2012). Atmospheric modelling is typically undertaken on global or regional scales, at spatial resolutions of around 1 – 20 km. The UK Met Office, for example, operates a regional meteorological ensemble at a resolution of approximately 2.2 km (with a 1.5 km deterministic model) (Hagelin et al., 2017), and a global meteorological ensemble model at approximately 20 km resolution (with a 10 km deterministic model)¹.

For the storm surge case study taken within this thesis, a hindcast of the meteorological conditions was provided by the National Oceanography Centre (personal communication, 2018).

Tide & surge models

As already described, the influence of the atmosphere on the ocean during a storm event generates perturbed sea surface heights, i.e. a storm surge. Regional scale models of the

¹<https://www.metoffice.gov.uk/research/approach/modelling-systems/unified-model/weather-forecasting>

ocean, typically at resolutions of a few km, are used to model ocean dynamics under surge forcing conditions, with modelled sea surface heights at the coastline representing the storm surge hazard. Such models typically employ the Navier-Stokes equations under the Boussinesq approximation, either in two or three dimensions. Since tide-surge interaction can have a significant influence on the hazard (Horsburgh and Wilson, 2007), tides are included within ocean models, via a boundary condition and/or the addition of astronomical forces within the model's governing equations. Tide-only modelling (in the absence of atmospheric forcing) is also often of interest, e.g. for tidal energy (Neill et al., 2018) or sediment transport applications (Xie et al., 2009).

Tide-surge modelling is the focus of this thesis, and the modelling and discretisation choices available for tide-surge modelling are discussed in detail in section 2.2.

Spectral wave models

The dominant mechanism through which winds transfer momentum to the ocean is via wind-generated waves (Brown and Wolf, 2009). These waves determine the drag between the atmosphere and ocean, but cannot be explicitly resolved in regional scale tide-surge models due to their short wavelength and period (compared with tides and surges). A modeller has two choices for dealing with this coupling. One approach is to couple the tide-surge model to a numerical spectral wave model. Such models solve a wave energy equation, by discretising according to the direction and frequency of the waves, in addition to a spatial discretisation. The effect of waves on ocean-atmosphere coupling can thereby be explicitly modelled. Commonly used spectral wave models for coupling with tide-surge models include SWAN (e.g. Suh et al. (2015)), WaveWatchIII (e.g. Kim and Yamashita (2008)) and WAM (e.g. Brown et al. (2010)).

However, a simpler approach which does not require an additional numerical model is to introduce a bulk parameterisation, utilising a drag coefficient which depends on the wind velocity; the empirical parameterisations of Smith and Banke (1975) and Wu (1982) are common choices. A parameterisation which accounts for the logarithmic law of the atmospheric boundary layer was introduced by Charnock (1955), and is another common choice, although its use requires the selection of an appropriate 'Charnock' parameter (Wu, 1980). Bulk parameterisations take some account of the effect of wind waves in enhancing the ocean-atmosphere drag coefficient, but may not be valid when the wind and waves are not in equilibrium (Brown and Wolf, 2009), and do not account for wave radiation stress or the influence of waves on the bed friction (Liu et al., 2006; Murty et al., 2019). A Charnock parameterisation is used throughout this thesis, as is common

Model	Mesh type	Discretisations
MITgcm	Structured	Finite volume
ROMS	Structured	Finite volume
Delft3D	Structured	Finite difference or finite volume
FVCOM	Unstructured	Finite volume
TELEMAC	Unstructured	Finite volume or finite element
ADCIRC	Unstructured	Finite element

Table 2.1: Some popular numerical models for coastal ocean modelling of tides and/or surges, and their corresponding mesh types and discretisation options.

in barotropic storm surge models (Brown et al., 2013) as a compromise between accuracy and computational cost.

Inundation models

The modelling of inundation is typically carried out using a separate model (or models), localised to the region of interest, using small domains forced using model outputs from regional scale models (Stansby et al., 2013). Such models are ideally required to resolve coastal defences and, depending on the inundated region, buildings and streets. Inundation can occur as a consequence of surge-induced sea surface levels, and may also require the inclusion of further models for wind-waves (Wu et al., 2018), overtopping (Pullen et al., 2007; De Rouck et al., 2009), and erosion or breaching of coastal defences (McCall et al., 2010; Bolle et al.). Inundation modelling is included within the example framework of figure 2.1 to emphasise that tide-surge models exist within a broader framework, and that tide-surge model outputs may be utilised by smaller scale studies. However, surge-induced sea surface heights are often taken as a key measure of hazard in their own right (Williams et al., 2016), and inundation modelling is not considered further within this thesis.

2.2 Tide-surge numerical modelling choices

There are several choices available regarding both the equations used to model tides and surges, and the discretisations used to approximate their solution via numerical methods. Some popular coastal ocean models, and their mesh types and discretisation options, are summarised in table 2.1, and the key modelling choices are discussed further here.

2D and 3D modelling

Fluid flow is described by the Navier-Stokes equations. In the context of regional coastal ocean numerical modelling, it is common to simplify the Navier-Stokes equations under the Boussinesq and hydrostatic assumptions (Kärnä et al., 2018). The Boussinesq assumption requires sufficiently small variation in density (such that its variation is neglected in all but the buoyancy term of the Navier-Stokes equations), and has the consequence that the fluid is modelled as incompressible. The hydrostatic assumption is that vertical accelerations within the fluid are negligible compared with the acceleration due to gravity, and therefore that the gravitational force is balanced by the vertical pressure gradient. While vertical acceleration has been neglected, the resulting set of equations are nevertheless three-dimensional, and commonly solved numerically by a discretisation into vertical layers, as is the case in ROMS (Shchepetkin and McWilliams, 2005), Delft3D (Delft Hydraulics, 2019) and FVCOM (Chen et al., 2003).

Further simplification can be made under the assumption that velocity is independent of the vertical coordinate, and therefore that the water is well approximated as moving in columns. This approximation is valid when the relevant horizontal length scales are much greater than the water depth, and typically holds well for hydrodynamics on continental shelves. In the North Sea, for example, water depths are typically $\mathcal{O}(100 \text{ m})$, while the wavelength of the tide is $\mathcal{O}(1000 \text{ km})$. This assumption results in the two-dimensional shallow water equations.

Since different equations are suited to different problems, many models offer flexibility in their underlying equations; for example, Delft3D (Delft Hydraulics, 2019), TELEMAC (Hervouet, 2007; Janin et al., 1992) and ADCIRC (Luettich and Westerink, 2004) all offer two- or three-dimensional modes of operation. Since the Boussinesq, hydrostatic and shallow water assumptions hold well for the case studies within this thesis, the shallow water equations are used throughout. These equations are described in greater detail in chapter 3.

Structured and unstructured meshes

All mainstream coastal ocean models are Eulerian in nature, and therefore require a mesh with which to discretise and solve the governing equations. Meshes fall into two categories, as differentiated in table 2.1: structured and unstructured. Models on structured meshes, such as those used by finite difference and some finite volume methods, tend to offer better computational performance than those on unstructured meshes (Danilov, 2013). However,

while the use of curvilinear grids (Ly and Luong, 1999) or nested meshes (Debreu et al., 2012) does allow some flexibility, structured meshes are not well suited to multi-scale modelling or representing complex coastlines. For example, issues can arise from the representation of coastal boundaries as a ‘staircase’ (Pain et al., 2005).

Unstructured meshes, on the other hand, offer great flexibility, with mesh elements often varying in size by orders of magnitude throughout the domain (Avdis et al., 2016), making them well suited to ocean modelling where geometric features typically vary in length scale from tens of metres to hundreds of kilometres (Avdis et al., 2018). As a result, mesh element edges can be aligned with coastal boundaries, avoiding many of the issues of structured meshes. While such multi-scale modelling can impose strong restrictions on the time step via the Courant number, this is often mitigated by the use of (semi-)implicit timestepping methods (Walters et al., 2007). The governing equations are typically discretised by the finite volume or finite element methods for solution on unstructured meshes. Unstructured meshes are used throughout this thesis.

Discretisation

The models of table 2.1 vary between finite difference, finite volume and finite element discretisations. As discussed above, the choice of discretisation is related to the choice of mesh type, and each discretisation also offers its own advantages. The finite volume method is common, and is utilised by MITgcm (Marshall et al., 1997), ROMS (Shchepetkin and McWilliams, 2005), Delft3D (Delft Hydraulics, 2019), FVCOM (Chen et al., 2003) and TELEMAC (Hervouet, 2007). The finite volume method offers good computational performance and is suited to advection-dominated problems (Kärnä et al., 2018).

The continuous-Galerkin (CG) finite element method, such as that used by ADCIRC (Luettich and Westerink, 2004), is suited to solving elliptic problems (Kärnä et al., 2018), but is typically less efficient than the finite volume method (Danilov, 2012). The discontinuous-Galerkin (DG) finite element method shares some of the advantages of finite volume methods; it is fully conservative, suited to advection problems, and offers high-order accuracy (Kärnä et al., 2018).

Within this thesis, modelling is undertaken using a discontinuous-Galerkin finite element method. The modelling framework is discussed in greater detail in chapter 3.

2.3 Uncertainty in tide-surge modelling

Tide-surge models require a variety of inputs and, as demonstrated by figure 2.1, exist within a broader modelling framework. Awareness of uncertainty in model inputs, and the consequences on model outputs, is therefore important, particularly within a forecast scenario. This section first reviews possible sources of uncertainty within tide-surge modelling. Approaches to sensitivity analysis and uncertainty quantification are then discussed, whereby the effect of uncertain inputs can be analysed and understood. Finally, methods for overcoming uncertainty are reviewed.

2.3.1 Sources of uncertainty

Sources of uncertainty within a general numerical model can be divided into four groups (Wagener and Pianosi, 2019): the choice of governing equations; the discretisation (including mesh and timestepping scheme); input parameters; and input data. The focus within this thesis is on the final two of these uncertainty sources, and the major uncertainties in the context of tide-surge modelling are:

- (i) **Meteorological inputs** As indicated in figure 2.1, tide-surge models rely on atmospheric data, which is typically taken from a meteorological model. In a forecast scenario, uncertain meteorological inputs are the dominant source of uncertainty (Flowerdew et al., 2013), and can often induce uncertainties on the order of 1 m (Flowerdew et al., 2010). For example, at a forecast lead time of 24 hours for the December 2013 Storm Xaver event (which is taken as a case study in chapter 4), the spread in the operational forecast ensemble for Immingham in the Humber Estuary was approximately 1 m (National Oceanography Centre, personal communication 2018).
- (ii) **Bottom friction coefficient** Friction between the ocean and the sea bed arises due to a boundary layer at the interface, and due to form drag induced by bathymetry undulations. The resulting momentum loss is not explicitly captured in coastal ocean models, but is instead typically incorporated via a parameterised drag term in the governing equations, which relates the water velocity to a frictional force. There are many possible choices of drag parameterisation (Zhang et al., 2011; Döös et al., 2004), each of which introduce a drag parameter which cannot be directly measured, and which in principle also varies spatially. Even when it can be related to land or sea floor classification using well-established tables, this parameter still carries significant

uncertainty (Mayo et al., 2014), and has been treated with sensitivity analysis and model calibration techniques in several studies, such as those by Maßmann (2010a); Lu and Zhang (2006); Wang et al. (2014).

- (iii) **Bathymetry** There are numerous widely available sources for bathymetric data, such as GEBCO² and Digimap³. However, due to finite resolution, morphological change, and errors in data acquisition, the use of bathymetric datasets introduces uncertainty into tide-surge models, as studied by Mourre et al. (2004); Maßmann (2010a); Heemink et al. (2002).
- (iv) **Boundary conditions** Regional scale tidal models typically impose tides via boundary conditions, which are generated from tidal harmonic databases such as the *TPXO* dataset (Egbert and Erofeeva, 2002). However, this can introduce errors, either directly from errors in the underlying dataset, or its implementation (e.g. choice of harmonic constituents). As such, it is common to perform sensitivity analysis and model calibration/data assimilation exercises to tidal boundary conditions; this has been performed by Chen et al. (2014); Maßmann (2010a); Heemink et al. (2002); Zhang and Chen (2013).

The above list is not exhaustive. For example, Li et al. (2013) use data assimilation techniques to simultaneously correct for uncertain initial conditions and a wind stress drag coefficient, and Heemink et al. (2002) also include spatially varying vertical viscosity in their parameter estimation study. However, the four uncertainty sources listed above are the most widely treated sources of uncertainty within tide-surge modelling.

2.3.2 Sensitivity analysis

Sensitivity analysis and uncertainty quantification are closely related, with significant similarity and compatibility in their methods. A common distinction between the two is that the focus of uncertainty quantification is on quantifying uncertainty in a model's output, while sensitivity analysis apportions uncertainty to different model inputs (Pianosi et al., 2016; Saltelli et al., 2008). Both sensitivity analysis and uncertainty quantification are therefore important in understanding uncertainty in tide-surge models, which can arise from a variety of sources (as described above).

Within operational storm surge forecasting, uncertainty is known to be dominated by meteorological inputs (Flowerdew et al., 2013). For this reason, sensitivity analysis as

²<https://www.gebco.net/>

³<https://digimap.edina.ac.uk/>

defined above (apportioning uncertainty to different inputs) is rarely performed, although recent work by Sochala et al. (2019) used a polynomial chaos expansion approach to perform storm surge sensitivity analysis with respect to storm track, peak wind velocity and bottom friction coefficient. However, there are a number of purposes of sensitivity analysis, as identified by Pianosi et al. (2016). One such purpose is *ranking*, where the aim is to sort model inputs by their overall influence on a given model output. While it is known that meteorological uncertainty dominates surge forecasts, ranking the remaining model inputs by their influence on surge model outputs is nevertheless valuable. Since these other model inputs do not depend on an individual surge event, their uncertainty can be reduced through data assimilation or model calibration exercises, based on previous surge events or tide-only modelling. Ranking their influence on surge model outputs helps to identify which of these inputs to prioritise with such methods, and is one of the aims of chapter 4 of this thesis.

A second purpose of sensitivity analysis which also motivates chapter 4 is to gain physical insight into the modelled system. Sensitivity analysis has previously been performed for the purpose of gaining physical insight in coastal oceanographic contexts by Maßmann (2010a); Nowak (2015); Villaret et al. (2016), and in a storm surge modelling context by Wilson et al. (2013); Sochala et al. (2019).

Pianosi et al. (2016) distinguish between global and local sensitivity analysis. In global sensitivity analysis, variations in model inputs over their entire variability space are considered (Wagener and Pianosi, 2019); such an analysis would be appropriate in the context of a statistical study of storm surge hazard. However, in a short-range forecast scenario, good estimates for all the uncertain model inputs are available. Uncertainties are sufficiently small that a local sensitivity analysis is sufficient, where perturbations in model inputs around an expected value are considered.

One technique for local sensitivity analysis is to calculate derivatives of model outputs with respect to model inputs (Pianosi et al., 2016). One way this can be achieved is by computing model outputs for perturbed values of model inputs, and approximating derivatives using finite differences. However, this approach requires $M + 1$ forward model runs, where M is the number of input parameters (or the dimension of the input parameter space). This rapidly becomes unfeasible for inputs of high dimension (e.g. spatially varying model inputs such as bathymetry or boundary conditions). For this reason, adjoint methods are commonly applied to sensitivity analysis (e.g. Sandu et al. (2005); Sykes et al. (1985); Hill et al. (2004)), and are used within chapter 4 of this thesis. Adjoint methods facilitate the computation of the gradient of a model output with respect to a vector of model inputs, at a computational cost which is independent of the length of the

input vector, and are discussed in detail in chapter 3.

2.3.3 Uncertainty quantification

Ensemble methods are the standard approach for quantifying uncertainty in surge model outputs due to uncertain meteorological inputs (Flowerdew et al., 2010; de Vries, 2009), and are also used within numerical weather prediction (Bowler et al., 2009; Buizza et al., 2005). In an ensemble method, the surge model is run multiple times, with each run forced by a different member of a meteorological forecast ensemble, constituting samples from the uncertain distribution of meteorological conditions. These ensemble members can be random, or carefully selected e.g. via singular value decomposition (Diaconescu and Laprise, 2012).

However, gradient-based methods via adjoint modelling can also be used for quantifying uncertainty. The (linear) variation in a model output is related to a perturbation in a model input by an inner product of the input perturbation with the adjoint-derived sensitivity (Smith and Heimbach, 2019). Uncertainty quantification can therefore also be carried out via adjoint methods. Wilson et al. (2013) use adjoint-derived model sensitivities to quantify uncertainty in a storm surge model output due to uncertain wind stress; this is achieved by mapping an ensemble of wind stress inputs onto surge model outputs, via the adjoint-derived sensitivity.

Chapter 4 of this thesis extends this existing literature by using adjoint methods to quantify uncertainty due to multiple model inputs, and for multiple model output locations. Chapter 4 also performs a preliminary investigation into the combined use of adjoint and ensemble methods for uncertainty quantification, and in the use of adjoint methods to construct models for rapid hazard assessment.

2.3.4 Model calibration and data assimilation

Model calibration can be defined as “the process of estimating the model parameters by maximising the model fit to (or at least consistency with) observations” (Pianosi et al., 2016). Within many parameter estimation studies, this term is used interchangeably with ‘data assimilation’.

Data assimilation techniques have long been applied in operational numerical weather prediction (Houtekamer and Mitchell, 1998) using a variety of methods including statistical interpolation and Kalman filtering (Lorenc, 1981), three-dimensional variational

(3DVAR) (Parrish and Derber, 1992) and, more recently, 4DVAR (Gauthier et al., 2007) approaches. These methods tend to be focused on updating a model's initial conditions, and are performed periodically to improve operational forecasts based on near real-time observations. While there is similarity in some of the methods employed, this form of data assimilation is not the focus of this thesis. Instead, the emphasis here is on one-off model calibration exercises in order to estimate parameters and model inputs which are, or are assumed to be, constant in time.

The formulation and solution of a model calibration problem can be divided into two main steps. Firstly, the model inputs must be defined, and secondly, a suitable parameter estimation technique must be employed.

Input parameter space

In any model calibration procedure, the first step is to select the model input(s) or parameter(s) to estimate. As already discussed, the bottom friction, bathymetry and boundary conditions are common choices. Since the calibration process is largely agnostic to the specific model input selected, the focus here is on the bottom friction coefficient. The chosen input must then be represented by a selected number of degrees of freedom, with several choices commonly used.

For bottom friction coefficient, the simplest possible approach is to assign a spatially uniform parameter. This is the commonly taken approach for many applications, both idealised as well as realistic. In contrast, the most complex possible choice is to allow the bottom friction coefficient to vary freely over the whole domain, i.e. to represent the bottom friction parameter using the same number of degrees of freedom as the model state variables. However, uniquely constraining such a large number of degrees of freedom would require a significant volume of observation data, and it is therefore common to supplement the observation data with a form of regularisation to avoid this 'over-fitting' problem (Maßmann, 2010b).

Intermediate complexity in the friction coefficient can be achieved via several approaches. One common approach is the so-called independent points scheme, where the friction coefficient field is determined by interpolation from a selected number of 'independent points' (Zhang et al., 2011; Chen et al., 2014), where the number of points can be selected appropriately based upon the volume of data to be assimilated, or the expected spatial variation in the input parameter. These independent points may be distributed uniformly, or according to physical features such as the bathymetry gradient (Lu and Zhang, 2006). A second intermediate-complexity approach is employed by Heemink et al. (2002), where the

model domain is divided into regions of similar influence on the model-observation misfit, calculated using an adjoint gradient-based method, also taking into account physical features such as amphidromic points and tidal phase lines.

A third approach is to incorporate other prior knowledge of the system. Guillou and Thiébot (2016) divide the domain according to the type of sediment found on the sea floor, since this determines the roughness length of the surface, and therefore the friction between the ocean and sea bed. Similar approaches are taken by Graham et al. (2017), where the domain is divided according to land classification types, and Sraj et al. (2014b), where the domain is divided by bathymetry contours.

Calibration technique

Once the input parameter space has been defined, there are numerous possible techniques for performing model calibration. The assumption is that there exists a set of observations, and that the aim of model calibration is to reduce the misfit between these observations and model outputs.

One common approach is to formulate the model calibration as an optimisation problem. Specifically, the model-observation misfit is defined mathematically, typically denoted J , and a suitable optimisation algorithm used to explicitly minimise this misfit. For input parameters with a small number of degrees of freedom (typically one degree of freedom corresponding to a spatially uniform input parameter), a simple brute force approach can be used; the model can be run a large number of times, each with a different value for the input parameter from a prior distribution (or feasible range), and the parameter which minimises J is found (Guillou and Thiébot, 2016).

This approach rapidly becomes unfeasible as the number of degrees of freedom increases, due to the computational cost of running the model with many combinations of parameters. For higher degrees of freedom, the use of adjoint-capable models (Chen et al., 2014; Lu and Zhang, 2006; Maßmann, 2010b,a; Zhang et al., 2011; Heemink et al., 2002) or other gradient-calculation methods (Sraj et al., 2014a) is common, as they allow the gradient of the model-observation misfit to be computed efficiently with respect to an arbitrarily large set of input parameters. This gradient information permits the use of efficient gradient-based optimisation algorithms in seeking the minimum model-observation misfit, and hence finding the optimal choice of input parameters, for any of the choices of parameter space outlined above. However, unless the Hessian is also computed alongside the gradient (Sraj et al., 2014a), such gradient-based methods do not provide a direct

estimate of uncertainty in the calibrated parameters. A second drawback of the gradient-based approach is that, depending on the choice of optimisation algorithm, a sub-optimal set of parameters may be returned if the algorithm terminates at a local minimum in the misfit functional J .

Another common approach to parameter estimation is Bayesian inversion, often via Markov Chain Monte Carlo (MCMC) methods (Hall et al., 2011; Sraj et al., 2013, 2014b). Such methods have the advantage over adjoint-based methods that they do not require the computation of the derivative of the numerical model (which can be hard to implement for complex codes (Mitusch et al., 2019)), and that they also yield estimates of the uncertainty in the inferred parameters. However, they rely on large numbers of forward model runs ($\mathcal{O}(10^4)$ or more is common (Tagade et al., 2013; Pall et al., 2020; Haario et al., 2001; Sraj et al., 2014b)), and the numerical model is therefore usually substituted with a fast surrogate model such as a Gaussian process emulator (Tagade et al., 2013) or polynomial chaos expansion (Sraj et al., 2014b), which is trained using a selected number of full model runs spanning the input parameter space (or prior distribution).

Statistical data assimilation using Kalman filters is commonly used for state estimation as described above, but has also been used for ‘joint estimation’ of both model state and uncertain input parameters (Evensen, 2009; Anderson, 2001; Aksoy et al., 2006), and also for parameter estimation alone (Mayo et al., 2014). However, the adjoint and Bayesian inversion approaches to parameter estimation are more common, and statistical data assimilation is not considered within this thesis.

While Sraj et al. (2014a) have used a polynomial chaos expansion to compare gradient and Bayesian approaches for wind drag parameter estimation, a detailed comparison of adjoint and Bayesian inference approaches has not been carried out in the context of parameter estimation in regional tidal models. This is addressed by chapter 5 of this thesis.

2.3.5 Implications for new observations

An implicit assumption in the use of model calibration techniques is that there is sufficient observation data available to constrain the unknown parameters. However, this may not always be the case, and it is therefore of significant value to be able to propose new observation locations, motivated by a future calibration exercise. A related idea is that of redundancy in observation data; while a sensible approach to model calibration is to assimilate all available observation data, this data is likely to contain a significant amount of redundant information about the unknown parameters.

Butler et al. (2015) define and solve a parameter estimation problem via a measure-theoretic approach, as an alternative to the calibration techniques described above. Within this framework, the number of model samples required to compute the parameter distribution (i.e. to solve the inversion problem) given a set of observation data is related to a measure of the condition of the inverse problem, namely the ‘skewness’ of the Jacobian matrix of the map from input parameters to the observation space. This information means that the map from parameters to observations, i.e. the choice of what, where and when to make observations for future data assimilation, can be selected in order to produce a well-conditioned inverse problem. This framework is used by Graham et al. (2017) to estimate bottom friction parameters using a real-world hurricane case study, where a variety of choices are made for which subset of observation data to assimilate, based on this skewness measure. They show that the minimisation of this skewness measure results in well-conditioned inverse problems, i.e. that a well-selected set of observation locations provides a better constraint on the unknown parameters than a poorly-selected set of observation locations.

This has implications for the proposal of new observations for the purposes of model calibration exercises, and is explored in chapter 6 of this thesis.

Chapter 3

Background

As described in chapter 2, there exist a wide variety of possible modelling assumptions, discretisations and software which can be applied to tide and storm surge modelling. This chapter will first outline the underlying model equations used throughout this thesis, namely the shallow water equations, in section 3.1. The discretisation of these equations by the finite element method is described in section 3.2, and the concept of adjoint modelling is described in section 3.3. The *Thetis* software implementing the governing equations within an adjoint-capable finite element framework is described in section 3.4. Finally, Gaussian process emulation is described in section 3.5, which is used within this thesis to create fast surrogate models for use in place of the full numerical model where large numbers of model runs are required.

3.1 Shallow water equations

The shallow water equations are used throughout this thesis for the modelling of regional scale coastal ocean flow. For simplicity of exposition, here these equations are derived from the Euler equations, which assume an inviscid, incompressible fluid with constant density, and are given by

$$\nabla \cdot \mathbf{u} = 0, \tag{3.1a}$$

$$\frac{D\mathbf{u}}{Dt} + \frac{1}{\rho} \nabla p + g\hat{\mathbf{z}} = 0, \tag{3.1b}$$

where \mathbf{u} is the three-dimensional velocity vector with components (u, v, w) in a Cartesian coordinate system, g is the gravitational acceleration which acts in the negative z -direction

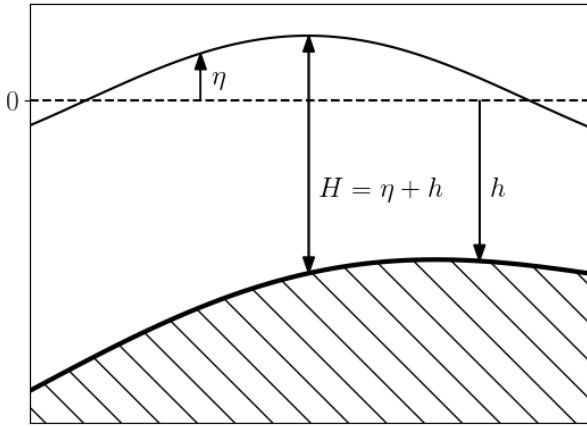


Figure 3.1: Definition of variables for the shallow water equations.

and the material derivative is defined as

$$\begin{aligned}\frac{D\phi}{Dt} &= \frac{\partial\phi}{\partial t} + \mathbf{u} \cdot \nabla\phi, \\ \frac{D\mathbf{A}}{Dt} &= \frac{\partial\mathbf{A}}{\partial t} + \mathbf{u} \cdot \nabla\mathbf{A},\end{aligned}\tag{3.2}$$

for scalar and vector fields ϕ and \mathbf{A} , respectively.

Considering first the continuity equation, equation (3.1a) can be expanded and integrated with respect to z from the sea floor surface $z = -h(x, y)$ to the free surface $z = \eta(x, y, t)$ (see figure 3.1), utilising Leibniz's rule, to give

$$\begin{aligned}0 &= \int_{-h}^{\eta} \left[\frac{\partial u}{\partial x} + \frac{\partial v}{\partial y} + \frac{\partial w}{\partial z} \right] dz \\ &= \frac{\partial}{\partial x} \int_{-h}^{\eta} u dz - u|_{z=-h} \frac{\partial \eta}{\partial x} - u|_{-h} \frac{\partial h}{\partial x} + \frac{\partial}{\partial y} \int_{-h}^{\eta} v dz - v|_{z=\eta} \frac{\partial \eta}{\partial y} - v|_{-h} \frac{\partial h}{\partial y} + w|_{\eta} - w|_{-h}.\end{aligned}\tag{3.3}$$

There is a no-normal flow condition at the $z = -h$ surface, implying

$$u|_{-h} \frac{\partial h}{\partial x} + v|_{-h} \frac{\partial h}{\partial y} + w|_{-h} = 0,\tag{3.4}$$

such that the three terms of equation (3.3) evaluated on the bottom surface sum to zero. A similar condition applies on the free surface $z = \eta$, leading to a kinematic boundary condition. Since, on this surface, $z - \eta = 0$ at all times, one can write $\frac{D(z-\eta)}{Dt} \Big|_{z=\eta} = 0$.

This implies $\frac{D\eta}{Dt}|_{\eta} = w|_{\eta}$, and hence

$$\frac{\partial \eta}{\partial t} + u|_{\eta} \frac{\partial \eta}{\partial x} + v|_{\eta} \frac{\partial \eta}{\partial y} = w|_{\eta}. \quad (3.5)$$

Substituting this expression into equation (3.3) yields

$$\frac{\partial \eta}{\partial t} + \frac{\partial}{\partial x} \int_{-h}^{\eta} u \, dz + \frac{\partial}{\partial y} \int_{-h}^{\eta} v \, dz = 0. \quad (3.6)$$

Defining depth-averaged horizontal velocities

$$\begin{aligned} \bar{u} &= \frac{1}{H} \int_{-h}^{\eta} u \, dz, \\ \bar{v} &= \frac{1}{H} \int_{-h}^{\eta} v \, dz, \end{aligned} \quad (3.7)$$

and substituting into equation (3.6), one obtains

$$\frac{\partial \eta}{\partial t} + \frac{\partial}{\partial x} (H\bar{u}) + \frac{\partial}{\partial y} (H\bar{v}) = 0. \quad (3.8)$$

In more compact notation, this depth-averaged continuity equation becomes

$$\frac{\partial \eta}{\partial t} + \nabla \cdot (H\mathbf{u}) = 0, \quad (3.9)$$

where it is understood that \mathbf{u} now represents the two-dimensional depth-averaged horizontal velocity vector, $\mathbf{u} = (\bar{u}, \bar{v})^T$.

The momentum equation (3.1b) is handled in a similar way. Expanding the equation into its three components gives

$$\begin{aligned} \frac{\partial u}{\partial t} + u \frac{\partial u}{\partial x} + v \frac{\partial u}{\partial y} + w \frac{\partial u}{\partial z} + \frac{1}{\rho} \frac{\partial p}{\partial x} &= 0, \\ \frac{\partial v}{\partial t} + u \frac{\partial v}{\partial x} + v \frac{\partial v}{\partial y} + w \frac{\partial v}{\partial z} + \frac{1}{\rho} \frac{\partial p}{\partial y} &= 0, \\ \frac{\partial w}{\partial t} + u \frac{\partial w}{\partial x} + v \frac{\partial w}{\partial y} + w \frac{\partial w}{\partial z} + \frac{1}{\rho} \frac{\partial p}{\partial z} + g &= 0. \end{aligned} \quad (3.10)$$

Under the assumption that vertical inertial terms are negligible (an underlying assumption of the shallow water equations), the z -component equation is now given by

$$\frac{1}{\rho} \frac{\partial p}{\partial z} + g = 0, \quad (3.11)$$

implying a hydrostatic pressure distribution. Assuming that surface tension is negligible, this can be integrated to give

$$p(x, y, z, t) = g\rho(\eta - z) + p_a, \quad (3.12)$$

where $p = p_a$ on the free surface boundary. This expression for p can be substituted into the x and y components of equation (3.10) to eliminate pressure. Again assuming that vertical terms can be neglected, one obtains

$$\begin{aligned} \frac{\partial u}{\partial t} + u \frac{\partial u}{\partial x} + v \frac{\partial u}{\partial y} + g \frac{\partial \eta}{\partial x} &= 0, \\ \frac{\partial v}{\partial t} + u \frac{\partial v}{\partial x} + v \frac{\partial v}{\partial y} + g \frac{\partial \eta}{\partial y} &= 0, \end{aligned} \quad (3.13)$$

which is written more compactly as

$$\frac{\partial \mathbf{u}}{\partial t} + \mathbf{u} \cdot \nabla \mathbf{u} + g \nabla \eta = 0, \quad (3.14)$$

where it is once again understood that \mathbf{u} now represents a two-dimensional depth-averaged velocity vector.

Terms for dissipation due to bottom friction and viscosity, the Coriolis force due to the Earth's rotation, and meteorological forcing due to atmospheric pressure gradient and surface stress due to wind, are added to produce the final set of equations used within the rest of this thesis, given by

$$\frac{\partial \eta}{\partial t} + \nabla \cdot (H \mathbf{u}) = 0, \quad (3.15a)$$

$$\frac{\partial \mathbf{u}}{\partial t} + \mathbf{u} \cdot \nabla \mathbf{u} + \mathbf{F}_C + g \nabla \eta + \frac{\nabla p_a}{\rho} = -\frac{\boldsymbol{\tau}_b}{\rho H} - \frac{\boldsymbol{\tau}_s}{\rho H} + \nabla \cdot (\nu (\nabla \mathbf{u} + \nabla \mathbf{u}^T)), \quad (3.15b)$$

where \mathbf{F}_C is the Coriolis force, $\boldsymbol{\tau}_b$ is the bottom stress, $\boldsymbol{\tau}_s$ the surface stress due to the wind, ν the eddy viscosity and p_a the atmospheric pressure at the surface. The viscosity term accounts for the diffusive effect of turbulence on unresolved scales, although in practice it is often used to suppress numerical instabilities (particularly near model boundaries). Throughout this thesis the eddy viscosity is a constant scalar, given a value of $1 \text{ m}^2 \text{s}^{-1}$.

The bottom friction is parameterised via Manning's n formulation, such that

$$\frac{\boldsymbol{\tau}_b}{\rho} = \frac{gn^2}{H^{\frac{1}{3}}} |\mathbf{u}| \mathbf{u}, \quad (3.16)$$

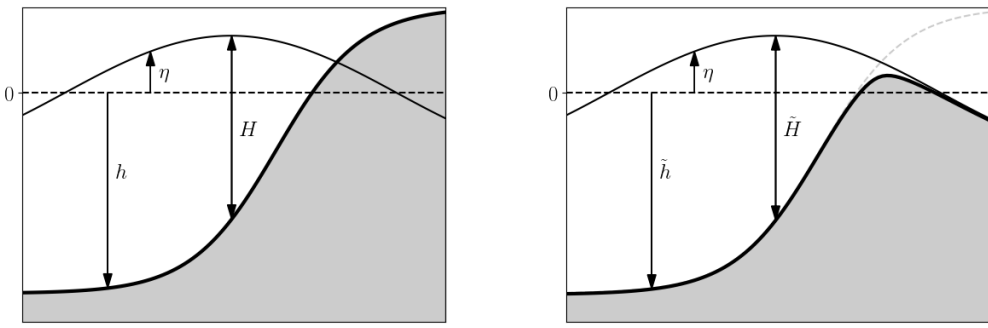


Figure 3.2: Original (left) and modified (right) shallow water variables, for the wetting-drying scheme by Kärnä et al. (2011).

where n is the Manning coefficient. The surface stress due to wind is related to the wind velocity using a Charnock parameterisation, via the system of equations

$$\begin{aligned}\boldsymbol{\tau}_s &= \rho_{\text{air}} |\mathbf{W}_*| \mathbf{W}_*, \\ \mathbf{W} &= \mathbf{W}_* \frac{1}{\kappa} \log \frac{z}{z_0}, \\ z_0 &= \frac{\alpha |\mathbf{W}_*|^2}{g},\end{aligned}\tag{3.17}$$

where ρ_{air} is the density of air, \mathbf{W}_* is the friction velocity, \mathbf{W} the wind velocity at a height z above the free surface (to be provided by a meteorological model), κ is the von Kármán constant, taken to be 0.4, z_0 the surface roughness, and α the Charnock parameter.

On ocean boundaries, a Dirichlet boundary condition is applied for the free surface height η , which introduces tidal forcing into the model. The velocity is treated with a symmetric condition on these ocean boundaries. Coastal boundaries are treated numerically by no-normal-flow conditions.

Wetting and drying

The wetting and drying of regions of the model domain is frequently of interest, and often required for accurate predictions, in tidal and storm surge models. For example, there may be intertidal regions which alternate between wet and dry with each tidal cycle, or inundation modelling may be of interest in the storm surge context. Dry regions, where the total water depth is zero (or negative) are not handled by the shallow water equations, and it is therefore necessary to treat dry regions differently within the model, which can be achieved through a variety of approaches (Medeiros and Hagen, 2013).

The method used within this thesis is based upon Kärnä et al. (2011), and utilises a dynamically modified bathymetry in order to avoid negative water depths. The modification is made through a vertical offset to the bathymetry by a function $f(H)$, leading to a modified bathymetry $\tilde{h} = h + f(H)$ and water depth $\tilde{H} = H + f(H)$. These original and modified variables are shown in figure 3.2, and it is this modified total depth \tilde{H} that is solved for by the modified shallow water equations; this is achieved by simply substituting \tilde{H} for H in the standard shallow water equations (3.15), which can then be solved over the entire domain provided that the function $f(H)$ satisfies two conditions:

- (i) The modified water depth must be positive for all H , i.e. $\tilde{H} = H + f(H) > 0$
- (ii) The modification to the shallow water equations should only apply near a wet-dry front, recovering the standard shallow water equations elsewhere. This requires that $f(H) \approx 0$ for large H .

The function $f(H)$ chosen by Kärnä et al. (2011) and used within this thesis is

$$f(H) = \frac{1}{2} \left(\sqrt{H^2 + \alpha^2} - H \right), \quad (3.18)$$

where α is a wetting-drying parameter which controls the wet-dry transition; the approximation becomes increasingly accurate as $\alpha \rightarrow 0$. The choice of a continuously differentiable function, such as equation (3.18), is necessary to ensure convergence of the numerical integration scheme; this also implies that there exists a minimum stable value for the parameter α , whose role is to smooth out the wet-dry front. The parameter is free to be chosen appropriately for each individual case. Motivated by numerical stability, Kärnä et al. (2011) proposed a rule of thumb for the selection of α given by

$$\alpha \approx L_x |\nabla h|, \quad (3.19)$$

where L_x is the horizontal length scale of the mesh elements near the wet-dry interface.

The reason for choosing this wetting-drying scheme is that it requires no modification to the computational domain or discretisation to facilitate wetting and drying, and therefore lends the model to use with adjoint methods (Funke, 2012), which are a key component of the work presented in this thesis. This is in contrast to schemes which move the mesh to track the wet-dry interface, or use discontinuous functions to determine whether individual elements are wet or dry, as is a common approach to wetting and drying (Medeiros and Hagen, 2013).

3.2 The finite element method

As discussed in section 2.2, the shallow water equations are commonly solved using either finite difference, finite volume or finite element based discretisation methods. Numerical methods take continuous equations and discretise them so that state variables are represented by vectors, and the model equations expressed as a matrix system; these three general methods take differing approaches to this discretisation. In the finite difference approach, derivatives in the equations themselves are discretised, via a truncated Taylor expansion, and thereby related to the values of the equation variables at neighbouring mesh nodes. The overheads associated with performing this method on unstructured meshes are prohibitive, and finite difference methods are therefore typically restricted to structured meshes only. The finite volume method involves integration of the governing equations over cells (or volumes), and as a result is written entirely in terms of fluxes between cells; this means that the finite volume method can be applied to either structured or unstructured meshes.

The finite element method (FEM) takes a different approach, whereby the solution to the governing equations is discretised (rather than the equations themselves) and required to exactly satisfy the governing equations in a weak sense. The finite element method is therefore very flexible in the choice of discretisation of the underlying solution (i.e. the choice of basis functions), and results in an approximate solution to the governing equations which is valid not only at individual nodes, as in the finite difference method, but throughout the entire domain.

Throughout this thesis, the discontinuous Galerkin (DG) form of the finite element method is employed. The model domain is divided into non-overlapping triangular elements. The formulation of the finite element method first requires the derivation of the weak form of the governing equations. This is obtained through multiplication of the governing equations by a discontinuous piecewise-polynomial test function, integration over the domain, and, where needed (or where chosen), the application of integration by parts on each element \mathcal{K} , whose boundaries are denoted e . Multiplying the continuity equation (3.15a) by a scalar test function ϕ , integrating over \mathcal{K} and integrating by parts, one obtains

$$\int_{\mathcal{K}} \frac{\partial \eta}{\partial t} \phi \, dx + \int_e (H\mathbf{u}) \phi \cdot \mathbf{n} \, dS - \int_{\mathcal{K}} (H\mathbf{u}) \cdot \nabla \phi \, dx = 0. \quad (3.20)$$

Taking the inner product of the momentum equation (3.15b) with a vector test function

ψ , and similarly integrating the appropriate terms by parts, yields

$$\begin{aligned} \int_{\mathcal{K}} \frac{\partial \mathbf{u}}{\partial t} \cdot \boldsymbol{\psi} dx - \int_{\mathcal{K}} \nabla \cdot (\mathbf{u} \boldsymbol{\psi}) \cdot \mathbf{u} dx + \int_e \mathbf{u} \cdot \boldsymbol{\psi} \mathbf{u} \cdot \mathbf{n} dS \\ + \int_e g\eta \boldsymbol{\psi} \cdot \mathbf{n} dS - \int_{\mathcal{K}} g\eta \nabla \cdot \boldsymbol{\psi} dx = 0, \end{aligned} \quad (3.21)$$

where for compactness, the terms for viscosity and external forces have been omitted.

To make progress within the finite element method, the local solution variables within each triangular element are written as a sum of basis functions, such that

$$\begin{aligned} \eta(\mathbf{x}, t) &= \sum_{i=1}^N \eta_i(t) \phi_i(\mathbf{x}), \\ \mathbf{u}(\mathbf{x}, t) &= \sum_{i=1}^N \mathbf{u}_i(t)^T \boldsymbol{\psi}_i(\mathbf{x}). \end{aligned} \quad (3.22)$$

Furthermore, since the weak form of the governing equations (equations (3.20) and (3.21)) holds for any test functions ϕ and $\boldsymbol{\psi}$, they must hold for each of the basis functions ϕ_j , $\boldsymbol{\psi}_j$. Substitution of equations (3.22) into equations (3.20) and (3.21), and setting $\phi = \phi_j$ and $\boldsymbol{\psi} = \boldsymbol{\psi}_j$, yields a set of N coupled ODEs for $\eta_i(t)$ and $\mathbf{u}_i(t)$ within the element \mathcal{K} ; one ODE for each value of j . This results in the same number of ODEs as unknowns, which constitutes a closed system of equations.

Coupling between elements is achieved via the integrals over element edges e , where the solution variables are multiply defined due to the discontinuities there. There are various possible approaches to deal with these integrals. Approximate Riemann solvers are popular, since they are a well-studied case of a hyperbolic conservation law featuring an initial condition containing a discontinuity. The approximate Riemann solver implemented by the modelling software used within this thesis (*Thetis*; see section 3.4) follows that of Kärnä et al. (2013). The advective terms are neglected, and it is assumed that $\eta \ll h$, in order to obtain the linear shallow water equations

$$\frac{\partial \eta}{\partial t} + \nabla(h\mathbf{u}) = 0, \quad (3.23a)$$

$$\frac{\partial \mathbf{u}}{\partial t} + g\nabla\eta = 0. \quad (3.23b)$$

The Riemann solution for the values on the boundary (η^*, \mathbf{u}^*) is then given by

$$\eta^* = \{\eta\} + \frac{h}{c} [\![\mathbf{u}]\!], \quad (3.24a)$$

$$\mathbf{u}^* = \{\mathbf{u}\} + \frac{c}{h} [\![\eta]\!], \quad (3.24b)$$

where $c = \sqrt{gh}$ is the wave celerity, and the standard notation $\{\bullet\} = \frac{\bullet_L + \bullet_R}{2}$ is used for the mean operator and $[\![\bullet]\!] = \frac{\bullet_L - \bullet_R}{2}$ for the jump operator, with L and R subscripts corresponding to the values on the left- and right-hand sides of the boundary respectively (Kärnä et al., 2013).

Finally, the time derivatives in the governing equations are dealt with using a suitable discrete timestepping method. Throughout this thesis, a generalised Euler timestepping scheme is used, whereby the general ODE

$$\frac{du}{dt} = F(u, x, t, \dots) \quad (3.25)$$

is approximated by

$$\frac{u_i^{n+1} - u_i^n}{\Delta t} \approx \theta F_i^{n+1} + (1 - \theta) F_i^n, \quad (3.26)$$

where θ is the ‘implicitness’ of the timestepping scheme. $\theta = 1$ corresponds to a fully implicit (i.e. backward Euler) timestepping scheme, while $\theta = 0$ corresponds to a fully explicit (forward Euler) scheme.

3.3 Adjoint modelling

The following exposition on adjoint modelling is largely based on Funke (2012). A system of PDEs can be written in the abstract general form

$$F(u, m) = 0, \quad (3.27)$$

where F is the appropriate PDE operator, u is the solution and m represents input parameters, which might encapsulate physical parameters, initial and boundary conditions or source terms. A functional of interest is given by a scalar function

$$J(u, m). \quad (3.28)$$

The purpose of the adjoint method is to compute the derivative of J with respect to the

input parameters m , i.e.

$$\frac{dJ}{dm}. \quad (3.29)$$

However, since u depends on m implicitly via the governing equation, it is necessary to apply the chain rule:

$$\frac{dJ}{dm} = \frac{\partial J}{\partial u} \frac{du}{dm} + \frac{\partial J}{\partial m}. \quad (3.30)$$

Note that if u and/or m are vectors then the above needs to be interpreted in terms of the appropriately sized tensors and corresponding inner product, e.g. assuming J is scalar-valued then $\frac{\partial J}{\partial u}$ is a gradient vector. Taking the derivative of the forward model (3.27) with respect to m gives

$$\frac{\partial F}{\partial u} \frac{du}{dm} + \frac{\partial F}{\partial m} = 0, \quad (3.31)$$

which can be inverted to obtain

$$\frac{du}{dm} = -\frac{\partial F^{-1}}{\partial u} \frac{\partial F}{\partial m}. \quad (3.32)$$

Substitution into equation (3.30) yields

$$\frac{dJ}{dm} = -\frac{\partial J}{\partial u} \frac{\partial F^{-1}}{\partial u} \frac{\partial F}{\partial m} + \frac{\partial J}{\partial m}, \quad (3.33)$$

which can be evaluated to obtain the desired derivative. There are two common approaches to the solution of equation (3.33): the tangent linear approach and the adjoint approach. The tangent linear approach is more efficient when there are a large number of functionals of interest J and a small number of parameters; however, this is not the case within this work. The adjoint approach is more efficient when there are a small number of functionals of interest and a large number of parameters; this is the typical case in PDE-constrained optimisation problems, and is applicable throughout this thesis.

The adjoint variable λ is defined as the solution to the adjoint equation

$$\frac{\partial F^*}{\partial u} \lambda = \frac{\partial J^*}{\partial u}, \quad (3.34)$$

such that

$$\lambda = \frac{\partial F^{-1*}}{\partial u} \frac{\partial J^*}{\partial u}, \quad (3.35)$$

where the asterisk denotes the adjoint operation (that is, the conjugate transpose or

Hermitian transpose). Note that λ^* is given by

$$\lambda^* = \frac{\partial J}{\partial u} \frac{\partial F^{-1}}{\partial u}, \quad (3.36)$$

and appears in equation (3.33). Since the other constituents of equation (3.33), $\frac{\partial F}{\partial m}$ and $\frac{\partial J}{\partial m}$, are often straightforward to compute, the solution of equation (3.34) is therefore the core of the adjoint method for the evaluation of the gradient $\frac{dJ}{dm}$.

There are two key properties of the adjoint equation (3.34) which contribute to its efficiency. Firstly, it is linear in λ and therefore often of lower computational cost to solve than the forward model, which may in principle be nonlinear. Secondly, the parameters m do not appear in the equation, and therefore its evaluation does not depend on the number of parameters.

For time-dependent models, the adjoint equation (3.34) is solved backwards in time. Supposing that the functional J depends only on the final state of the model variables, it is intuitive to interpret the right hand side of this equation as an initial condition, which is propagated backwards in time by the adjoint equations. If $\frac{\partial F}{\partial u}$ depends on u (i.e. if the forward model is nonlinear), it is necessary to store the value of u from all time steps throughout the forward model evaluation, for use in the solution of the adjoint equations. The numerical solution of the adjoint equations therefore typically places high demand on memory; this problem can be avoided by checkpointing schemes if the available memory is insufficient, at the cost of additional CPU time in recomputing parts of the forward model (Griewank, 1992).

There are three possible routes to the development of a numerical adjoint model. The first option is to discretise the continuous adjoint equations, which may for example be derived by hand. The advantages of this method include the possibility of using different discretisation methods for the forward and adjoint systems, which may be useful in cases where the forward and adjoint solutions have differing characteristics, e.g. leading to differing numerical stability constraints. Another advantage is that spatial and/or temporal adaptivity can be used for each of the forward and adjoint problems. However, the main disadvantage of such methods is that the resulting forward and adjoint numerical models are not guaranteed to be consistent; that is, the derivatives computed via the adjoint model are not exact derivatives of the forward model.

There are a further two options for the development of a numerical adjoint model, which both fall under the term ‘algorithmic differentiation’ (AD). Advantages of such methods are that there is no need to derive the continuous adjoint equations, and that the resulting adjoint numerical model is consistent with the forward model. In the conventional AD

approach, adjoint source code is generated from the source code of the forward numerical model by a decomposition into elementary functions whose Jacobians can be easily computed (Bischof et al., 1992; Giering and Kaminski, 1998; Tber et al., 2007). While ‘algorithmic’, a perceived problem with this approach is that “a substantial amount of manual intervention is still necessary” (Sraj et al., 2014a), particularly in the maintenance of the adjoint code for every development in the forward model. Such AD tools are also typically programming language-specific, and therefore lack flexibility. However, they have the advantage that they can be applied directly to existing implementations of forward models.

The alternative AD approach, which is utilised by the software used throughout this thesis, avoids the drawbacks of the conventional AD approach by deriving the adjoint equations from the discretised forward model equations (Farrell et al., 2013). This is performed before the generation of the forward model source code, and as such the adjoint source code is generated independently from that of the forward model. This is facilitated by the use of abstracted frameworks such as Firedrake (Rathgeber et al., 2016) or FEniCS (Alnæs et al., 2015), and an adjoint library such as pyadjoint (Mitusch et al., 2019).

3.4 Thetis

Within this work, the open-source finite element coastal ocean model *Thetis* (Kärnä et al., 2018) is used, in its two-dimensional configuration (Vouriot et al., 2019), which solves the nonlinear shallow water equations given by equation (3.15). *Thetis* is implemented within the Firedrake finite element code generation framework (Rathgeber et al., 2016), where the weak form of the governing equations is provided via the high-level Unified Form Language (Alnæs et al., 2014), and Firedrake automatically generates efficient C code implementing the finite element method (Homolya et al., 2018). The use of Firedrake results in an efficient and highly flexible modelling framework, with several possible choices of finite element discretisation. The $P_1^{\text{DG}}\text{-}P_1^{\text{DG}}$ finite element pair is used throughout this thesis. Firedrake utilises pyadjoint (Mitusch et al., 2019) for automated generation of adjoint code, as described in section 3.3.

3.5 Gaussian process emulation

When a large number of expensive numerical model runs are required by a given application, such as the Bayesian inversion algorithm employed in chapters 5 and 6 of this

thesis, it is common to substitute the full numerical model with a fast surrogate, such as a Gaussian process emulator (GPE) (Hall et al., 2011; Tagade et al., 2013) or polynomial chaos expansion (Sraj et al., 2014b). Within this thesis, a GPE is used for this purpose, and such emulators are outlined in this section, largely following Rasmussen (2003).

The underlying assumption of Gaussian process emulation is that a vector of model outputs \mathbf{f} follows a multivariate Gaussian distribution, with mean $\boldsymbol{\mu}$ and covariance matrix Σ , such that

$$\mathbf{f} \sim \mathcal{N}(\boldsymbol{\mu}, \Sigma). \quad (3.37)$$

The purpose of emulation is to predict unseen model outputs based on a set of known inputs. A set of ‘training’ (i.e. known) model inputs is denoted \mathbf{X} , and the corresponding outputs denoted \mathbf{f} . The objective is to predict model outputs \mathbf{f}_* corresponding to unseen ‘test’ model inputs \mathbf{X}_* . The joint probability distribution of \mathbf{f} and \mathbf{f}_* is given by

$$\begin{bmatrix} \mathbf{f} \\ \mathbf{f}_* \end{bmatrix} \sim \mathcal{N} \left(\begin{bmatrix} \boldsymbol{\mu} \\ \boldsymbol{\mu}_* \end{bmatrix}, \begin{bmatrix} \Sigma & \Sigma_* \\ \Sigma_*^T & \Sigma_{**} \end{bmatrix} \right), \quad (3.38)$$

where $\boldsymbol{\mu}_*$ denotes the test mean, Σ_{**} the corresponding covariance matrix for the test points, and Σ_* denotes the covariance between the training and test points. The conditional distribution of \mathbf{f}_* given \mathbf{f} , i.e. the probability distribution for the predicted model outputs \mathbf{f}_* based on the known output values \mathbf{f} , is given by

$$\mathbf{f}_* | \mathbf{f} \sim \mathcal{N} (\boldsymbol{\mu}_* + \Sigma_*^T \Sigma^{-1} (\mathbf{f} - \boldsymbol{\mu}), \Sigma_{**} - \Sigma_*^T \Sigma^{-1} \Sigma_*). \quad (3.39)$$

Note that the $\Sigma_*^T \Sigma^{-1} \Sigma_*$ term in the posterior covariance is always positive, and therefore that the presence of observation data provides a constraint on the predicted outputs and subsequently reduces the covariance of their estimated values. The crux of Gaussian process emulation is the determination of appropriate mean vectors and covariance matrices; the subsequent evaluation of the above equations is trivial.

The mean vector $\boldsymbol{\mu}$ is taken as a function of the corresponding input vector \mathbf{X} , via a set of basis functions. This can be written

$$\boldsymbol{\mu} = g(\mathbf{X})^T \cdot \boldsymbol{\beta}, \quad (3.40)$$

where $g(\mathbf{X})$ is a matrix of basis functions evaluated at the points \mathbf{X} , and has shape $(M \times N)$, where M is the number of basis functions and N the length of the vector \mathbf{X} . $\boldsymbol{\beta}$ is a vector of regression coefficients of length M , to be determined later. The equivalent expression for $\boldsymbol{\mu}_*$ is

$$\boldsymbol{\mu}_* = g(\mathbf{X}_*)^T \cdot \boldsymbol{\beta}, \quad (3.41)$$

where the basis functions and regression coefficients are the same as in equation (3.40). The basis functions are commonly taken as linear or quadratic functions of the input parameters. While it is important that the selected basis functions are appropriate to the problem, the ‘heavy lifting’ of Gaussian process emulation is performed by the $\Sigma_*^T \Sigma^{-1}(\mathbf{f} - \boldsymbol{\mu})$ term of equation (3.39).

The covariance matrices are taken as

$$\begin{aligned}\Sigma &= k(\mathbf{X}, \mathbf{X}), \\ \Sigma_* &= k(\mathbf{X}, \mathbf{X}_*), \\ \Sigma_{**} &= k(\mathbf{X}_*, \mathbf{X}_*),\end{aligned}\tag{3.42}$$

where $k(x, x')$ is a covariance function. A common choice for this function is given by

$$k(x, x') = \sigma^2 C(x, x'),\tag{3.43}$$

where σ^2 is a covariance parameter and $C(x, x')$ a correlation function. This approach is taken within this thesis, with the correlation function given by

$$C(x, x') = \exp\left(-\frac{(x - x')^2}{2l^2}\right),\tag{3.44}$$

where l is a correlation length, i.e. the length scale (in the input space) over which model outputs are correlated.

A number of hyperparameters have been introduced within the above mean and covariance functions: $\boldsymbol{\beta}$, σ^2 , l . A robust method for selecting these hyperparameters, collectively denoted $\boldsymbol{\theta}$, is via maximum likelihood estimation. The likelihood of observing the training data given the input points and the hyperparameters is given by

$$L(\mathbf{f}|\mathbf{X}, \boldsymbol{\theta}) = |\Sigma|^{-1/2} \frac{1}{\sqrt{(2\pi)^N}} \exp\left(-\frac{1}{2}(\mathbf{f} - \boldsymbol{\mu})^T \Sigma^{-1}(\mathbf{f} - \boldsymbol{\mu})\right),\tag{3.45}$$

where N is the number of training points, or the length of the vectors \mathbf{X} and \mathbf{f} . The optimal hyperparameters are taken to be those which maximise $L(\mathbf{f}|\mathbf{X}, \boldsymbol{\theta})$. The maximisation is commonly performed on the log of the likelihood, given by

$$\log L(\mathbf{f}|\mathbf{X}, \boldsymbol{\theta}) = -\frac{1}{2} \log |\Sigma| - \frac{1}{2}(\mathbf{f} - \boldsymbol{\mu})^T \Sigma^{-1}(\mathbf{f} - \boldsymbol{\mu}) - \frac{N}{2} \log 2\pi.\tag{3.46}$$

The first term of this equation penalises large covariances, favouring a tight constraint, while the second term favours small misfits between emulator outputs and observations (relative to the estimated covariance). The final term is a normalisation, and can be

omitted in the maximisation of the log likelihood.

Once the hyperparameters have been appropriately selected, the GPE, given by equations (3.39), can be utilised to estimate unseen observations at low computational cost, given an adequate set of training data. This thesis uses GPEs with multiple input dimensions and multiple model outputs. These extensions to the above exposition are described in the documentation of the Python package GPy (since 2012), which is used within this work for the construction of GPEs.

Chapter 4

Adjoint-based sensitivity analysis and uncertainty quantification for a storm surge model

The content within this chapter is based on

S. C. Warder, K. J. Horsburgh, and M. D. Piggott. *Understanding the contribution of uncertain wind stress to storm surge predictions*. In 4th IMA International Conference on Flood Risk, Swansea, 2019.

S. C. Warder, K. J. Horsburgh, and M. D. Piggott. *Adjoint-based sensitivity analysis for a numerical storm surge model*. Ocean Modelling, Submitted 2020.

4.1 Introduction

Essential to the intelligent application of any storm surge model is an understanding of the model's sensitivity to its uncertain inputs. In a forecast scenario, the dominant source of model uncertainty arises from the meteorological forcing (Flowerdew et al., 2013), namely the surface stress due to wind and the atmospheric pressure gradient. For this reason, it is common to employ ensemble methods for uncertainty quantification (Flowerdew et al., 2010). While such ensemble methods provide a practical approach to uncertainty quantification within an operational forecast framework, they provide little insight into the patterns (in space and/or time) of the underlying model sensitivity, and they depend on the choice of meteorological ensemble.

An alternative approach to sensitivity analysis is provided by the adjoint method, whereby a model's sensitivity to its (spatially and temporally varying) inputs can be computed algorithmically. Adjoint methods have previously been applied to the modelling and sensitivity analysis of storm surges by Wilson et al. (2013), who applied the MITgcm model and its adjoint to a surge event in the North Sea in December 2007, with a focus on computing the sensitivity of modelled peak surge height with respect to wind stress. Since wind stress is a function of space and time, so too is the sensitivity of the model. Wilson et al. (2013) observed that the pattern of sensitivity of a surge-induced sea surface height observation to earlier wind stress behaves like a shallow water wave propagating backwards in time, originating at the point of observation. They also demonstrated how adjoint-derived surge model sensitivities can be applied to uncertainty quantification.

Within this chapter, the Thetis model is applied to storm surge sensitivity analysis for a case study in the North Sea in December 2013; this event is described in section 4.2, along with some useful terminology and a description of the UK operational surge model. The implementation and validation of atmospheric pressure forcing within Thetis is then described in section 4.3, and the construction and calibration of a North Sea storm surge model using Thetis is described in section 4.4, including a comparison of model performance with the UK operational surge model for this event.

Section 4.5 uses the adjoint mode of Thetis for the purposes of sensitivity analysis and uncertainty quantification. This constitutes an extension to the work of Wilson et al. (2013), by performing uncertainty quantification with respect to multiple model inputs, namely the wind stress, bottom friction coefficient and bathymetry; the latter two model inputs are typically neglected within operational uncertainty quantification frameworks, but included here. These results are used to gain physical insight into surge generation and propagation in the North Sea, and to estimate and compare the uncertainty in surge model outputs arising from each of these inputs, and at different locations across the model domain. A further extension to the existing literature is made by approaching the sensitivity of modelled surges to wind stress analytically.

The connection between adjoint and ensemble uncertainty quantification methods is explored in section 4.6, where adjoint-computed sensitivities are utilised to approximate members of an ensemble forecast, at low computational cost. This idea is further extended in section 4.7 to a model-free approximation to surge hazard. Finally, the results and implications of this chapter are discussed in section 4.8, and a summary can be found in section 4.9.

4.2 Background

4.2.1 Definitions

This section defines some terms used throughout this chapter, which are also shown schematically in figure 4.1.

Surge residual is defined as the difference between the total (tidally and meteorologically induced) sea surface level and the sea surface level which would be expected in the absence of surge forcing, i.e. due only to astronomical tidal forcing. The surge residual therefore contains the direct effect of the meteorological forcing, plus the tide-surge interaction (Horsburgh and Wilson, 2007), and is a function of both space and time. In operational forecasting, modelled surge residuals are combined with astronomical tidal predictions in order to produce forecasts of total sea level, thus minimising the effect of inaccuracies in the modelled tides. The modelled surge residual is obtained by subtracting the output from a tide-only model run (without meteorological inputs) from a fully forced (tide + surge) model run. The surge residual can also be extracted from observation data. For this, long-term observation data is required, so that a harmonic analysis can be performed. The tidal component of observations can then be calculated from this harmonic analysis, and subtracted from the observed sea surface levels during a surge event, to obtain the surge residual.

Skew surge is defined as the maximum surge height above the astronomically predicted high water within a tidal cycle, and as such varies in space only. Skew surge is a more relevant measure of storm surge severity than the surge residual, and from a hazard assessment perspective is independent of the state of the tide (e.g. within the spring-neap cycle) (Williams et al., 2016).

4.2.2 Case study event: Storm Xaver

One of the most severe storm surges to impact the UK in the last century occurred on 5th – 6th December 2013, and was caused by Storm “Xaver” (Haigh et al., 2016). This event is chosen as a case study throughout this chapter because of its severity, and due to the availability of observation data and meteorological hindcasts.

Spencer et al. (2015) have performed a detailed analysis of Storm Xaver and its impact. The storm was a “SE tracking” event within the categorisation of North Sea storms defined by Muir Wood and Bateman (2005). Such storms induce high southward-directed winds

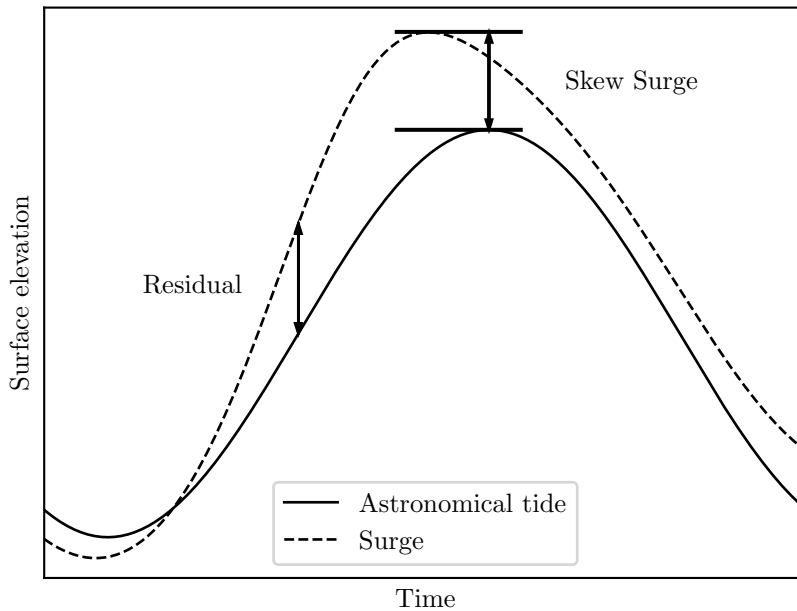


Figure 4.1: Definitions of surge residual and skew surge.

over the western North Sea, and this event caused surge residuals in excess of 2 m along part of the east coast of the UK (Spencer et al., 2015). During this event, peak residuals typically occurred in close proximity to the astronomical high tide; this is unusual, since tide-surge interaction typically suppresses surge residuals at high tide (Horsburgh and Wilson, 2007), and in this case caused significant skew surges in excess of 2 m at some locations.

4.2.3 The UK operational storm surge model

Until recently, operational surge modelling in the UK was undertaken using the Extended Area Continental Shelf Model, CS3X, which spans the European continental shelf using a structured grid of $1/9^\circ$ latitude by $1/6^\circ$ longitude, or approximately 12 km. Refinement to 2 km and 1 km is achieved within the Bristol Channel and Severn Estuary respectively via nested models. While this model has recently been replaced operationally by NEMO (Nucleus for European Modelling of the Ocean), here the focus is on CS3X, which was the operational model at the time of Storm Xaver.

In forecasting this event, CS3X was forced using meteorological forecasts taken from the MOGREPS atmospheric ensembles. These ensembles were available at various lead times and resolutions (longer-term forecasts were available at lower resolutions), and were used for the purpose of quantifying uncertainty due to the meteorological forcing. For this

event, the surge ensemble showed risk of “very significant surge activity” approximately 5.5 days in advance of the event using 168-hour meteorological ensemble forecasts. Very high alert level exceedance probabilities at several key east coast tide gauge locations were forecast once the surge event fell within the shorter-range (66-hour) meteorological ensemble forecasts, and for most tide gauge locations the true sea surface heights fell within the ensemble range for forecasts up to a few days prior to the event (National Oceanography Centre, personal communication 2018).

CS3X therefore performed adequately in forecasting this event. Its performance using hindcast meteorological data is discussed in section 4.4.2, and is used as a benchmark for the performance of the Thetis surge model.

4.3 Implementation of atmospheric pressure forcing within Thetis

Prior to this work, the atmospheric pressure gradient forcing term of the governing equations (3.15) was not implemented within Thetis. However, it is an important mechanism for surge generation, and the first step towards storm surge modelling within Thetis was therefore to implement and test this term. The term takes the form

$$\frac{\nabla p_a}{\rho}, \quad (4.1)$$

where p_a is the atmospheric pressure, and ρ the density of water. Since this is a simple source term, the weak form is trivial to derive, requiring no special treatment. Taking the inner product with a vector-valued test function ψ and integrating over Ω gives

$$\int_{\Omega} \frac{\nabla p_a}{\rho} \cdot \psi \, dx. \quad (4.2)$$

This term was implemented in Thetis, and tested using a pseudo-1D analytic test case on a rectangular domain of dimension $l_x = 10$ km in the x -direction and $l_y = 1$ km in the y -direction, and using a $P_1^{\text{DG}}\text{-}P_1^{\text{DG}}$ discretisation. A variety of meshes were used, each consisting of one element in the y -direction, and a resolution Δx in the x -direction, as shown in figure 4.2. A constant bathymetry of $h = 5$ m was applied, and the atmospheric pressure was prescribed as

$$p_a(x) = -\rho g A \cos \frac{\pi x}{l_x}, \quad (4.3)$$

with $A = 2$ m. The model was run until a steady state was reached, starting from an

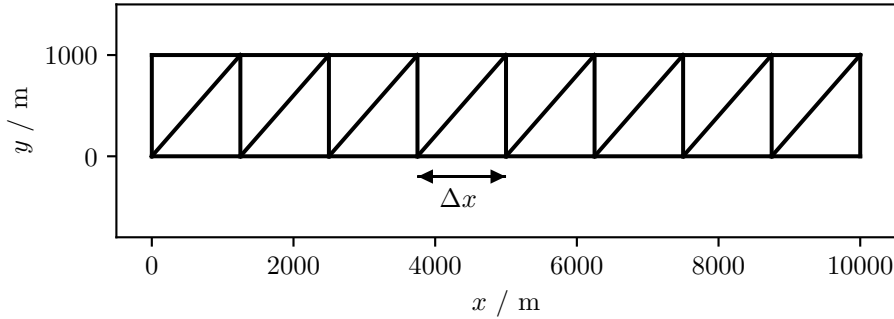


Figure 4.2: Example mesh used for pseudo-1D atmospheric pressure test case.

initial condition of zero elevation and velocity. A high value for the Manning bottom friction coefficient of $5 \text{ s m}^{-1/3}$ was used in order to suppress oscillations and help reach the steady state quickly.

The analytic solution for this simple problem is derived by substitution of the prescribed atmospheric pressure (equation (4.3)) into the governing equations (3.15). For the stationary solution, the velocity is zero everywhere and all time derivatives vanish, such that the surface gradient $g\nabla\eta$ exactly balances the atmospheric pressure gradient $\nabla p_a/\rho$ in the momentum equation (3.15b). The analytic solution for the prescribed p_a of equation (4.3) is therefore

$$\eta(x) = A \cos \frac{\pi x}{l_x}. \quad (4.4)$$

The above experiment was performed within Thetis using values for Δx of $2.5/2^n$ km for $n = 0, 1, 2, 3, 4$. For each experiment, the analytic solution given by equation (4.4) was projected onto the P_1^{DG} function space used to represent η in the model solution. Figure 4.3 shows a comparison between the computed and analytic solutions for the $n = 0$ and $n = 2$ meshes, along the $y = 500$ m transect. For the $n = 0$ case, the individual elements can be observed in the solution and the discrepancy between the Thetis and analytic solutions is significant. However, for the $n = 2$ case, the Thetis and analytic solutions are visually indistinguishable. For each experiment, the L2 norm of the error between the computed and analytic solutions was calculated over the whole domain, and the convergence of this norm with respect to the mesh resolution is shown in figure 4.4. The convergence rate is second order, as expected for the use of a P_1^{DG} function space for the surface elevation.

The experiment was repeated for a fully two-dimensional case, with $l_x = l_y = 10$ km and mesh resolutions $\Delta x = \Delta y = 2.5/2^n$ km for $n = 0, 1, 2, 3, 4$; an example mesh is shown in

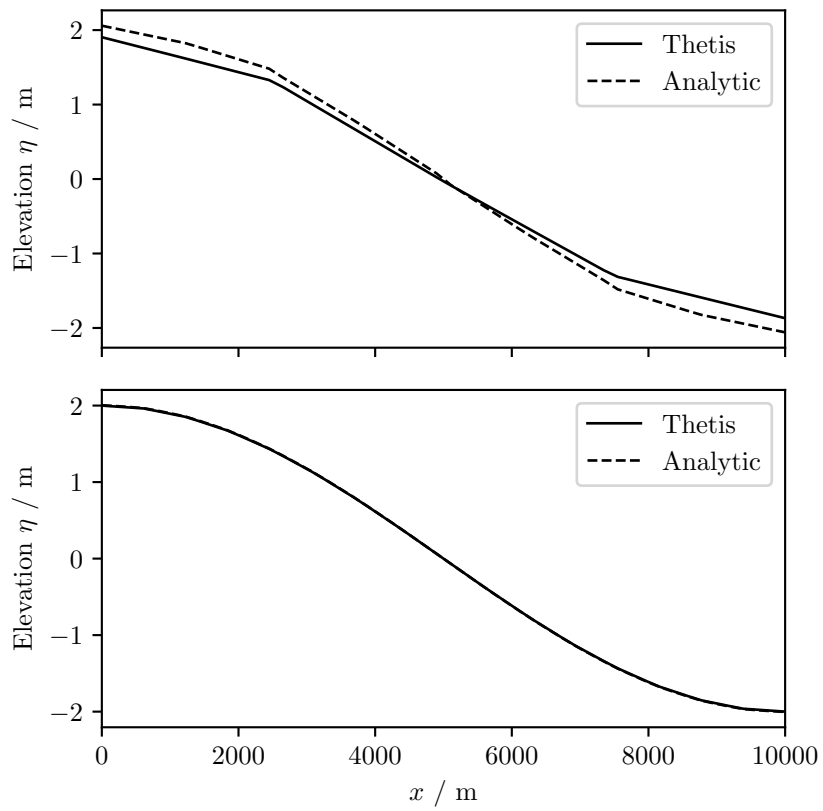


Figure 4.3: Comparison of two spatial resolutions for the pseudo-1D atmospheric pressure test case, along the $y = 500$ m transect. Top: $\Delta x = 2500$ m. Bottom: $\Delta x = 625$ m.

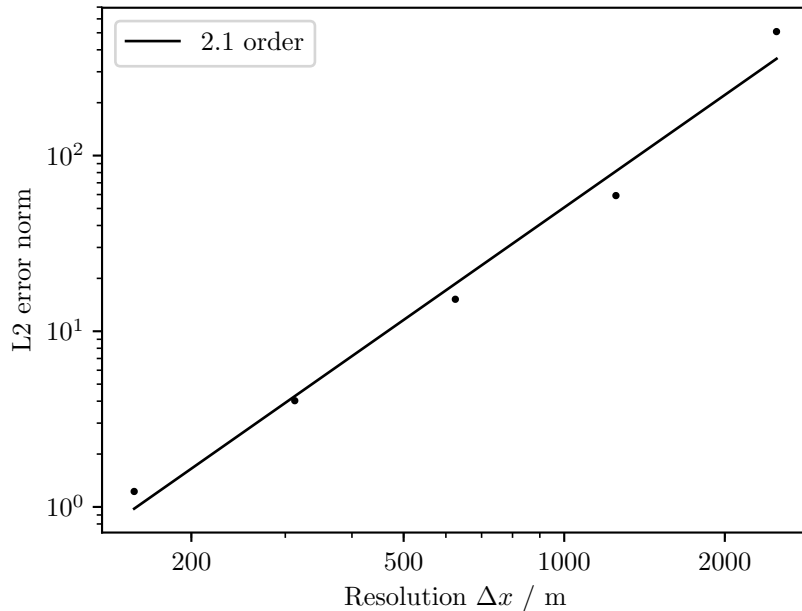


Figure 4.4: Convergence test for pseudo-1D atmospheric pressure test case. Second order convergence is achieved.

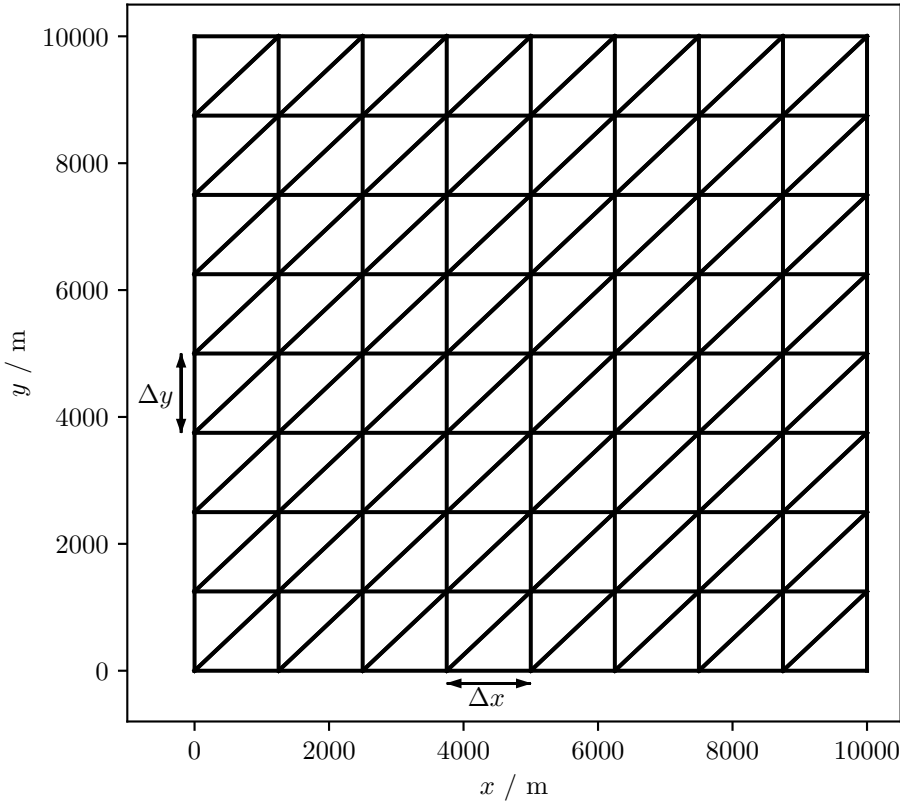


Figure 4.5: Example mesh used for 2D atmospheric pressure test case.

figure 4.5. The prescribed atmospheric pressure was given by

$$p_a(x) = -\rho g A \cos \frac{\pi x}{l_x} \cos \frac{\pi y}{l_y}, \quad (4.5)$$

with $A = 2$ m. The corresponding analytic solution is

$$\eta(x) = A \cos \frac{\pi x}{l_x} \cos \frac{\pi y}{l_y}. \quad (4.6)$$

Using the same $P_1^{\text{DG}}\text{-}P_1^{\text{DG}}$ discretisation, second order convergence was again attained, as shown in figure 4.6. This 2D test case was added to the Thetis test suite.

4.4 Forward storm surge modelling

4.4.1 Model setup

This section describes the Thetis model setup used throughout this chapter.

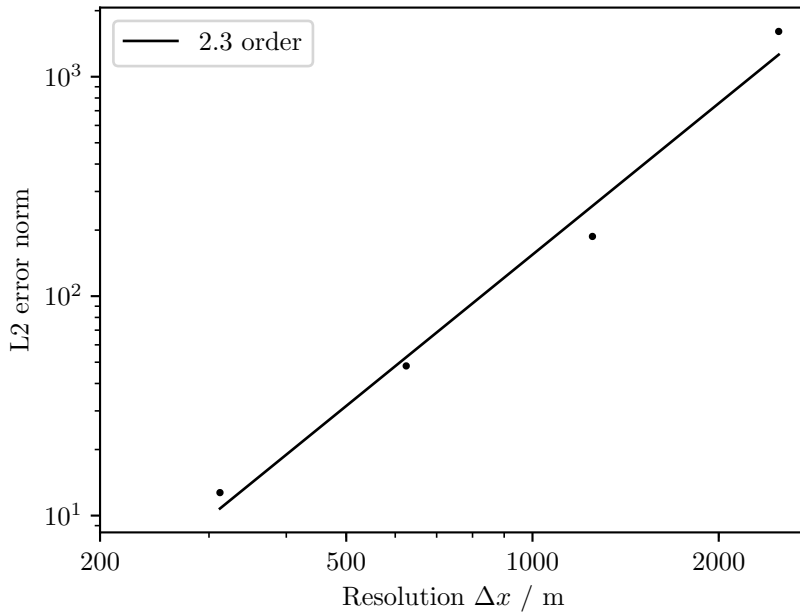


Figure 4.6: Convergence test for 2D atmospheric pressure test case. Second order convergence is achieved.

The mesh is shown in figure 4.7, and was generated on a UTM31 coordinate projection, using the Python package *qmesh* (version 1.0.1) (Avdis et al., 2018), which interfaces the mesh generator *Gmsh* (version 2.10.1) (Geuzaine and Remacle, 2009). The mesh resolution varies from 3 km at the coastlines to 25 km in open regions, resulting in a total of 23,120 triangular elements. The coastline data is from the Global Self-consistent, Hierarchical, High-resolution Geography Database (GSHHG) (Wessel and Smith, 1996). Thetis is run using a timestep $\Delta t = 100$ s, with implicitness $\theta = 1$ (i.e. a backward Euler scheme); the use of a fully implicit scheme avoids numerical instability issues which were present in earlier preliminary work.

The GEBCO 2014 dataset is used for the bathymetry, using a mean sea level datum, with a minimum depth of 10 m applied to avoid the need for wetting and drying. A constant and spatially uniform Manning coefficient n is applied. Storm surge forcing is included via the atmospheric pressure and wind stress forcing terms in the governing equations, with a constant and spatially uniform Charnock parameter α used for the wind stress parameterisation. Meteorological hindcast data for the modelled event were provided by the National Oceanography Centre (personal communication, 2018). These data were provided on a uniform grid of resolution $1/6^\circ$ longitude by $1/9^\circ$ latitude, at a temporal resolution of one hour, and are linearly interpolated onto the mesh nodes and between time steps for use within Thetis.

Tidal forcing is included by applying a Dirichlet boundary condition for the free surface height on the open ocean boundaries, generated from eight harmonic constituents from the TPXO database (Egbert and Erofeeva, 2002) (M2, S2, N2, K2, Q1, O1, P1, K1). This boundary condition is further modified by a correction calculated from the inverse barometer effect, which can be used to approximate surge generated externally to the model domain. The correction assumes that, on the boundaries, the sea surface level η is in equilibrium with the atmospheric pressure p_a , and hence

$$\eta = \eta_{\text{tidal}} - \frac{p_a - p_0}{\rho g}, \quad (4.7)$$

with p_0 the mean atmospheric pressure, taken to be $1.01325 \cdot 10^5$ Pa, and η_{tidal} the tidally generated boundary condition value.

Figure 4.8 indicates two physical features within the model domain, to which reference is made later in this chapter.

4.4.2 Model calibration & validation

Spatially and temporally constant values for both the Manning coefficient n and Charnock parameter α are used throughout this chapter. The selection of each of these parameters was based on a simple model calibration exercise, which is described here. The data used for calibration is from the 12 tide gauge stations shown in figure 4.7, where quality controlled data is available from the British Oceanographic Data Centre (BODC)¹. By performing a harmonic analysis on data from each of these locations, both tidal harmonics and surge residuals can be computed.

First, the Manning coefficient n was selected by minimising model-observation misfit based on tidal harmonics. After a spin-up period of 10 days, the model was run in tide-only mode for one month, and a harmonic analysis performed at the 12 tide gauge stations, using the same eight harmonic constituents as the tidal boundary condition used to force the model (M2, S2, N2, K2, Q1, O1, P1, K1). The Python package *uptide* (Kramer et al., 2020) was used for the harmonic analysis. The model-observation misfit was then computed via the combined root mean squared error (RMSE) of the amplitudes of the

¹This study uses data from the National Tidal and Sea Level Facility, provided by the British Oceanographic Data Centre and funded by the Environment Agency.

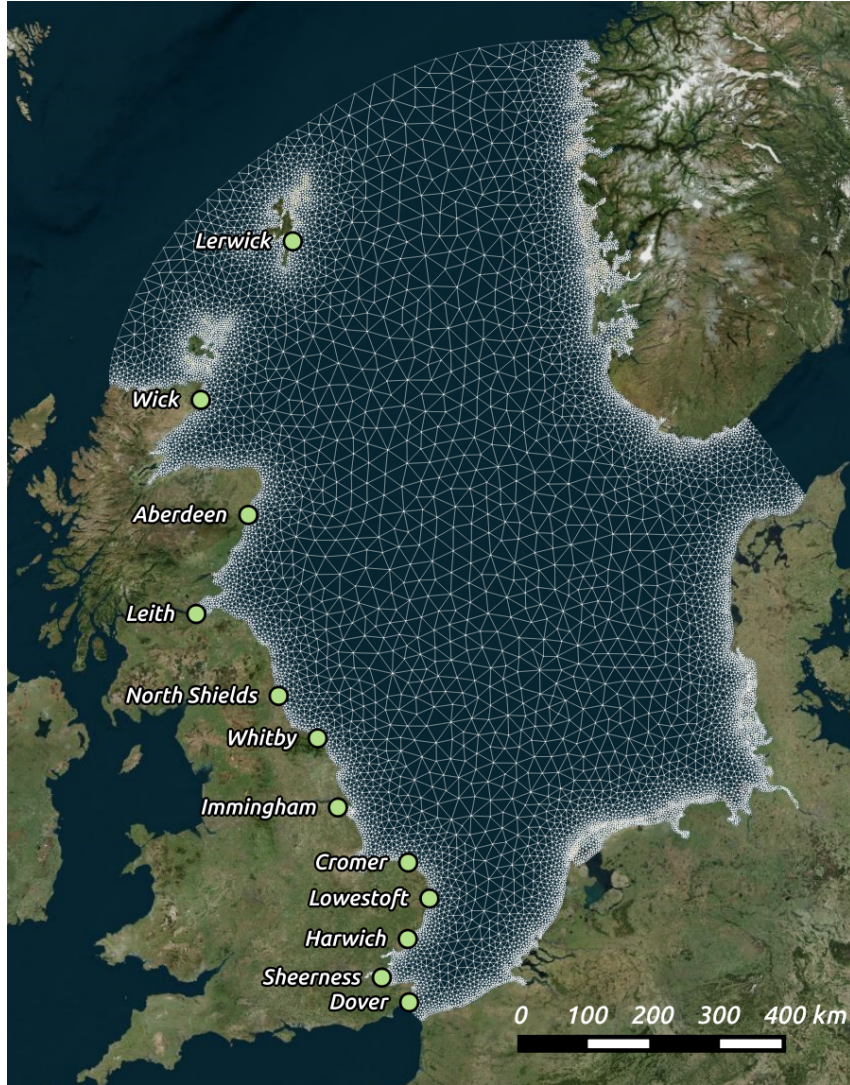


Figure 4.7: Mesh used for North Sea tide-surge simulations. Tide gauge locations are labelled.

eight harmonic constituents C by

$$\text{RMSE} = \sqrt{\frac{1}{8} \sum_C \frac{1}{12} \sum_{i=1}^{12} (A_{C,i} - \hat{A}_{C,i})^2}, \quad (4.8)$$

where $A_{C,i}$ and $\hat{A}_{C,i}$ are the modelled and observed amplitudes of the harmonic constituent C at tide gauge location i , respectively. Errors in the computed harmonics due to the use of a one-month model run to analyse all eight constituents were neglected; the RMSE values are in any case dominated by the M2 and S2 constituents, which can be well resolved by a model run of this length. The model was run as described above, for values of the Manning coefficient n from $0.015 \text{ s m}^{-1/3}$ to $0.04 \text{ s m}^{-1/3}$ in steps of $0.0025 \text{ s m}^{-1/3}$. The resulting RMSEs for each value of n are shown in figure 4.9. The smallest RMSE

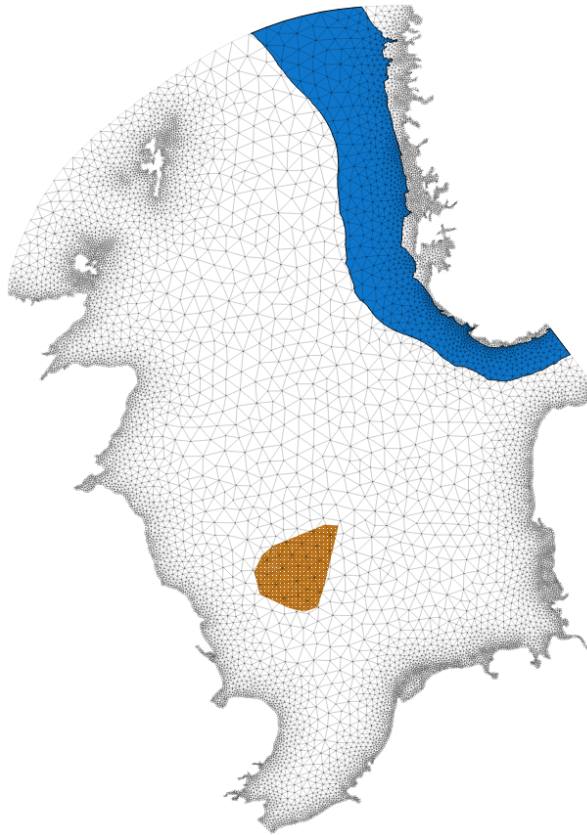


Figure 4.8: Two key physical features within the model domain. Blue region in north-east: Norwegian Trench, extracted from 200 m contour. Orange region, below centre: Dogger Bank, extracted from 20 m contour.

is 5.7 cm, achieved with $n = 0.025 \text{ s m}^{-1/3}$. This value is used for the remainder of this chapter.

Second, the Charnock parameter α was selected by minimising model-observation misfit based on surge residuals. However, the addition of surge forcing introduces a variety of new sources of uncertainty; the choice of wind stress parameterisation, as well as errors in both the meteorological forcing and the observation data, can all impact the misfit between modelled and observed surge residuals. A thorough calibration exercise should therefore be based on a large number of surge events. However, since the purpose of this work is model sensitivity analysis and uncertainty quantification, such an extended calibration exercise was not undertaken. Instead, the model-observation misfit was minimised for the Storm Xaver case study event only.

The surge model was run using varying values of α . For each simulation, the model was first spun up (in tide-only mode) for 10 days, prior to the wind and atmospheric pressure forcing terms being switched on approximately 10 days in advance of the peak surge. A comparison with observations for this event was made based on the modelled and observed

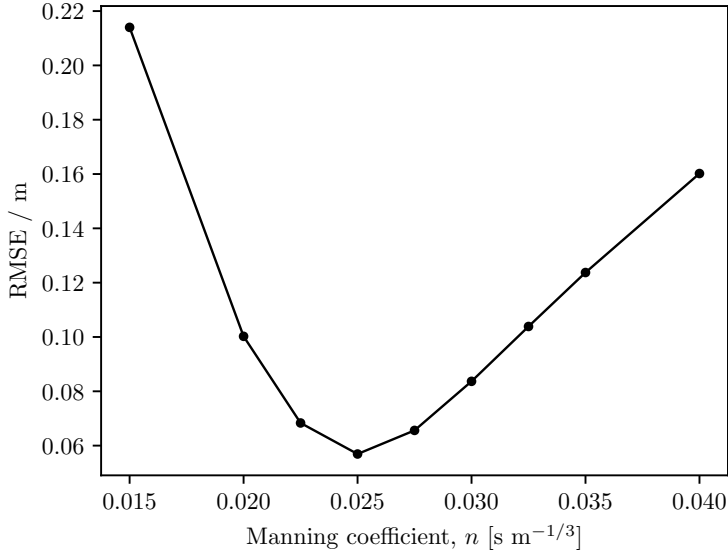


Figure 4.9: Calibration of the tide-only model with respect to the Manning coefficient n . The optimal choice is $n = 0.025 \text{ s m}^{-1/3}$.

surge residuals at the BODC tide gauge locations. The model-observation error is defined as the root mean squared error (RMSE) of the residual timeseries, over a two day period T capturing the peak surge. For a given tide gauge location i , the RMSE is given by

$$\text{RMSE}_i = \sqrt{\frac{1}{T} \int (r_i(t) - \hat{r}_i)^2 dt}, \quad (4.9)$$

where r_i and \hat{r}_i are the modelled and observed surge residuals at the tide gauge location i , respectively. The time integral can be approximated by a suitable discrete method using the model timesteps, linearly interpolating the observed residuals which are available at 15-minute intervals. The overall RMSE was determined by averaging over a subset of the available tide gauge data locations. The conditions for the inclusion of a tide gauge location in the overall RMSE were (i) that the surge residual was significant at that location, and (ii) that the gauge recorded a sufficiently complete timeseries surface elevation record during the event. This resulted in eight tide gauge locations, as plotted in figure 4.11. The surge model was run as described, for values of the Charnock parameter α from 0.01 to 0.03, in steps of 0.002. The residual RMSE values are shown in figure 4.10. The smallest RMSE is 15.9 cm, obtained using $\alpha = 0.028$, which is a value consistent with literature (Brown and Wolf, 2009). This value is used throughout the remainder of this chapter.

Using these calibrated Manning and Charnock parameters, a comparison between modelled and observed surge residuals for the December 2013 surge event is shown in figure

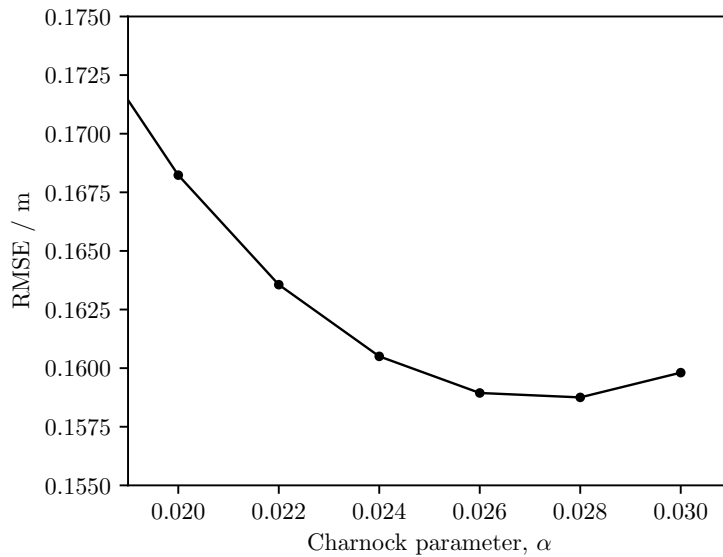


Figure 4.10: Calibration of the surge model, with respect to the Charnock parameter α . The optimal choice is $\alpha = 0.028$.

4.11, for the eight selected tide gauge locations described above. A good agreement is attained; the overall shape of the surge residual as a function of time is well captured at all eight locations. Figure 4.12 shows an equivalent comparison for the outgoing UK operational surge model, CS3X, where the overall RMSE across the eight locations is 16.4 cm. Since the Thetis RMSE is 15.9 cm, the performance of Thetis and CS3X is comparable. Note that the CS3X model has been extensively calibrated using a large number of events, whereas the Thetis result has been achieved by selecting an optimal Charnock parameter for this single event. Caution should therefore be exercised in drawing conclusions regarding the overall surge modelling performance of Thetis compared with CS3X, without a broader benchmarking study. Nevertheless, for the case study event of this chapter, the performance of Thetis is on par with that of CS3X.

4.5 Sensitivity analysis & uncertainty quantification

This section describes the application of the Thetis model and its adjoint to sensitivity analysis and uncertainty quantification. The previous application of such adjoint methods to storm surge modelling is limited to an analysis of sensitivity to wind stress by Wilson et al. (2013), but this work constitutes a broader sensitivity analysis and uncertainty quantification study. The objectives of this work were

- (i) to compute the spatial (and temporal) pattern of sensitivity of modelled skew surges

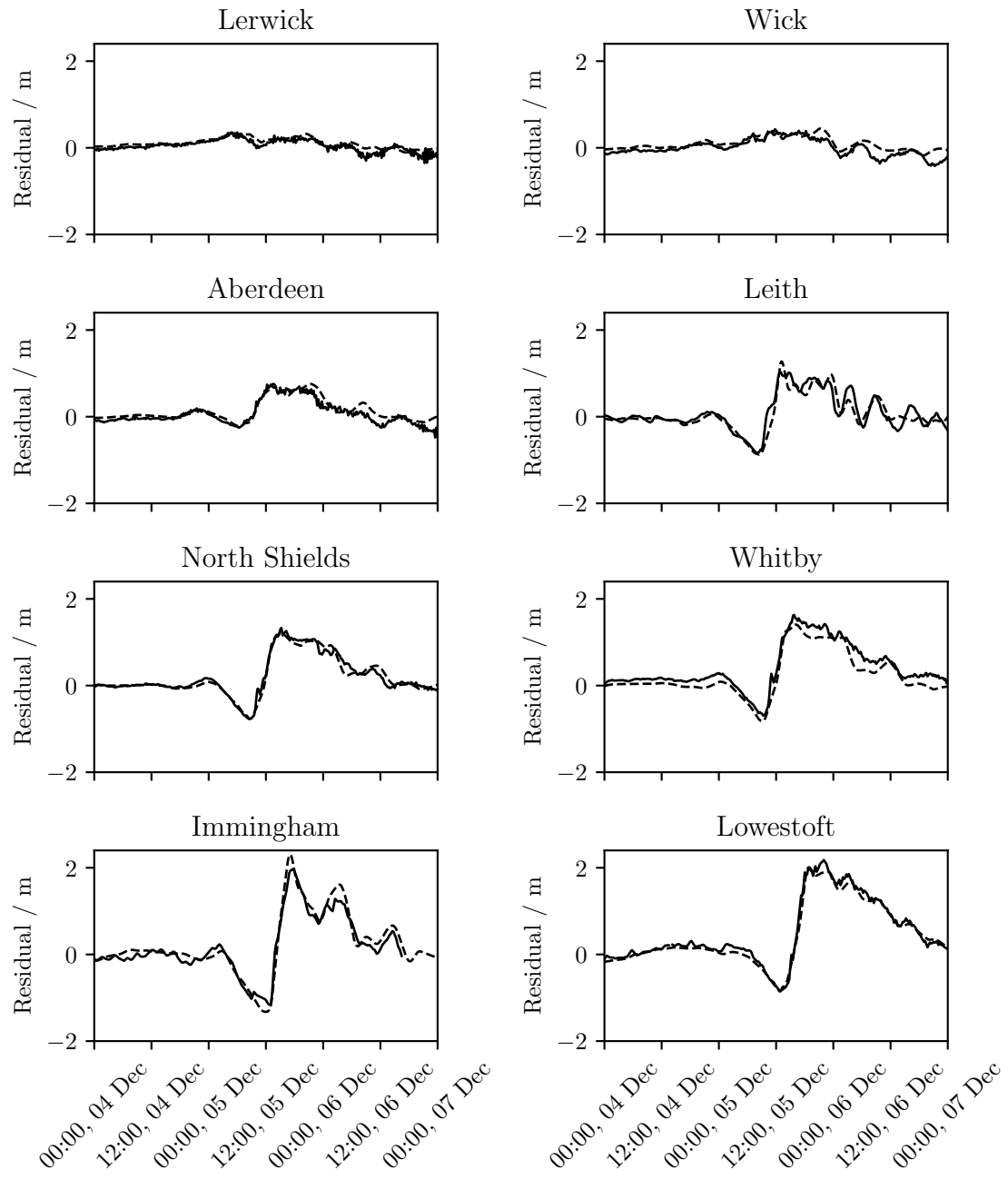


Figure 4.11: Comparison between Thetis model and observations for the Xaver surge event, at the eight tide gauge locations used for the calibration of the Charnock parameter. Solid line: observed residuals. Dashed line: modelled residuals using Thetis. The overall RMSE is 15.9 cm.

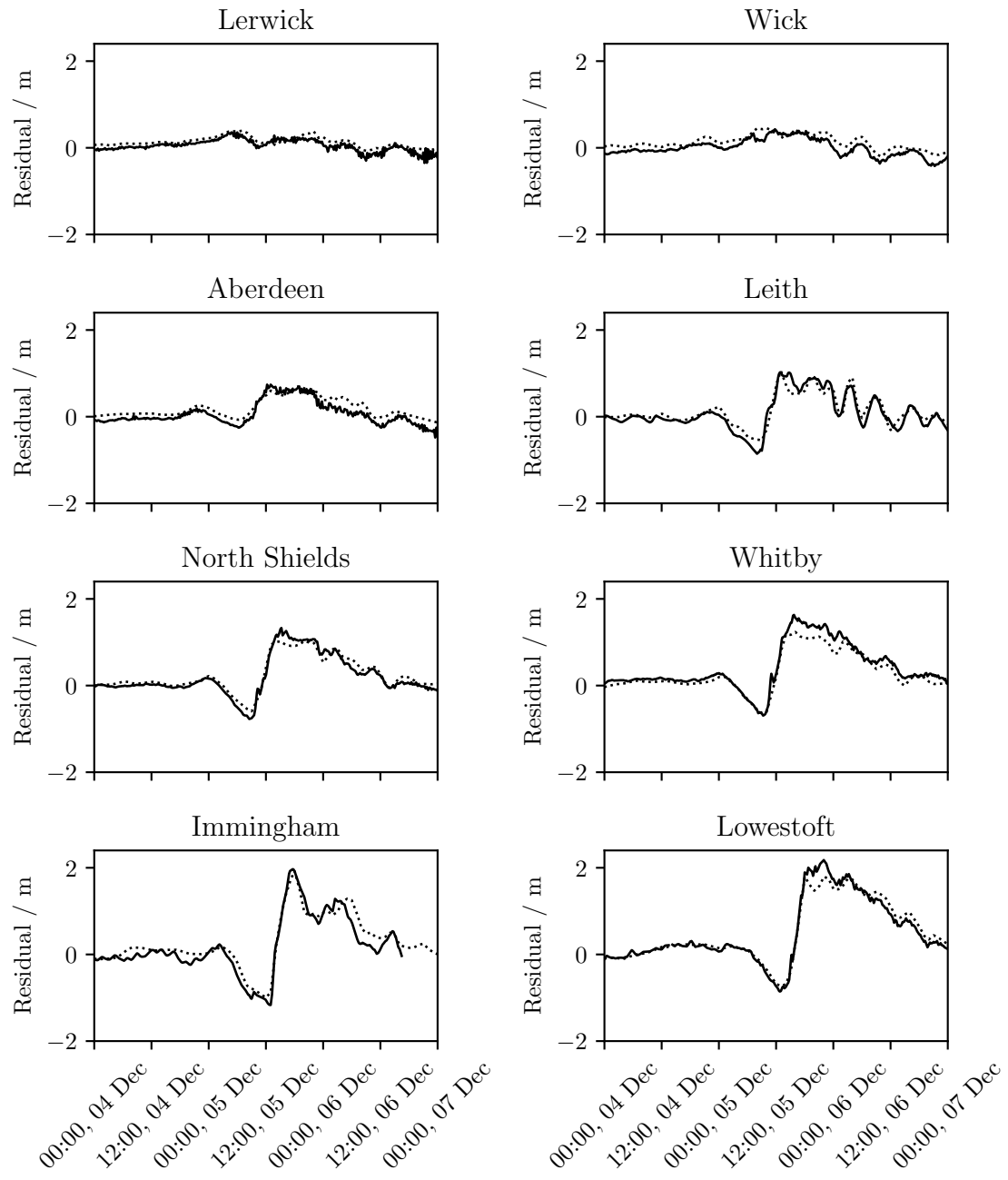


Figure 4.12: Comparison between CS3X model and observations for the Xaver surge event, at the eight tide gauge locations used for the calibration of the Charnock parameter within Thetis. Solid line: observed residuals. Dotted line: modelled residuals using CS3X. The overall RMSE is 16.4 cm.

to three model inputs, namely bottom friction, bathymetry and wind stress;

- (ii) to qualitatively compare patterns of sensitivity to different model inputs, and for different model output locations;
- (iii) to explain the physical significance of these patterns and use them to gain insight into the modelled system;
- (iv) to quantify the uncertainty in model outputs due to uncertainty in each of the three selected model inputs.

4.5.1 Method

Numerical adjoint methods can be used to calculate the gradient vector $\frac{\partial J}{\partial \mathbf{m}}$ of a scalar model output functional J , with respect to a vector of model inputs \mathbf{m} . Since the computational cost of the adjoint model is independent of the length of \mathbf{m} , this vector can therefore contain a sufficient number of degrees of freedom to represent a fully spatially and/or temporally varying field $m(x, y, t)$. The gradient vector computed via the numerical adjoint method can therefore be interpreted as a spatially and/or temporally varying field $\frac{\partial J}{\partial m}(x, y, t)$. By computing this gradient, the use of adjoint methods facilitates a local sensitivity analysis, whereby the effect on model outputs of perturbations in model inputs is investigated.

Within this work, four different model output functionals J are considered. The first three are the skew surges at single target locations (North Shields, Immingham and Lowestoft), and the fourth is the mean skew surge along a section of coastline (measuring approximately 400 km, from Bridlington in the north to Great Yarmouth in the south, and including the Humber Estuary and the Wash). These four target locations are highlighted in figure 4.13. The choice of skew surge as the selected model output at each target location was motivated by Williams et al. (2016); the skew surge constitutes a more meaningful measure of surge severity than the surge residual.

The three selected model inputs ($m(x, y, t)$, represented by the vector \mathbf{m}) are the bottom friction coefficient n , bathymetry h and wind stress $\boldsymbol{\tau}_s$. Alternative possible choices of model inputs include tidal boundary conditions and atmospheric pressure. However, the skew surge is independent of the tide in a probabilistic sense (Williams et al., 2016), and on a single-event basis is influenced only by any tide-surge interaction, since in the calculation of skew surge the modelled tide is subtracted from the modelled (tide plus) surge. The sensitivity of the modelled skew surge to the tidal boundary condition is therefore likely to

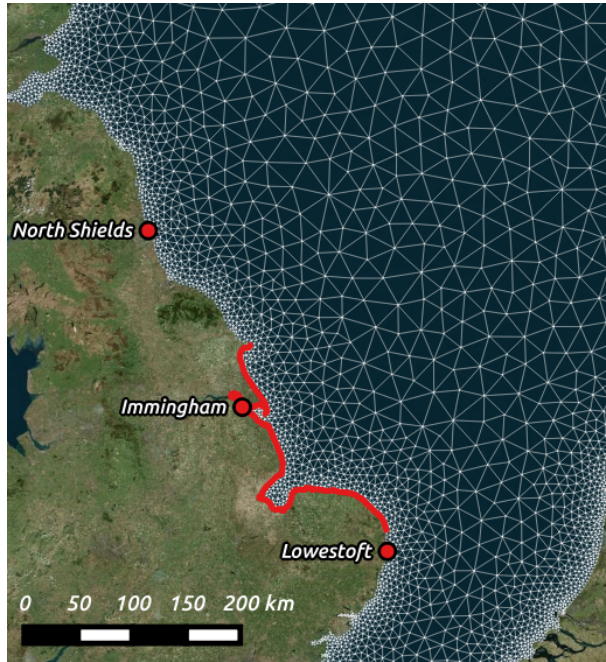


Figure 4.13: Selected target locations for sensitivity analysis and uncertainty quantification. Three tide gauge locations are selected, along with an integrated measure along the section of coastline indicated by the red line.

be small. Likewise, the influence of atmospheric pressure is small compared to the effect of the wind stress for the event studied here. Through a series of numerical experiments it was found that the contribution of atmospheric pressure to the modelled skew surge, averaged across North Shields, Immingham and Lowestoft, is less than 10% of the total skew surge, with wind stress (and some small interaction between the two) accounting for the remainder. The tidal boundary condition and atmospheric pressure are therefore neglected in the sensitivity analysis and uncertainty quantification exercise.

Bottom friction coefficient and bathymetry are both scalar fields which are constant with respect to time, and the sensitivity pattern computed with respect to these inputs is therefore also only spatially varying. Wind stress is a vector field which varies in both space and time, and the sensitivity of modelled skew surges with respect to wind stress is therefore also a spatially and temporally dependent vector field.

In the cases of bottom friction coefficient and bathymetry, the sensitivity of the skew surge must be computed in two parts, requiring one pair of forward and adjoint runs for each. First, the fully surge-forced model is run in forward and adjoint modes, with the functional J defined as the peak sea surface elevation. Then, the tide-only model is run in forward and adjoint modes, with the functional J defined as the peak high water value within the same tidal cycle. The resulting adjoint-derived gradients can be subtracted to

obtain the sensitivity of the skew surge. That is,

$$J_{\text{skew surge}} = J_{\text{peak surge height}} - J_{\text{high tide}}, \quad (4.10)$$

and hence

$$\frac{\partial J_{\text{skew surge}}}{\partial m} = \frac{\partial J_{\text{peak surge height}}}{\partial m} - \frac{\partial J_{\text{high tide}}}{\partial m}. \quad (4.11)$$

This process is not necessary in the case of wind stress, since the tide-only peak sea surface height ($J_{\text{high tide}}$) does not depend on the wind stress, hence

$$\frac{\partial J_{\text{skew surge}}}{\partial m} = \frac{\partial J_{\text{peak surge height}}}{\partial m}. \quad (4.12)$$

Note that, since $J_{\text{peak surge height}}$ is defined at a fixed time (given by the peak surge height of the forward model), these sensitivities will not capture the influence of model input perturbations which alter the surge timing, and may therefore underestimate the true sensitivities. However, they will capture the leading effect of the sensitivity.

$\frac{\partial J}{\partial m}$ represents the spatially (and temporally) varying sensitivity of J to the model input m , and its visualisation can provide physical insight into the modelled system. Furthermore, the spatial patterns of the sensitivity to different inputs can be compared. However, the magnitudes of these sensitivities to different inputs cannot be directly compared, since they have incommensurable units. Instead, the gradients can be combined with estimated uncertainties in each input, in order to estimate the contribution of each input to uncertainty in the model outputs J . Given an estimated input uncertainty Δm , a convolution with the sensitivity $\frac{\partial J}{\partial m}$ gives

$$\Delta J \approx \int \int \int \frac{\partial J}{\partial m}(x, y, t) \cdot \Delta m(x, y, t) \, dx \, dy \, dt, \quad (4.13)$$

which may be directly compared for different inputs m . Note that this is equivalent to performing a first-order Taylor expansion with respect to the input m , and that the resulting ΔJ may be positive or negative for a given perturbation Δm . For the purpose of uncertainty quantification within this chapter, only spatially uniform Δm are considered. This is an approximation to the true uncertainty, since real input uncertainties are likely to vary spatially. However, in the absence of information about the spatial correlation of input uncertainties, this method offers a simple approach to estimating model output uncertainties ΔJ .

4.5.2 Results

Sensitivity to bottom friction

The skew surge at each target location depends on the bottom friction coefficient across the whole domain. Note that, while the parameter is specified within the model as a spatially uniform value, the sensitivity of a given model output to the bottom friction coefficient nevertheless varies spatially. In principle the sensitivity to bottom friction coefficient also evolves with time (i.e. the skew surge depends more strongly on the bottom friction at shorter times before the peak), but since the bottom friction coefficient is constant in time, here the temporal dependence is removed by performing the adjoint run over a period of approximately 10 days prior to the peak surge. The resulting sensitivities therefore include the cumulative effect of the bottom friction parameter over the 10-day period. This period was found to be sufficient, with any extension beyond 10 days having a negligible effect on the computed sensitivities.

The resulting fields of sensitivity to bottom friction coefficient are shown in figure 4.14 for each of the four target locations. The greatest sensitivity magnitudes are found within relatively small regions in the vicinity of each target location. The sensitivity of the skew surge at North Shields exhibits the smallest sensitivity magnitudes, due to its position on an exposed section of coastline; the propagation of the surge as a coastally trapped wave is not strongly affected by local features, and the local value of the bottom friction coefficient therefore has only a weak effect on the skew surge at the North Shields tide gauge. This is in contrast to the large sensitivity magnitudes for the skew surge at Immingham; here, high sensitivity is observed in and around the Humber Estuary and the Wash. The dynamics of surge propagation around this region are complex, and the waters here are particularly shallow. The $1/H$ proportionality in the wind stress and bottom stress terms of the governing equations (3.15) therefore increases the model's sensitivity to bottom friction, as well as to bathymetry and wind stress, in shallow waters. This high sensitivity to the friction coefficient in the region of the Humber Estuary and the Wash is also evident for the skew surge at Lowestoft, suggesting that the interaction between the surge and this region of coastline has a lasting effect on the surge as it travels further south.

Common to the sensitivity patterns for all target locations is the pattern in the far-field, i.e. in the north of the domain. This is because any effect of the bottom friction on the surge in the north of the domain is propagated with the surge as it travels south as a coastally trapped wave, and therefore has the same effect on the skew surge at all target locations.

In order to estimate the total impact of an uncertain bottom friction coefficient on model outputs via equation (4.13), it is first necessary to estimate the uncertainty in the bottom friction coefficient (Δm in equation (4.13)). Based on typical values for the Manning coefficient (Arcement and Schneider, 1989) for the types of sediment found in the North Sea (Digimap, 2011), an uncertainty in the Manning coefficient of $0.005 \text{ s m}^{-1/3}$ is assumed. Using equation (4.13) to convolve a uniform uncertainty of $0.005 \text{ s m}^{-1/3}$ with the adjoint-derived sensitivities shown in figure 4.14 produces skew surge uncertainties of -8.1 cm at North Shields, -17.3 cm at Immingham and -16.1 cm at Lowestoft, with the negative signs indicating that an increase in the friction coefficient would induce reductions in the skew surge. This is expected, since bed friction extracts energy from the surge. The uncertainty in the mean skew surge along the coastline section, estimated by the same method, is -19.9 cm; this is of similar magnitude to the estimated uncertainties at Immingham (which is within the coastline section) and Lowestoft (just to the south of the coastline section).

Sensitivity to bathymetry

The sensitivities of modelled skew surges to bathymetry are shown in figure 4.15. The temporal dependence of the skew surges on the bathymetry was again removed by performing the adjoint run over 10 days prior to the peak surge, and the influence of the bathymetry accumulated over this period. The observed spatial patterns of sensitivity to bathymetry share similar features to those of the sensitivity to bottom friction coefficient of figure 4.14. The greatest magnitudes of sensitivity to bathymetry are found within localised regions around each target location, and these localised sensitivities share similar spatial patterns with those observed for bottom friction, but with the opposite sign. This is likely to be due to the $1/H$ proportionality of the bottom stress term in the governing equations; the influence of this term would induce opposite sensitivities with respect to the bottom friction coefficient and the bathymetry.

In the north of the domain, it is again observed that the patterns of bathymetry sensitivity are similar for all target locations, due to the propagation of the surge as a coastally trapped wave from north to south. Any influence of the bathymetry on the surge in the north of the domain is propagated south with the surge and impacts all subsequent observation locations.

To estimate the impact of this sensitivity on model outputs, it is again necessary to first estimate the uncertainty in the bathymetry itself. For this, the root mean square (RMS) difference between two bathymetric datasets is computed. The GEBCO bathy-

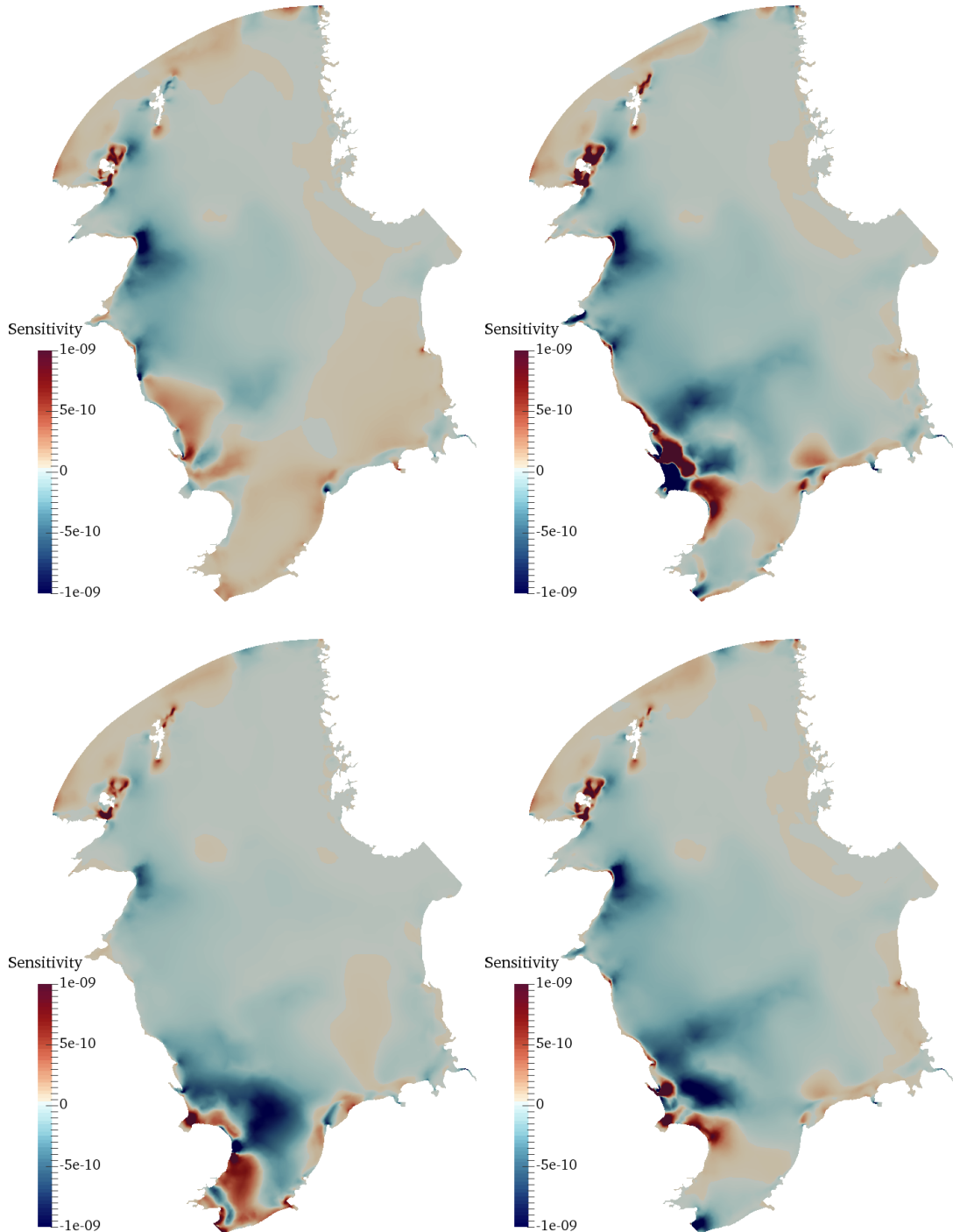


Figure 4.14: Sensitivity of modelled skew surges to bottom friction coefficient. Units: $\text{m s}^{-1} \text{m}^{1/3} \text{m}^{-2}$ (metres of surge, per unit Manning coefficient, per unit area). Top left: North Shields. Top right: Immingham. Bottom left: Lowestoft. Bottom right: mean along coastline section.

	North Shields	Immingham	Lowestoft	Coastline section
Bottom friction coefficient ($\pm 0.005 \text{ s m}^{-1/3}$)	$\mp 8.1 \text{ cm}$	$\mp 17.3 \text{ cm}$	$\mp 16.1 \text{ cm}$	$\mp 19.9 \text{ cm}$
Bathymetry ($\pm 2.7 \text{ m}$)	$\mp 2.3 \text{ cm}$	$\pm 6.7 \text{ cm}$	$\mp 4.8 \text{ cm}$	$\mp 3.7 \text{ cm}$

Table 4.1: Summary of estimated skew surge uncertainties due to bottom friction coefficient and bathymetry. \pm signs indicate that skew surges would be increased by a uniform positive perturbation in the model input, with \mp signs indicating a decrease in skew surges.

metry dataset used within the model is compared with data from Digimap (Digimap, 2013), which is available at higher resolution than GEBCO, but does not cover the entire model domain. In the region of the model domain in which both GEBCO and Digimap datasets are available, the RMS difference between the two is 2.7 m. Convolving a uniform 2.7 m bathymetry uncertainty with the adjoint-computed bathymetry sensitivities according to equation (4.13) produces skew surge uncertainties of -2.3 cm, 6.7 cm and -4.8 cm at North Shields, Immingham and Lowestoft, respectively, and -3.7 cm for the mean skew surge along the coastline section. The minus signs for North Shields, Lowestoft and the coastline section indicate that an increase in bathymetry (i.e. an increase in water depth) would induce a decrease in the skew surge, with the opposite being the case at Immingham.

One feature common to the bathymetry sensitivity for Immingham, Lowestoft and the coastline section is the region of positive sensitivity coinciding with Dogger Bank, to the north-east of the Humber Estuary (as shown in figure 4.8). The depth of this bank is around 20 m, while the depths immediately surrounding the bank exceed 60 m. The positive sign of the bathymetry sensitivity in this region indicates that an increase in bathymetry (i.e. the removal of the bank) would produce an increase in the peak residuals at Immingham, Lowestoft and the coastline section, and therefore that the bank protects the coastline to its south from the surge.

Table 4.1 summarises the estimated uncertainties due to bottom friction coefficient and bathymetry, at each of the target locations.

Sensitivity to wind stress

Since the wind stress varies in space and time, so too do the sensitivities of modelled skew surges with respect to the wind stress. Figure 4.16 shows three snapshots of the sensitivity of the skew surge at Immingham to wind stress at two, four and six hours prior to the peak surge. In each snapshot, there is a well defined region of influence of the wind

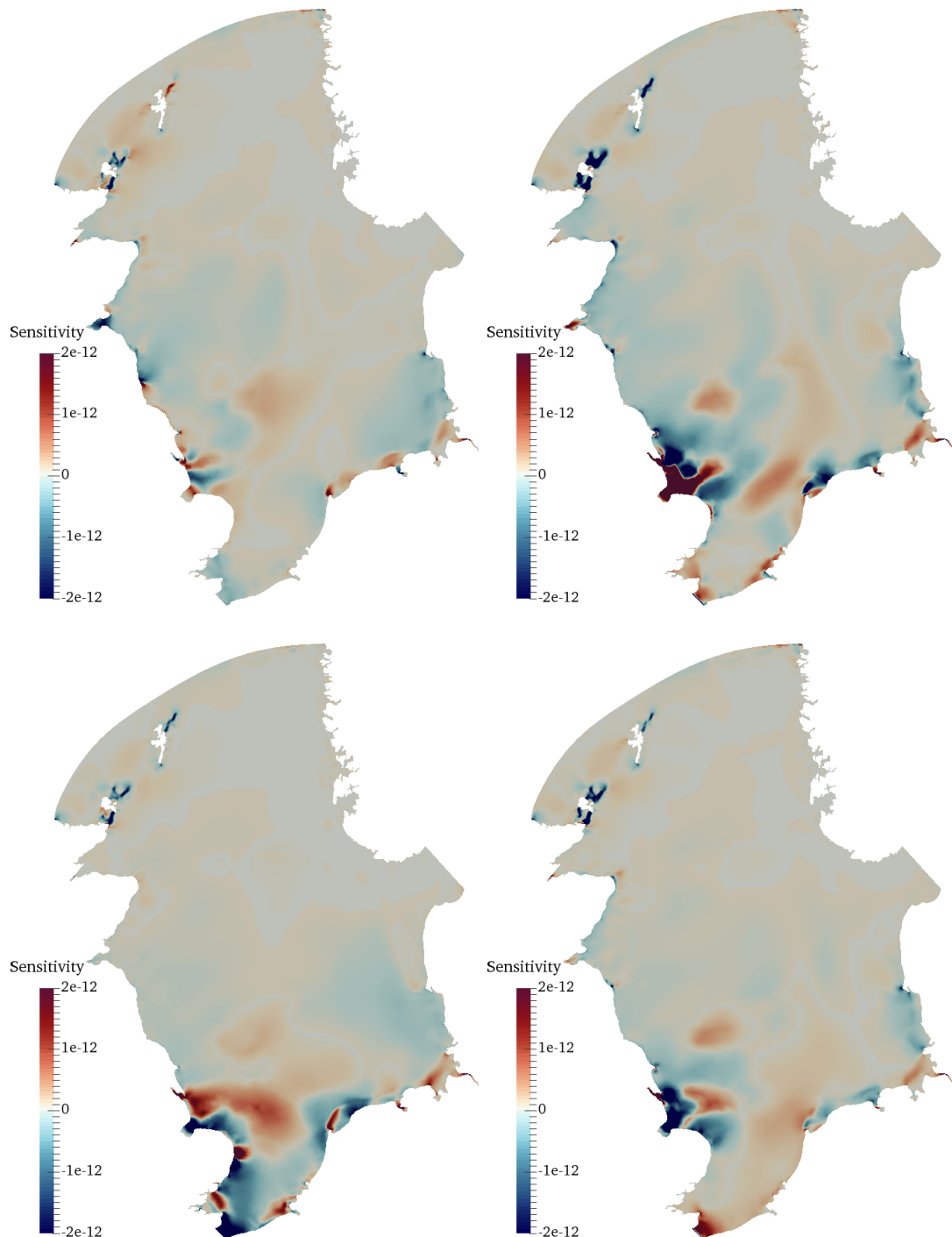


Figure 4.15: Sensitivity of modelled skew surges to bathymetry. Units: $\text{m m}^{-1} \text{m}^{-2}$ (metres of surge, per metre of bathymetry, per unit area). Top left: North Shields. Top right: Immingham. Bottom left: Lowestoft. Bottom right: mean along coastline section.

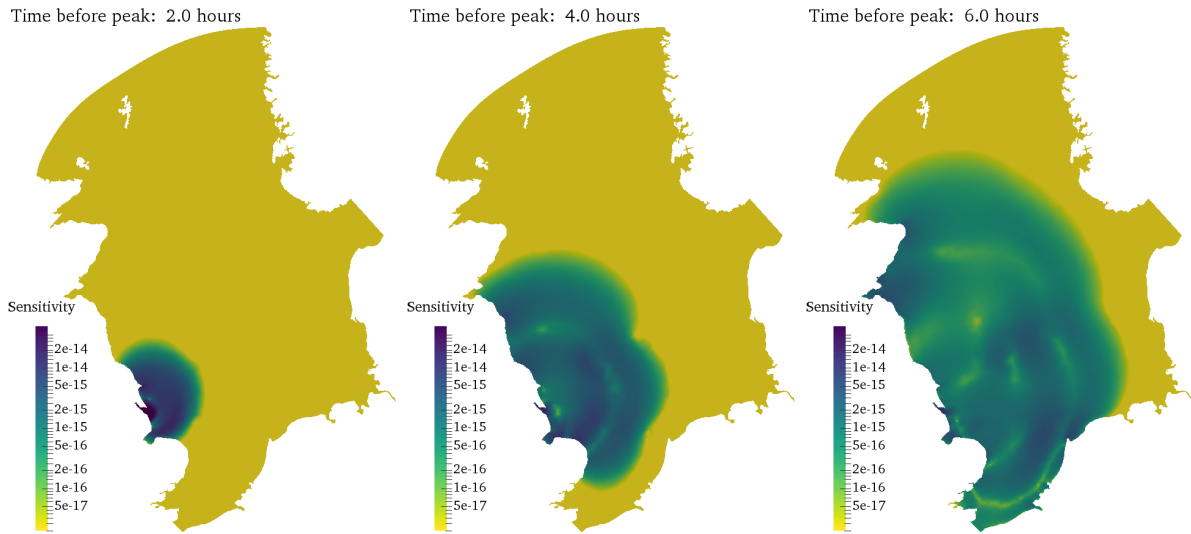


Figure 4.16: Snapshots of the magnitude of the skew surge sensitivity at Immingham to wind stress at previous times, as labelled. Units: $\text{m Pa}^{-1} \text{m}^{-2} \text{s}^{-1}$ (metres of surge, per Pa wind stress, per unit area, per second).

stress on the peak surge height, and the spatial extent of this region increases backwards in time. Beyond this region of influence, any perturbation induced by the wind stress has insufficient time to have any effect on the peak surge height at Immingham, since these perturbations cannot travel any faster than the shallow water wave speed. The sensitivity of the skew surge to the wind stress therefore behaves as a shallow water wave, which propagates backwards in time, originating at the point at which the skew surge is measured. This phenomenon has been explored previously by Wilson et al. (2013), and can be further confirmed by an analytic approach; see section 4.5.3.

In order to make progress comparing the wind stress sensitivities of skew surges at different locations, it is helpful to integrate the wind stress sensitivity field with respect to time, to produce an overall spatial pattern. These time-integrated sensitivities are shown in figure 4.17 for each target location. Similarly to the sensitivities to bottom friction coefficient and bathymetry, there are regions of high sensitivity magnitude in the vicinity of each target location, where local winds at short times before the peak surge occurs have a significant effect on the value of the peak sea surface height (and hence skew surge). All four target locations exhibit similar patterns of sensitivity to wind stress in the north of the domain, but differ more in the south, because any perturbations induced by wind stress in the north of the domain affect the coastally trapped wave which then impacts all target locations as it travels south. This is consistent with the patterns of sensitivity to bottom friction and bathymetry discussed above.

The magnitudes of wind stress sensitivity are generally greater in the west of the domain.

This is due to the southerly propagation of the surge along the western coastal boundary of the model domain (the east coast of the UK). Winds in the east of the domain therefore have relatively little effect on the surge impacting the UK locations considered within this study. In particular, sensitivity magnitudes over the Norwegian Trench (see figure 4.8) are very small. This is likely to be due to the very large depths in this region, and the $1/H$ proportionality in the wind stress term in the governing equations (3.15).

It is not possible to make a generally applicable estimate of the uncertainty associated with wind stress, since in a forecast scenario this depends strongly on the forecast least time, and will vary with different surge events. To make a simple comparison between the overall wind stress contribution to uncertainty for each target location, it is assumed that there is a 5% uncertainty in the wind stress magnitude, with no uncertainty in its direction, i.e. $\Delta m = 0.05 \cdot \tau_s$. By a convolution of this uncertainty with the adjoint-derived sensitivities via equation (4.13), uncertainties of 4.3 cm, 5.8 cm, 7.8 cm and 6.8 cm are calculated for the skew surges at North Shields, Immingham, Lowestoft and the coastline section, respectively. This shows an increasing trend for gauges further south, due to the southward propagation of the surge and the corresponding accumulation of influence of the wind stress, and the positive signs indicate that increased wind stress induces increased skew surges, as would be expected.

4.5.3 Aside: analytic adjoint approach

Section 4.5.2 took a purely numerical approach to investigating the sensitivity of skew surges to each model input. Here, an analytic adjoint approach is taken to deriving the equations governing the sensitivity of the peak free surface elevation (or equivalently the skew surge) at a single location to wind stress at earlier times. The objective is to analytically confirm the shallow water wave-like behaviour of the wind stress sensitivity pattern which is observed in the numerical results, which have been justified in section 4.5.2 based on physical intuition.

For simplicity, the bottom stress and viscosity terms are neglected, and the starting point is taken as the linear shallow water equations in conservative form, given by

$$\begin{aligned} \frac{\partial \eta}{\partial t} + \nabla \cdot (h\mathbf{u}) &= 0, \\ \frac{\partial \mathbf{u}}{\partial t} + g\nabla\eta - \frac{\boldsymbol{\tau}_s}{\rho h} &= 0. \end{aligned} \tag{4.14}$$

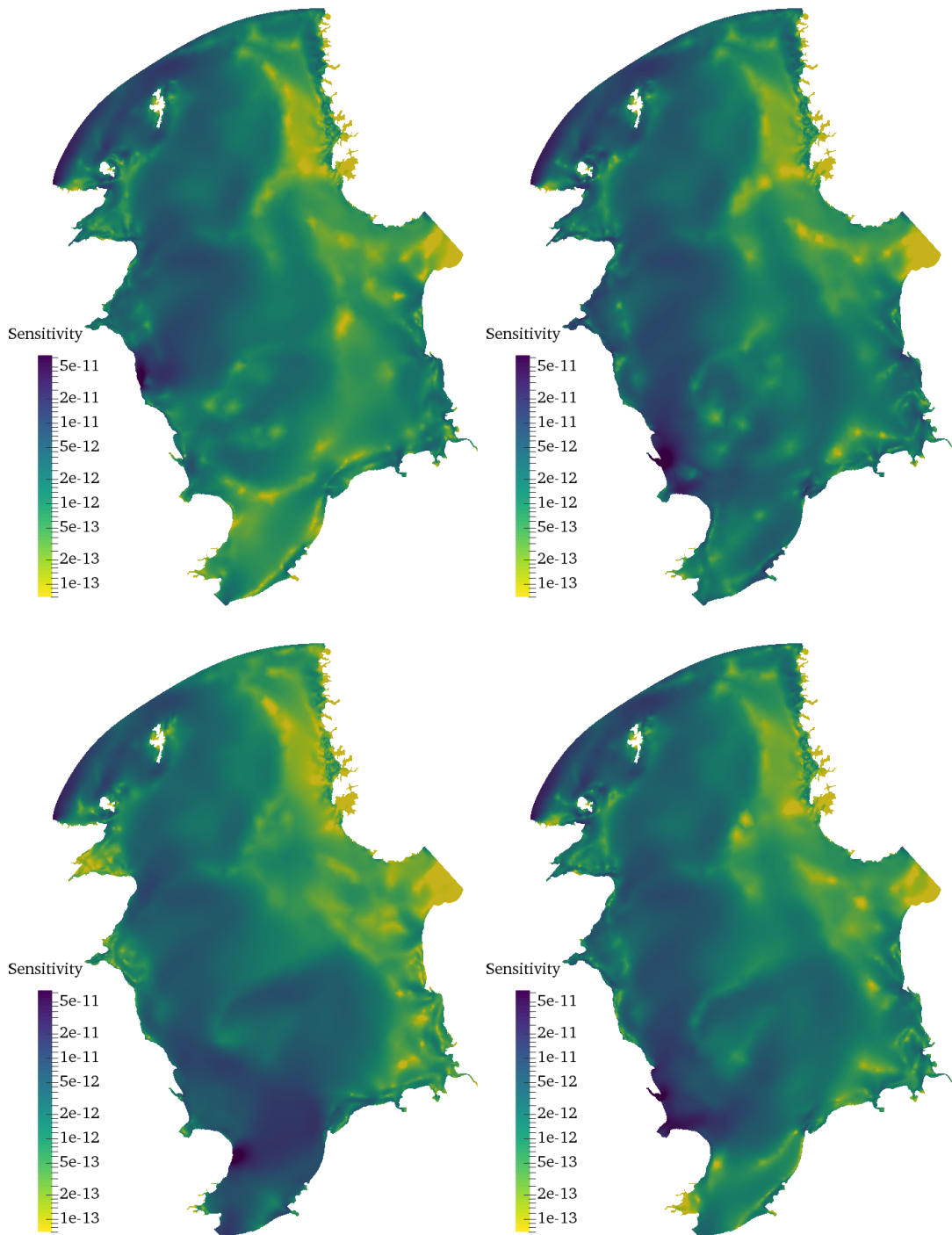


Figure 4.17: Magnitude of the time-integrated sensitivity of modelled skew surges to wind stress. Units: $\text{m Pa}^{-1} \text{m}^{-2}$ (metres of surge, per Pa wind stress, per unit area). Top left: North Shields. Top right: Immingham. Bottom left: Lowestoft. Bottom right: coastline section. Note the logarithmic scale.

A general functional is defined as

$$J = \int_x \int_y \int_t r(\eta, \mathbf{u}; x, y, t) dt dy dx. \quad (4.15)$$

Since the focus of this work is on the sensitivity of an instantaneous measurement of the free surface elevation η at a location \mathbf{x}_0 and time t_0 , r can be considered in the form

$$r = \eta \delta(\mathbf{x} - \mathbf{x}_0) \delta(t - t_0), \quad (4.16)$$

where $\delta(\cdot)$ is the Dirac delta function. \mathbf{x}_0 will be chosen to be the location of the tide gauge at Immingham, and t_0 the time of the peak surface elevation at that location. Introducing Lagrange multipliers $\lambda_\eta, \boldsymbol{\lambda}_{\mathbf{u}}$ for the variables η, \mathbf{u} respectively, the Lagrangian is given by

$$\begin{aligned} \mathcal{L} = \int_x \int_y \int_t & \left[r + \lambda_\eta \left(\frac{\partial \eta}{\partial t} + \nabla \cdot (h\mathbf{u}) \right) \right. \\ & \left. + \boldsymbol{\lambda}_{\mathbf{u}} \cdot \left(\frac{\partial \mathbf{u}}{\partial t} + g\nabla\eta - \frac{\boldsymbol{\tau}_s}{\rho h} \right) \right] dt dy dx. \end{aligned} \quad (4.17)$$

The forward model equations are recovered by requiring that the variation of \mathcal{L} with respect to each of the Lagrange multipliers is zero, i.e.

$$\begin{aligned} \frac{\delta \mathcal{L}}{\delta \lambda_\eta} &= 0, \\ \frac{\delta \mathcal{L}}{\delta \boldsymbol{\lambda}_{\mathbf{u}}} &= 0. \end{aligned} \quad (4.18)$$

Similarly, the adjoint equations are derived by requiring that the variation of \mathcal{L} with respect to each of the forward variables is also zero, i.e.

$$\begin{aligned} \frac{\delta \mathcal{L}}{\delta \eta} &= 0, \\ \frac{\delta \mathcal{L}}{\delta \mathbf{u}} &= 0. \end{aligned} \quad (4.19)$$

Note that, while the forward equations do not depend on the functional J , the adjoint equations do, via the dependence of r on the forward model variables.

In order to make progress, \mathcal{L} is first integrated by parts to give

$$\begin{aligned} \mathcal{L} = \int_x \int_y \int_t & \left[r - \eta \frac{\partial \lambda_\eta}{\partial t} - h \mathbf{u} \cdot \nabla \lambda_\eta \right. \\ & \left. - \mathbf{u} \cdot \frac{\partial \boldsymbol{\lambda}_u}{\partial t} - g \eta \nabla \cdot \boldsymbol{\lambda}_u - \frac{\boldsymbol{\tau}_s}{\rho h} \cdot \boldsymbol{\lambda}_u \right] dt dy dx \\ & + \text{boundary terms.} \end{aligned} \quad (4.20)$$

The boundary terms pertain to the boundary conditions of the adjoint problem, which are simply the homogeneous versions of the forward model boundary conditions (Funke et al., 2014). The variation of this expression with respect to the forward model variables η and \mathbf{u} can be taken straightforwardly. Setting these equal to zero yields the adjoint equations

$$\begin{aligned} \frac{\partial \lambda_\eta}{\partial t} + g \nabla \cdot \boldsymbol{\lambda}_u &= \frac{\partial r}{\partial \eta}, \\ \frac{\partial \boldsymbol{\lambda}_u}{\partial t} + h \nabla \lambda_\eta &= 0. \end{aligned} \quad (4.21)$$

Since, in this example, r is not an explicit function of \mathbf{u} , it only appears in the first adjoint equation. Note the similarity with the starting point of this analytic approach, the linear shallow water equations of equation (4.14). These equations can be combined to produce a shallow water wave equation with a source term on the right hand side,

$$\frac{\partial^2 \boldsymbol{\lambda}_u}{\partial t^2} - gh \nabla^2 \boldsymbol{\lambda}_u = -h \nabla \frac{\partial r}{\partial \eta}. \quad (4.22)$$

The interest of this work is in the sensitivity of the functional J with respect to the wind stress $\boldsymbol{\tau}_s$, broken down into its contribution as a function of space and time. The variation of J with respect to $\boldsymbol{\tau}_s$ is given by

$$\frac{\delta J}{\delta \boldsymbol{\tau}_s} = \frac{\delta \mathcal{L}}{\delta \boldsymbol{\tau}_s} = \int_x \int_y \int_t -\frac{\boldsymbol{\lambda}_u}{\rho h} dt dy dx, \quad (4.23)$$

where the first equality is valid due to the forward and adjoint equations being satisfied. The contribution of a given point in space and time to wind stress sensitivity, henceforth denoted $\boldsymbol{\sigma}$, is therefore given by

$$\boldsymbol{\sigma} = -\frac{\boldsymbol{\lambda}_u}{\rho h}. \quad (4.24)$$

By substitution into equation (4.22), the equation governing the sensitivity of a measure-

ment to instantaneous wind stress is therefore given by

$$\frac{\partial^2 \boldsymbol{\sigma}}{\partial t^2} - g \nabla^2 (h \boldsymbol{\sigma}) = \frac{1}{\rho} \nabla \frac{\partial r}{\partial \eta}, \quad (4.25)$$

which is simply a linear shallow water wave equation with a source term on the right hand side.

This source term is determined from equation (4.16). Since the right-hand side is therefore only non-zero at $t = t_0$ and the flow of information in an adjoint problem is in the reverse time direction, this is interpreted as an initial condition for the sensitivity PDE (equation (4.25)). Furthermore, the physical interpretation of equation (4.25) is that the sensitivity of the peak surge height to wind stress behaves as a shallow water wave propagating outwards from the observation location, and backwards in time. This is consistent with the numerical result observed in section 4.5.2. The derivation here, starting with the linear shallow water equations with no drag or viscosity terms, includes only the leading order effects. Inclusion of all terms would produce additional terms in the wind stress sensitivity PDE, and the full adjoint equations for the nonlinear shallow water equations can be found in e.g. Funke et al. (2014). However, the leading order effect derived here is sufficient to explain the observations from the numerical results.

4.6 Connection to ensemble methods

The estimation of skew surge uncertainties via equation (4.13) constitutes a linearisation of the modelled skew surge with respect to an input parameter m , which is valid for small perturbations Δm . In section 4.5.2 this has been applied to uniform uncertainties in order to approximate the overall impact of uncertain model inputs. However, the use of spatially and/or temporally varying $\Delta m(x, y, t)$ is also possible, and can be linked to ensemble methods for uncertainty quantification.

In operational storm surge forecasting, the forecast uncertainty is assumed to be dominated by the meteorological forecast used to force the surge model, with uncertainty typically quantified using ensemble methods. Focusing here on wind stress, a deterministic skew surge forecast is given by

$$J(\boldsymbol{\tau}_s), \quad (4.26)$$

where $\boldsymbol{\tau}_s$ is the deterministic wind stress forecast. A given wind stress forecast ensemble member $\boldsymbol{\tau}_s + \Delta \boldsymbol{\tau}_s$ constitutes a perturbation from this deterministic forecast. The

corresponding skew surge forecast ensemble member is given by

$$J(\boldsymbol{\tau}_s + \Delta\boldsymbol{\tau}_s). \quad (4.27)$$

The ensemble method for uncertainty quantification simply takes a set of perturbations $\Delta\boldsymbol{\tau}_s$ and performs forward model runs to determine $J(\boldsymbol{\tau}_s + \Delta\boldsymbol{\tau}_s)$ for each perturbation.

However, the use of adjoint methods provides an alternative approach for estimating equation (4.27). For small perturbations $\Delta\boldsymbol{\tau}_s$, a first-order Taylor expansion gives

$$J(\boldsymbol{\tau}_s + \Delta\boldsymbol{\tau}_s) = J(\boldsymbol{\tau}_s) + \int_{t=-\infty}^{t_0} \int_y \int_x \frac{\partial J}{\partial \boldsymbol{\tau}_s} \cdot \Delta\boldsymbol{\tau}_s \, dx \, dy \, dt + \text{truncation error}, \quad (4.28)$$

where the adjoint model can be used to compute $\partial J / \partial \boldsymbol{\tau}_s$. t_0 is the time at which the functional J is defined, and the lower limit of the time integral can be truncated at a suitable point where the sensitivity $\partial J / \partial \boldsymbol{\tau}_s$ becomes negligible. Note that this is equivalent to equation (4.13).

There are a number of issues to address regarding the direct use of equation (4.28) within an ensemble method. Firstly, the relative computational cost should be considered. For the Thetis model used here, the adjoint model run for the evaluation of the derivative $\frac{\partial J}{\partial \boldsymbol{\tau}_s}$ requires between three and four times the computation time of the forward model for evaluating $J(\boldsymbol{\tau}_s)$ (or explicitly evaluating $J(\boldsymbol{\tau}_s + \Delta\boldsymbol{\tau}_s)$). However, once the derivative has been computed, the evaluation of equation (4.28) requires negligible computation time in comparison to running the numerical model. The use of equation (4.28) is therefore more computationally efficient than the traditional ensemble approach when the number of ensemble members $N \geq 5$. For reference, the UK operational model uses an ensemble of $N = 12$ members. The number of degrees of freedom in a wind stress forecast is very large, and the adjoint-based approach of equation (4.28) can explore the response of the surge model to arbitrarily many degrees of freedom at the computational cost of around five forward model runs. Meanwhile, the traditional ensemble approach incurs a computational cost of one forward model run for every degree of freedom explored. This is the key advantage of adjoint methods for uncertainty quantification.

The second issue to address regarding the use of equation (4.28) is its restriction to ‘small’ perturbations $\Delta\boldsymbol{\tau}_s$, such that the response of the modelled skew surge to wind stress perturbations is linear and the truncation error is therefore negligible. The question of what constitutes a small sufficiently perturbation can be answered by performing a series of full forward model runs with varying $\Delta\boldsymbol{\tau}_s$, and comparing the explicitly computed $J(\boldsymbol{\tau}_s + \Delta\boldsymbol{\tau}_s)$ with the adjoint-estimated values calculated from equation (4.28).

However, $\boldsymbol{\tau}_s$ exists within a very high-dimensional space; within Thetis it is represented by a continuous, piecewise linear function, with a total number of degrees of freedom given by $2 \times (\text{number of mesh nodes}) \times (\text{number of time steps})$. A thorough study into the validity of equation (4.28) is therefore challenging (i.e. one runs into the disadvantage of traditional ensemble methods outlined above re computational cost).

In order to make progress, an experiment was performed using the Storm Xaver case study, with $\Delta\boldsymbol{\tau}_s$ assumed to be directly proportional to the hindcast wind stress. Hence a ‘storm factor’ is defined, which scales the deterministic wind stresses such that

$$\boldsymbol{\tau}_s + \Delta\boldsymbol{\tau}_s = (\text{storm factor}) \times \boldsymbol{\tau}_s. \quad (4.29)$$

The adjoint-derived model sensitivities therefore linearise the model about a storm factor of 1. Using this definition, a series of forward model runs was performed, for varying values of the storm factor. For each storm factor, the explicitly computed $J(\boldsymbol{\tau}_s + \Delta\boldsymbol{\tau}_s)$ can be compared with its approximation via equation (4.28). The results are shown in figure 4.18, for storm factors in the range 0 – 2.4, and J defined as the skew surge at each of the North Shields, Immingham and Lowestoft tide gauges. The absolute difference between the approximation and the full model output is shown in figure 4.19 and is equal to the truncation error of equation (4.28). For Immingham, this truncation error remains below 5 cm for storm factors in the range 0.41 – 1.84, spanning a range of skew surges of 1.7 m. For comparison, at a lead time of approximately 24 hours, the range of skew surges from the CS3X operational forecast ensemble at Immingham for this event was approximately 1 m (National Oceanography Centre, personal communication 2018). This suggests that the range of linear response may, under certain conditions, be large enough for adjoint-derived results via equation (4.28) to be consistent with an ensemble of forward model runs, for non-negligible lead times. However, this constitutes a preliminary study and further work would be required to rigorously investigate the validity of adjoint-derived ensembles.

Note that, for the perturbations $\Delta\boldsymbol{\tau}_s$ considered here, the leading order truncation error of equation (4.28) is negative. Equivalently, the second derivative of the response curve shown in figure 4.18 is negative. The use of the adjoint-based approximation therefore leads to overestimates of the full model response. This can be understood by considering how the nonlinearity, which is due to tide-surge interaction, is introduced by the shallow water equations (3.15). The wind stress term is inversely proportional to the water depth H , which means that the larger the surge residual, or equivalently the greater the water depth H , the smaller the effect of additional wind stress (Horsburgh and Wilson, 2007). Further work is required to investigate whether this effect holds for a broader class of

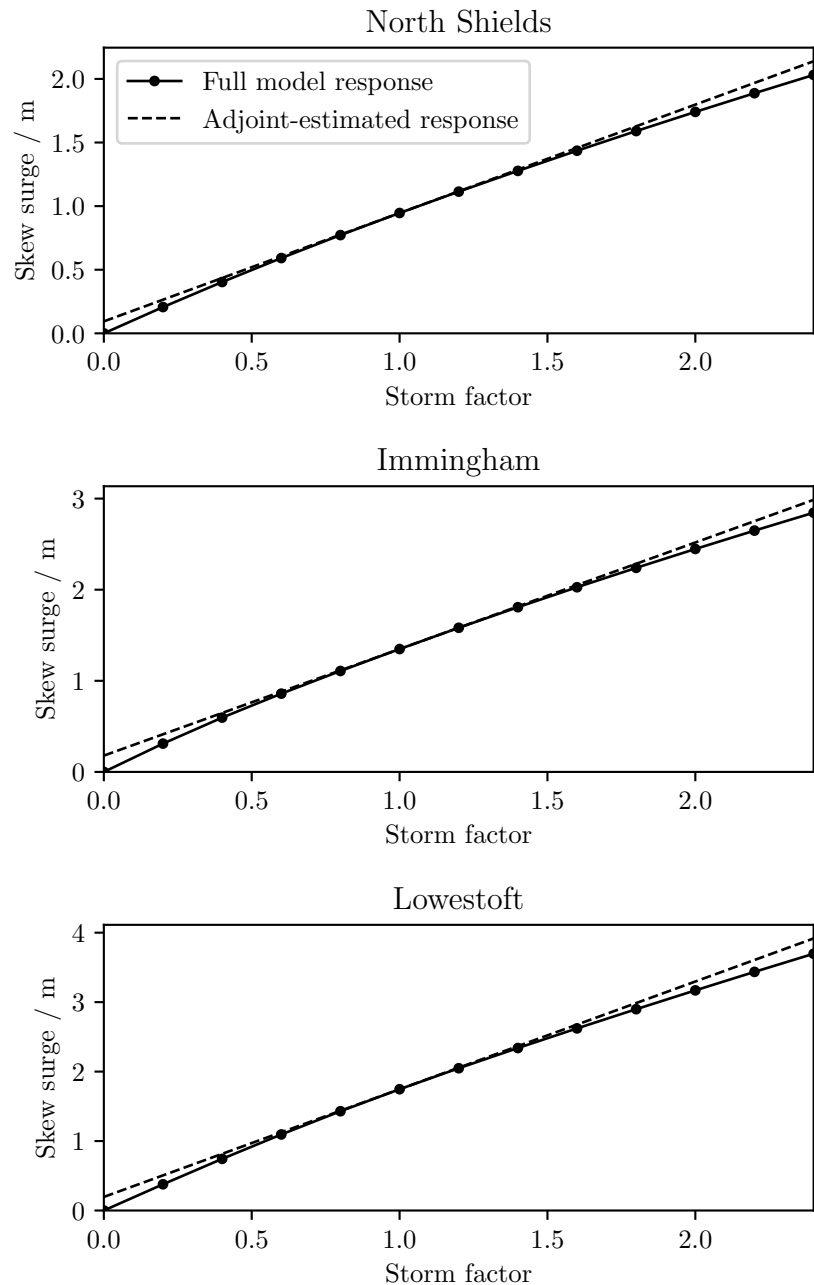


Figure 4.18: Comparison of linearised response to wind stress and full model outputs for the surge residuals at North Shields, Immingham and Lowestoft.

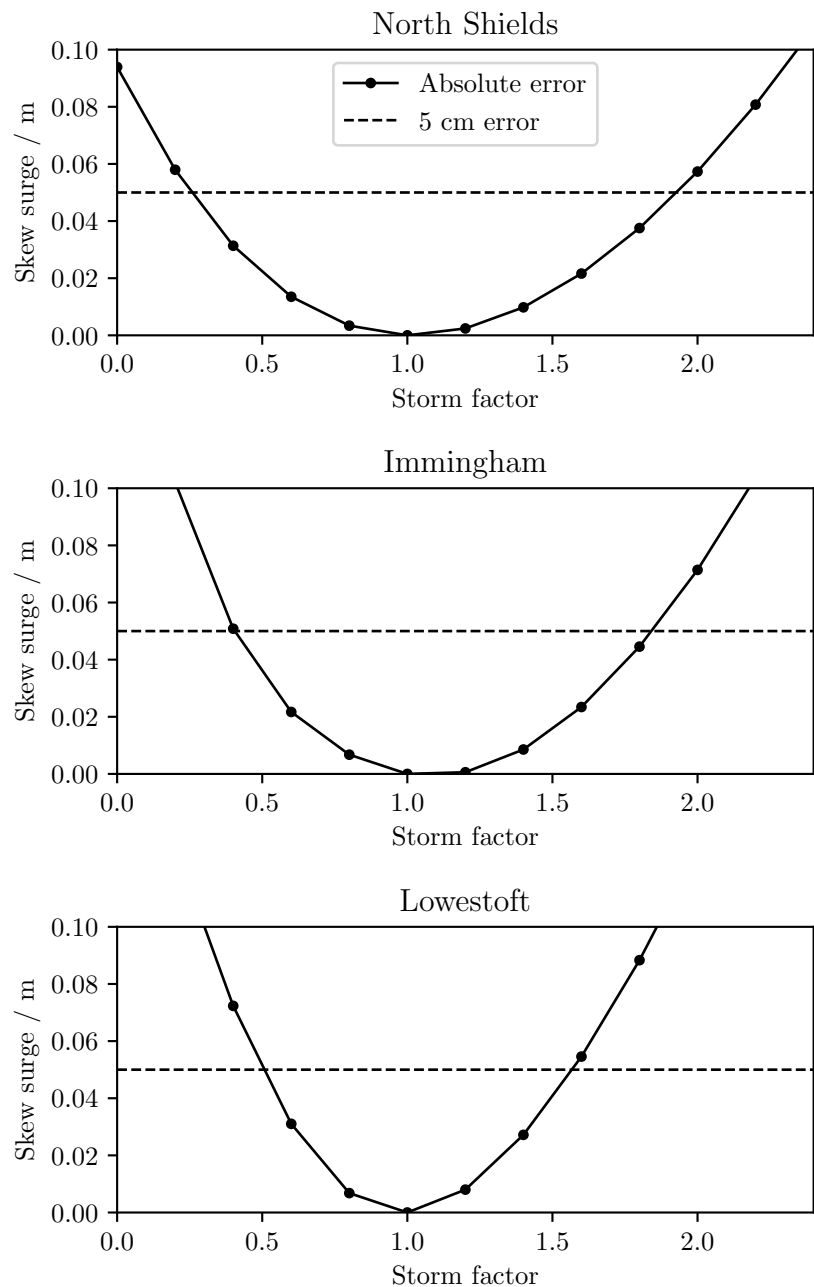


Figure 4.19: Errors in the linearised response to wind stress, compared with full model outputs, for the surge residuals at North Shields, Immingham and Lowestoft.

perturbations $\Delta\tau_s$.

The third drawback of the use of equation (4.28) is that it considers a functional J which is defined at a fixed time. Any change in the arrival time of the peak surge caused by the perturbation $\Delta\tau_s$ cannot be captured by the linearised model. In the ‘storm factor’ test described above, the use of perturbations which are linearly proportional to the deterministic wind stress τ_s is unlikely to significantly alter the arrival time of the peak surge. However, a realistic ensemble of meteorological forecasts is likely to include a variety of storm tracks, which may induce a greater variation in peak surge arrival time than simply scaling the wind stresses by a temporally constant and spatially uniform factor.

Finally, the most prohibitive drawback of the use of equation (4.28) in place of traditional ensemble methods is that it considers only a single (scalar) model output J (i.e. one adjoint model run is required per functional J , since J appears as a source term in the adjoint equations). In the comparison of computational cost above, it was implicitly assumed that a surge forecast is desired at only one location, and at only one instant in time. In reality, this is of course not the case. Given that the traditional ensemble approach provides an estimate of model uncertainty at all locations and times, it remains the most efficient method for operational forecast uncertainty quantification over a large scale. Nevertheless, the use of the adjoint method described here constitutes a powerful tool when a small number of model outputs require more detailed treatment.

4.7 Model-free hazard assessment

Section 4.6 has explored the linear response of a surge forecast with respect to the wind stress, linearised about a deterministic forecast. This made use of a Taylor expansion, and a connection with conventional ensemble methods for forecast uncertainty quantification has been drawn. In this section, this principle is taken further in order to estimate the first-order response of the sea surface height to arbitrary wind stress forcing, without the use of a forward numerical model. This has possible applications to rapid hazard assessment, and is facilitated by performing a Taylor expansion about $\tau_s = 0$, and in the absence of tidal boundary conditions and atmospheric pressure. A schematic diagram illustrating the difference between this formulation and that of section 4.6 is shown in figure 4.20.

For simplicity of exposition, consider a problem in which a model output defined at a time t_0 , denoted J_{t_0} , depends on a temporally varying input $m(t)$, and for which if the

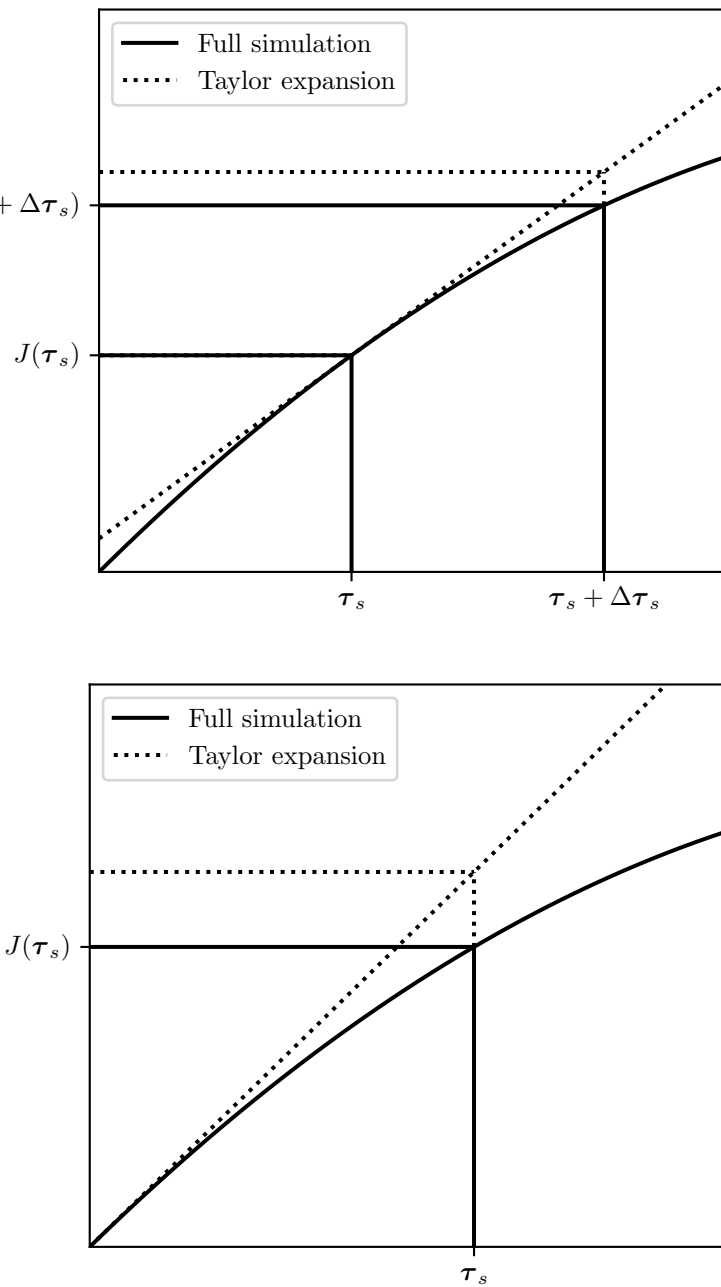


Figure 4.20: Schematic diagram of two approaches to the use of Taylor expansions to evaluate approximations to model outputs. Top: expansion about a deterministic forecast. Bottom: expansion about zero forcing. Solid lines show the response curve of the full numerical model. Dotted lines show the linearised response, via a Taylor expansion.

input is zero at all times, $m(t) = 0$, then the model output is zero at all times, $J_t = 0 \forall t$. Denoting the instantaneous influence on J_{t_0} of the parameter m at time t by

$$\frac{\partial J_{t_0}}{\partial m}(t), \quad (4.30)$$

a Taylor expansion about $m = 0$ then gives

$$J(m)_{t_0} \approx \int_{-\infty}^{t_0} \frac{\partial J_{t_0}}{\partial m} \Big|_{m=0} (t') \cdot m(t') dt', \quad (4.31)$$

where t' is a dummy time variable. The output J_{t_0} depends on the history of the input parameter $m(t)$, up to the time t_0 , and can therefore be approximated by the convolution of $\partial J_{t_0}/\partial m|_{m=0}$ with the non-zero input m .

Provided that the instantaneous influence of $m(t')$ on J_{t_0} depends only on $t_0 - t'$, then for any t ,

$$\frac{\partial J_t}{\partial m}(t') = \frac{\partial J_{t_0}}{\partial m}(t' + t_0 - t), \quad (4.32)$$

such that equation (4.31) can be generalised to a functional defined at any time t by

$$J(m)_t \approx \int_{-\infty}^t \frac{\partial J_{t_0}}{\partial m} \Big|_{m=0} (t' + t_0 - t) \cdot m(t') dt'. \quad (4.33)$$

The use of this expression facilitates the approximation of the output J_t at any time t , and for any input parameter $m(t)$, using only the gradient information $\partial J_{t_0}/\partial m|_{m=0}$, which for a numerical model can be obtained from a single adjoint run.

This simplified case applies directly to the problem of approximating surge residuals, where the model input $m(t)$ is replaced with the spatially and temporally varying wind stress field $\boldsymbol{\tau}_s(x, y, t)$, and the functional J_{t_0} is defined as the free surface elevation η at a time t_0 and location \mathbf{x}_0 . Here, the Thetis surge model can be run without tidal boundary conditions or atmospheric pressure forcing, and with the wind stress set to zero in the forward model run, $\boldsymbol{\tau}_s(x, y, t) = 0$. This ensures that $J_t(\boldsymbol{\tau}_s = 0) = 0 \forall t$, and therefore that equation (4.31) is appropriate. Since the influence of the wind stress is not explicitly time dependent, equation (4.32) is also valid. Equation (4.33) can therefore be used to estimate the timeseries response of J_t to non-zero wind stress $\boldsymbol{\tau}_s(x, y, t)$. Denoting this residual timeseries by $r(t)$, equation (4.33) implies

$$r(t) \approx \int_{t'=-\infty}^{t'=t} \int_x \int_y \frac{\partial J_{t_0}}{\partial \boldsymbol{\tau}_s} \Big|_{\boldsymbol{\tau}_s=0} (x, y, t' + t_0 - t) \cdot \boldsymbol{\tau}_s(x, y, t') dy dx dt'. \quad (4.34)$$

The power of this approximation is that the adjoint model run required to compute

the derivative $\partial J_{t_0} / \partial \boldsymbol{\tau}_s|_{\boldsymbol{\tau}_s=0}$ is a one-off overhead for each location at which the residual timeseries is desired. This expression can then be used to approximate the surge residual at any time, and for an arbitrary wind stress field $\boldsymbol{\tau}_s(x, y, t)$. This means that an estimate of the surge residual at a given location can be computed without running the full numerical model.

As an aside, note the similarity in the assumptions underlying this approximation with those made for the analytic approach of section 4.5.3, which used the linearised shallow water equations as a starting point. The resulting analytic equation, governing the sensitivity of a surge measurement to wind stress at earlier times, did not depend on the forward model variables, and as such was valid for all times and all values of the wind stress. The same approach has been taken here; all nonlinearity, including any tide-surge interaction, has been lost. Nevertheless, the leading order effect of the wind stress on the sea surface height is captured.

Figure 4.21 shows a comparison of the residual timeseries from the approximation given by equation (4.34) and from the full numerical model (including tidal boundary conditions, wind stress and atmospheric pressure forcings). In the evaluation of equation (4.34), the lower limit on the time integral was taken as $t' = t - 2$ days; this was found to be a sufficiently long period, beyond which the sensitivity of the functional to wind stress was small. While the discrepancies introduced by the implicit truncation errors of equation (4.34) are large at times, it is clear that the leading order effect of the wind stress on the surface elevation is captured. In particular, the initial increase in surge residual is well captured for North Shields and Immingham. The peak surge residual is overestimated for all locations, with a particularly poor approximation for Lowestoft, which exhibited a complex pattern of tide-surge interaction for this event (Spencer et al., 2015) and therefore suffers most from the approximations of this approach. For all locations, the approximated residuals fall away too rapidly after the initial surge.

Despite the loss of predictive skill compared with the full numerical model, this approach might be useful within a probabilistic hazard assessment. For example, the wind field resulting from each member of a large ensemble of synthetic storms could be applied within this simple model to estimate the resulting coastal hazard without applying each wind field to the full numerical model, thus saving computational cost.

For surge events where the atmospheric pressure gradient has significant surge-generating effects, this approach can be trivially extended by repeating the above with atmospheric pressure gradient replacing the wind stress, and linearly combining the estimated perturbations due to the atmospheric pressure and wind stress. Alternatively, a simpler approach could use the inverse barometer effect to approximate atmospheric pressure ef-

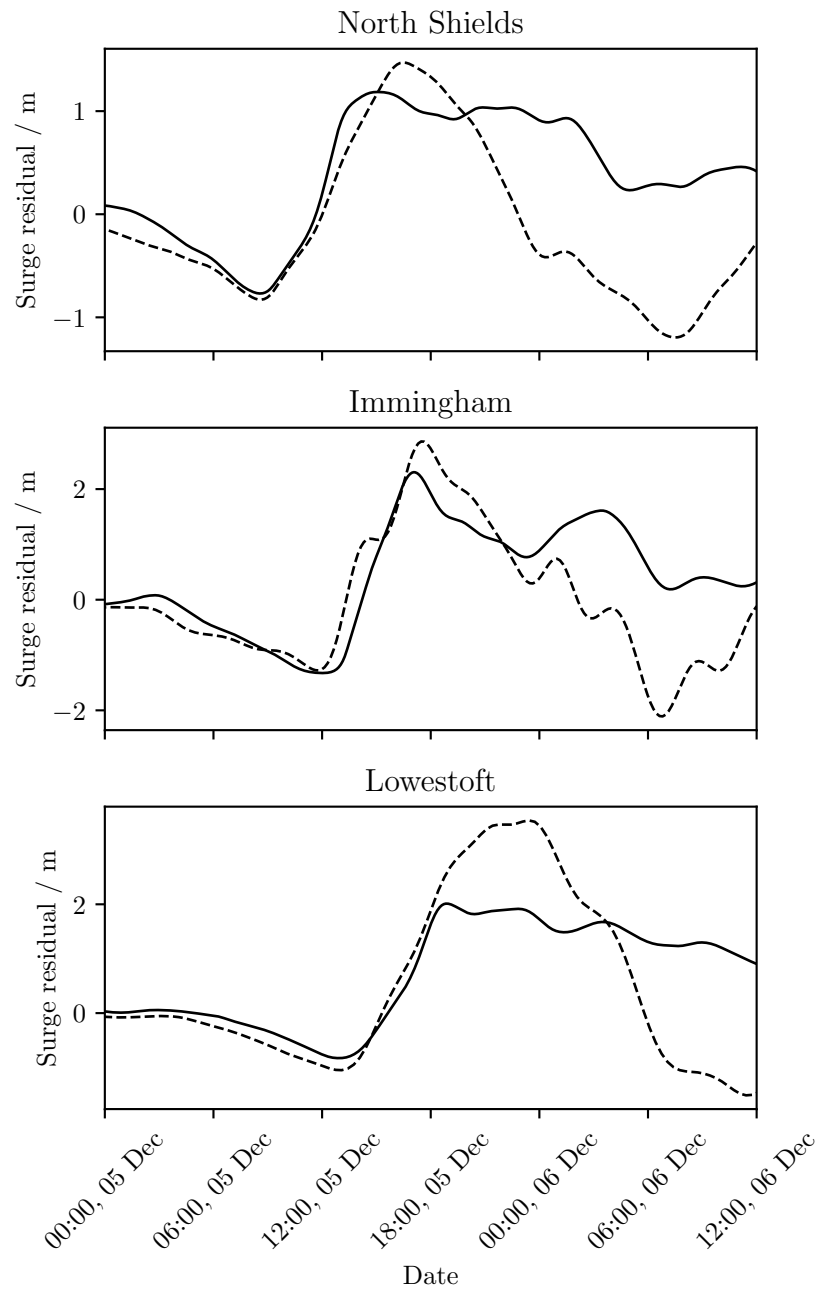


Figure 4.21: Comparison of approximated residual timeseries (dashed line) with results from the full numerical model (solid line).

fects. Further possible improvements could include an empirical correction to account for some tide-surge interaction, such that estimated residuals are suppressed at high tide and enhanced at low tide. Further investigation and development of this method is beyond the scope of this work, but may be considered in future.

4.8 Discussion

In section 4.5, Thetis and its adjoint were used to explore the spatial patterns of storm surge model sensitivity to its uncertain inputs. In the cases of bottom friction coefficient and bathymetry, uncertainties in modelled skew surges were estimated by a convolution of the model sensitivity with estimated model input uncertainties. In contrast to the raw sensitivities, these estimated output uncertainties can be directly compared. Three key observations can be made based on these results:

- (i) Estimated uncertainties due to bottom friction are of greater magnitude than those due to bathymetry. However, it should be noted that only very simple estimates were made for the uncertainties in the inputs, and for a well-calibrated model these uncertainties would likely be significantly reduced. This is particularly the case for the bottom friction coefficient, and these results highlight the importance of achieving a tight constraint on bottom friction coefficient through model calibration methods.
- (ii) The uncertainty contributed by the bottom friction is of smaller magnitude for the northernmost target location (North Shields) than for the locations further south, which all exhibit similar magnitudes. This pattern is explained by the accumulation of uncertainty over the propagation path of the surge along the east coast of the UK; bottom friction acts to remove energy from the surge, and this effect is cumulative along the path of the surge from north to south.
- (iii) In contrast, the overall contribution of uncertain bathymetry exhibits a more variable pattern across the domain, suggesting that the effect of the bathymetry on the skew surge arises through a variety of mechanisms. The similarity (with opposite signs) between the localised spatial patterns (around the observation location) of sensitivity to bottom friction coefficient and bathymetry (figures 4.14 and 4.15) suggests that a proportion of the sensitivity to bathymetry in these regions arises from the bottom friction term of the governing equations, which is inversely proportional to the water depth. However, given the contrasting patterns of estimated uncertainty due to each

input summarised in table 4.1, it is clear that the sensitivity to bathymetry is more complex, and must also derive significant contributions from the other terms of the governing equations (3.15) in which the bathymetry h appears, i.e. the wind stress and surface elevation advection terms.

A direct comparison of uncertainties due to bottom friction and bathymetry with uncertainty due to wind stress is not possible, since the uncertainty in the wind stress depends strongly on the forecast lead time, and the original meteorological ensembles were not available for this case study. However, it is known from ensemble surge forecasts for this event that uncertainty due to meteorological inputs was on the order of 1 m at a forecast lead time of 24 hours. This is far greater than the uncertainties due to bottom friction and bathymetry estimated here. The quantitative results of this study are therefore consistent with the perceived limitations of the operational model at the time, namely that storm surge forecast model performance is limited by the accuracy of the meteorological forecast providing the wind stress (and atmospheric pressure). These results are also consistent with Sochala et al. (2019), who compared sensitivity to storm track, wind velocity and Manning coefficient using an ensemble approach via a polynomial chaos expansion.

The results of an adjoint sensitivity analysis as performed within this study are highly relevant at the interface between models and observations. The spatial pattern of sensitivity to bottom friction coefficient could, for example, be used to inform the intelligent application of a spatially varying bottom friction coefficient, for the purposes of more sophisticated model calibration. For example, a choice of length scale of variation in bottom friction coefficient could be made based on the spatial variability of the model sensitivity, since variations on smaller length scales would not be constrained by observations. Similarly, the high magnitudes of sensitivity to bathymetry found locally to each observation location suggest that bathymetric surveys, particularly in regions prone to morphological change, could be valuable in reducing uncertainty in storm surge forecasts. Finally, the observed patterns of sensitivity to wind stress could be used to inform effort to enhance meteorological models, by identifying regions in which uncertainty in wind stress has the greatest impact on overall surge uncertainty.

In addition to assisting in analysing surge model performance, the adjoint-based sensitivity analysis performed within this chapter is capable of providing physical insight into surge generation and propagation. The skew surges at Immingham, Lowestoft and the coastline section all show a positive gradient with respect to the bathymetry of Dogger Bank, to the north-east of the Humber Estuary (see figure 4.8); this is visible in figure 4.15. This reveals the protective effect of this bank for the south-east coast of the UK, against this storm surge event. Similarly, the sensitivity to wind stress of figure 4.17 shows

very low sensitivity over the Norwegian Trench, due to the deep water in this region. Features such as these are simple to interpret within the physics contained in the model's governing equations. However, quantifying the impact of these features on the generation and propagation of the surge is non-trivial, but is achieved at relatively low computational cost by the adjoint techniques employed here. The results are also consistent with the propagation of the surge as a coastally trapped wave, from north to south along the east coast of the UK; this explains the similar sensitivity patterns observed in the north of the domain in each of figures 4.14, 4.15 and 4.17.

The sensitivity analysis approach taken here consists of computing gradients of model outputs with respect to model inputs. This facilitates a linearisation of the model with respect to the inputs considered, i.e. the use of a Taylor expansion as a substitute for the full forward model. Section 4.6 has shown that, for an ensemble of meteorological forecasts with a sufficiently narrow range, the resulting skew surge at a single location can be estimated at low computational cost by linearising with respect to wind stress, and computing an ensemble of skew surges via a Taylor expansion. For the experiments performed here, consisting of wind stress perturbations which are proportional to the hindcast wind stress, the range of linear response appears to be sufficient to capture a realistic ensemble range for non-negligible forecast lead time. However, further investigation is required into the validity of the Taylor expansion approach as a direct substitute for ensemble methods.

The use of Taylor expansions has been further extended in section 4.7, where the full surge residual timeseries has been approximated by a Taylor expansion. This method requires only one adjoint run in order to estimate a full residual timeseries for an arbitrary wind stress field. A comparison of this approach with results from the full numerical model show that the leading order effect of the surge is captured. However, a caveat of this work is that only one case study event has been undertaken. The Storm Xaver case study was selected in part due to its severity, which was caused by the peak residual occurring in close proximity to the high tide; this is an unusual feature of storm surges, due to tide-surge interaction (Horsburgh and Wilson, 2007). Since tide-surge interaction is neglected to varying extents by the adjoint-based approximation methods employed within sections 4.6 and 4.7, further work is required to thoroughly investigate the validity of these approximations.

4.9 Summary

This chapter has presented the construction of a tide-surge model of the North Sea within Thetis, and a simple model calibration exercise with respect to the bottom friction and wind stress parameters. For a case study consisting of Storm Xaver in December 2013, the Thetis model performs comparably with the CS3X model, which was the UK operational surge model at the time of the event.

Taking both numerical and analytic adjoint approaches, the patterns of sensitivity of modelled skew surges to three of the model's uncertain inputs, namely the bottom friction coefficient, bathymetry and wind stress forcing, have been investigated. The pattern of sensitivity to wind stress obtained within this work, which resembles a shallow water wave propagating backwards in time, is consistent with literature. The numerical adjoint-derived model sensitivities have been further utilised to construct simplified models via Taylor expansions, and a connection has been drawn to both traditional ensemble uncertainty quantification methods and to rapid hazard assessment via a model-free approach.

Regarding sensitivity to other uncertain model inputs, it has been found that an uncertainty of 2.7 m in bathymetry produces uncertainties in skew surge predictions on the order of 5 cm, while an uncertainty of $0.005 \text{ s m}^{-1/3}$ in the Manning coefficient induces uncertainties in skew surge predictions up to 20 cm. While uncertainty in surge forecasts is dominated by the meteorological inputs, these findings show that other model inputs can still be significant, and emphasises the importance of model calibration in reducing these uncertainties.

Chapter 5

Bottom friction parameter estimation in the Bristol Channel

The content within this chapter is based on

S. C. Warder, A. Angeloudis, S. C. Kramer, C. J. Cotter and M. D. Piggott. *A comparison of Bayesian inference and gradient-based approaches for friction parameter estimation.* Ocean Modelling, Submitted 2020.

5.1 Introduction

Numerical tidal models have a wide range of applications; studies of tidal energy systems (Neill et al., 2018) or coastal sediment transport (Xie et al., 2009) are example applications which rely directly on tidal modelling of varying complexity, while tides are also a crucial component of storm surge and other coastal hazards. Tides are therefore a central component of coastal ocean models, and much effort goes into the development and calibration of tidal models.

Tidal models rely on a number of uncertain parameters, which a user may tune in order to obtain good agreement between model outputs and observations. Motivated by the findings of chapter 4, where estimated uncertainty in bottom friction was found to induce uncertainties of up to 20 cm in modelled surge heights, the focus of this chapter is on calibration with respect to a spatially varying Manning's n coefficient for bottom friction. Here, a case study region consisting of the Bristol Channel and Severn Estuary is selected. This region exhibits one of the highest semidiurnal tidal ranges in the world (Lewis et al.,

2015), and is of significant interest in the marine renewable energy industry (Neill et al., 2018; Harcourt et al., 2019); accurate modelling of its tidal dynamics is therefore valuable. Observation data exists within this domain in the form of both tidal harmonic constituent data at 11 locations, and timeseries surface elevation data at a further five locations; see figure 5.1. This region therefore constitutes a data-rich area in which to investigate model calibration techniques, with the further application to larger model domains, such as the European Continental Shelf, planned within future work.

Section 5.2 first describes the models and data sources which are used for the purpose of model calibration and validation, and briefly summarises the choices of bottom friction parameter space used within this chapter. Two such input parameter spaces are used: a freely spatially varying bottom friction parameter, and a set of three parameters corresponding to three groups of sediment type found within the model domain. Section 5.3 describes the two model calibration methods which are compared within this work, namely gradient-based optimisation via adjoint modelling, and Bayesian inference via a Markov Chain Monte Carlo algorithm. The results from the application of the adjoint method to the estimation of a fully spatially varying bottom friction coefficient are presented in section 5.4, and section 5.5 presents results from the application of both adjoint and MCMC methods to estimation of the three sediment-based parameters. Finally, these results are compared and discussed in section 5.6, and the chapter is summarised in section 5.7.

5.2 Data, models and inputs

This section describes the available sources of data in the study region, the Thetis tidal model setup, a second numerical model, TELEMAC-2D, which is used for validation of calibrated parameters, and the choices of input parameter space used within the calibration methods of this chapter.

5.2.1 Data sources

Observation data within the model domain, which is used here for the purposes of both model calibration and validation, is from two sources:

- (i) 11 locations at which tidal harmonic data is available (National Oceanography Centre, personal communication 2018), which are shown as green squares in figures 5.1 and 5.2. To compare modelled results with these data, the model must be run for

a suitably long time (ideally a month or more), and a harmonic analysis performed at these locations.

- (ii) Five tide gauges where quality controlled timeseries surface elevation data is available from the British Oceanographic Data Centre (BODC)¹. These locations are shown in figures 5.1 and 5.2 by red circles. At these locations, modelled surface elevations can be compared directly with observations without the need for harmonic analysis, provided that the model adequately captures any meteorological effects influencing the tide gauge signal during the comparison window, or that the meteorological conditions are sufficiently calm that their effect can be neglected.

5.2.2 Thetis model setup

The primary model used within this chapter is Thetis, which has been described in detail in chapter 3, and applied to tide-surge modelling in chapter 4. Since the Bristol Channel and Severn Estuary contain significant intertidal regions, wetting and drying is included via the scheme described in chapter 3. The wetting-drying parameter α , which controls the transition from wet to dry regions, is taken to be 0.5 m.

The mesh used within this chapter (except where stated otherwise) is shown in figure 5.1, and was generated on a UTM30 coordinate projection, using the Python package *qmesh* (version 1.0.1) (Avdis et al., 2018), which interfaces the mesh generator *Gmsh* (version 2.10.1) (Geuzaine and Remacle, 2009). The mesh resolution varies from 1 km at the coastlines to 10 km in open regions, and the mesh contains a total of 8,704 triangular elements. Thetis is run using a $P_1^{\text{DG}}\text{-}P_1^{\text{DG}}$ discretisation, and a timestep $\Delta t = 100$ s with implicitness $\theta = 1$ (selected for numerical stability). Tidal dynamics are introduced through a Dirichlet boundary condition for the surface elevation at the ocean boundary, based on the eight leading order constituents from the *TPXO* database (M2, S2, N2, K2, Q1, O1, P1, K1) (Egbert and Erofeeva, 2002). The bathymetry is subsampled from 30 m resolution data available from Digimap (Digimap, 2016). Digimap bathymetry is provided in chart datum, and a correction to mean sea level datum is therefore applied.

5.2.3 TELEMAC-2D

In addition to Thetis, this chapter also uses the TELEMAC-2D model (Hervouet, 2007), henceforth referred to as Telemac. Telemac solves the shallow water equations in a similar

¹This study uses data from the National Tidal and Sea Level Facility, provided by the British Oceanographic Data Centre and funded by the Environment Agency.

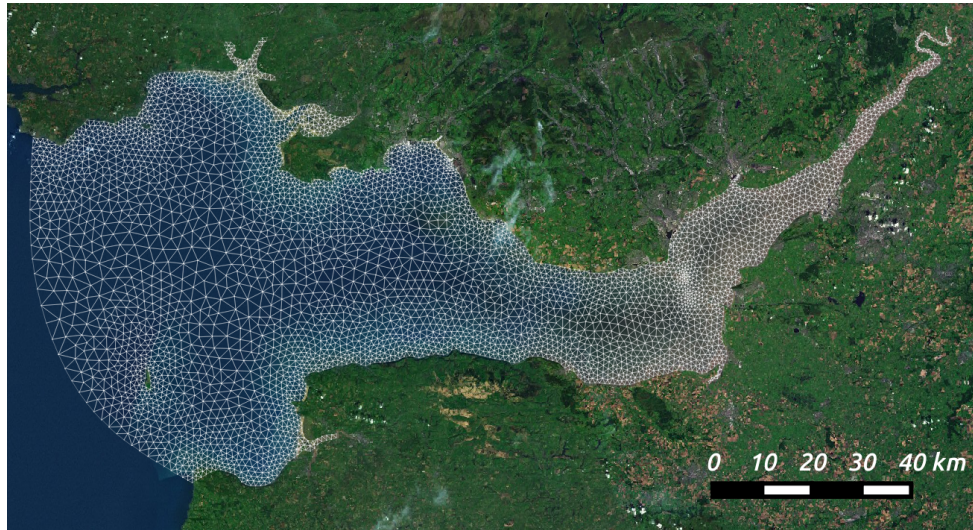


Figure 5.1: Mesh used for all simulations within this chapter. Locations where tidal harmonic data are available are shown as green squares. Red circles indicate BODC tide gauges, where timeseries surface elevation data is available.

form to Thetis (see equation (3.15)), and is used here in its finite element mode with default continuous Galerkin discretisation, consisting of linear elements in velocity and depth; see the Telemac user manual for further detail (Lang et al., 2014). Telemac is used with the same unstructured mesh as for the Thetis simulations, and a semi-implicit timestepping scheme with a timestep of 10 s. The bottom friction formulation used for the Telemac simulations is identical to that used in Thetis, and Telemac results are used in later sections to validate the friction parameters selected by the Thetis-based calibration techniques.

5.2.4 Choices of calibration parameter space

The first step in a model calibration procedure is to select the input parameter space with respect to which the model will be calibrated. Common choices for the input parameter space have been described in chapter 2, and this section describes the choices made within this work.

Freely varying friction parameter

Within section 5.4, the friction coefficient is allowed to vary freely over the whole domain. This means that the number of degrees of freedom in the parameter space, which must all be constrained by observations, is very large; in the case of a linear CG field as considered

here, this is equal to the number of vertices in the mesh. In order to avoid the problem of over-fitting, it is common to supplement the observation data with a form of regularisation (Maßmann, 2010b), which represents prior knowledge of the unknown parameters. This method is described further in section 5.3.1.

Division of domain based on sediment type

Possible approaches to intermediate complexity in the friction coefficient input parameter space (i.e. somewhere between spatially uniform and freely varying) have been discussed in chapter 2. Within this chapter, this is achieved via a physics-based approach. The model domain is divided according to the type of sediment found on the sea bed; this is similar to the approaches of Guillou and Thiébot (2016) and Sraj et al. (2014b), and incorporates prior knowledge about the bottom friction process via grain size (and hence roughness length) data.

This sediment-based division of the domain is achieved using data from SHOM (Service Hydrographique et Océanographique de la Marine) (SHOM, 2019). The sediment types from this dataset are divided into three groups: (1) rock (NFRoche in the SHOM dataset), (2) sediment containing gravel (NFG, NFSG, NFSGV) and (3) sediment containing only sand (NFS, NFSV, NFV, NFVS), and a different Manning coefficient (n_1, n_2, n_3) assigned to each sediment group respectively. This choice of three sediment groups is a cautious approach to avoiding an ill-posed calibration problem where observation data is insufficient to constrain the parameters; a study of alternative choices was not undertaken, since methodologies in selecting the input parameter space were not the focus of this work. The spatial distribution of the selected sediment groups is indicated in figure 5.2.

5.3 Methods

5.3.1 Gradient-based optimisation via the adjoint

Numerical adjoint methods were described in chapter 3, and have been applied within chapter 4 for the purpose of sensitivity analysis and uncertainty quantification. Here, adjoint methods are applied within a gradient-based optimisation algorithm for the purpose of model calibration.

An adjoint model can be used to compute the gradient of a model output (or functional), denoted J , with respect to a number of model inputs. In this work, the functional J is

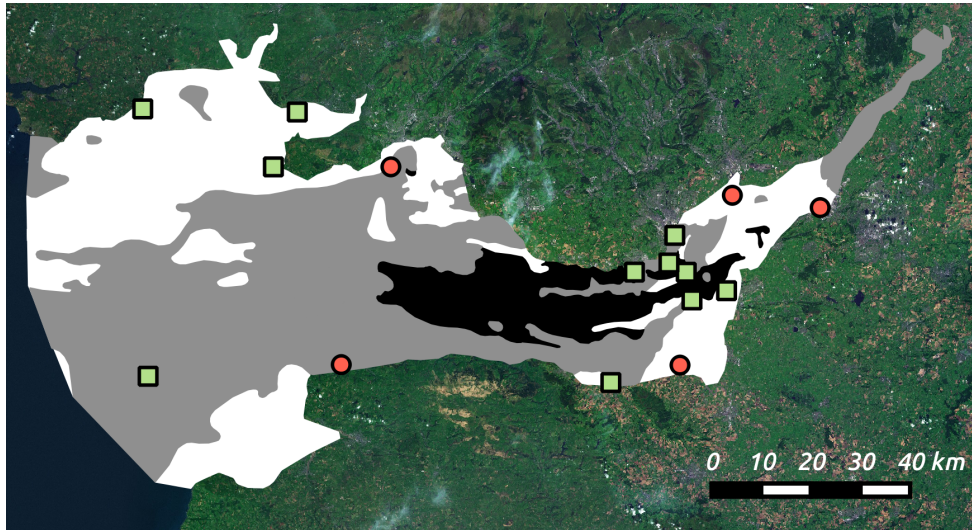


Figure 5.2: Distribution of sediment types: rock (black), gravel (grey), sand (white). Locations where tidal harmonic data are available are shown as green squares. Red circles indicate BODC tide gauges, where timeseries surface elevation data is available.

chosen to be some measure of the misfit between the model and a set of observation data, and the inputs are the vector of unknown Manning coefficients \mathbf{n} . In the case of the freely varying friction parameter, \mathbf{n} contains as many elements as there are nodes in the mesh. In the case of the sediment-based variation of the Manning coefficient, \mathbf{n} contains only three elements, corresponding to the Manning coefficient for each sediment group. The adjoint model can be used to compute the gradient vector $\frac{\partial J}{\partial \mathbf{n}}$. The power of the adjoint method lies in the fact that the computational cost of the adjoint model run is comparable to that of the forward model, independent of the length of the vector \mathbf{n} .

The use of adjoint methods to compute gradients in this way therefore facilitates the solution of the model calibration problem via gradient-based optimisation. Since J is a measure of the model-observation misfit, the objective of the calibration method is therefore to minimise J . This minimisation is performed within this work using the *L-BFGS-B* gradient-based optimisation algorithm (Zhu et al., 1997) within the Python scientific computing library *SciPy*. Each iteration of the algorithm requires a forward and adjoint run of Thetis, in order to calculate the functional value J and its gradient vector $\frac{\partial J}{\partial \mathbf{n}}$, respectively. The algorithm is terminated when the change in the functional value between successive iterations falls below a given threshold, i.e. when $|\Delta J|_i = |J_i - J_{i-1}| < \epsilon J_0$, where ϵ is a selected tolerance and the subscript denotes the iteration number. For the use of a freely spatially varying friction coefficient, this tolerance is taken as $\epsilon = 10^{-5}$, while for the sediment-based friction parameter, the tolerance is $\epsilon = 10^{-6}$.

Within this chapter, two choices are made for the misfit functional J , based on the two

sources of data described in section 5.2.1.

Assimilation of harmonic data

Here, the calibration process is based on the assimilation of tidal harmonic constituent data from the 11 gauges indicated in figure 5.1. The challenge in assimilating this data via a numerical adjoint model is the high demand on computational resources, in particular memory, by adjoint models. This is compounded by the definition of the misfit between the model and harmonic tide gauge data, which requires a sufficiently long model run that a harmonic analysis may be performed on the simulated timeseries. In order to limit the computational cost of assimilating harmonic data, here only the M2 harmonic is assimilated, so that a short assimilation period of 3 days is sufficient. For this, the model is forced with the M2 tidal constituent only, and after an initial spin-up period of 10 days with a uniform Manning coefficient $n = 0.02 \text{ s m}^{-1/3}$, the forward and adjoint models are run for 3.5 days for each iteration. Out of the 3.5 day simulation period, the first 12 hours are used as additional spin-up with the updated friction parameters, to eliminate the dependence of the model outputs on the spin-up parameters. After performing a harmonic analysis (for the M2 constituent only) based on the final 3 days of each simulation, the model-observation misfit is defined as

$$J = \sum_{i=1}^{11} (A_i - \hat{A}_i)^2, \quad (5.1)$$

where A_i and \hat{A}_i are the modelled and observed M2 amplitudes at the 11 gauges i , respectively.

Assimilation of timeseries data

There are five locations within the model domain at which free surface elevation timeseries are sampled at 15 minute intervals (see red circles in figure 5.1). To assimilate this data, model-observation misfit is computed over a 24-hour period commencing on 21st June 2010. This assimilation period was chosen to coincide with relatively calm meteorological conditions, since the calibration seeks parameters for tide-only performance and for simplicity the model does not include any meteorological effects. The model is first run for a spin-up time of 10 days prior to the assimilation period, with a uniform Manning coefficient $n = 0.02 \text{ s m}^{-1/3}$. Each optimisation iteration first commences with an additional 12-hour spin-up with the updated set of friction parameters, before the 24-hour

assimilation period. The model-observation misfit is defined as

$$J = \frac{1}{T_1 - T_0} \sum_{i=1}^5 \int_{T_0}^{T_1} (\eta_i(t) - \hat{\eta}_i(t))^2 dt, \quad (5.2)$$

where $\eta_i(t)$ and $\hat{\eta}_i(t)$ are the modelled and observed surface elevations at each of the five tide gauges i , respectively. The time integral spans the 24-hour assimilation period described above and is approximated by a suitable discrete method applied to the model time steps, with the observation data linearly interpolated where required.

This method has the advantage that each optimisation iteration requires forward and adjoint model runs of only 36 hours each (12-hour spin-up plus 24-hour assimilation window), and the computational cost of the optimisation algorithm is therefore relatively low. However, tide gauge timeseries data are available at only five locations within the model domain, all confined to be close to the coastline, and the assimilated observations must all have been obtained during the same time period to keep the assimilation window short. The assimilation window must also coincide with calm meteorological conditions to avoid the need to model the effects of wind stress and atmospheric pressure gradient. These conditions were easily met by the data available within this study, but would need to be considered in any future application of this method.

Regularisation

In the case of the freely varying friction parameter, regularisation is used in order to avoid the problem of over-fitting. In the context of friction parameter estimation, overfitting occurs when regions of the domain which have only a small influence on the value of the misfit functional take unrealistic values of the Manning coefficient. This occurs because the data is insufficient to constrain the large number of degrees of freedom in the input parameter space. The idea of regularisation is to include some prior knowledge of the unknown parameter within the optimisation.

The regularisation used within this chapter takes the form of a penalty term J_{penalty} , which is added to the misfit functional to be minimised by the optimisation algorithm. The purpose of this term is to penalise large changes in the friction coefficient from some prior value, so that regions of the domain which are not constrained by the observations instead remain close to this specified value. In this work, L2 regularisation is employed, such that the penalty term is related to the L2 norm of the deviation of the friction

parameter $n(x, y)$ from some fixed value n_0 ,

$$J_{\text{penalty}} = \gamma \int \int (n(x, y) - n_0)^2 \, dx \, dy. \quad (5.3)$$

The full functional for the assimilation of timeseries data is therefore given by

$$J = \frac{1}{T_1 - T_0} \sum_{i=1}^5 \int_{T_0}^{T_1} (\eta_i(t) - \hat{\eta}_i(t))^2 \, dt + \gamma \int \int (n(x, y) - n_0)^2 \, dx \, dy. \quad (5.4)$$

n_0 represents the prior knowledge of the friction parameter, and is taken within this work as $n_0 = 0.02 \text{ s m}^{-1/3}$; this is a reasonable value for the Manning coefficient based on Arcement and Schneider (1989).

The use of regularisation introduces a new regularisation parameter, γ , which controls the balance between the misfit and regularisation terms, and must be selected appropriately. There are several possible methods for the optimal selection of γ . Within this work, a cross-validation approach is employed, similar to Ullman and Wilson (1998). In this method, the optimisation is performed several times, for varying values of γ . Using the optimised friction parameter field resulting from each regularisation parameter, the M2 harmonic-based misfit given by equation (5.1) is calculated. The optimal choice of γ corresponds to the minimum value of this second misfit measure. This method has the advantage that it does not require any additional prior knowledge about the unknown parameter. However, a second set of observation data is required; this is not a problem in this study, but in a relatively data-poor application may be prohibitive.

5.3.2 Bayesian inference

Bayesian inference is a powerful statistical technique for inverse problems, and has been applied to bottom friction parameter estimation previously (Hall et al., 2011; Sraj et al., 2014b). Here, a Markov Chain Monte Carlo (MCMC) method is used. Since MCMC methods rely on large numbers of model runs, a Gaussian process emulator is used as a computationally efficient surrogate model in place of the full Thetis model. This method has the advantage that the main computational cost is in the creation of the emulator training dataset, and the subsequent emulator training and MCMC algorithm can be performed relatively cheaply.

Bayesian inference is used for the estimation of the sediment-based friction parameters, but not for the freely varying parameter. This is because the method scales poorly with

the number of degrees of freedom in the unknown parameter space; this is discussed in section 5.6.

Gaussian process emulator

Gaussian process emulators (GPEs) have been described in detail in chapter 3. In this section, a GPE is employed as a surrogate for the prediction of full Thetis model outputs in the form of tidal harmonic amplitudes at the 11 locations indicated in figure 5.1. For a given constituent C , the vector (of length 11) of modelled harmonic amplitudes is denoted by $\mathbf{G}_C(\mathbf{n})$ for a set of input parameters \mathbf{n} . Given a set of training data, the GPE gives the best linear unbiased prediction of full model outputs for unseen values of the model inputs. The GPE also computes a covariance matrix encapsulating the uncertainty in the GPE estimate. The GPE output interpolates the training data, with zero covariance at the training points.

The emulator training data is generated from a harmonic analysis (at the 11 harmonic data locations) of Thetis model outputs. The Thetis training runs were configured using 40 samples from the input parameter space, drawn from uninformative priors in the range $[0.01, 0.05]$, using Latin hypercube sampling. These parameter ranges were chosen based on typical values for Manning coefficients from Arcement and Schneider (1989). According to the ‘ $10d$ ’ rule (Sobol, 2001; Hristov et al., 2017), it is common to train a Gaussian process emulator using at least $10d$ samples, where d is the number of input parameters. For the sediment-based input parameter space, there are three input parameters, and the emulators are trained using 40 samples.

Within this chapter, Bayesian inversion is performed using two different sets of harmonic data. First, only M2 amplitude data is assimilated, so that a direct comparison can be made with the adjoint gradient-based approach described in section 5.3.1, which is applied to M2 amplitude data only. Secondly, in order to observe the effect of an increased volume of assimilated data on the estimated parameters and their uncertainty, data for four semi-diurnal constituents (M2, S2, N2, K2) is assimilated.

An initial 10-day spin-up is run using a uniform Manning coefficient $n = 0.02 \text{ s m}^{-1/3}$. Each training sample follows from this spin-up and is run for 30 days, with a full harmonic analysis (using the Python package *uptide* (Kramer et al., 2020)) performed at the 11 gauge locations, so that either combination of harmonics can be assimilated using the same emulator training dataset. Assimilation of M2 data could have been achieved using an emulator trained using a set of shorter model runs, but since the longer runs are

required for the assimilation of multiple constituents, they are reused for the M2-only assimilation to save computational cost.

To validate the emulators, the full Thetis model was run for a further 10 random samples from the input parameter space, and these results compared with GPE outputs. Figure 5.3 shows histograms of the error between the emulator outputs and the full Thetis model results, for the case of the four-constituent emulator. The normal distributions superimposed on the histograms are based on the emulator-estimated variance for each constituent, which is found to be a good estimate of the true variance between the emulator outputs and the full numerical model. There is a small negative bias in the emulator estimates for each constituent, but this bias is less than 1 mm for all constituents. Since the magnitudes of the M2 and S2 constituents are over 1 m and the magnitudes of the K2 and N2 constituents are both in the 10s of cm, this bias is small and the GPE performance is therefore considered adequate. The M2-only emulator performs similarly well.

Markov Chain Monte Carlo algorithm

The Bayesian inversion framework follows a similar approach to Srivastava et al. (2014b, 2013). The set of observed tidal harmonic amplitudes is denoted $\{\mathbf{y}_C\}$, corresponding to the set of harmonic constituents $\{C\} = \{C_1, C_2, \dots\}$, where each \mathbf{y}_C is a vector of length $N = 11$ (for the 11 tidal harmonic observation locations indicated in figure 5.1). The set of emulator outputs, estimated for a vector of Manning coefficients $\mathbf{n} = (n_1, n_2, n_3)^T$, is denoted $\{\mathbf{G}_C(\mathbf{n})\}$. Bayes' theorem gives

$$\Pi(\mathbf{n}|\{\mathbf{y}_C\}) \propto L(\{\mathbf{y}_C\}|\mathbf{n}) \prod_{i=1}^3 q(n_i), \quad (5.5)$$

where Π is the posterior distribution of the parameters \mathbf{n} given the observed data $\{\mathbf{y}_C\}$, L is the likelihood of observing the outputs $\{\mathbf{y}_C\}$ given the parameters \mathbf{n} , and q is the prior distribution of each of the parameters n_i . Each prior is taken as uniform in the range $[0.01, 0.05]$, hence

$$q(n_i) = \begin{cases} \frac{1}{0.05-0.01} & \text{for } 0.01 < n_i < 0.05 \\ 0 & \text{otherwise.} \end{cases} \quad (5.6)$$

For a constituent C , it is assumed that the model-observation discrepancies, which are the components of the vector $\mathbf{y}_C - \mathbf{G}_C(\mathbf{n})$, are independent and identically distributed variables with zero mean and variance σ_C^2 . The likelihood $L(\{\mathbf{y}_C\}|\mathbf{n})$ for a set of constituents

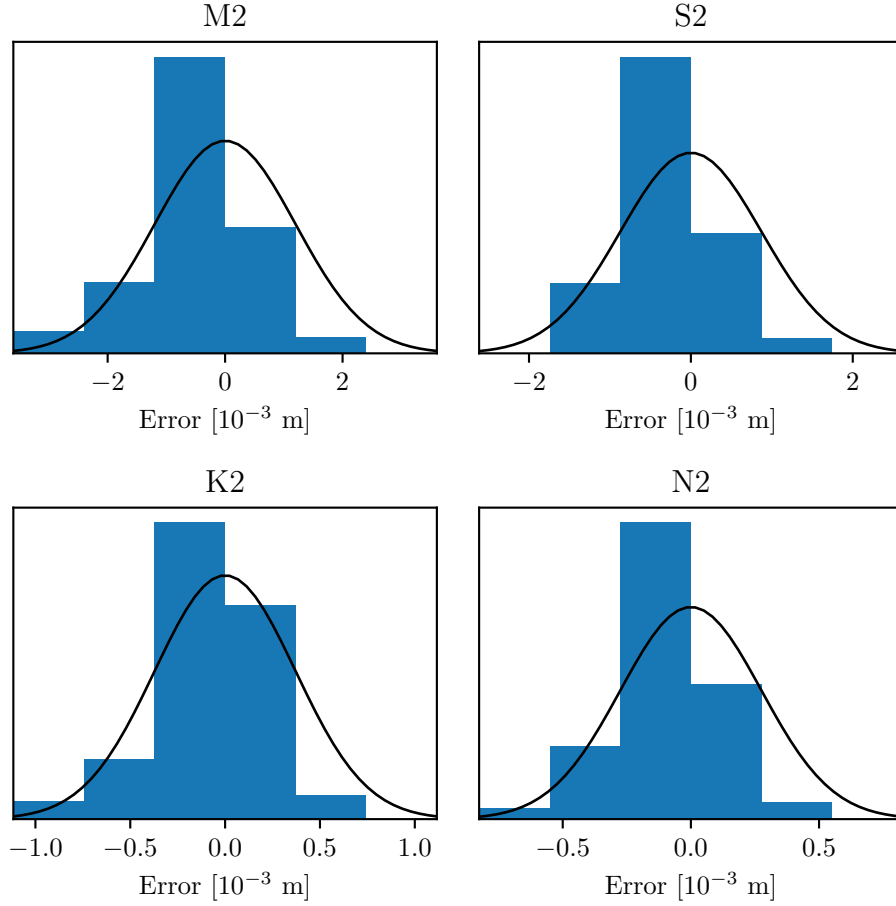


Figure 5.3: Histograms showing the errors between GPE outputs and full Thetis model runs for the 11 gauge locations, and across 10 random samples of the input parameters. The superimposed normal distributions have zero mean and variances estimated by the GPE.

C is therefore given by

$$L(\{\mathbf{y}_C\}|\mathbf{n}) = \prod_C \left[(2\pi\sigma_C^2)^{-N/2} \exp\left(-\frac{1}{2}\frac{|\mathbf{y}_C - \mathbf{G}_C(\mathbf{n})|^2}{\sigma_C^2}\right)\right]. \quad (5.7)$$

The covariance in the model outputs $\mathbf{G}_C(\mathbf{n})$ due to the use of the GPE, which is estimated as part of the GPE evaluation, is assumed to be small compared to the variances σ_C^2 , and neglected within the Bayesian inversion. Since these σ_C^2 are unknown *a priori*, they are treated as hyperparameters, i.e. they are included as additional parameters to be inferred by the MCMC algorithm. The full vector of unknowns is denoted $\boldsymbol{\theta} = (n_1, n_2, n_3, \log \sigma_{C_1}^2, \log \sigma_{C_2}^2, \dots)$, and the full posterior distribution is therefore given

by

$$\Pi(\boldsymbol{\theta}|\{\mathbf{y}_C\}) \propto \prod_C \left[(2\pi\sigma_C^2)^{-N/2} \exp\left(-\frac{1}{2} \frac{|\mathbf{y}_C - \mathbf{G}_C(\mathbf{n})|^2}{\sigma_C^2}\right) \right] \prod_{i=1}^3 q(n_i) \prod_C q(\sigma_C^2). \quad (5.8)$$

For the unknown variances σ_C^2 , the only prior information is that they must be positive. Following Sraj et al. (2014b), Jeffreys priors are assumed (Sivia and Skilling, 2006), such that

$$q(\sigma_C^2) = \begin{cases} \frac{1}{\sigma_C^2} & \text{for } \sigma_C^2 > 0 \\ 0 & \text{otherwise.} \end{cases} \quad (5.9)$$

Note that, while $q(\sigma_C^2) \rightarrow \infty$ as $\sigma_C^2 \rightarrow 0$, equation (5.8) remains a valid PDF due to the exponential. It is in fact the case that $\Pi(\boldsymbol{\theta}|\{\mathbf{y}_C\}) \rightarrow 0$ as $\sigma_C^2 \rightarrow 0$.

The posterior distribution $\Pi(\boldsymbol{\theta}|\{\mathbf{y}_C\})$ of equation (5.8) gives the probability distribution of the unknown Manning coefficients and variances σ_C^2 , given the set of observations $\{\mathbf{y}_C\}$, and its evaluation represents the model calibration problem. A technique for sampling this posterior distribution when it cannot be directly calculated is the Markov Chain Monte Carlo (MCMC) method, which has the advantage that the constant of proportionality need not be determined. This work uses an implementation of the Random Walk Metropolis Hastings MCMC algorithm (Hastings, 1970), which is given by algorithm 1. The algorithm requires the selection of an appropriate proposal distribution covariance matrix, Σ_{step} , governing the size of the random steps within the parameter space. Here, this matrix is set to

$$\Sigma_{\text{step}} = \begin{bmatrix} 0.001^2 & 0 & 0 & 0 & \dots & 0 \\ 0 & 0.001^2 & 0 & 0 & \dots & 0 \\ 0 & 0 & 0.001^2 & 0 & \dots & 0 \\ 0 & 0 & 0 & 0.1^2 & \dots & 0 \\ \vdots & \vdots & \vdots & \vdots & \ddots & \vdots \\ 0 & 0 & 0 & 0 & \dots & 0.1^2 \end{bmatrix}, \quad (5.10)$$

so that the random steps in each of the Manning coefficients have zero mean and a standard deviation of $0.001 \text{ sm}^{-1/3}$, and the random steps in each $\log \sigma_C^2$ have zero mean and a standard deviation of 0.1. These step sizes were found to give satisfactory results, without the need for an adaptive MCMC algorithm.

In the results presented here, the number of MCMC samples is selected as $M = 10^6$, with the first $2 \cdot 10^5$ samples discarded as a burn-in period. The resulting chain of values $\mathbf{n}^{[i]}$ generated by the MCMC algorithm constitute samples from the posterior distribution.

The joint probability distribution of the input parameters given the set of observations can be visualised by a histogram of these $\mathbf{n}^{[i]}$ values, and the results presented herein are smoothed through kernel density estimation. The mean and standard deviation of the samples correspond to a best estimate and uncertainty of each parameter, respectively.

Note that, for the assimilation of M2 constituent data only, the minimisation of the misfit functional of equation (5.1) is equivalent to the maximisation of the posterior distribution of equation (5.8), and the results from these two approaches should therefore be consistent.

Algorithm 1: Random Walk Metropolis Hastings algorithm

Initial guess for parameters $\boldsymbol{\theta} = \boldsymbol{\theta}^{[0]}$;

for $i = 1 : M$ **do**

1. Draw proposed set of parameters $\boldsymbol{\theta}^*$ from multivariate normal proposal distribution: $\boldsymbol{\theta}^* \sim \mathcal{N}(\boldsymbol{\theta}^{[i-1]}, \Sigma_{\text{step}})$
2. Compute posterior $\Pi(\boldsymbol{\theta}^* | \{\mathbf{y}_C\})$ from Eq. (5.8)
3. Calculate $p_{\text{accept}} = \min\left(1, \frac{\Pi(\boldsymbol{\theta}^* | \{\mathbf{y}_C\})}{\Pi(\boldsymbol{\theta}^{[i-1]} | \{\mathbf{y}_C\})}\right)$
4. Generate $u \sim U(0, 1)$ and set $\boldsymbol{\theta}^{[i]} = \boldsymbol{\theta}^*$ if $p_{\text{accept}} > u$. Otherwise, set $\boldsymbol{\theta}^{[i]} = \boldsymbol{\theta}^{[i-1]}$.

end

5.3.3 Assessment of calibrated parameters

Quadratic bottom friction parameterisations, of which the Manning's n formulation used here is a variation, are suitable for flow over flat surfaces, and parameterise the effect of turbulence caused by roughness (i.e. subgrid topography) (Döös et al., 2004). Since the bottom friction parameter therefore aims to capture a real physical process, an ideal model calibration should select physically meaningful values for the parameter. In reality, however, the calibration process corrects for multiple sources of error, including

- additional contributions to the bottom friction effect (such as turbulence induced by *resolved* bathymetry (Döös et al., 2004));
- assumptions made in the underlying model equations;
- the discretisation and numerical solution of the equations;
- other uncertain model inputs such as bathymetry and tidal boundary conditions.

The calibration process is also influenced by potential errors in the observations.

In order to assess the friction parameters selected by each calibration method, three measures of model-observation misfit are used throughout this chapter:

- (1) Normalised root mean square error (NRMSE) of **Thetis** results compared with **time-series** data at the five BODC tide gauge locations shown as red circles in figure 5.1. This is given by

$$\text{NRMSE} = \sqrt{\frac{\sum_i \int (\eta_i - \hat{\eta}_i)^2 dt}{\sum_i \int \hat{\eta}_i^2 dt}}, \quad (5.11)$$

where $\eta_i = \eta_i(t)$ and $\hat{\eta}_i = \hat{\eta}_i(t)$ are the modelled and observed surface elevations at each of the five tide gauges i , respectively, and the time integral is over the 24-hour assimilation window as described in section 5.3.1.

- (2) NRMSE of **Thetis** results compared with **harmonic constituent** data at the 11 locations shown as green squares in figure 5.1. The NRMSE is given by

$$\text{NRMSE} = \sqrt{\frac{\sum_C \overline{(A_C - \hat{A}_C)^2}}{\sum_C \overline{\hat{A}_C^2}}}, \quad (5.12)$$

where A_C and \hat{A}_C are the modelled and observed amplitudes of the harmonic constituent C , respectively, and overlines denote the mean over the 11 tide gauge locations. The constituents C are the eight leading-order harmonic constituents (M2, S2, N2, K2, Q1, O1, P1, K1).

- (3) NRMSE of **Telemac** results compared with **harmonic constituent** data at the 11 locations shown as green squares in figure 5.1; as (2) above, using Telemac results in place of Thetis.

The only model used within each calibration method is Thetis, and only one set of data (either harmonics or timeseries) is assimilated within each calibration experiment. The first two misfit measures defined above will therefore indicate whether the assimilation of timeseries data results in improved values for the modelled harmonics, and vice versa. The third measure will be used as an indicator of the applicability of calibrated parameter sets across different numerical models. If the calibrated parameters produce improved performance in an independent numerical model, then the model-specific errors listed above might be assumed to have had minimal influence on the parameter estimation process, therefore suggesting that the estimated parameters are physically meaningful.

Calibrated parameters	Thetis timeseries	Thetis harmonic	Telemac harmonic
Initial guess	14.4 %	10.2 %	11.4 %
Unregularised result	2.8 %	5.3 %	5.4 %
Regularised result	2.9 %	5.3 %	5.4 %

Table 5.1: Summary of misfit measures using calibration results, with a freely spatially varying Manning coefficient. Values are normalised root mean squared errors as described in section 5.3.3.

5.4 Results: freely varying friction parameter

This section describes the results from the assimilation of the timeseries surface elevation data (which is available at the five locations indicated in figure 5.1), in order to estimate the Manning coefficient, which is permitted to vary spatially over the domain by taking a different value at each mesh node.

The model setup here differs from that of the rest of the chapter, in that a finer mesh was used, consisting of a total of 21,508 elements. The bounds on the friction parameter within the optimisations were [0.005, 0.1].

5.4.1 Results without regularisation

Here, the misfit functional is defined according to equation (5.2), with no regularisation term added. The initial guess for the Manning coefficient is a uniform value of $0.02 \text{ s m}^{-1/3}$. The convergence of the L-BFGS-B algorithm is shown in figure 5.4; the algorithm converged in 64 iterations, resulting in a decrease in the value of the misfit functional of around 95 %. The final optimised Manning coefficient field is shown in figure 5.5. The field takes the upper bound value of 0.1 in significant sections of the domain, and some of the prominent features of the optimised field appear to align with the tide gauge locations, suggesting that the spatial distribution of the friction coefficient is not physically meaningful.

As discussed in section 5.3.3, three measures of the model-observation misfit are used to assess the ‘success’ of a given calibration experiment. Using the optimised field of Manning coefficient values, the three misfit measures are summarised in table 5.1, where the Telemac result was obtained using the same (finer) mesh. The use of the optimal Manning coefficient field produces significant improvements in all three misfit measures.

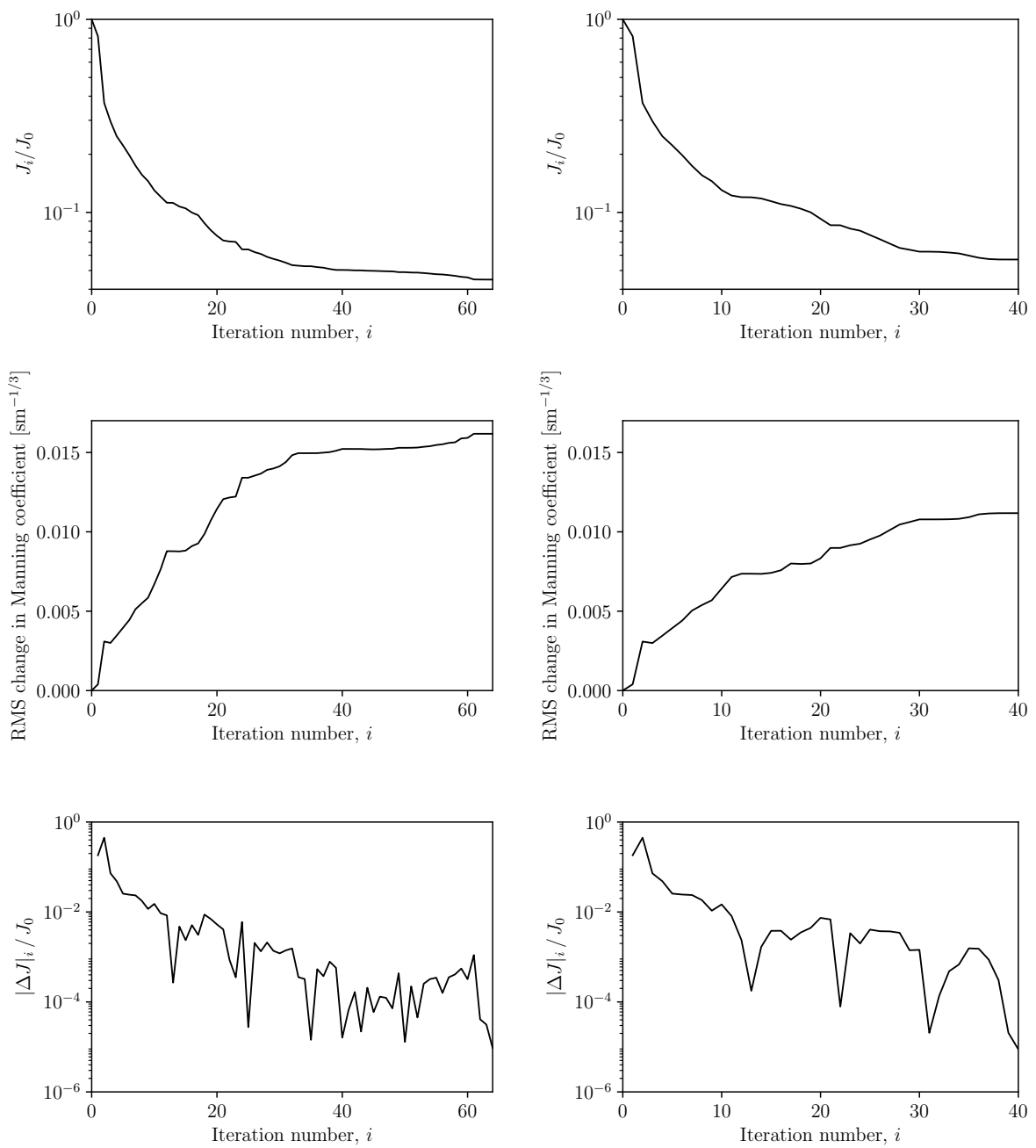


Figure 5.4: Results from adjoint-based assimilation of timeseries data using L-BFGS-B algorithm, for a freely spatially varying Manning coefficient. Top: Evolution of misfit functional. Middle: RMS change in Manning coefficient from initial guess ($n = 0.02 \text{ s m}^{-1/3}$). Bottom: Convergence. Left: without regularisation. Right: with regularisation, $\gamma = 10^{-10}$.

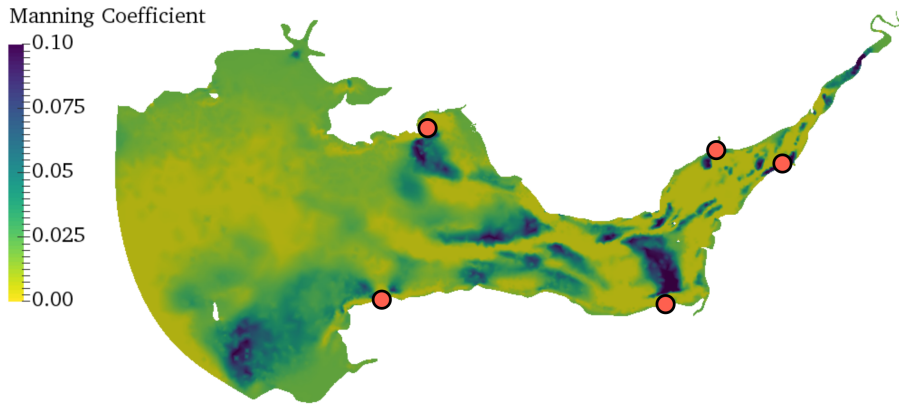


Figure 5.5: Optimised Manning coefficient field, without regularisation.

5.4.2 Results with regularisation

The use of regularisation is attempted in order to improve upon the unregularised result above, particularly in reducing the unrealistic values taken by the Manning coefficient in some regions. This is achieved through the addition of a regularisation term, as described in section 5.3.1. When a regularisation term is included, the functional which is minimised by the optimisation algorithm is given by equation (5.4), and a cross-validation method based on minimising the misfit to M2 harmonic data (given by equation (5.1)) is used to select the optimal regularisation parameter, γ .

Figure 5.6 shows the value of the harmonic-based misfit functional given by equation (5.1), for varying values of γ . For very small γ , the optimised friction coefficient field becomes indistinguishable from that of the unregularised optimisation, since the modification to the misfit functional becomes negligible. Large values of γ , on the other hand, produce optimised friction fields which are close to being uniform fields with a value $n = 0.02 \text{ s m}^{-1/3}$, since in this case the regularisation term dominates. For intermediate values of γ , it is found that the M2 harmonic-based misfit functional has a minimum, at $\gamma = 10^{-10}$. Therefore, while only the timeseries data has been directly assimilated by this calibration method, the misfit to the harmonic dataset is also minimised with respect to the regularisation parameter.

The convergence of the optimisation algorithm using this ‘optimal’ regularisation is shown in figure 5.4. The algorithm converged in fewer iterations than the unregularised case, while resulting in a similar reduction in the misfit functional. The corresponding optimised friction coefficient field is shown in figure 5.7. This regularised result takes the bounding values (0.005, 0.1) in slightly smaller regions of the domain than the unregularised result

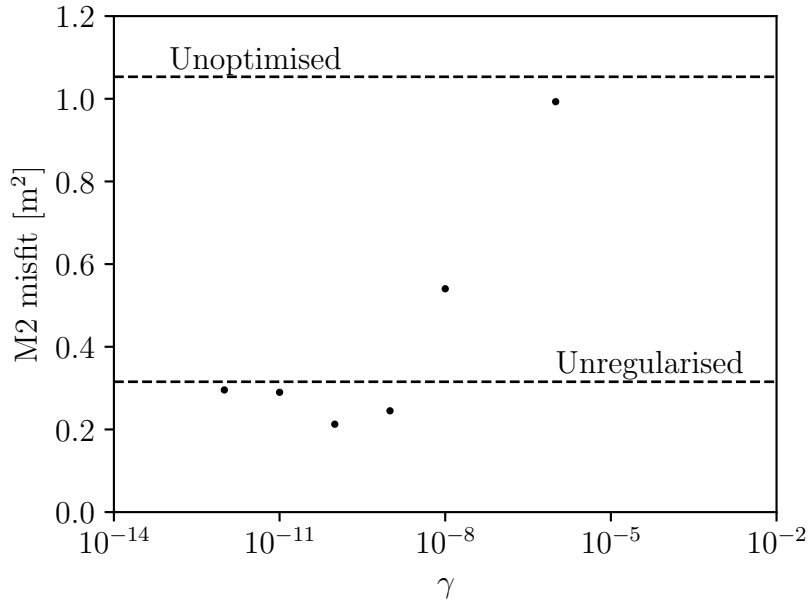


Figure 5.6: Results from the cross-validation method for selection of the regularisation parameter γ .

of figure 5.5, and in general the coefficient takes values closer to $0.02 \text{ s m}^{-1/3}$, due to the regularisation term; this is also visible by comparing the middle panels of figure 5.4. However, the overall spatial pattern is similar to the unregularised result, including features which appear to align with the tide gauge locations; the use of regularisation has not addressed the unphysical nature of the spatial distribution of the parameter. The use of this regularised friction coefficient field has only a very small effect on the model misfits, as summarised in table 5.1.

5.5 Results: sediment-based friction parameter

This section presents results from the use of both the gradient-based and Bayesian inversion calibration methods, applied to the estimation of the sediment-based friction parameter.

5.5.1 Synthetic experiment

In order to validate the calibration methods, a ‘synthetic’ experiment is first performed. For this, the Thetis model is run for one month using specified friction parameters $\mathbf{n} =$

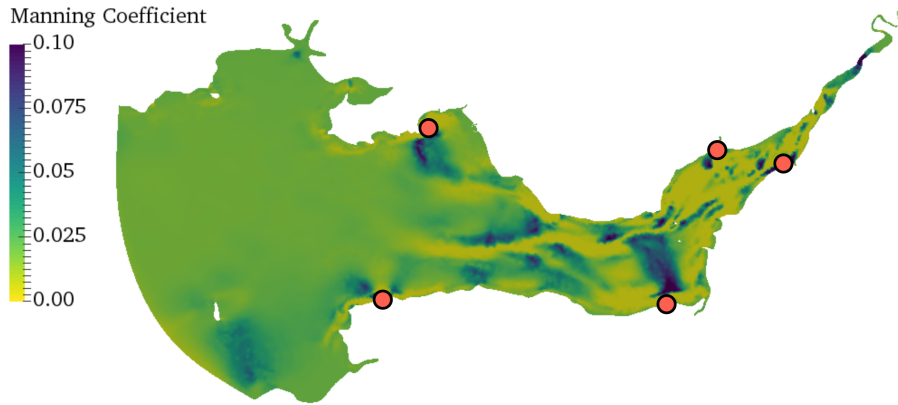


Figure 5.7: Optimised Manning coefficient field, with regularisation term with $\gamma = 10^{-10}$.

$(0.036, 0.027, 0.022)^T \text{ s m}^{-1/3}$ and the resulting model outputs used as ‘observation’ data for each calibration algorithm, to test that the calibration methods constitute well-posed problems, and are capable of recovering the synthetic friction parameters to acceptable accuracy and at a reasonable computational cost.

The results of this synthetic experiment are summarised in tables 5.2 and 5.3. They show the values of the calibrated parameters for each method, and the number of forward and adjoint runs taken by each method to achieve the result, respectively. Additional comments on each of the calibration methods/datasets are made here:

1. MCMC assimilation of harmonic data, M2 only

Since the true model-observation variance σ_C^2 for this synthetic case is zero, a fixed $\sigma_C^2 = 0.0025 \text{ m}^2$ is specified within the MCMC method; this is equivalent to assuming an uncertainty $\sigma_C = 0.05 \text{ m}$ in the synthetic observations. The resulting posterior joint probability density function (PDF) is shown in figure 5.8, and it is observed that the ‘true’ values of the friction coefficients lie close to the peak in the posterior PDF. There is strong covariance between the estimated Manning coefficients corresponding to rock and gravel, while the coefficient for sand shows little covariance with the other parameters.

2. MCMC assimilation of harmonic data, 4 constituents

Uncertainty in the observations is again simulated by specifying a fixed $\sigma_C^2 = 0.0025 \text{ m}^2$ for all constituents C . The resulting joint PDF is shown in figure 5.9, and is very similar to the result from the assimilation of only the M2 constituent. In general, the resulting PDF is narrower, as reflected in both the histograms of figure 5.9 and the uncertainties in the estimated parameter values of table 5.2. This shows that

	n_1	n_2	n_3
True value	0.036	0.027	0.022
MCMC result, M2 only	0.037 ± 0.007	0.027 ± 0.009	0.022 ± 0.005
MCMC result, 4 constituents	0.036 ± 0.005	0.028 ± 0.007	0.022 ± 0.004
Harmonic adjoint calibration result	0.0360	0.0270	0.0220
Timeseries calibration result	0.0359	0.0271	0.0220

Table 5.2: Summary of estimated Manning coefficients (units $\text{s m}^{-1/3}$) for the ‘synthetic’ experiment.

	Forward runs	Adjoint runs
MCMC result, M2 only	40×28 days	
MCMC result, 4 constituents	40×28 days	
Harmonic adjoint calibration result	15×3.5 days	15×3.5 days
Timeseries calibration result	16×1.5 days	16×1.5 days

Table 5.3: Summary of computational demand for the ‘synthetic’ experiment. The MCMC run-count is for the training data set; the computational cost of training and running the GPE is negligible compared to the full model.

assimilation of additional data can be used to overcome uncertainty in observation data, resulting in a tighter constraint on the unknown parameters. However, the high covariance between the estimated rock and gravel friction parameters remains present.

3. Adjoint-based assimilation of harmonic data

The algorithm converged in 14 iterations, requiring a total of 15 model runs; this includes line search steps as part of the optimisation algorithm, hence this is greater than the number of iterations. The implementation of the L-BFGS-B optimisation algorithm used within this work performs equal numbers of forward and adjoint runs, even in line search steps. The misfit functional J decreased to approximately $3 \cdot 10^{-7}\%$ of its original value during the optimisation, with the synthetic Manning coefficients recovered to within an absolute value of $2 \cdot 10^{-5} \text{ s m}^{-1/3}$.

4. Adjoint-based assimilation of timeseries data

The algorithm converged in 9 iterations, requiring a total of 16 forward and adjoint runs, where this again includes line search steps. The misfit functional J was decreased to less than $3 \cdot 10^{-8}\%$ of its original value, with the Manning coefficients converging to within an absolute value of $1.2 \cdot 10^{-6} \text{ s m}^{-1/3}$ of the prescribed synthetic values.

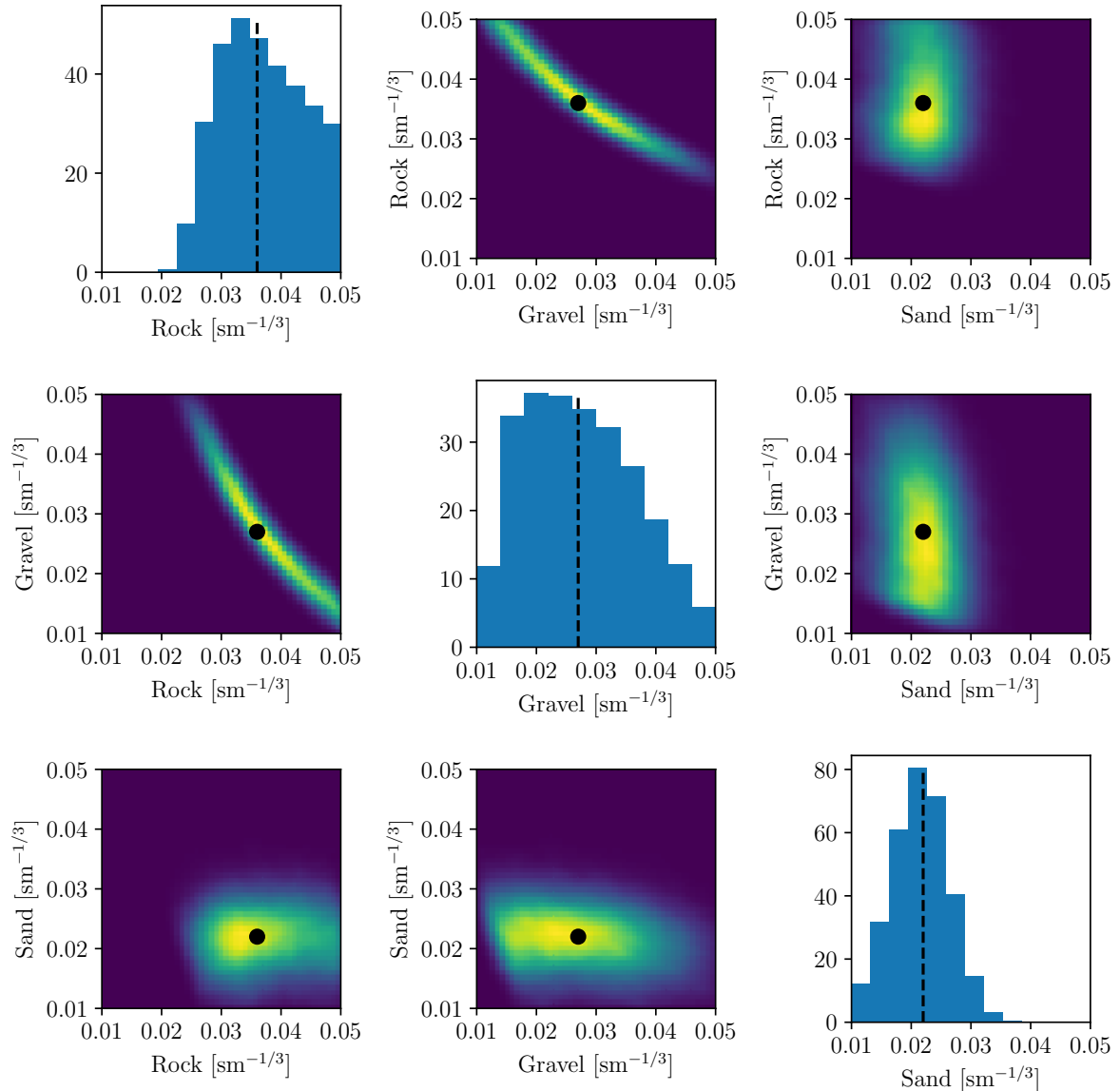


Figure 5.8: Posterior joint probability density function (PDF) obtained from MCMC sampling, based on assimilation of M2 harmonic amplitudes, using ‘synthetic’ observations and using a fixed $\sigma_C^2 = 0.0025 \text{ m}^2$. Black points/lines show original synthetic friction values.

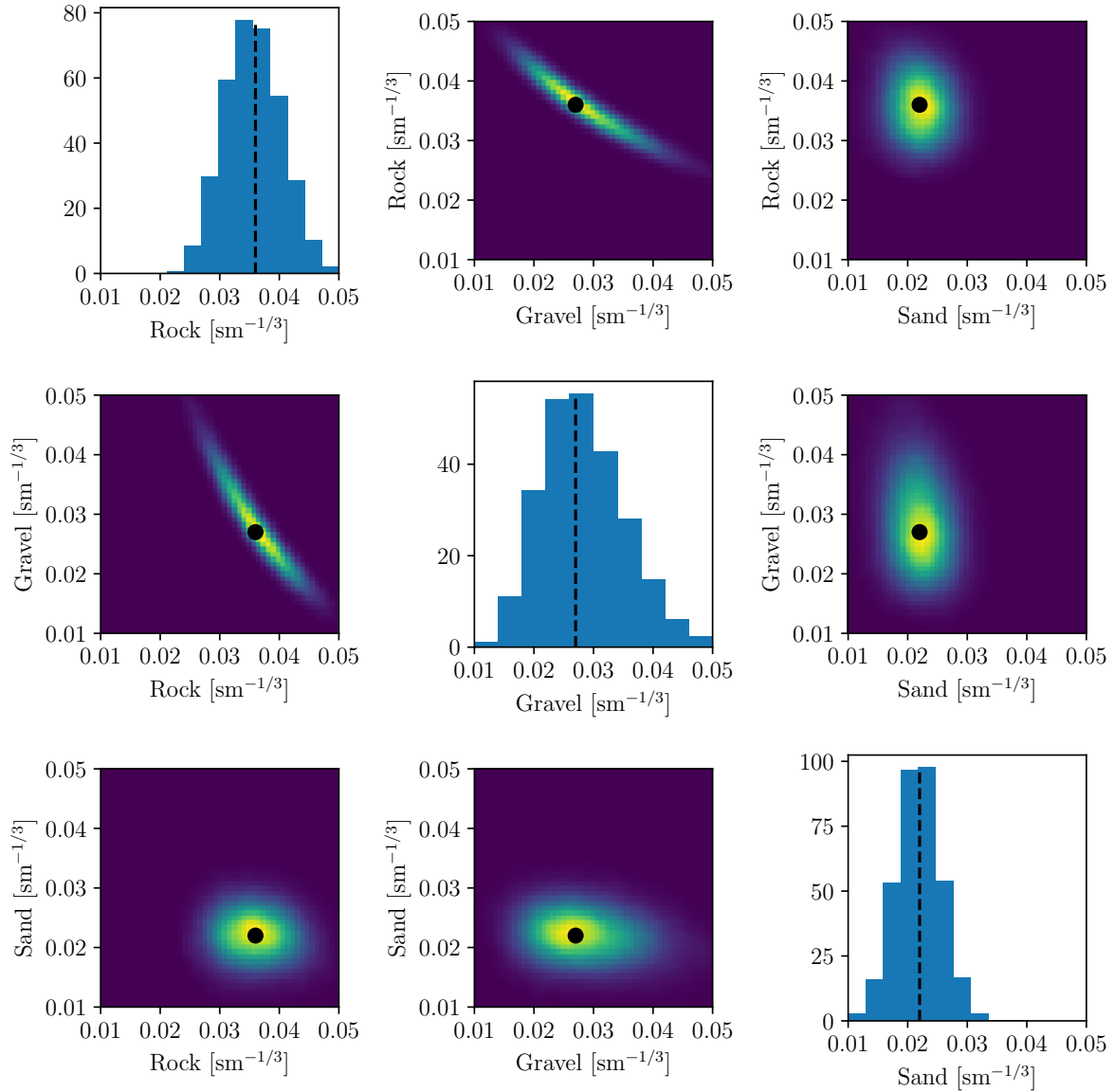


Figure 5.9: Posterior joint PDF obtained from MCMC sampling, based on assimilation of M2, S2, N2 and K2 harmonic amplitudes, using ‘synthetic’ observations and using a fixed $\sigma_C^2 = 0.0025 \text{ m}^2$. Black points/lines show original synthetic friction values.

5.5.2 Assimilation of real data

Each calibration method is now applied to the assimilation of real data, with results summarised in tables 5.4 and 5.5 and described below:

1. MCMC assimilation of harmonic data, M2 only

The posterior joint PDF of the estimated friction parameters is shown in figure 5.10, along with a histogram of the $\log \sigma_{M2}^2$ values. The estimated covariance matrix due to the GPE has elements on the order of 10^{-7} or smaller, and the magnitude of the inferred values for σ_{M2}^2 therefore justifies the assumption that the GPE covariances can be neglected. Similarly to the corresponding ‘synthetic’ assimilation, there is strong covariance between the estimated coefficients for rock and gravel, while the coefficient for sand shows no significant covariance with the other parameters. The estimated sand coefficient lies at the lower bound of the prior distribution.

2. MCMC assimilation of harmonic data, 4 constituents

The posterior joint PDF is shown in figure 5.11, along with histograms of each of the $\log \sigma_C^2$ values. The estimated Manning coefficients are consistent with the M2-only MCMC result, but exhibit smaller uncertainties due to the additional data assimilated. In this case, the covariance between the coefficients for rock and gravel makes them almost indistinguishable, and it is again found that the sand coefficient lies on the lower bound of the prior distribution.

3. Adjoint-based assimilation of harmonic data

The convergence of the L-BFGS-B algorithm is shown in figure 5.12. The misfit was reduced to approximately 2% of its original value during the optimisation, which converged after 15 iterations, using a total of 16 forward and adjoint runs. The resulting estimated friction parameters are consistent with the distributions estimated by both MCMC results.

4. Adjoint-based assimilation of timeseries data

The convergence for the assimilation of timeseries data is shown in figure 5.12. The misfit was reduced to around 25% of its original value, converging after 11 iterations, with a total of 12 forward and adjoint runs. The resulting Manning coefficients are somewhat different from those estimated by the assimilation of harmonic data (particularly the gravel coefficient), but still consistent within the uncertainty estimate of the M2-only MCMC approach.

It is incidentally noted that, in chapter 4, uncertainty in the Manning coefficient was assumed to be $0.005 \text{ s m}^{-1/3}$; this assumption is consistent with the estimated uncertainties

in the Manning coefficients inferred by the MCMC algorithms here, which vary between 0.002 and 0.009 $\text{sm}^{-1/3}$.

As described in section 5.3.3, three measures of model-observation misfit are used as indicators of the ‘success’ of each calibration method. The results for each of these misfit measures are summarised in table 5.6. For comparison purposes, optimal results for each misfit measure using a spatially uniform friction parameter are also included, which were determined from a brute force approach using model runs with values of n from 0.01 $\text{sm}^{-1/3}$ to 0.05 $\text{sm}^{-1/3}$ in steps of 0.0025 $\text{sm}^{-1/3}$, and taking the minimum NRMSE.

Three observations are made:

- (i) All four calibration experiments produce friction parameters which improve all three measures of model-observation misfit, compared with the initial guess (a uniform Manning coefficient of 0.02 $\text{sm}^{-1/3}$).
- (ii) The minimum achievable misfit to a given set of observation data is reduced by the use of a sediment-based friction coefficient, compared with an optimally-selected spatially uniform coefficient. For example, the Thetis timeseries NRMSE, using the sediment-based parameters selected by the calibration method which directly assimilated timeseries data, is 7.2%. In contrast, the best result achieved using a uniform coefficient is 8.4%. This shows the reduction in misfit which can be achieved by increasing the number of degrees of freedom in the tuning parameters.
- (iii) For Telemac, the use of the friction parameters selected using either the adjoint harmonic calibration or M2-only MCMC calibration results in a smaller NRMSE than can be achieved using any uniform coefficient, despite the sediment-based optimal values being selected using a different model (Thetis).

	n_1	n_2	n_3
MCMC result, M2 only	0.037 ± 0.007	0.029 ± 0.009	0.014 ± 0.003
MCMC result, 4 constituents	0.034 ± 0.005	0.033 ± 0.007	0.012 ± 0.002
Harmonic adjoint calibration result	0.0369	0.0302	0.0161
Timeseries calibration result	0.0336	0.0243	0.0155

Table 5.4: Summary of estimated Manning coefficients (units $\text{sm}^{-1/3}$) for the assimilation of real data.

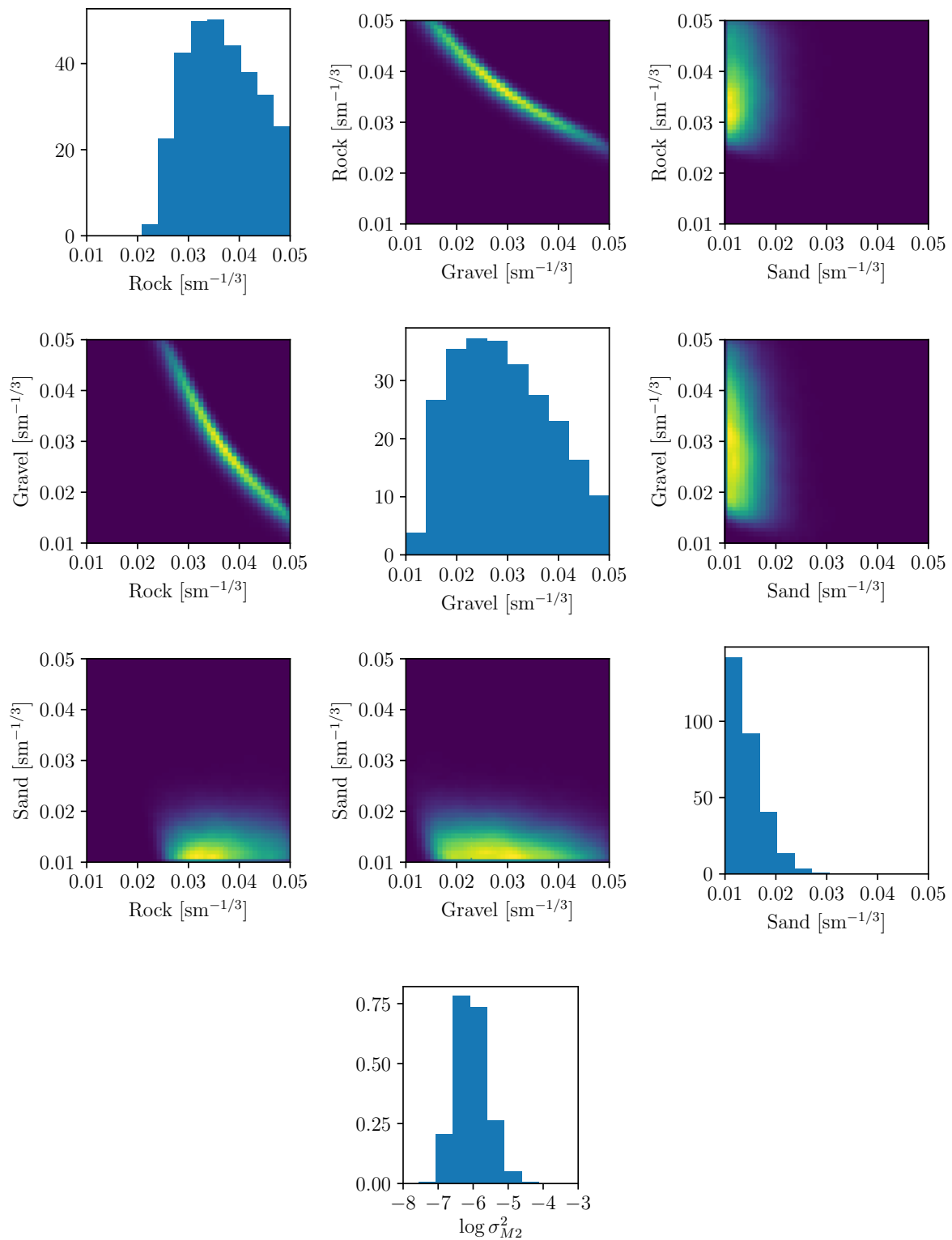


Figure 5.10: Posterior joint PDF obtained from MCMC sampling, based on assimilation of M2 harmonic amplitudes, using real observations.

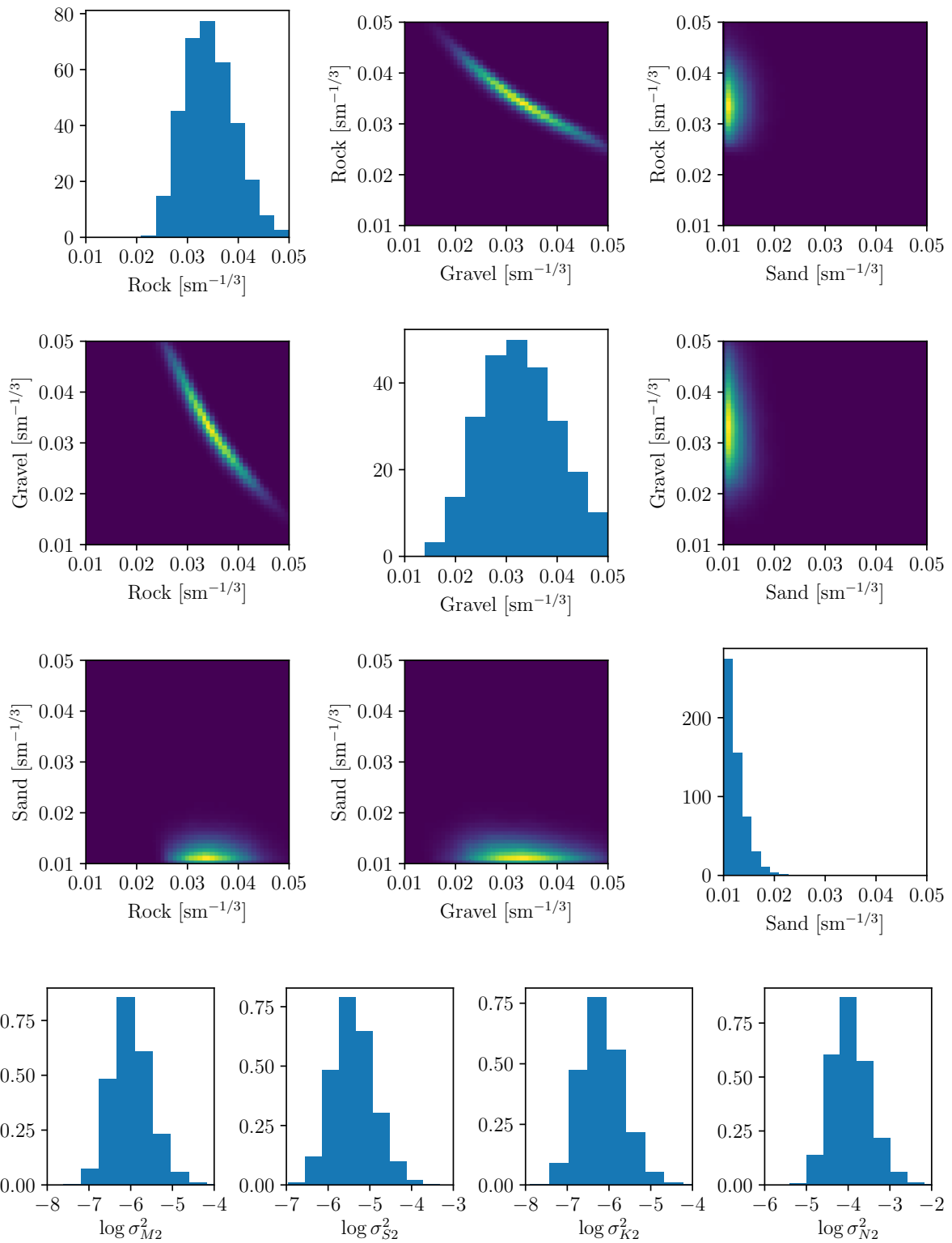


Figure 5.11: Posterior joint PDF obtained from MCMC sampling, based on assimilation of M2, S2, K2 and N2 harmonic amplitudes, using real observations.

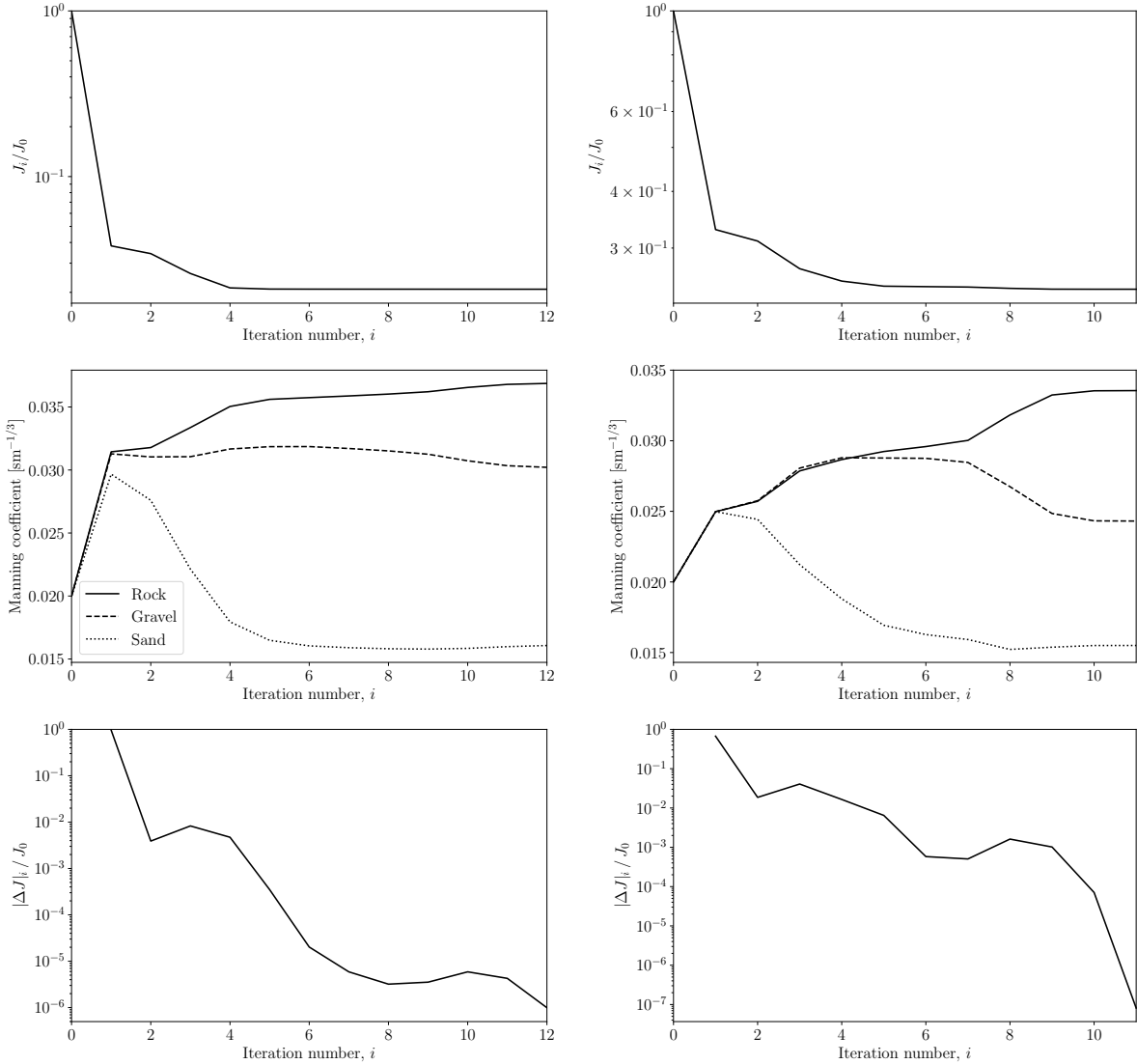


Figure 5.12: Results from adjoint-based assimilation of M2 harmonic data (left) and timeseries data (right) using L-BFGS-B algorithm. Top: Evolution of misfit functional. Middle: Evolution of estimated parameter values. Bottom: Convergence.

	Forward runs	Adjoint runs
MCMC result, M2 only	40×28 days	
MCMC result, 4 constituents	40×28 days	
Harmonic adjoint calibration result	16×3.5 days	16×3.5 days
Timeseries calibration result	12×1.5 days	12×1.5 days

Table 5.5: Summary of computational demand of each calibration method, for the assimilation of real data.

Calibrated parameters	Thetis timeseries	Thetis harmonic	Telemac harmonic
Initial guess ($n = 0.02 \text{ s m}^{-1/3}$)	13.9%	9.9%	9.7%
MCMC, M2 only	9.2%	4.5%	5.5%
MCMC, 4 constituents	9.2%	4.4%	6.0%
Adjoint harmonic calibration	10.6%	4.6%	5.5%
Adjoint timeseries calibration	7.2%	5.4%	6.2%
Uniform $n = 0.025 \text{ s m}^{-1/3}$	8.4%		
Uniform $n = 0.03 \text{ s m}^{-1/3}$		5.1%	
Uniform $n = 0.0275 \text{ s m}^{-1/3}$			5.9%

Table 5.6: Summary of misfit measures using sediment-based parameter calibration results. Values are NRMSEs as described in section 5.3.3. Coefficients of 0.025, 0.03 and $0.0275 \text{ s m}^{-1/3}$ are the optimal uniform-coefficient values for the Thetis timeseries, Thetis harmonic and Telemac harmonic NRMSEs, respectively.

5.6 Discussion

5.6.1 Comparison of freely varying and sediment-based friction parameters

Within this chapter, the gradient-based optimisation method has been applied to the assimilation of timeseries data, for the estimation of both freely spatially varying and sediment-based Manning coefficient fields. This allows a direct comparison of these two choices of calibration parameter space, although caution should be exercised due to the differences in the implementation of these calibration experiments (they used different meshes, and were subject to different convergence tolerances).

The use of a freely spatially varying Manning coefficient resulted in significant reductions in all three measures of the model-observation misfit. However, very high values for the coefficient were estimated in some small patches; the physical basis of these high-friction regions is unknown, and prominent features in the optimised Manning coefficient field appear to coincide with the locations of the tide gauges. This is a fundamental issue in solving an ill-posed optimisation problem (Hofmann, 1986). The use of regularisation

slightly reduces the spatial extent of these high-friction patches, but the alignment with the tide gauge locations is still present, suggesting that the results are not physically meaningful. There is scope for further work regarding the selection of the regularisation parameter or the n_0 value representing the prior knowledge of the coefficient, or the use of alternative regularisation terms.

The unknown physical significance of the freely-varying result was the original motivation for the use of sediment data to constrain the input parameter space. Note that the use of sediment data in this way can be considered a form of regularisation in itself, since it incorporates prior knowledge to constrain the input parameter space. However, this prior knowledge is more physically motivated than the use of the L2 regularisation term used in section 5.4. The physical significance of the sediment-based results is supported by the fact that the estimated coefficients fall in order of typical grain size; the coefficient for sand is typically the smallest, with the coefficient for rock the greatest (in cases where it can be distinguished from the gravel coefficient). The use of sediment data to *a priori* constrain the input parameter is therefore considered to give more physically realistic results, despite the relatively modest (compared with the freely varying case) reductions in the model-observation misfit measures.

Regarding the computational cost of the two approaches, the estimation of the freely varying parameter required significantly more iterations than the sediment-based parameter, although note that the ratio of the number of required iterations is orders of magnitude smaller than the ratio in the number of degrees of freedom. Future work is required to determine the most appropriate number of degrees of freedom in the input parameter space, as a compromise between the performance of the calibrated model, the computational cost of the calibration method, and the availability of data to reliably constrain the unknown parameters in a physically meaningful way.

5.6.2 Comparison of calibration methods for sediment-based friction parameter

A broader set of calibration experiments has been performed using the sediment-based friction parameter, and this section discusses these results in greater detail. Section 5.5 has shown that, for the sediment-based input parameter space, all of the calibration methods perform well both in the synthetic experiment, where the prescribed friction coefficients are accurately recovered by all methods, and in the assimilation of real data, where all estimated friction parameter sets are consistent (within the uncertainties estimated by the M2-only MCMC method). For the assimilation of real data, all four calibration

experiments produce parameters which offer an improvement across all three measures of misfit, compared with the initial guess for the parameters. This includes the misfit as measured using a second model, Telemac. Furthermore, the calibrated parameter sets selected by the harmonic adjoint-based or M2-only MCMC methods produce lower Telemac NRMSE values than any uniform friction coefficient (i.e. not only compared to the naive initial guess), and the results from the other calibration methods also come very close to this optimal uniform-coefficient performance. This suggests that the calibration methods have avoided excessive influence from model-specific errors. However, it should be noted that the two numerical models used here (Thetis and Telemac) employ similar equations and have used the same mesh, bathymetry and boundary conditions, although the details of the finite element discretisation are different. Future work would be needed to investigate the applicability of calibrated friction parameters across models which differ more significantly in the aspects listed in section 5.3.3.

In the PDFs of figures 5.10 and 5.11, the Manning coefficient for sand is estimated to be at the lower bound of the prior distribution. This highlights the need for a physically motivated prior distribution; through additional numerical experiments it was found that the reduction of this lower bound resulted in parameter sets which produced greater NRMSEs (computed using eight harmonics as described in section 5.3.3), and therefore that the placement of the lower bound was influential. The posterior PDFs also exhibit strong covariance between the gravel and rock friction coefficients, indicating that the assimilated data are not sufficient to distinguish between these two parameters. This suggests that a similar result could have been achieved by combining the rock and gravel sediment groups together and performing a two-parameter calibration instead. Data at additional locations may be helpful in distinguishing these two parameters; chapter 6 considers how sensitivity analysis-based frameworks can be utilised to propose new observation locations which result in the best constraints on unknown parameters.

In addition to comparing the performance of the calibrated parameter sets, the computational cost of each calibration method can also be compared, as outlined in tables 5.3 and 5.5. Here it important to consider the relative computational cost of forward and adjoint model runs, since the computational cost of a well-implemented adjoint model is typically greater than that of the forward model by a multiplier slightly larger than unity (Griewank and Walther, 2008). For the Thetis adjoint model, this multiplier is approximately 3.6. The gradient-based calibration using timeseries data is therefore the least computationally expensive of the methods used within this work, due to its short 1.5-day runs, while the MCMC approach is the most expensive, due to the long 28-day runs used to train the surrogate model. However, note that this choice of a 28-day run length was selected for the purpose of training an emulator resolving four harmonic constituents. The assimila-

tion of only M2 harmonic data could have been achieved using an emulator trained using much shorter model runs, such as those used in the adjoint gradient-based assimilation of M2 data, i.e. 3.5 days. In this case, the computational costs of the gradient-based and MCMC methods for assimilating M2 harmonic data would have been comparable. It is also noted that, while all simulations were performed in parallel across 16 cores, the emulator training runs could take greater advantage of available computational resources since each training run could be performed concurrently. This is in contrast to the gradient-based optimisation approach, where the model runs for each iteration must clearly be performed sequentially.

For the assimilation of data for a single harmonic constituent, the minimisation of the functional in the adjoint approach (equation (5.1)) is equivalent to the maximisation of the posterior distribution of the MCMC method (equation (5.8)). Consequently, the parameter estimates resulting from the two M2-based calibration methods are consistent, within the uncertainties estimated by the MCMC method. It is therefore clear that there is more information obtained from the MCMC method than from the adjoint approach; specifically, the MCMC method provides the full posterior distribution, and can therefore estimate uncertainties in the estimated friction parameters. For the three-dimensional input parameter space used here, the MCMC approach therefore has the potential to be more computationally efficient, by providing more information than the gradient-based approach, at a similar computational cost.

Since the computationally expensive component of the MCMC framework is in the generation of the emulator training dataset, the subsequent training and use of emulators is flexible, as demonstrated here by the training of two emulators using different combinations of harmonic constituents. By comparing the use of single and multiple constituents for the definition of the likelihood in the MCMC algorithm, the reduced uncertainty resulting from the assimilation of a greater volume of data has been demonstrated. However, since the number of full model runs required to train an emulator depends strongly on the number of degrees of freedom in the input parameter space (via the ‘10d’ rule (Hristov et al., 2017; Sobol, 2001)), the MCMC approach will not scale well with increased complexity in the friction parameter space. Some of the computational expense of training high-dimensional surrogate models can be mitigated by incorporating gradient information derived from an adjoint model (e.g. Han et al. (2017)), but this was beyond the scope of this work. The computational cost of the gradient-based calibration approach, on the other hand, is almost independent of the dimension of the parameter space; the cost of the adjoint model run is constant, and the number of iterations required for convergence depends relatively weakly on the number of degrees of freedom in the input parameter space, as shown by the use of a freely-varying Manning coefficient (with $\mathcal{O}(10^4)$ degrees of

freedom) in section 5.4. In this study, a three-dimensional parameter space was used for the unknown Manning coefficient, and it has been argued that the MCMC and gradient-based approaches can be applied at similar computational cost. Given the considerations above, for a parameter space of four or more dimensions, the computational cost of the MCMC approach would likely exceed that of the adjoint approach, whereas for two or fewer dimensions, the emulator training would be cheaper than the adjoint approach. It is for this reason that the MCMC approach was not attempted for the freely varying friction parameter with $\mathcal{O}(10^4)$ degrees of freedom.

Lastly, regarding the choice of data to assimilate within a calibration method, the availability of timeseries tide gauge data is typically limited to locations on the coastline, while harmonic data is often also available in open locations (e.g. at oil rigs). While a direct investigation of the relative information contributed by coastal tide gauges compared with open-ocean locations has not been performed, it is likely that assimilating data from a variety of observation location environments (e.g. situated in regions of differing sediment types or hydrodynamic regimes) is useful in constraining unknown parameters. The greater availability of harmonic data, across varied locations, suggests that its assimilation is likely to yield tighter constraints on unknown friction parameters, and/or facilitate model calibration with respect to a greater number of degrees of freedom. Some of these aspects are explored in chapter 6. The assimilation of tidal current observations (e.g. from ADCPs) has not been considered within this thesis, but is planned in future work.

5.7 Summary

The aim of this chapter was to estimate a spatially varying Manning coefficient by assimilating observation data, using a case study of the Bristol Channel and Severn Estuary. This was first attempted using a freely spatially varying field of Manning coefficient values, by assimilating timeseries data via an adjoint gradient-based method. The optimal coefficient field produced significant reductions in multiple measures of model-observation misfit. However, the physical features of the optimised field appeared to align with the locations of observation data, and the field is therefore not considered to represent reality.

A second set of experiments was performed using sediment data to *a priori* constrain the spatial variation of the friction parameter. Using this input parameter space, both adjoint gradient-based optimisation and Bayesian inversion via a Markov Chain Monte Carlo (MCMC) algorithm were used to solve the parameter estimation problem. The results from each of these methods were consistent within the parameter uncertainties estimated

via the MCMC approach, and were again found to reduce multiple measures of model-observation misfit, including when used within a second numerical model, TELEMAC-2D. The use of physical knowledge (via sediment data) was used in the construction of the input parameter space and the estimated parameters are consistent with expectations about the relative roughness of each sediment type. The resulting parameter estimates are therefore considered to be physically meaningful.

The assimilation of timeseries data via the adjoint is the least computationally expensive calibration method, and scales well with the number of degrees of freedom in the input parameter space; this is demonstrated by its application to a fully spatially varying friction coefficient containing $\mathcal{O}(10^4)$ degrees of freedom. It has been argued that the computational costs associated with the assimilation of M2 harmonic data via the adjoint gradient-based and MCMC methods share a similar computational cost. Since the MCMC method estimates not only the unknown parameters but also the associated parameter uncertainties, it is considered a more efficient approach for this problem where three parameters are estimated. However, since the MCMC method relies on the training of an emulator as a surrogate for the full numerical model, and the required size of an emulator training dataset scales linearly with the number of degrees of freedom in the input parameter space, it is concluded that for input parameter spaces of four or more dimensions, an adjoint-based method is likely to be more computationally efficient, while for two or fewer dimensions, the MCMC-via-emulator method is likely to be more efficient.

The case study of this chapter constitutes a data-rich region, which has enabled a comparison of parameter estimation approaches. The next chapter considers a scenario where available observation data is insufficient to constrain unknown parameters, and compares two approaches to the proposal of new observation locations, motivated by a parameter estimation exercise.

Chapter 6

Guiding new tidal observations

6.1 Introduction

Chapter 4 has provided motivation for the use of calibration methods for reducing uncertainty in a bottom friction parameter, in order to reduce uncertainty in modelled storm surges. Following from this, chapter 5 has compared two approaches for bottom friction parameter estimation; good results have been achieved via the use of a spatially varying Manning's n coefficient for the bottom friction parameterisation, and the use of Bayesian inversion via a Markov Chain Monte Carlo algorithm to estimate three such friction parameters corresponding to three groups of sediment types found within the case study model domain.

One major assumption throughout chapter 5 is that a sufficient set of observation data exists, which can be used to constrain the unknown parameters via data assimilation techniques. The selection of the case study region of chapter 5, consisting of the Bristol Channel and Severn Estuary, was made because it constitutes a data-rich region, with data available at a total of 16 locations across the domain. However, this chapter considers the scenario where observation data is insufficient to constrain the unknown model parameters, and seeks to answer the question: *how should new observations be made in order to produce the best constraint on a given set of unknown model parameters?* This work follows from chapter 5, with a focus on estimating unknown Manning coefficients, governing bottom friction.

As already described in chapter 2, Butler et al. (2015) approach bottom friction parameter estimation via a measure-theoretic approach, which they apply to an idealised inlet case study. They focus on a definition of the 'condition' of the stochastic inverse problem

(which is analogous to, but distinct from, the condition number of an invertible matrix), and demonstrate how it can be used to select combinations of model outputs which form well-posed inverse (e.g. parameter estimation) problems. Graham et al. (2017) utilise the same measure-theoretic approach for an application to a realistic hurricane case study, with a focus on experiment design; the ‘condition’ of the stochastic inverse problem is used to select a configuration of observation buoys recording the storm surge which constitute an optimal inverse problem for estimating unknown Manning’s n coefficients. The work described in this chapter applies the ‘condition’ definition of Butler et al. (2015) to the selection of optimal observation locations for use within a Bayesian inference framework, with an application to two real-world case study regions.

Section 6.2 describes the general parameter estimation problem and summarises the Bayesian inversion approach used within this chapter for solving such problems. Section 6.3 presents two measures for quantifying the condition of the parameter estimation problem. The first of these measures is that of Butler et al. (2015), and the second is an alternative approach, intended to overcome some shortcomings in the first measure.

Section 6.4 takes the Bristol Channel case study of chapter 5, and applies the two condition measures to this region in order to identify combinations of three observation locations which provide the best constraint on the three unknown friction parameters. The inverse problems selected by optimising each condition measure can be solved using real data for this case study. Section 6.4 also proposes new observation locations, motivated by obtaining an improved constraint on the unknown parameters than can be achieved using current observation datasets. This application to the Bristol Channel case study constitutes a preliminary step towards the proposal of new observation locations in data-poor regions; section 6.5 uses the North Malé Atoll in the Maldives as such a case study. The results are discussed in section 6.6, and a summary can be found in section 6.7.

6.2 The parameter estimation problem

The problem of parameter estimation via data assimilation in the presence of noise constitutes a stochastic inverse problem. The friction parameter estimation problem is outlined here, along with the solution method used within this work.

A vector of model inputs to be estimated is denoted $\mathbf{n} = (n_1, n_2, \dots)^T$. A given vector of model outputs, which may be compared with corresponding observations, is denoted $\mathbf{Q}(\mathbf{n}) = (Q_1(\mathbf{n}), Q_2(\mathbf{n}), \dots)^T$. The stochastic inverse problem is to find the probability

distribution function (PDF) of the vector of inputs \mathbf{n} , given a PDF of observed values for \mathbf{Q} .

Throughout this chapter, a Bayesian inversion approach similar to that of chapter 5 is used to solve problems of this kind. In this approach, the posterior distribution of the input parameters \mathbf{n} given a set of observed values \mathbf{y} corresponding to the model outputs \mathbf{Q} is given by

$$\Pi(\mathbf{n}|\mathbf{y}) \propto (2\pi\sigma^2)^{-N/2} \exp\left(-\frac{1}{2}\frac{|\mathbf{y} - \mathbf{Q}(\mathbf{n})|^2}{\sigma^2}\right) \prod_i q(n_i), \quad (6.1)$$

where it is assumed that the model-observation discrepancies $\mathbf{y} - \mathbf{Q}(\mathbf{n})$ are independent and identically distributed variables with variance σ^2 , N is the length of the vectors \mathbf{Q} and \mathbf{y} , and $q(n_i)$ is the prior distribution of the input parameter n_i . This posterior distribution can be estimated by sampling using a Markov Chain Monte Carlo (MCMC) algorithm, avoiding the need to compute the constant of proportionality. Within this chapter, as in chapter 5, a Gaussian process emulator is used as a surrogate for the full numerical model in estimating $\mathbf{Q}(\mathbf{n})$, due to the large number of samples required to estimate the posterior distribution.

In chapter 5, one choice of model outputs $\mathbf{Q}(\mathbf{n})$ was the set of M2 harmonic amplitudes at the 11 locations within the Bristol Channel model domain at which such observation data was available. In such examples where observation data is plentiful, a practical approach is to use all available data for the purposes of parameter estimation. However, such data typically contains redundant information. For example, constraining three unknown input parameters is possible via the assimilation of only three observations, provided that those three observations provide different information, i.e. that they have differing sensitivities to each of the three model inputs. The aim of the methods used within this chapter is to guide the optimal selection of model outputs \mathbf{Q} , which provide the tightest possible constraint on the unknown input parameters, using the fewest possible observations.

6.3 Methods

6.3.1 Skewness method

Butler et al. (2015) utilise a measure-theoretic algorithm for solving stochastic inverse problems, which requires fewer assumptions than the Bayesian inversion method used within this work. Within their work, the set of model outputs \mathbf{Q} is considered as a

physical map from model inputs onto model outputs. They find that the number of samples of the forward model which are required to solve the inverse problem via the measure-theoretic approach is related to the skewness of the Jacobian matrix of the map $\mathbf{Q}(\mathbf{n})$. This Jacobian is given by

$$J_{i,j} = \frac{\partial Q_i(\mathbf{n})}{\partial n_j}. \quad (6.2)$$

The definition of the skewness follows here. Consider a matrix V , whose rows are given by vectors \mathbf{v}_i . For each i , there must exist vectors \mathbf{v}_i^\perp and \mathbf{v}_i^0 such that

$$\begin{aligned} \mathbf{v}_i &= \mathbf{v}_i^\perp + \mathbf{v}_i^0 \\ \mathbf{v}_i^\perp &\perp \mathbf{v}_i^0 \\ \mathbf{v}_i^0 &\in \text{span}\{\mathbf{v}_{j \neq i}\}, \end{aligned} \quad (6.3)$$

provided that the vectors \mathbf{v}_i are geometrically distinct, i.e. the rows of the matrix V are linearly independent. The skewness for a vector \mathbf{v}_i is defined as

$$\text{skew}(V, \mathbf{v}_i) = \frac{|\mathbf{v}_i|}{|\mathbf{v}_i^\perp|}. \quad (6.4)$$

The skewness of the matrix V is subsequently defined as

$$\text{skew}(V) = \max_i \{\text{skew}(V, \mathbf{v}_i)\}. \quad (6.5)$$

To illustrate this example, consider a stochastic inverse problem where two model outputs $\mathbf{Q} = (Q_1, Q_2)^T$ are used for the estimation of two model inputs $\mathbf{n} = (n_1, n_2)^T$, with a resulting 2×2 Jacobian matrix

$$J = \begin{pmatrix} \frac{\partial Q_1}{\partial n_1} & \frac{\partial Q_1}{\partial n_2} \\ \frac{\partial Q_2}{\partial n_1} & \frac{\partial Q_2}{\partial n_2} \end{pmatrix}. \quad (6.6)$$

Figure 6.1 shows example sensitivity vectors $\frac{\partial Q_i}{\partial \mathbf{n}}$ (i.e. the rows of this Jacobian matrix) for well-conditioned and poorly-conditioned stochastic inverse problems. In the well-conditioned case (top panel), the skewness is small and the two model outputs exhibit contrasting sensitivity with respect to the input parameters. The sensitivity vectors span the input parameter space with minimal redundancy, such that both input parameters would be constrained by observations of Q_1 and Q_2 . In the poorly-conditioned case (bottom panel), the skewness is high, and the information about the model inputs provided

by the two model outputs is very similar, i.e. there is significant redundancy in the information provided by each model output.

In this two-dimensional case, it is also simple to show that $\text{skew}(J) = 1/\sin \alpha$, where α is the angle between the two sensitivity vectors as indicated in figure 6.1. It is clear that when the sensitivity vectors are close to being aligned (or antialigned), the redundancy in the information provided about the model inputs is high, and the skewness is correspondingly large, while when α is close to 90° , the skewness is small and the two model outputs provide differing information about the model inputs; this is captured by the $1/\sin \alpha$ relationship.

A practical framework for selecting an optimal set of observation locations based on this skewness measure is as follows, and roughly follows Graham et al. (2017):

1. Propose a set of candidate observation locations.
2. Form a list of all possible combinations of model outputs \mathbf{Q} , under the constraint that the number of model outputs (i.e. the length of the vector \mathbf{Q}) may not exceed the number of unknown parameters, since the skewness definition breaks down under these conditions. There are ${}^N C_r = \frac{n!}{r!(n-r)!}$ possible vectors \mathbf{Q} , where N is the number of candidate observation locations, and r is the length of the vector \mathbf{Q} , i.e. the number of observations proposed.
3. For each possible map \mathbf{Q} , calculate or estimate the corresponding Jacobian $J(\mathbf{n})$, defined by equation (6.2). Within Graham et al. (2017), this Jacobian is estimated using forward differences. Since the problem is nonlinear, the Jacobian is sampled at 16 random sets of input parameters \mathbf{n} from a prior distribution. Note that, since each model run produces outputs at all candidate locations, a single set of model runs can be used to estimate the Jacobians corresponding to an arbitrary map \mathbf{Q} .
4. Calculate the skewness of the Jacobians corresponding to each map \mathbf{Q} , according to equation (6.5), and average the skewnesses across the input parameter samples.
5. Sort the candidate maps \mathbf{Q} by their average skewness. The lowest skewness corresponds to the optimal map.

The software used within this chapter for steps 2–5 above is the Butler-Estep-Tavener (BET) python package (Graham, 2015; Graham et al., 2013). Note that the application of this skewness method for the optimal selection of observation locations within this chapter is outside its original scope; its theoretical basis is within the measure-theoretic

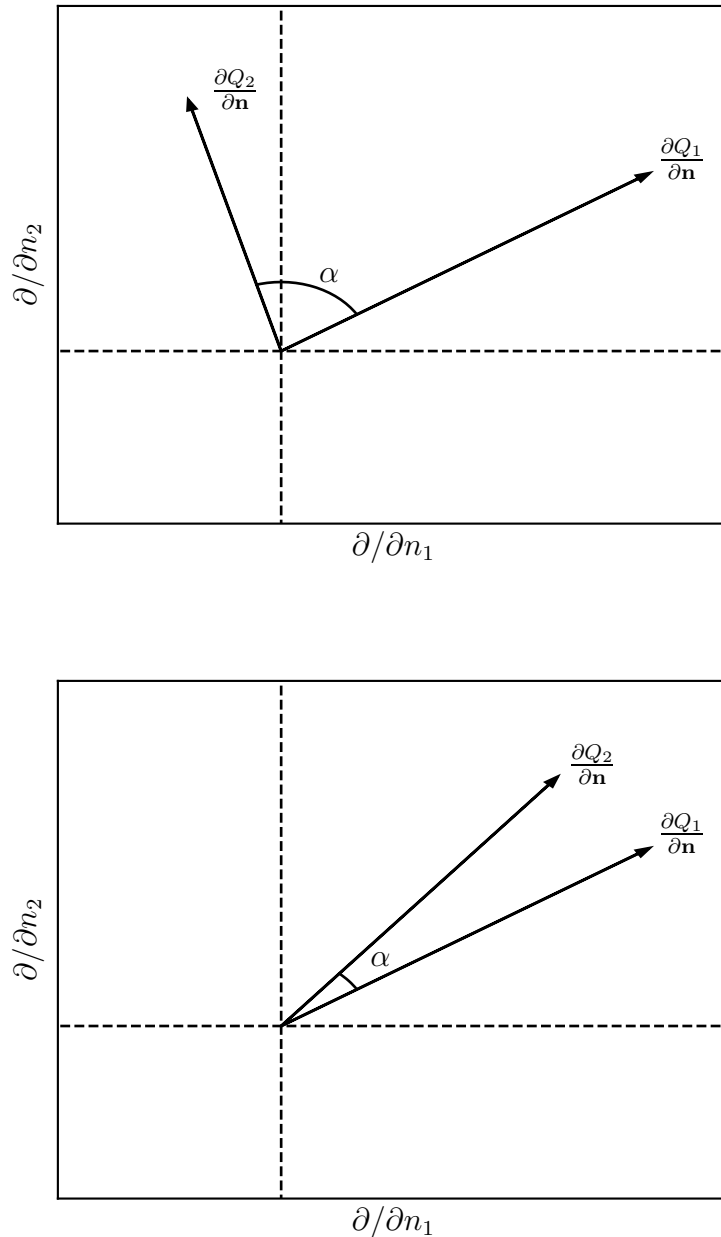


Figure 6.1: Examples of sensitivity vectors for well-conditioned (top) and poorly-conditioned (bottom) inverse problems, using a simple two-dimensional example. The skewness is low in the well-conditioned case, and high in the poorly-conditioned case.

approach of Butler et al. (2015), but it is applied here for parameter estimation via Bayesian inversion.

6.3.2 Volume method

One drawback of the skewness method described above is that the skewness is independent of the scale of the vectors $\frac{\partial Q}{\partial n}$. This means that the selection of observations based on skewness does not favour model outputs whose sensitivity to the model inputs is greater. Pianosi et al. (2016) comment that “high local sensitivity to a parameter indicates high accuracy of its optimal estimate, while low sensitivity suggests that the parameter is poorly identified and uncertainty is large”. For example, consider the simple two-dimensional cases shown in figure 6.2. While the sensitivity vectors in the top panel are approximately perpendicular and therefore exhibit low skewness, an inverse problem based on the model outputs whose sensitivity vectors are depicted in the bottom panel may well fare better in overcoming observation uncertainty, and produce tighter constraints on the parameter estimates, due to the greater sensitivity magnitudes.

In using the skewness method, Graham et al. (2017) overcome this problem by filtering out model outputs with low sensitivity during the proposal of candidate observation locations. This was motivated by reducing the number of candidate maps \mathbf{Q} for which the skewness must be evaluated, but has the additional benefit of avoiding the low-skewness-low-sensitivity scenario depicted in the top panel of figure 6.2.

In this section, an alternative measure is proposed, which favours model outputs exhibiting high sensitivity to model inputs, and removes the requirement for such manual intervention in the process. This method is based on the total (hyper)volume enclosed by the sensitivity vectors constituting the rows of the Jacobian J of a given map. In the simple two-dimensional example, this corresponds to the area as depicted in figure 6.3. An optimal inverse problem is one in which this area (or, more generally, hypervolume) is maximised.

This volume-based metric has a number of advantages over the skewness metric of Butler et al. (2015). In addition to being a simpler metric (avoiding the definition of skewness), and favouring greater sensitivity magnitudes, this method can also be generalised to the selection of a greater number of model outputs than model inputs, by the summation of volumes, as depicted in figure 6.4. Chapter 5 has demonstrated how the assimilation of a greater volume of data can result in tighter constraints on unknown parameters; the ability to propose an arbitrary number of outputs is therefore valuable.

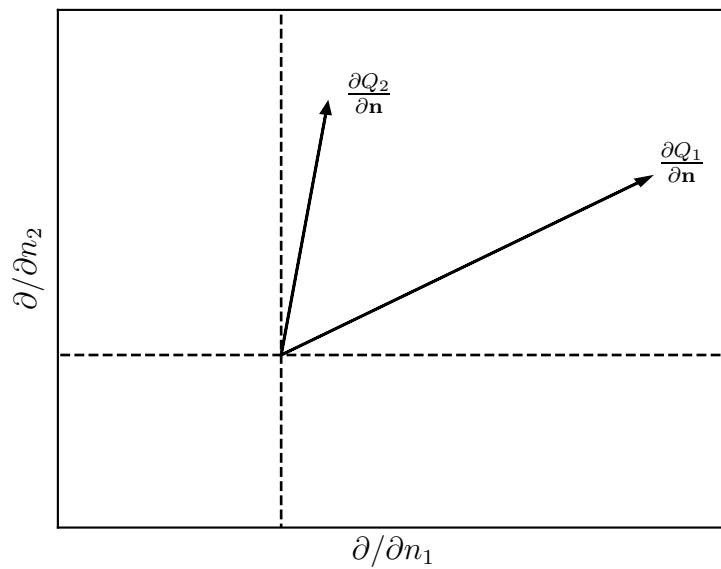
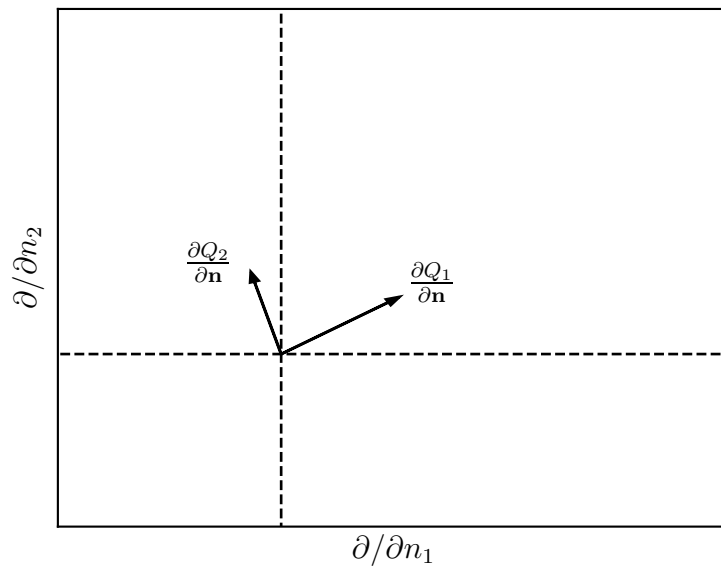


Figure 6.2: Top: sensitivity vectors for an inverse problem exhibiting low skewness, but small sensitivity magnitudes. Bottom: sensitivity vectors exhibiting moderate skewness, but large sensitivity magnitudes.

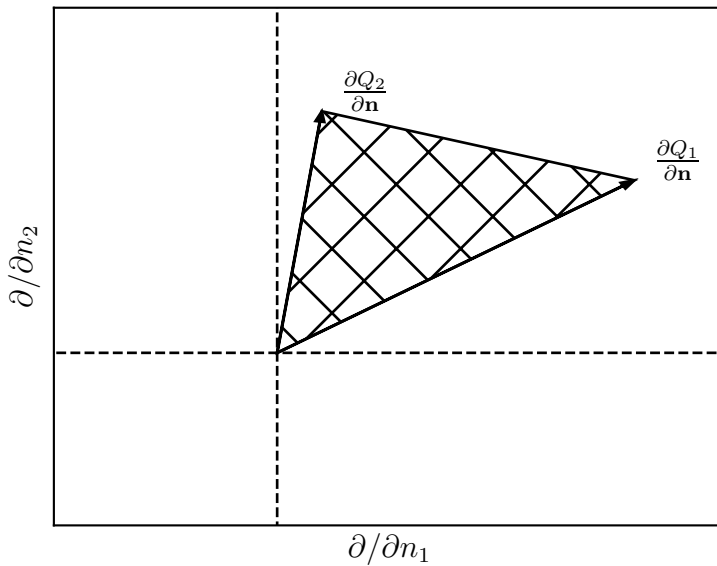


Figure 6.3: The area between two sensitivity vectors.

One disadvantage of this volume-based metric is that hypervolumes of different dimensions cannot be compared, due to their incommensurable units. This would be relevant in the case where the number of proposed observations may be less than the number of input parameters, and one wishes to compare observation strategies of varying numbers of observations. This would apply, for example, to a comparison between the use of two observations and three observations, in a scenario with three unknown parameters. In this case, the hypervolume for the two-observation strategy is an area, and for the three-observation strategy is a volume. However, this scenario applies only to under-constrained problems; within the rest of this chapter it is assumed that the number of unknown parameters is less than or equal to the number of proposed observations, and this issue is therefore not relevant.

The framework described above for the skewness method is modified here to utilise the volume measure:

1. Propose a set of candidate observation locations.
2. Form a list of all possible combinations of model outputs \mathbf{Q} . There is no constraint that the number of selected model outputs must be less than or equal to the number of model inputs.
3. For each possible map \mathbf{Q} , calculate or estimate the Jacobian $J(\mathbf{n})$ of the selected outputs with respect to the inputs (e.g. using forward differences), and sample this

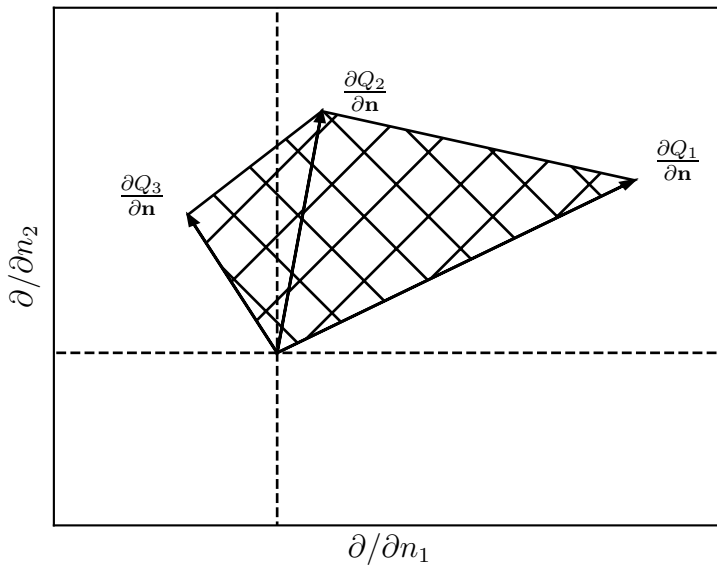


Figure 6.4: Segment areas can be summed, generalising the volume-based measure to a greater number of model outputs.

Jacobian at random samples from the prior distribution of the input parameters.

4. Calculate the volume enclosed by the sensitivity vectors (the rows of the Jacobians) corresponding to each map \mathbf{Q} , and average the volumes across the input parameter samples. Within this work, these volumes are computed using QHull (Barber et al., 1996), via the Python scientific computing library *SciPy*.
5. Sort the candidate maps \mathbf{Q} by their average volume. The highest volume corresponds to the optimal map.

6.4 Application to the Bristol Channel

6.4.1 Background

Within this section, the case study of chapter 5, consisting of the Bristol Channel and Severn Estuary, is reused. This model domain is shown in figure 6.5, along with the locations where harmonic data is available. The observation data used within this section consists of the M2 amplitude at each of these 16 locations; this combines the two sources of data used within chapter 5 (11 locations at which harmonic data was already available

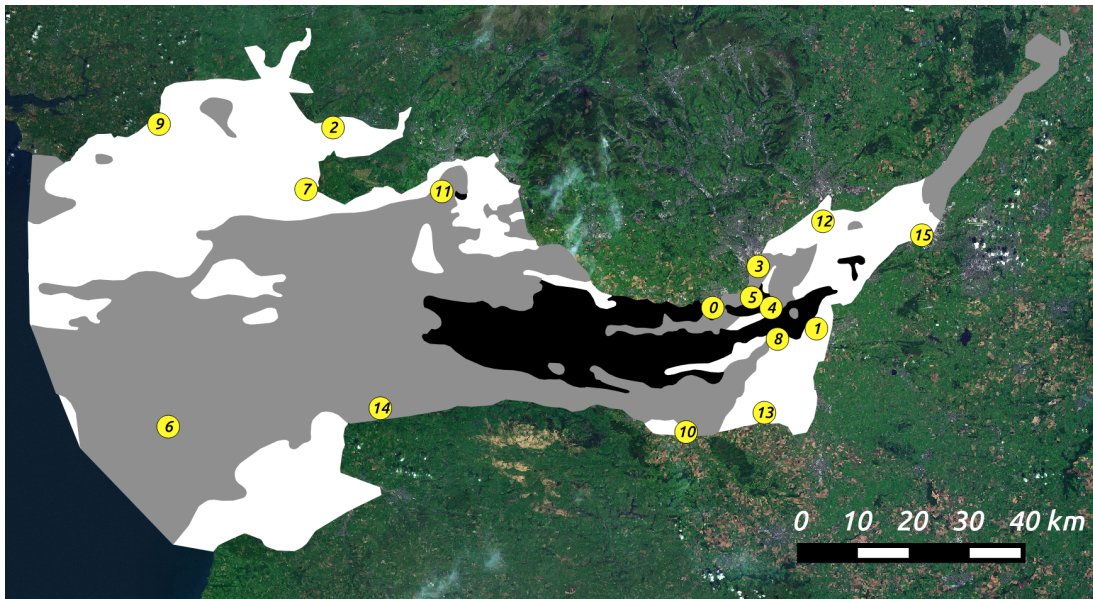


Figure 6.5: Bristol Channel model domain, showing locations of existing data, labelled by an index for identification purposes. Background colours show sediment type: rock (black), gravel (grey) and sand (white).

(National Oceanography Centre, personal communication 2018), plus a harmonic analysis of data from the five tide gauges recording free surface timeseries¹).

Here, the model domain is again divided according to the type of sediment found at the sea bed, as described in chapter 5. This results in a parameterisation of the Manning's n coefficient throughout the domain, based on three reference coefficients n_1, n_2, n_3 corresponding to rock, gravel and sand, respectively; figure 6.5 shows the distribution of these sediment types throughout the domain. The rest of the model setup is also as described in chapter 5.

This section performs a series of experiments for the optimal selection of observation locations, such that the parameter estimation problem can be solved as accurately as possible, using only three observation locations (since there are three unknowns). To test the optimally selected observation locations from the skewness and volume methods, the parameter estimation problem is then solved using the MCMC method, assimilating only data at the selected observation locations.

¹This study uses data from the National Tidal and Sea Level Facility, provided by the British Oceanographic Data Centre and funded by the Environment Agency.

6.4.2 Selection of locations from within existing data

Here, an optimal set of three observation locations is selected from within the existing set of observation data, using both the skewness and volume measures described above.

The first step in the implementation of either the skewness- or volume-based selection of observation locations is the proposal of candidate observation locations. These locations are simply the 16 locations shown in figure 6.5 where M2 amplitude data are available; the indices shown in the figure will be used to refer to each location. The second step is the listing of all possible combinations of these model outputs. This results in ${}^{16}C_3 = 560$ possible combinations of three model outputs, which are possible maps $\mathbf{Q}(\mathbf{n}) = (Q_1(\mathbf{n}), Q_2(\mathbf{n}), Q_3(\mathbf{n}))^T$.

The third step is the estimation of the Jacobian $J_{i,j} = \frac{\partial Q_i}{\partial n_j}$ for each possible map $\mathbf{Q}(\mathbf{n})$. Since the problem is nonlinear, this Jacobian $J(\mathbf{n})$ is estimated at 20 random samples from uniform prior distributions based on the results of chapter 5. The Jacobians are estimated by forward differences, i.e.

$$J_{i,j}(\mathbf{n}) \approx \frac{Q_i(\mathbf{n} + \Delta n \cdot \hat{\mathbf{e}}_j) - Q_i(\mathbf{n})}{\Delta n}, \quad (6.7)$$

where $\hat{\mathbf{e}}_j$ is the unit vector in the j -direction of the input parameter space, and the step size was taken as $\Delta n = 0.0004 \text{ s m}^{-1/3}$. The approximation of J for a given value of \mathbf{n} requires a total of four forward model runs, and the approximation of all 20 samples of the Jacobian therefore requires a total of 80 model runs. Since each model run produces outputs for all 16 locations, the same set of 80 model runs can be used to estimate the Jacobian for any combination of outputs.

For each candidate map \mathbf{Q} , both the skewness and volume measures are calculated, averaged over the 20 random samples, and used to rank the candidate maps. The optimal maps selected by the skewness and volume metrics are the locations [2, 4, 14] and [3, 11, 15], respectively. For both of these optimal maps, the selected observation locations are well spread out across the domain, and situated within or nearby a variety of sediment types. The values of the skewness and volume metrics for each of these maps, along with the median values among the 560 candidate maps, are summarised in table 6.1. This shows that, for this example, the optimal-skewness map performs well in the volume metric, and vice versa.

To test each optimal map, the parameter estimation problem is solved using the Bayesian inversion method summarised in section 6.2, assimilating only the observation data at the locations given by each optimal map. A Gaussian process emulator is trained for use as

Metric	Optimal-skewness map	Optimal-volume map	Median value
Skewness	1.8	4.3	14.6
Volume	95.0	221.1	10.1

Table 6.1: Summary of values for each metric, for the optimal maps from each metric, selected from within existing observation locations. Note that optimal skewness corresponds to the minimum value, while optimal volume corresponds to the maximum value.

a surrogate for the full numerical model within the Bayesian inversion algorithm; this is as described in section 5.3.2.

For each optimal map, a ‘synthetic’ experiment is first performed. For this, the forward model is run using prescribed friction parameters $\mathbf{n} = (0.036, 0.027, 0.022)^T$, and these model outputs used as ‘observation’ data. Within the Bayesian inversion algorithm, the MCMC algorithm is run for 10^6 samples, with the first $2 \cdot 10^5$ discarded as a burn-in period, and the model-observation variance σ^2 is fixed at a value of 0.0025 m^2 , to represent observation uncertainty of 5 cm. The prior distributions of the input parameters are taken as uniform in the range $[0.01, 0.05]$. After validation using this synthetic experiment, the optimal maps are also tested using real observation data, where for simplicity the variance σ^2 is again fixed at 0.0025 m^2 . The results using each optimal map are described below.

Optimal skewness

The Bayesian inversion results using synthetic observation data at the locations given by the optimal-skewness map are shown in figure 6.6, where the black points indicate the ‘true’ synthetic values. The prescribed friction coefficients are recovered well, as summarised in table 6.2.

The equivalent result for the assimilation of real data is shown in figure 6.7, and the parameter estimates are summarised in table 6.3. This PDF appears very similar to the result from assimilating data at 11 locations, as shown in figure 5.10. This shows that the full set of observation data contains a large amount of redundant information, and the careful selection of a smaller number of observation data locations can achieve similar results. Note that the high covariance in the posterior PDFs between the estimated coefficients for rock and gravel, which is visible in figures 6.6 and 6.7, was also present when all available data was assimilated, in chapter 5.

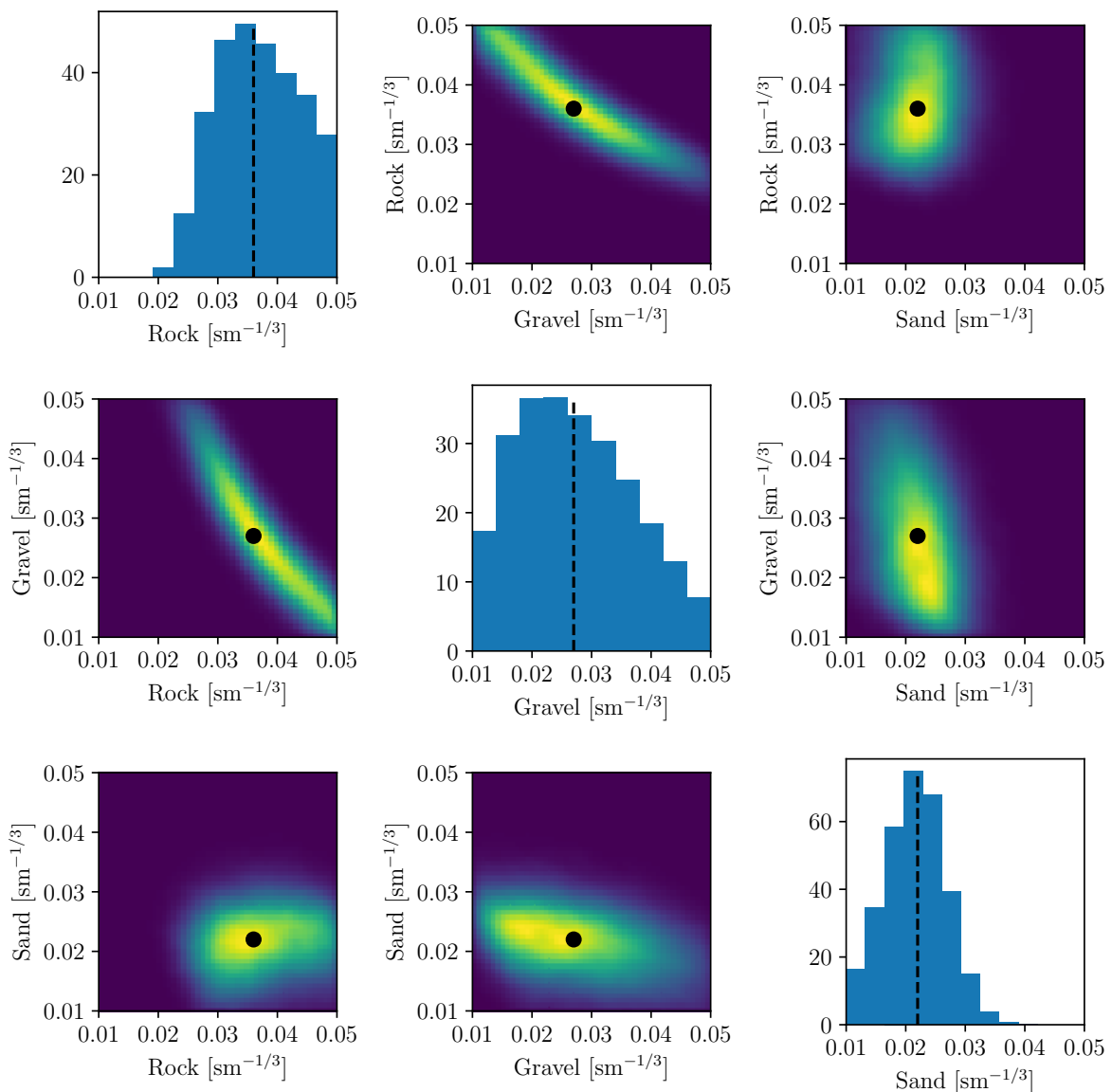


Figure 6.6: Posterior PDF from the assimilation of synthetic data at the locations specified by the optimal-skewness map, selected from within existing observations. The prescribed friction coefficients (shown as black points/lines) are well recovered.

Map	n_1	n_2	n_3
True value	0.036	0.027	0.022
Optimal skewness	0.037 ± 0.007	0.027 ± 0.010	0.022 ± 0.005
Optimal volume	0.037 ± 0.007	0.027 ± 0.009	0.022 ± 0.003

Table 6.2: Summary of estimated parameters for the synthetic experiment, using optimal maps selected from within existing observation locations. Units: $\text{sm}^{-1/3}$.

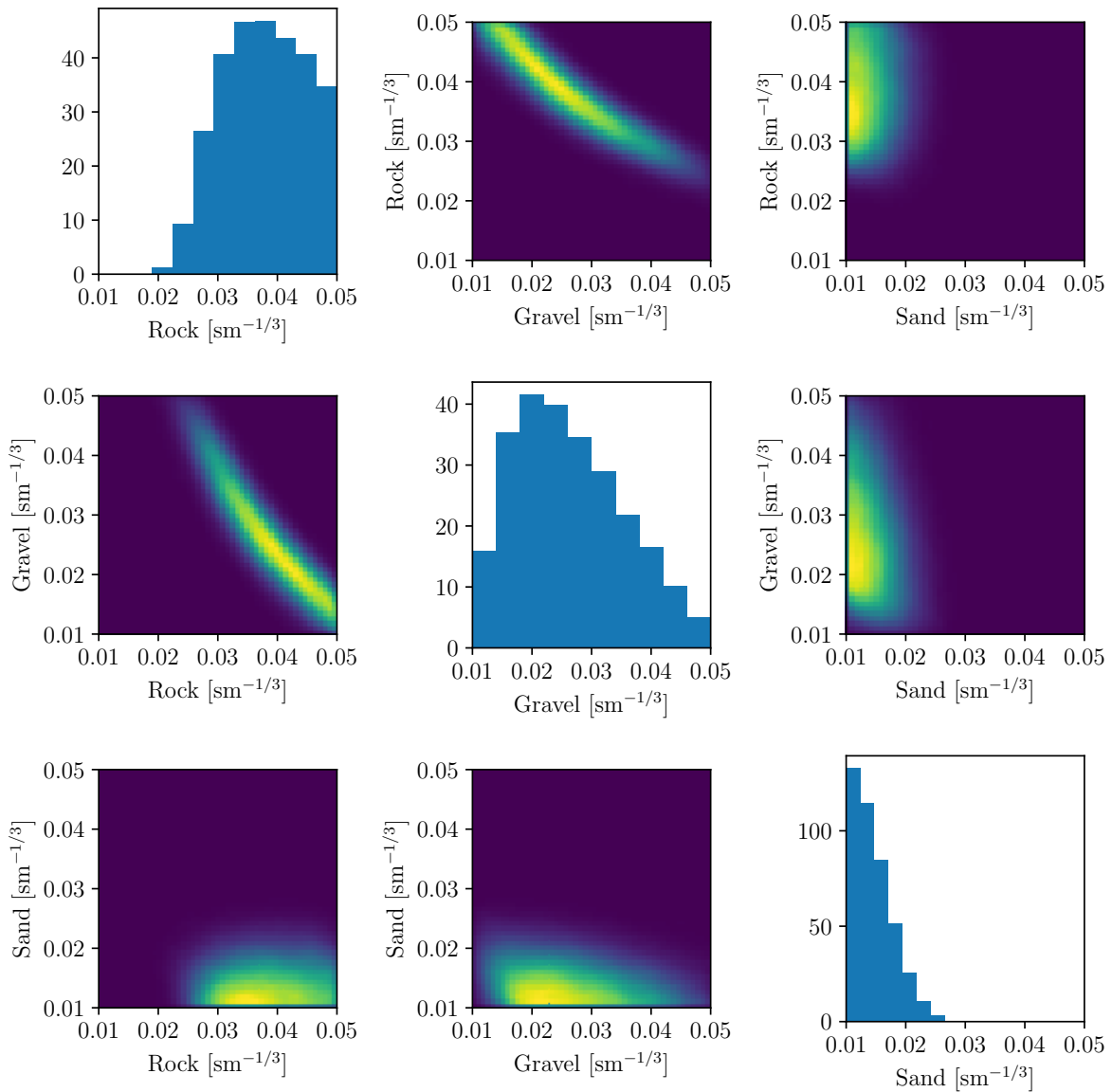


Figure 6.7: Posterior PDF from the assimilation of real data at the locations specified by the optimal-skewness map, selected from within existing observations.

Map	n_1	n_2	n_3
Optimal skewness	0.038 ± 0.007	0.027 ± 0.009	0.015 ± 0.003
Optimal volume	0.039 ± 0.007	0.027 ± 0.009	0.015 ± 0.003

Table 6.3: Summary of estimated parameters for the assimilation of real data, using optimal maps selected from within observation locations. Units: $\text{s m}^{-1/3}$.

Optimal volume

The posterior PDF using the optimal-volume map for the assimilation of synthetic data is shown in figure 6.8, and the prescribed friction values are well recovered, as summarised in table 6.2. The greatest difference between the posterior PDFs from the optimal-skewness and optimal-volume cases is the reduced variance of the estimated coefficient for sand resulting from the optimal-volume method. The corresponding result from the assimilation of real data is shown in figure 6.9, with results summarised in table 6.3. The results from the use of the optimal-volume map are consistent with those from the optimal-skewness map. Again, the use of data from only three carefully selected locations achieves a result which is comparable with the assimilation of a much larger set of data (see results from chapter 5, figure 5.10), due to the redundant information contained in the full dataset.

Both the skewness and volume metrics have therefore been found to perform well at selecting a subset of observation data which removes redundant information, and results in well-conditioned inverse problems. The good performance of both maps in the assimilation of synthetic data appears to be an indicator that the maps also work well for the assimilation of real data. Throughout the rest of this chapter, only synthetic experiments are performed, since new observation locations are proposed where real observation data is not available.

6.4.3 Proposal of new observation locations

The aim of this section is to use the skewness- and volume-based metrics to propose new locations within the Bristol Channel model domain at which observations would provide improved constraints on the unknown Manning coefficients compared to existing observations. The first step is to propose candidate locations for new observations; these are proposed based on a uniform square 10 km grid, and are shown in figure 6.10 in addition to the existing locations. There are a total of 82 locations, resulting in a total of ${}^{82}C_3 = 88,560$ possible maps \mathbf{Q} .

Following the same framework as in section 6.4.2, the skewness and volume metrics are utilised to select optimal combinations of the proposed observation locations, with which to perform parameter estimation for the three unknown Manning coefficients.

The set of locations selected by minimising the skewness are [27, 43, 69], while the maximum-volume locations are [58, 77, 81]. The skewness and volume metrics for each of these sets of locations are summarised in table 6.4. The optimal-volume map performs

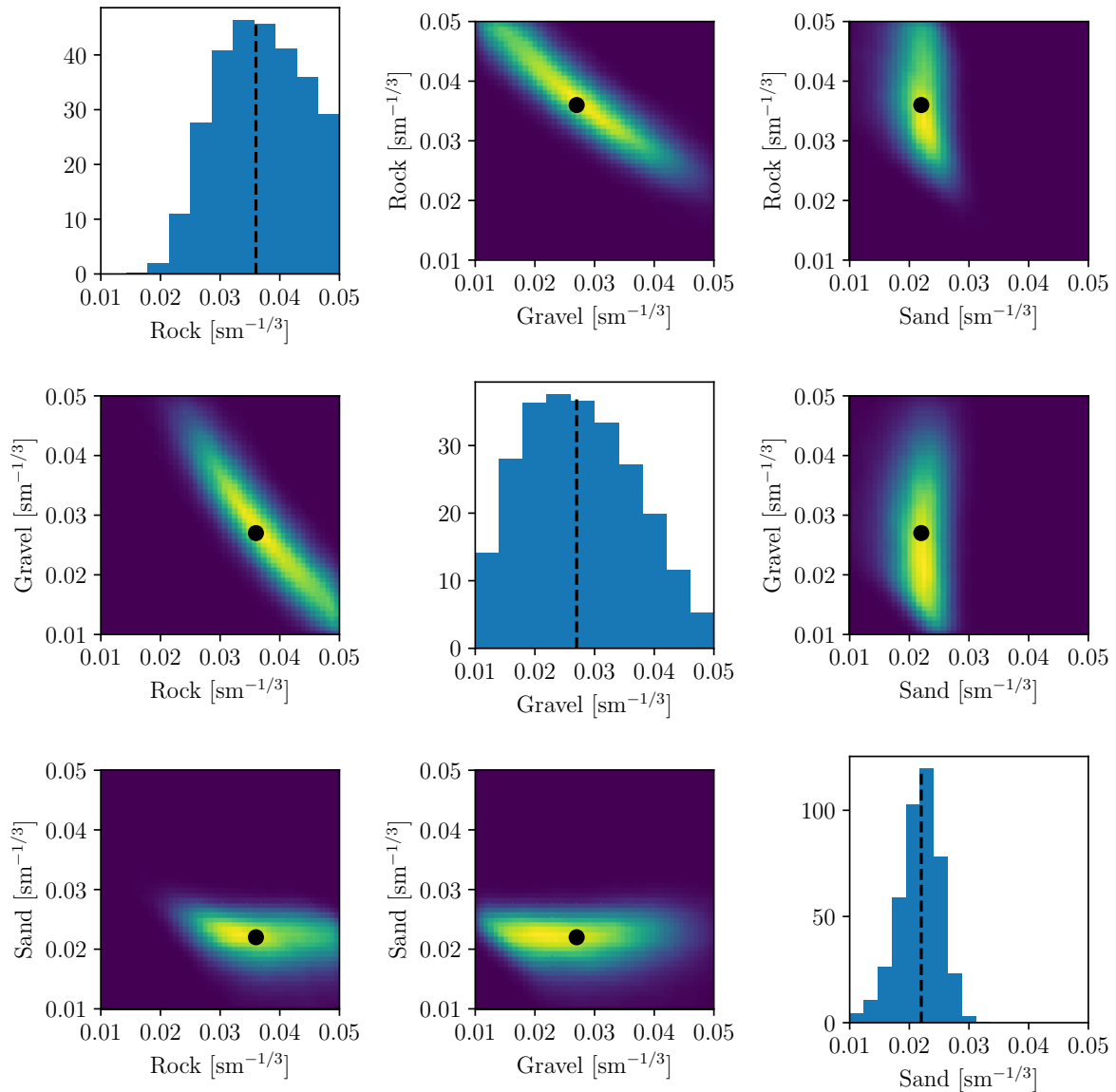


Figure 6.8: Posterior PDF from the assimilation of synthetic data at the locations specified by the optimal-volume map, selected from within existing observations. The prescribed friction coefficients (shown as black points/lines) are well recovered.

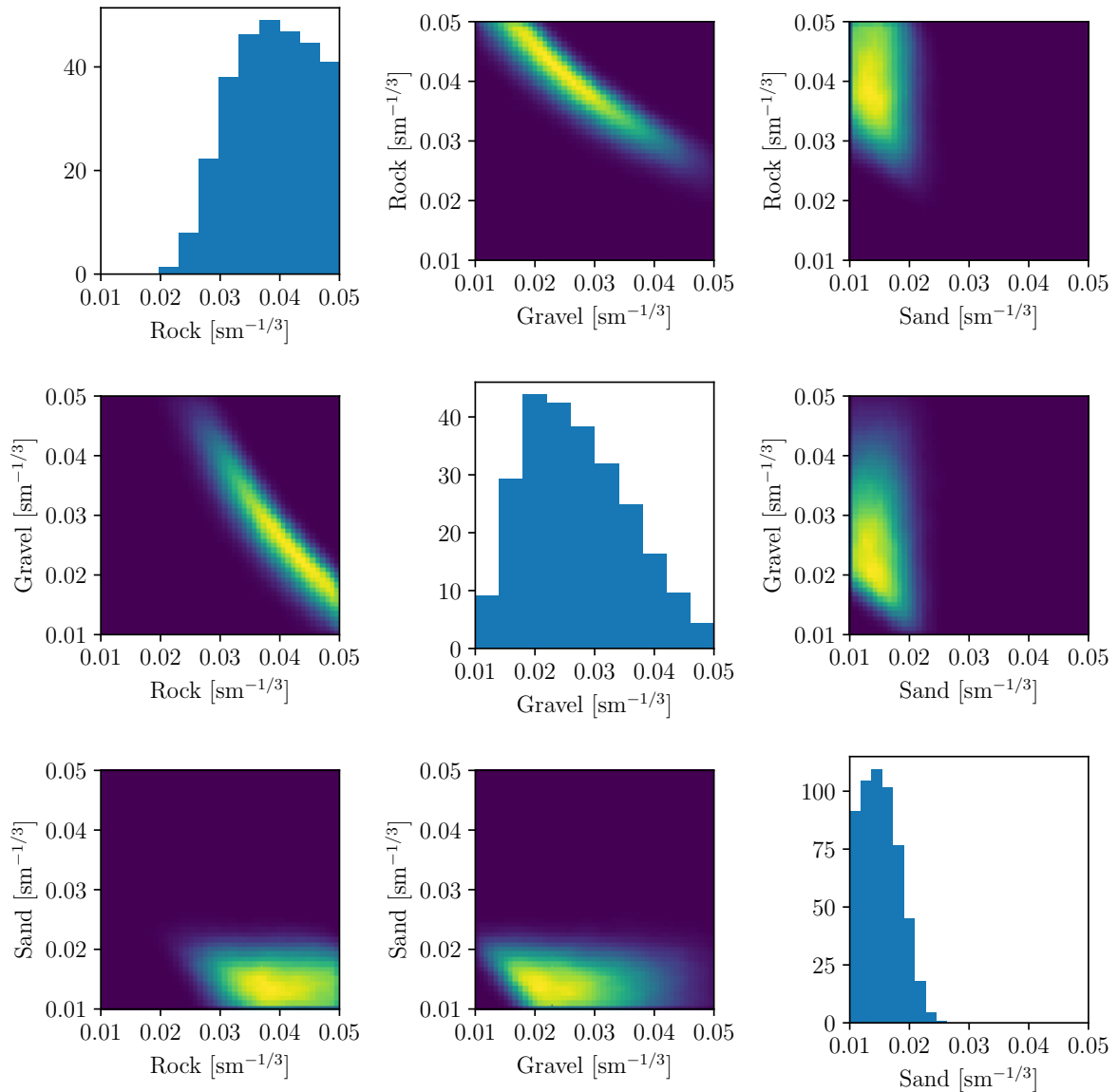


Figure 6.9: Posterior PDF from the assimilation of real data at the locations specified by the optimal-volume map, selected from within existing observations.

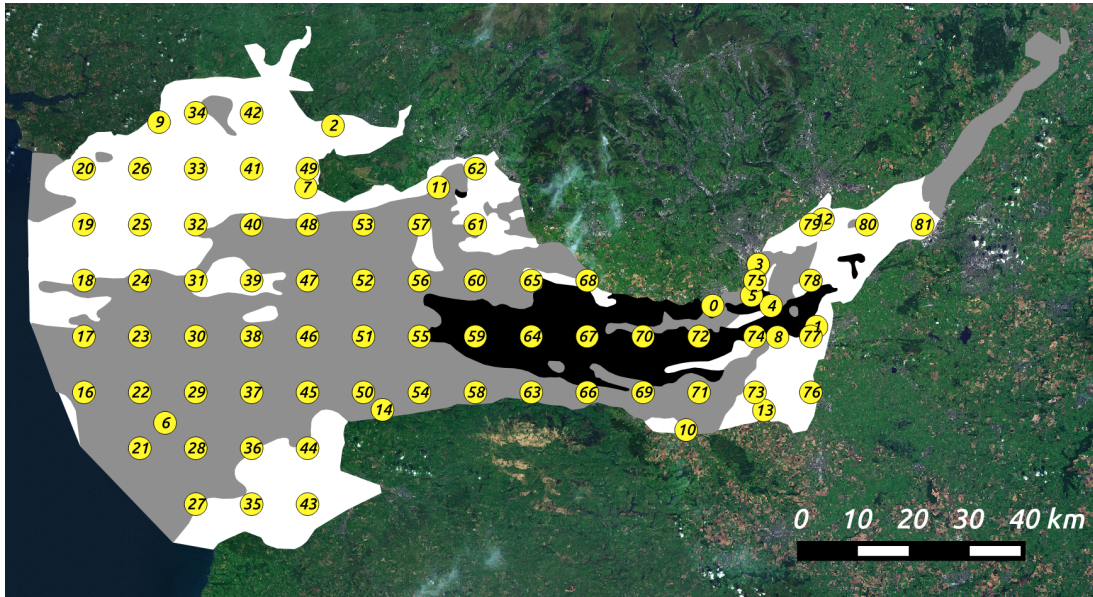


Figure 6.10: Existing (numbered 0–15) and proposed (16–81) observation locations.

Metric	Optimal-skewness map	Optimal-volume map	Median value
Skewness	1.5	2.6	8.7
Volume	1.4	349.6	1.2

Table 6.4: Summary of values for each metric, for the optimal maps from each metric, selected from the proposed observation locations.

well in the skewness metric, but the optimal-skewness map performs only slightly better in the volume metric than the median of the 88,560 candidate maps. This is because the locations selected by minimising the skewness exhibit low sensitivity magnitudes with respect to the unknown Manning coefficients; this has been discussed in section 6.3 as a drawback of the skewness approach.

To further exhibit the differences between the optimal maps selected by each metric, a synthetic experiment is performed, as described in section 6.4.2. The resulting posterior PDF from using the optimal-skewness observation locations is shown in figure 6.11, and the corresponding result using the optimal-volume locations is shown in figure 6.12, with the resulting parameter estimates summarised in table 6.5. The use of the optimal-skewness locations provides poor constraints on the unknown parameters, in particular the coefficient for sand. This is because the magnitudes of the sensitivities of these model outputs with respect to the model inputs are too small, compared with the uncertainty in the observations (which is assumed as $\sigma^2 = 0.0025 \text{ m}^2$). The optimal-volume locations, on the other hand, perform well.

However, even for the optimal-volume case, very little improvement in the estimated

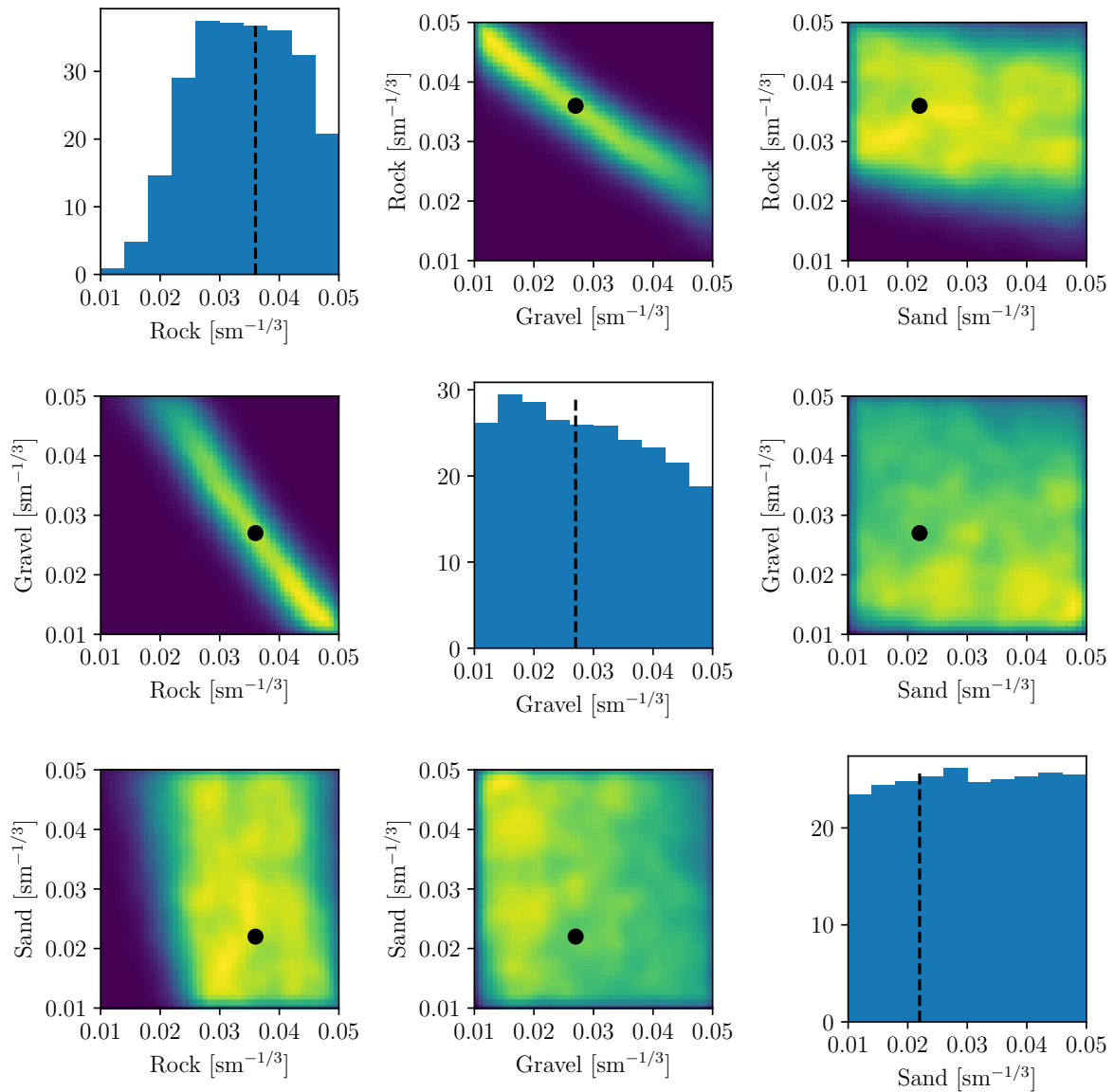


Figure 6.11: Posterior PDF from the assimilation of synthetic data at the locations specified by the optimal-skewness map, selected from the proposed observation locations. The prescribed friction coefficients (shown as black points/lines) are poorly recovered.

Map	n_1	n_2	n_3
True value	0.036	0.027	0.022
Optimal skewness	0.034 ± 0.008	0.029 ± 0.011	0.030 ± 0.011
Optimal volume	0.037 ± 0.007	0.027 ± 0.008	0.022 ± 0.003

Table 6.5: Summary of estimated parameters for the synthetic experiment, using optimal maps selected from within proposed observation locations. Units: $\text{sm}^{-1/3}$.

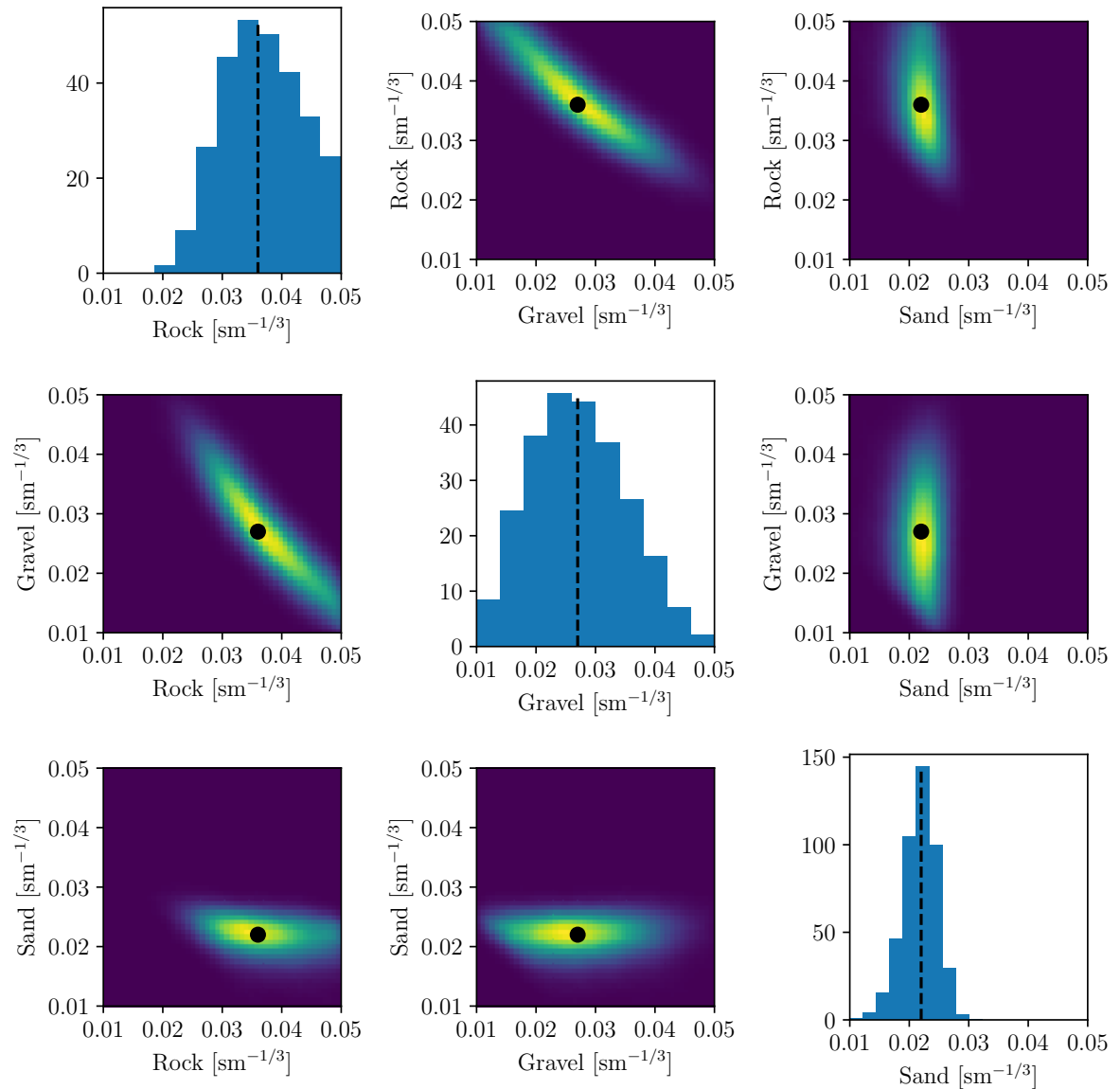


Figure 6.12: Posterior PDF from the assimilation of synthetic data at the locations specified by the optimal-volume map, selected from the proposed observation locations. The prescribed friction coefficients (shown as black points/lines) are well recovered.

parameters is achieved, compared with the optimal selection of locations from within the existing observation dataset (comparing tables 6.2 and 6.5). This suggests that, within the assumed observation uncertainties, the selected input parameters cannot be constrained more tightly by any of the observations proposed here. By comparing results from within the existing observation data (figure 6.8) and from proposed observation data (figure 6.12), it is also found that the high covariance between the rock and gravel coefficients in the posterior PDF cannot be overcome by the proposed new observations. This information can be used to feed back into the design of the overall experiment, since these results imply that the friction coefficients resulting from the selected grouping of sediment types are difficult to independently constrain using observations of the kind considered here.

As an additional experiment, the optimal-skewness map can be improved by first filtering out locations which exhibit low sensitivity to the input parameters (as in the approach taken by Graham et al. (2017)). These locations are mostly found near the ocean boundary, since in these regions the modelled harmonic amplitudes are dominated by the tidal boundary condition. For this experiment, the criterion for inclusion of a proposed model output $Q(\mathbf{n})$ in the set of candidate locations is

$$\text{mean} \left(\left| \frac{\partial Q}{\partial \mathbf{n}} \right| \right) > 5 \text{ m}^{4/3} \text{ s}^{-1}, \quad (6.8)$$

where the mean is over the 20 random samples of the input parameters. This filtering out of low-sensitivity locations results in a reduction from 82 to 40 candidate locations. The optimal-skewness map using these filtered locations is given by [2, 54, 69]. Using these observation locations within the synthetic experiment produces the posterior PDF shown in figure 6.13, and the parameter estimates are $(n_1, n_2, n_3) = (0.036 \pm 0.007, 0.026 \pm 0.009, 0.022 \pm 0.005) \text{ sm}^{-1/3}$. The performance of this map is therefore a significant improvement on the unfiltered optimal-skewness map, although it still does not perform as well as the optimal-volume map, which did not require any filtering. This optimal-skewness map could be improved further by fine-tuning the filtering, but this is not attempted here.

6.4.4 Characterising ‘good’ observation locations

The frameworks used within this chapter for the selection of optimal observation locations are based on ranking combinations of locations, rather than identifying individual locations as ‘good’ or otherwise. Nevertheless, it is possible to identify general characteristics of a ‘good’ observation location; two such patterns are described here.

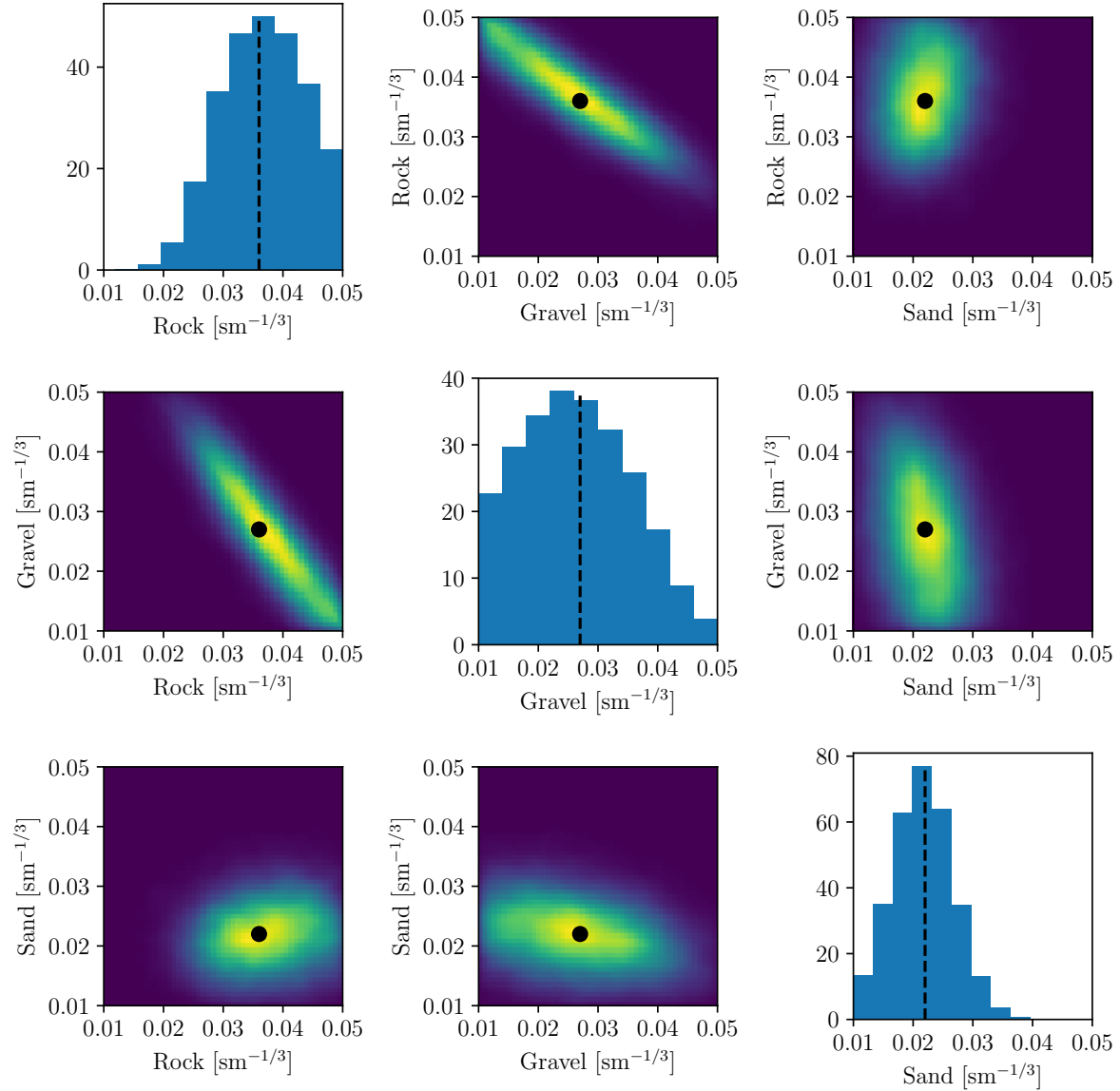


Figure 6.13: Posterior PDF from the assimilation of synthetic data at the locations specified by the optimal-skewness map, selected from a filtered subset of the proposed observation locations. The prescribed friction coefficients (shown as black points/lines) are well recovered.

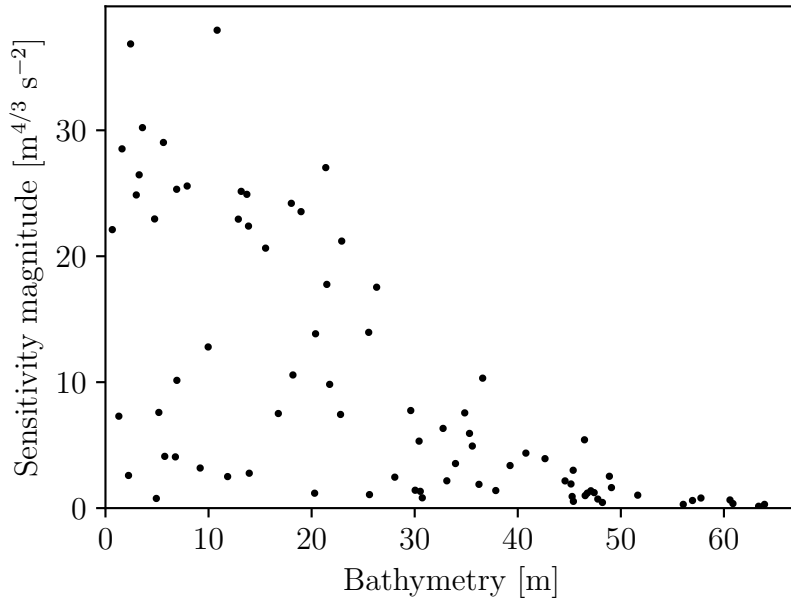


Figure 6.14: A negative correlation is observed between sensitivity magnitude and bathymetry.

Firstly, it is possible to identify characteristics which lead to large sensitivity magnitudes, which are favoured by the optimal-volume method. Within this case study, a number of hypothetical M2 amplitude observation locations are proposed, as shown in figure 6.10. Denoting the observation at each location by Q , a negative correlation is observed between the magnitude of the sensitivity vector, $|\frac{\partial Q}{\partial n}|$, and the bathymetry at the observation location. This correlation is shown in figure 6.14. This shows that observations made in shallow water tend to exhibit stronger sensitivity to the unknown friction parameters than observations in deep water. This is to be expected, since in the governing equations (3.15), the bottom stress term is inversely proportional to the water depth H , and this term is therefore more influential in shallow water. This pattern may be applicable more widely than this case study alone.

It is also possible to observe patterns in the sensitivities to individual model inputs. Here, a hypothesis is that an observation Q at a location within a region of sediment type i exhibits stronger sensitivity to the parameter n_i , i.e. that an observation made within a sand region is more sensitive to the Manning coefficient corresponding to sand, etc. This hypothesis is tested using the proposed observation locations of figure 6.10. Within this set of 82 proposed locations, there are 8 locations in rock regions, 41 in gravel regions and 33 in sand regions. Figure 6.15 shows histograms of $\frac{\partial Q}{\partial n_1}$, $\frac{\partial Q}{\partial n_2}$ and $\frac{\partial Q}{\partial n_3}$ for the 8 locations on the rock sediment type. While the conclusions are limited by the small number of samples, it is found that, in general, observations made in rock regions exhibit stronger

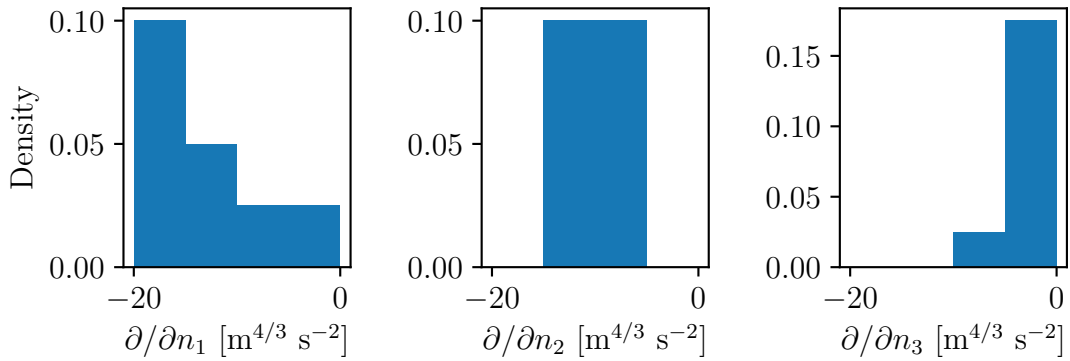


Figure 6.15: Distributions of $\frac{\partial Q}{\partial n_1}$, $\frac{\partial Q}{\partial n_2}$ and $\frac{\partial Q}{\partial n_3}$ for observations Q made in rock regions. The greatest sensitivity magnitudes are shown with respect to n_1 , which is the Manning coefficient corresponding to rock.

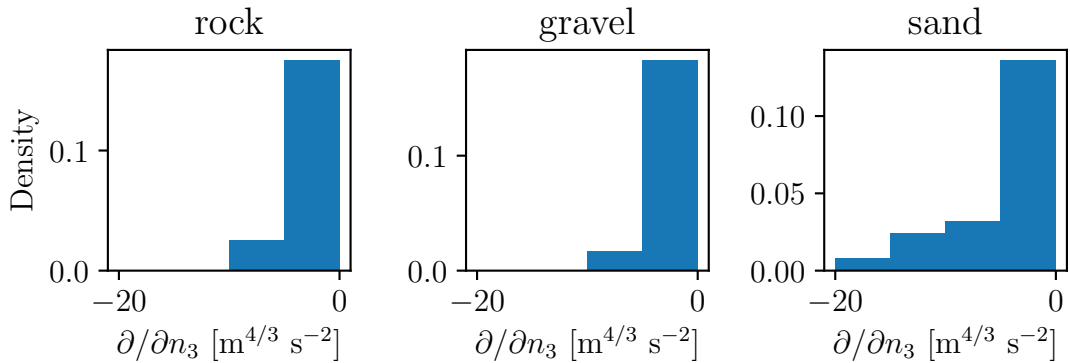


Figure 6.16: Distributions of sensitivity to the sand coefficient (n_3) for each of the sets of observation points (rock locations, gravel locations, sand locations). The greatest sensitivities to the sand coefficient are exhibited by observations made in sand regions.

sensitivities to n_1 (corresponding to rock) than to either of the other parameters. A second pattern is demonstrated in figure 6.16, which shows histograms of the sensitivity to the sand coefficient (n_3) for each of the sets of observation points (rock locations, gravel locations, sand locations). It is observed that the strongest sensitivities to the sand Manning coefficient (n_3) are exhibited by the observations made in sand regions. While only a small number of samples have been considered, these patterns lend support to the hypothesis that observations exhibit strong sensitivity to the local Manning coefficient. A ‘good’ combination of observation locations may therefore consist of observations from within each sediment region.

6.5 Application to the Maldives

In this section, the optimal-volume method is used to propose locations for new observations in the Maldives, motivated by constraining unknown friction parameters in a tidal model of the North Malé Atoll. This constitutes preliminary work, demonstrating the application of these methods to an atoll environment.

6.5.1 Background & model setup

A recent development in tidal modelling of the Maldives archipelago has been provided by the creation of a new bathymetric dataset, merging data from a variety of sources (Rasheed et al., 2020). However, validation and calibration of tidal models around the Maldives is limited by a severe lack of observation data. This section focuses on tidal modelling of the North Malé Atoll. There is only one tide gauge within this atoll, and the thorough validation or calibration of a tidal model of this region is therefore not possible with current observation datasets.

The atoll rim is characterised by relatively deep channels between coral reefs and islands, with the shallow (~ 50 m deep) interior of the atoll featuring numerous reefs, islands and lagoons. With these features well captured by the new bathymetric dataset (Rasheed et al., 2020) (see figure 6.17), the next challenge to accurate modelling of the region is the adequate representation of the spatial variation in the bottom friction, e.g. due to the presence of corals on the sea bed. The motivation of this work is therefore the calibration of a tidal model with respect to the bottom friction coefficient, with the aim of identifying locations at which new observations would provide the best constraints on unknown friction coefficients. Since the modelled region is relatively small (the atoll spans approximately 60 km in the north-south direction and 40 km in the east-west direction), the spatial variation in the sea surface elevation is small, and observations of sea surface height are therefore unlikely to be helpful in a model calibration procedure.

The focus is instead on measurements of tidal currents. In particular, the proposed observations are the peak velocity magnitudes within the flood phase of a specified tidal cycle. Since the currents around the atoll rarely exceed 1 m s^{-1} , the use of peak velocities ensures that the effect of any observation uncertainty is minimised. Furthermore, considering a field which varies only spatially ensures consistency with the Bristol Channel case study, and avoids additional complexity in the optimal observation framework. Within this preliminary study, the time window within which the maximum velocity is taken is 0530 to 1200 UTC on 20th September 2020.

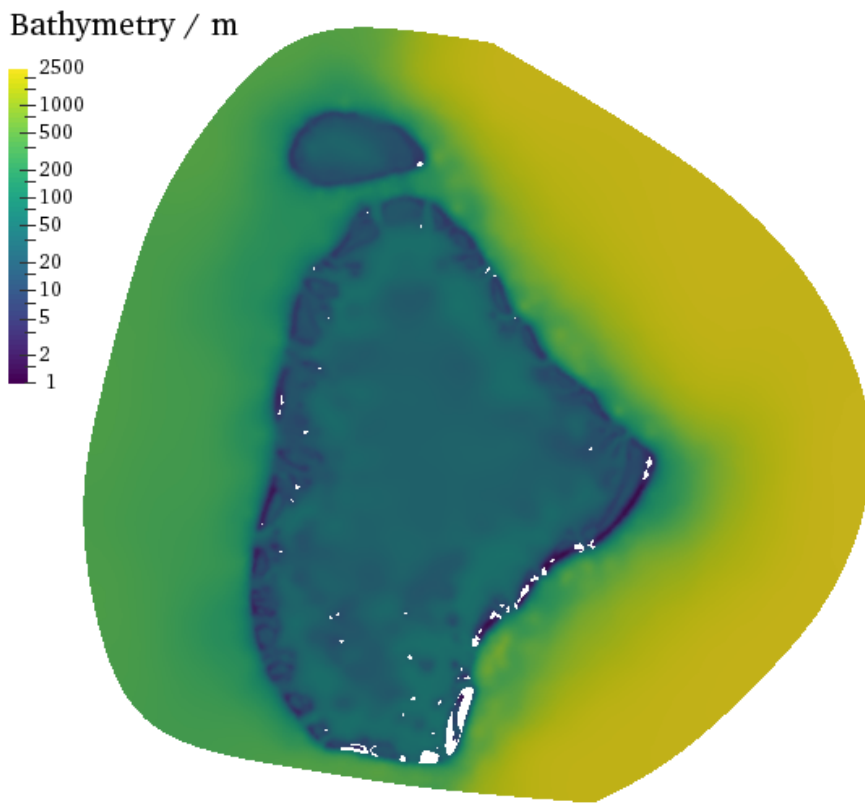


Figure 6.17: Bathymetry of the North Malé Atoll region.

Tidal modelling is undertaken within this section using Thetis. The mesh used for all simulations is shown in figure 6.18, and was generated on a UTM43 coordinate projection, with mesh resolution varying from 150 m around the atoll rim to 3 km in open regions, resulting in a total of 115,938 elements. The timestep is $\Delta t = 100$ s, with implicitness $\theta = 1$ (selected for numerical stability). A Dirichlet tidal boundary condition is applied on the ocean boundaries, generated from the eight leading order harmonic constituents from the TPXO database (Egbert and Erofeeva, 2002).

Each model run in this section first starts with a 10-day spin-up using a spatially uniform Manning coefficient $n = 0.02 \text{ s m}^{-1/3}$, which ends at 0000 UTC on 18th September 2020. Using each spatially varying friction parameter, the model is run for a further time of approximately two days before the peak-velocity window commences, which acts as additional spin-up to remove the dependence of the peak velocities on the spin-up friction parameters. An example of the spatially varying peak velocity magnitude is shown in figure 6.19.

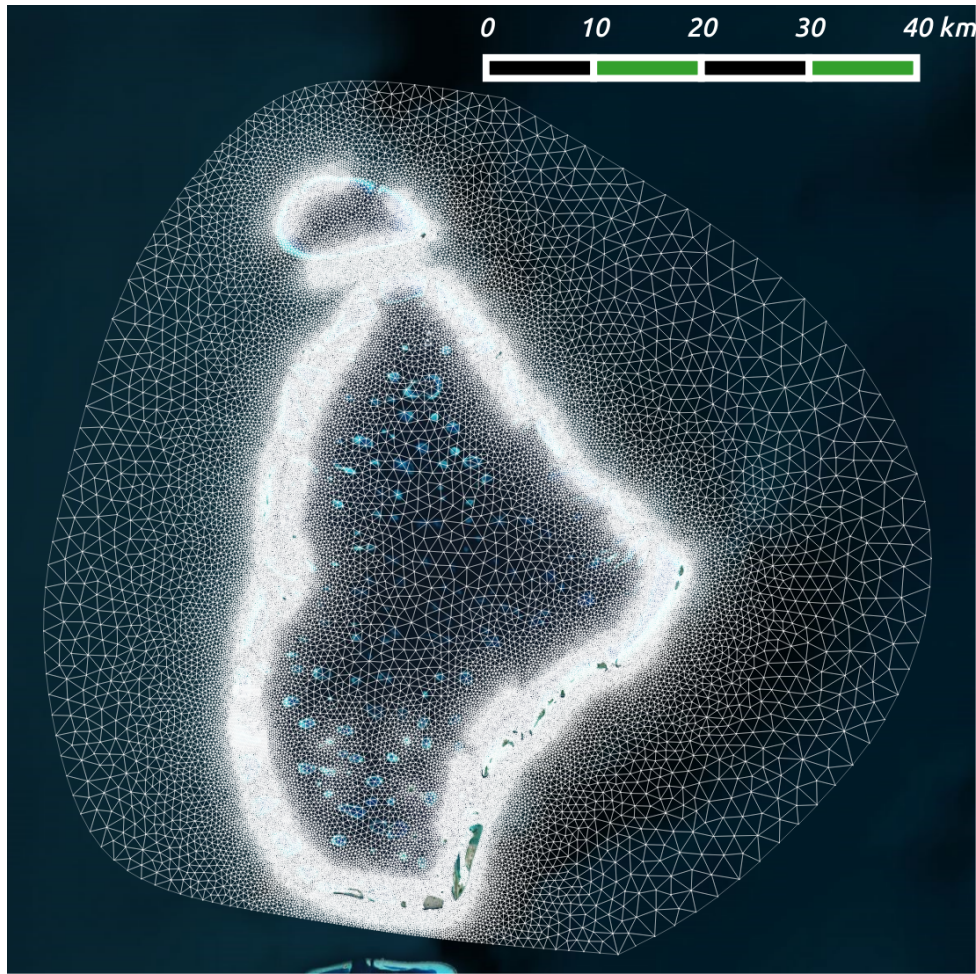


Figure 6.18: Mesh used for tidal modelling of the North Malé Atoll.

6.5.2 Selection of bottom friction parameter space

The parameterisation of the spatial variation of the bottom friction coefficient for this application proceeds in a similar manner to that of the Bristol Channel case study. It is expected that a larger friction coefficient is required to capture the effects of corals present on the sea floor. Since no dataset is available which maps the distribution of corals within the model domain, here it is assumed that corals are exclusively present in shallow regions where the depth is less than 12 m; the 12 m contour is in reasonably good visual agreement with reefs visible in satellite images. Different values for the Manning coefficient are applied in the $h > 12$ m and $h < 12$ m regions. A third Manning coefficient is applied outside of the atoll, where the bathymetry rapidly falls away; this threshold is

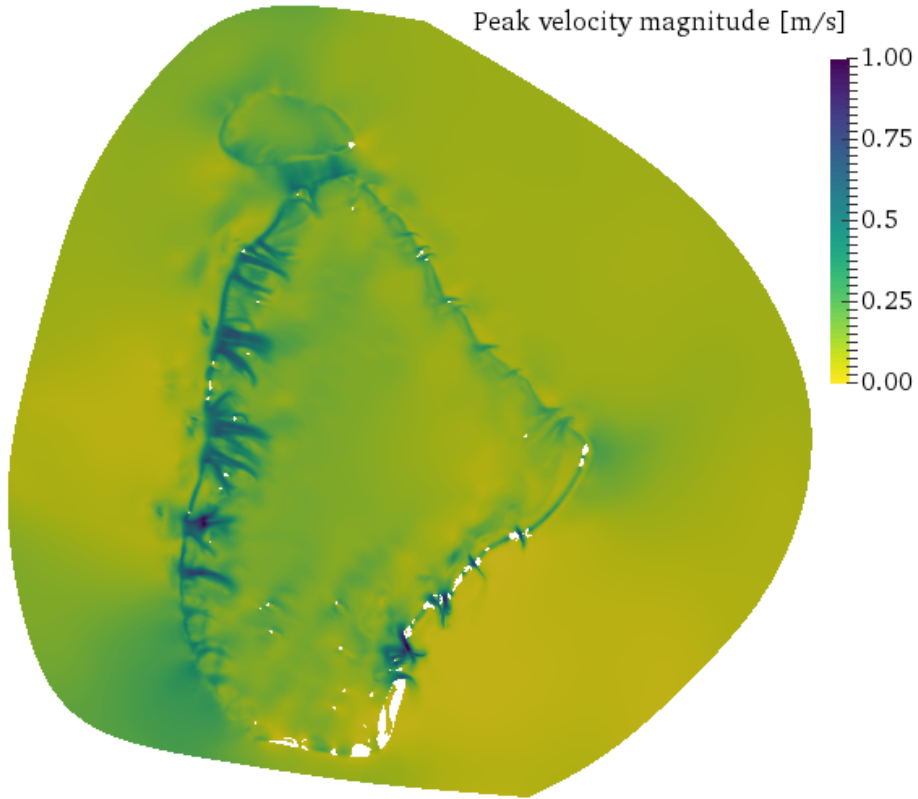


Figure 6.19: Example of the peak velocity magnitude throughout the model domain. The greatest velocity magnitudes are found within the channels around the atoll rim.

selected as the 100 m contour. The Manning coefficient is thus given by

$$n = \begin{cases} n_1 & \text{for } h > 100 \text{ m}, \\ n_2 & \text{for } 100 \text{ m} > h > 12 \text{ m}, \\ n_3 & \text{for } h < 12 \text{ m}. \end{cases} \quad (6.9)$$

The spatial distribution of these three friction parameters within the model domain is shown in figure 6.20.

6.5.3 Selection of optimal observation sites

Initially, the peak velocity magnitudes at any of the 57,914 mesh nodes are considered as candidate observation locations; each of these model outputs can be denoted $Q(\mathbf{n})$, where $\mathbf{n} = (n_1, n_2, n_3)^T$. The derivatives of these outputs with respect to the input parameters, $\frac{\partial Q}{\partial \mathbf{n}}$, are approximated by forward differences, similarly to equation (6.7).

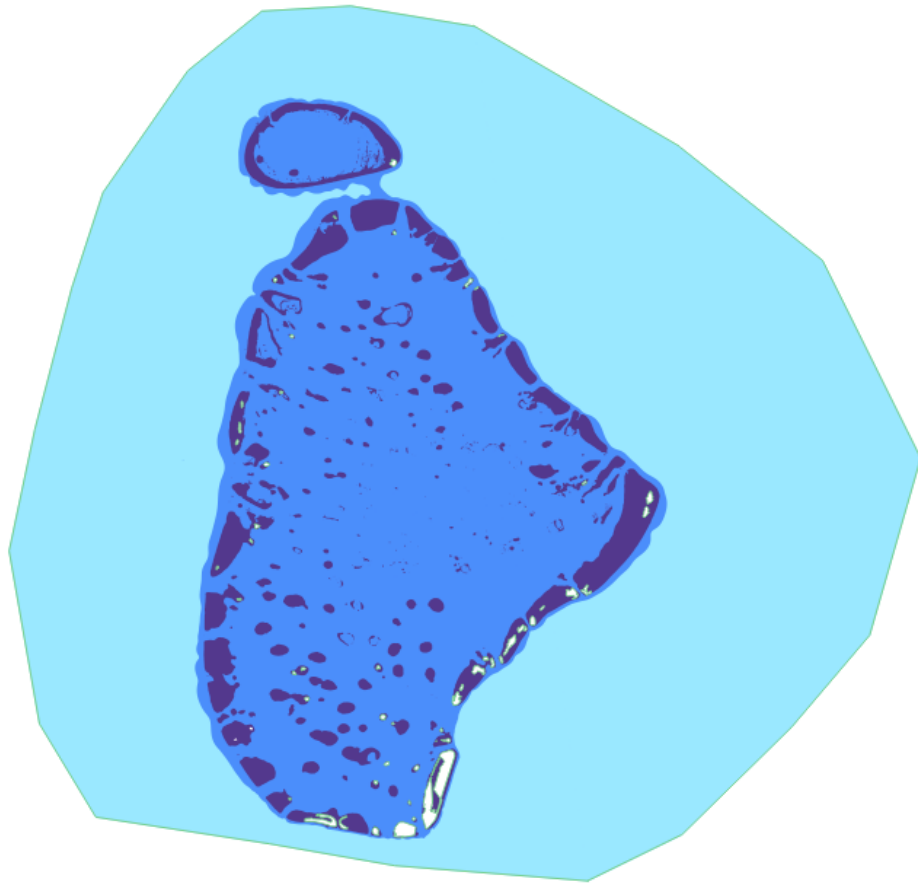


Figure 6.20: Distribution of friction coefficients within the North Malé Atoll model domain. Light blue: Deep water, n_1 . Darker blue: atoll interior, n_2 . Purple: coral reefs, n_3 .

Since the problem is nonlinear, the approximation of these derivatives is performed at 15 samples from the input parameter space, selected using Latin hypercube sampling from uniform prior distributions

$$\begin{aligned} n_1 &\sim U(0.01, 0.05), \\ n_2 &\sim U(0.01, 0.1), \\ n_3 &\sim U(0.02, 0.2). \end{aligned} \tag{6.10}$$

These parameter ranges are based on typical values for the Manning coefficient for coral (Rosman and Hench, 2011), and other sea floors (Arcement and Schneider, 1989), making minimal assumptions about the sediment present in the $12 \text{ m} < h < 100 \text{ m}$ region, corresponding to n_2 .

The resulting derivatives $\frac{\partial Q}{\partial \mathbf{n}}$ can be used to construct the Jacobian matrix

$$J_{i,j} = \frac{\partial Q_i}{\partial n_j} \quad (6.11)$$

for any vector of model outputs $\mathbf{Q} = (Q_1, Q_2, \dots)^T$, for use within the optimal-volume method for selecting combinations of model outputs.

Reduction of input parameter space

As a preliminary step, the typical magnitudes of the sensitivity to each friction parameter are investigated. While values for $\frac{\partial Q}{\partial n_2}$ and $\frac{\partial Q}{\partial n_3}$ are typically found to share similar magnitudes, $\frac{\partial Q}{\partial n_1}$ is much smaller. This implies that the deep-water ($h > 100$ m) Manning coefficient has very little influence on the model outputs. This is because the velocities outside of the atoll are small, and the dynamics in these regions are dominated by the boundary condition.

For the remaining analysis, the deep-water coefficient is therefore held fixed at $n_1 = 0.02 \text{ s m}^{-1/3}$, and observation locations are sought only to constrain the two most influential Manning coefficients, $\mathbf{n} = (n_2, n_3)^T$.

Candidate observation locations

The objective is to propose locations in order to constrain two unknown model inputs (n_2, n_3), and optimal combinations of two or three observation locations are sought for this purpose. Using every mesh node as a candidate observation location, this results in a total of ${}^{57914}C_2$ and ${}^{57914}C_3$ possible model output combinations in the two- and three-output cases, respectively. This exceeds 10^{13} in the three-output case, and evaluating the volume metric for all candidate output combinations is therefore not feasible. For this reason, the mesh nodes are first filtered. The model output Q at a given mesh node is included if it satisfies three criteria:

1. $\text{mean}(Q) > 0.5 \text{ m s}^{-1}$, where the mean is over the 15 input parameter samples
2. $\text{mean}\left(\left|\frac{\partial Q}{\partial \mathbf{n}}\right|\right) > 5 \text{ m}^{4/3} \text{ s}^{-2}$, where the mean is over the 15 input parameter samples
3. The mesh node is no closer than 800 m to any other node already included in the list of candidate locations

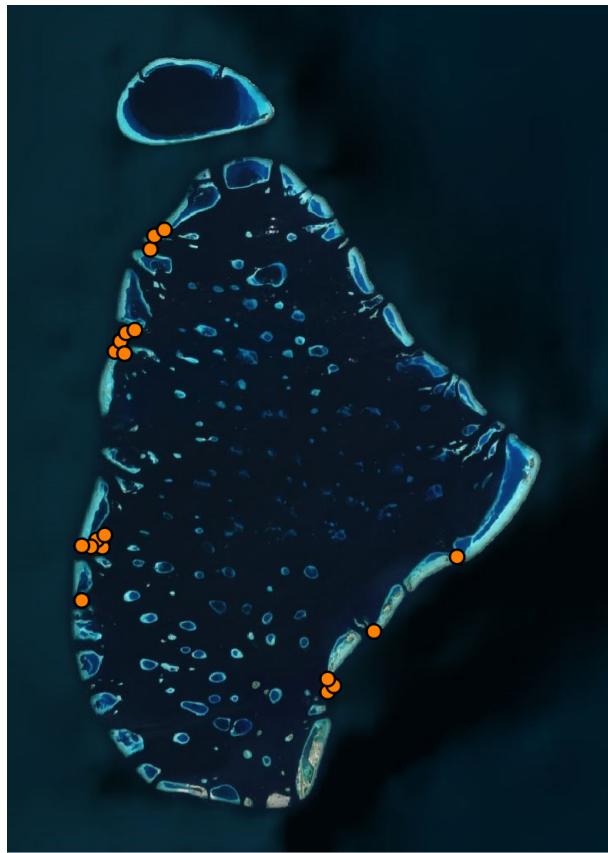


Figure 6.21: Candidate observation locations within the North Malé Atoll domain. Most locations are within channels in the atoll rim, where velocities are greatest.

The application of these criteria results in a total of 19 candidate locations, whose locations are shown in figure 6.21. Most of the locations are found within or nearby the channels between reefs and islands on the atoll rim, where the observed velocities are greatest. The selection of 19 candidate locations results in a total of $^{19}C_2 = 171$ and $^{19}C_3 = 969$ possible maps **Q** for the two- and three-location cases, respectively.

Optimal observation sites

The optimal-volume method for selecting combinations of observation locations, as described in section 6.3.2 and utilised for the Bristol Channel case study, selects the locations shown in figures 6.22 and 6.23 for the two- and three-location cases, respectively. In the two-location case, the pair of selected locations are very close. In the three-location case, two locations are in close proximity, with the third location on the opposite side of the atoll.

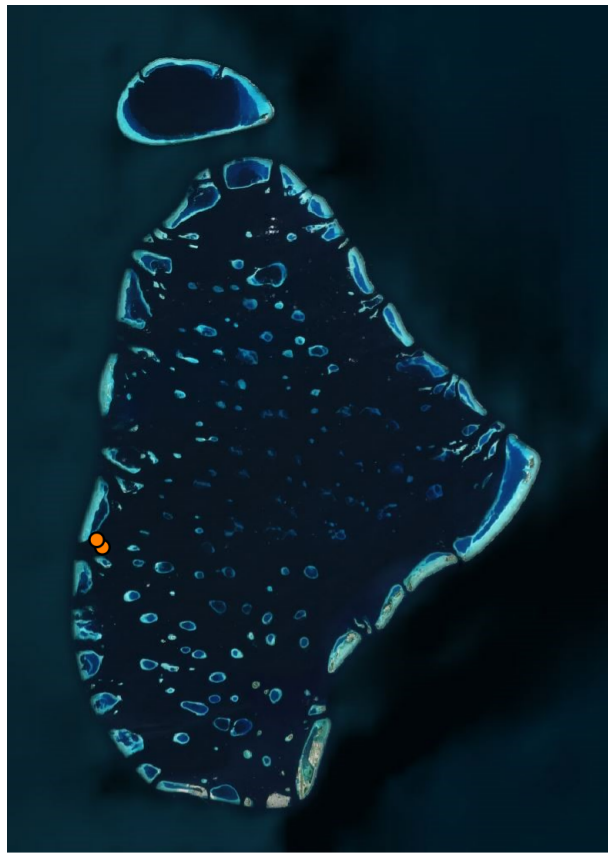


Figure 6.22: Optimal set of two observation locations within the North Malé Atoll domain, selected via the maximum-volume method.

6.5.4 Assimilation test: synthetic data

Similar to the Bristol Channel case study, the parameter estimation problem can be solved using Bayesian inversion, via a Markov Chain Monte Carlo (MCMC) algorithm. This is facilitated by the use of a Gaussian process emulator (GPE) in place of the full numerical model. A set of training runs is performed, using 40 samples from the input parameter space, sampled from the uniform priors of equation (6.10) using Latin hypercube sampling. Peak velocities are output at all mesh nodes by each sample, so that GPEs using any combination of observation locations can be trained from the same set of 40 model runs. The MCMC algorithm has been described in section 6.3, and already applied within this chapter for the Bristol Channel case study.

Here, a series of ‘synthetic’ experiments are performed, using outputs from full numerical model runs as ‘observation’ data. Four random samples from the input parameter prior distributions are used to generate four such synthetic experiments. In all cases, the MCMC algorithm is run using 10^6 samples, discarding the first $2 \cdot 10^5$ as a burn-in period, and there is an assumed observation uncertainty of $\sigma = 0.01 \text{ m s}^{-1}$.

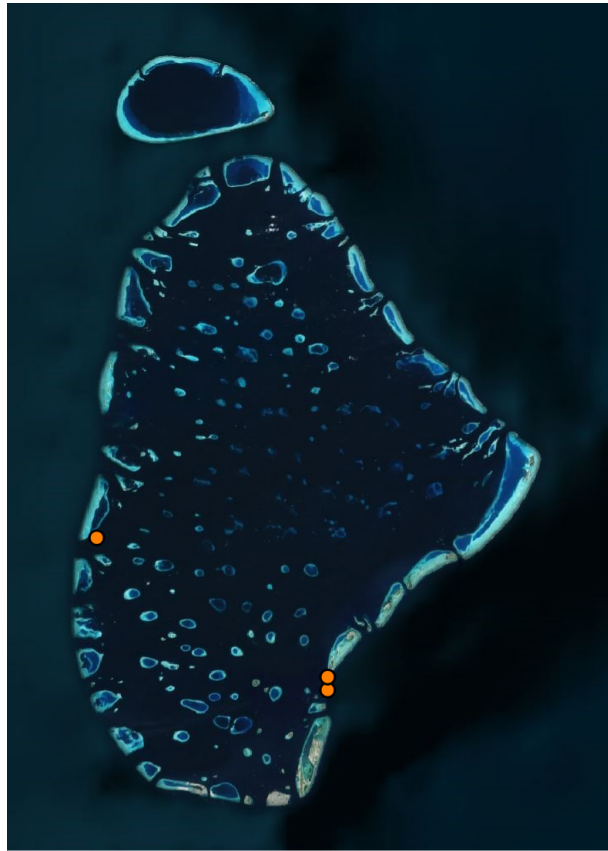


Figure 6.23: Optimal set of three observation locations within the North Malé Atoll domain, selected via the maximum-volume method.

The posterior PDFs from the Bayesian inversion algorithm are shown in figure 6.24 for the two-location case, with the black point indicating the true friction coefficients used to generate the synthetic observation data. In all four cases, n_2 is very well recovered, but n_3 is poorly constrained by the observations.

The Bayesian inversion is more successful in the three-location case, as shown by the posterior PDFs of figure 6.25. For three of the four synthetic experiments, the use of three observations achieves a similar constraint on n_2 to the two-location case, but provides a much tighter constraint on n_3 . The optimal-volume method has automatically selected locations which provide a tighter constraint on the less well-constrained input parameter. Note that this would not have been possible using the optimal-skewness method, due to its restriction that the number of outputs cannot exceed the number of inputs.

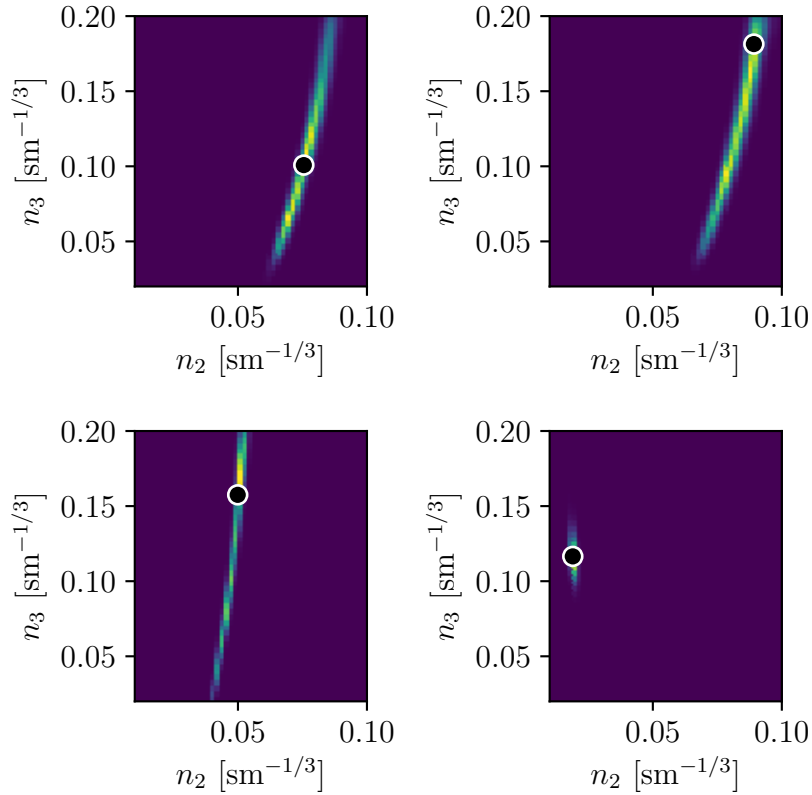


Figure 6.24: Posterior PDFs from four synthetic experiments using optimal set of two locations, with $\sigma = 0.01 \text{ m s}^{-1}$. Black points indicate true parameters.

6.5.5 Response to observation uncertainty

The results of figures 6.24 and 6.25 have assumed an observation uncertainty of $\sigma = 0.01 \text{ m s}^{-1}$. Here, a larger $\sigma = 0.05 \text{ m s}^{-1}$ is assumed, in order to test the response of the parameter estimation problem to increased observation uncertainty. The same four synthetic experiments are performed, and the posterior PDFs resulting from the use of two and three output locations are shown in figures 6.26 and 6.27 respectively.

While the true parameters lie within the posterior PDFs for both sets of observations, the three-output case handles increased observation uncertainty better than the two-location case. This is expected, since overcoming observation uncertainty was the original motive for including additional locations via an optimal-volume method. Nevertheless, n_3 is poorly constrained by either set of observation locations, suggesting that the observation uncertainty must be less than $\sigma = 0.05 \text{ m s}^{-1}$ in order to obtain a good constraint on n_3 using the observations considered here.

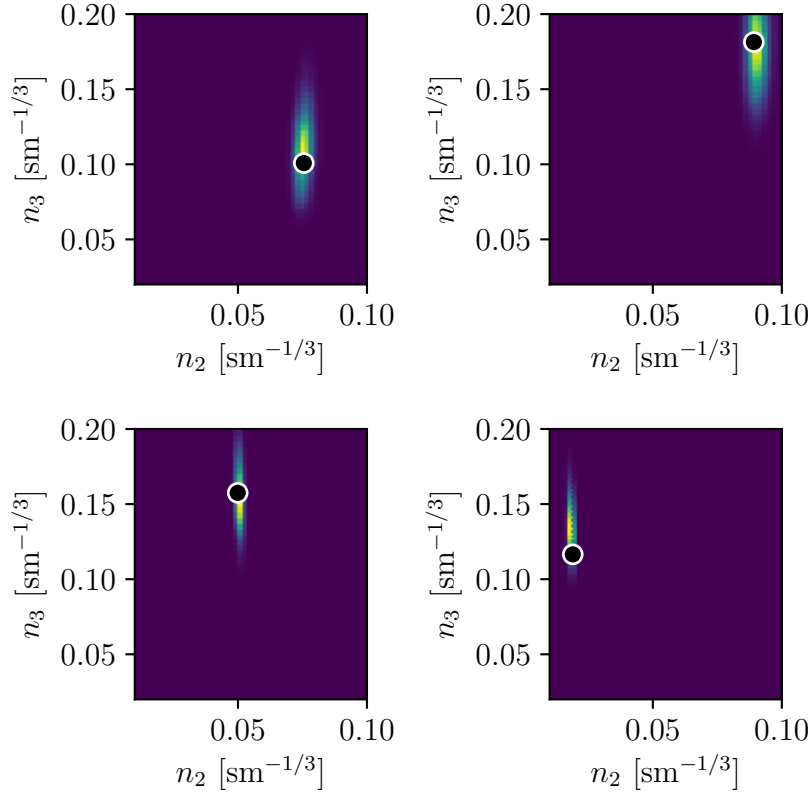


Figure 6.25: Posterior PDFs from four synthetic experiments using optimal set of three locations, with $\sigma = 0.01 \text{ m s}^{-1}$. Black points indicate true parameters.

6.6 Discussion

Graham et al. (2017) remark that data-rich inverse problems typically contain a significant amount of redundant information. This is observed within the Bristol Channel case study of this chapter, where a similar result can be achieved by solving the parameter estimation problem assimilating data from only three observation locations, compared with assimilating all available data. This is achieved by carefully selecting locations which combine to provide information which constrains all three uncertain input parameters. In this case study, similar results could be achieved using observation locations selected by optimising either the skewness measure of Butler et al. (2015), or the volume measure introduced here.

For the Bristol Channel case, both of these methods are also capable of proposing new observation locations. However, since the skewness method does not favour locations with high magnitudes of sensitivity to the input parameters, the adequate performance of the skewness method relies on first filtering out locations with low sensitivity to the input

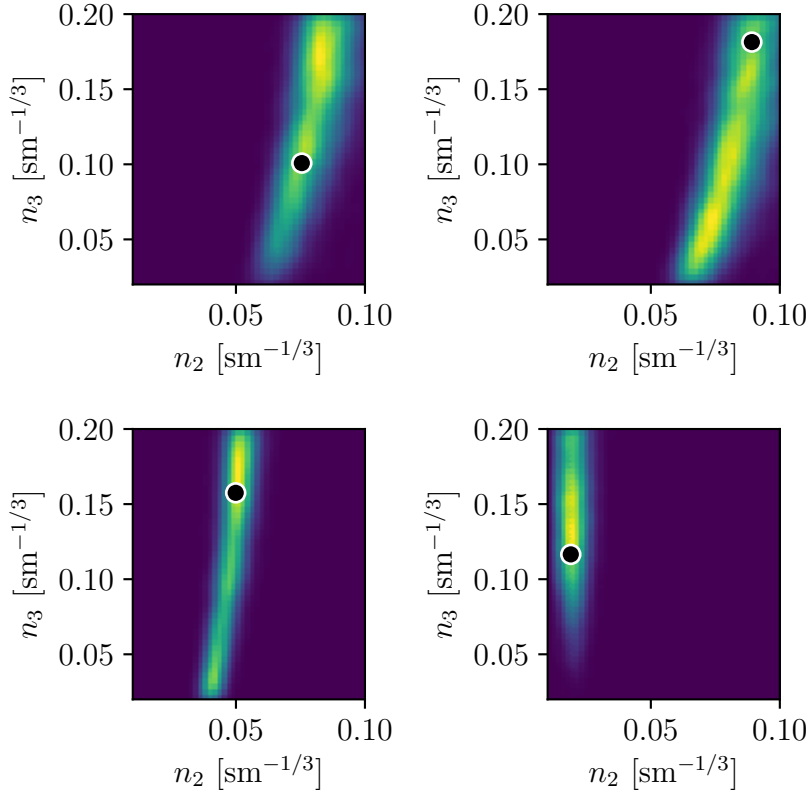


Figure 6.26: Posterior PDFs from four synthetic experiments using optimal set of two locations, with $\sigma = 0.05 \text{ m s}^{-1}$. Black points indicate true parameters.

parameters. The volume method, on the other hand, does not require this filtering step. Therefore, while it has been found that the skewness method can be applied outside of its original context (its theoretical basis is within the measure-theoretic algorithm of Butler et al. (2015), but has been used here within Bayesian inversion via MCMC), the volume method appears to provide a more robust approach to selecting observation locations for the solution of parameter estimation problems.

A further advantage of the volume method has been demonstrated through its application to a case study of the North Malé Atoll in the Maldives. Here, it has been shown that better constraints on two unknown input parameters can be achieved by selecting three observation locations than selecting only two. The use of a greater number of observations than unknown model inputs is not possible using the skewness method, but well handled by the volume method.

Within the North Malé Atoll case study, the filtering of observation locations was performed in order to reduce the total number of observation location combinations, making the problem of finding their optimal combination tractable. The sensitivity of the results

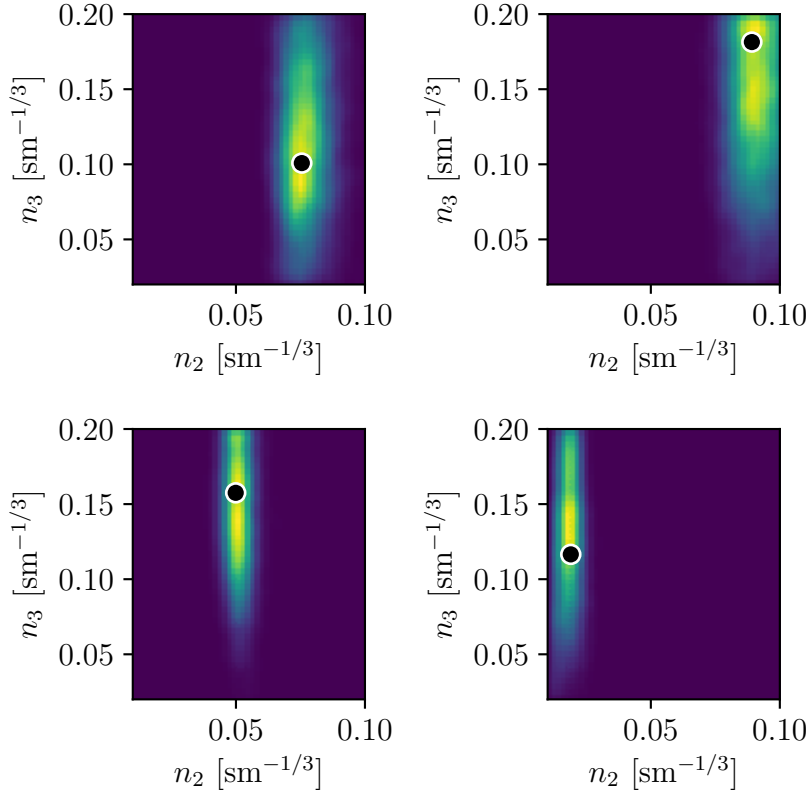


Figure 6.27: Posterior PDFs from four synthetic experiments using optimal set of three locations, with $\sigma = 0.05 \text{ m s}^{-1}$. Black points indicate true parameters.

to these filtering parameters has not been explored. The criteria applied here reduced the 57,914 candidate locations (corresponding to every mesh node) to only 19 locations. The relatively poor constraints achieved on n_3 (the friction coefficient for coral reefs) in the synthetic parameter estimation experiments might be attributable to the exclusion of mesh nodes with low velocities, such that observations made on reefs were not considered. However, this was partially overcome by the inclusion of a third observation location, where the effect of the optimal-volume selection method was to automatically target observations providing a tighter constraint on this parameter.

The work of this chapter offers several avenues for further work. While one-off measurements, such as those made via targeted drone observations, might plausibly make instantaneous observations, the deployment of a fixed detector, such as an ADCP, would record timeseries data. This work has not considered temporally varying observation data, and the scheme for selecting observation locations would need to be extended for this purpose. One possible approach might be to consider the volume swept by the sensitivity vector over time, for example over a full tidal cycle. This would be equivalent to considering every data point in the timeseries as a separate observation, and combin-

ing them as described in this work. An additional challenge here is the assimilation of such data, and the use of an alternative surrogate model which can better emulate time-varying quantities, such as a Polynomial chaos expansion (as used by Sraj et al. (2013)), may be appropriate. A gradient-based method using the adjoint model is another possible approach well suited to the assimilation of timeseries data, as performed in chapter 5.

The optimal observation selection framework used here can be extended to the estimation of additional parameters, if a broader model calibration exercise is required. This work has made assumptions about the spatial distribution of corals throughout the domain. A map of coral distribution would therefore be valuable, and may also facilitate the application of different friction coefficients to coral species with different geometric characteristics; this would be similar to the use of sediment data used to constrain the input parameter space in the Bristol Channel case study. This framework could further be used in an iterative process, whereby additional uncertainty sources are included as more observation data becomes available.

Finally, this scheme has so far been used to propose observation locations which provide the best constraints on a given set of unknown parameters. However, it could also be used in the opposite sense, to select a set of model parameters whose values would be well constrained by a given set of already available observation data. In the Bristol Channel case study where sediment types have been combined into three groups in a fairly arbitrary manner, this scheme could be used to propose an improved grouping of the sediment types, such that the friction parameters for all three (or more/fewer) groups can be independently constrained. It has been found that the estimated friction parameters corresponding to rock and gravel exhibit strong covariance, i.e. that they cannot be distinguished, even by hypothetical new observations. This type of framework could be used to propose a new grouping of sediment types which avoids this problem.

6.7 Summary

This chapter has attempted to address the issue of how to propose new observation locations, with the motivation of model calibration with respect to a given set of input parameters. Two methods for the optimal selection of observation locations have been used. The first, by Butler et al. (2015), suffers from two drawbacks: it gives no preference to observations which have high sensitivity to the unknown parameters; and it can only be used to select a number of observations which is less than or equal to the number of unknown parameters. These drawbacks are overcome by the second method proposed

within this chapter.

Both methods have been applied to the selection of a subset of the observations available within the Bristol Channel parameter estimation case study of chapter 5. The results show that there is a high level of redundancy in the observation dataset, and that the assimilation of data from a carefully selected set of three observation sites can give very similar results to the assimilation of all available data. A further set of hypothetical new observations is also proposed. However, it is found that the proposed new observations are not capable of significantly improving upon the parameter constraints provided by the existing observation dataset.

The framework has also been applied to the proposal of observations in a data-poor region where model validation and calibration is currently not possible, taking the North Malé Atoll in the Maldives as a case study. Observations of peak tidal currents have been proposed to constrain two friction parameters, corresponding to the presence or otherwise of coral. While further work is required to extend the framework to the hypothetical deployment of current-measuring devices such as ADCPs, this preliminary study indicates that the optimal observation selection framework can be successfully applied to the guidance of new field studies in the Maldives.

Chapter 7

Conclusions

7.1 Summary of thesis achievements

Chapter 4 has built on existing literature in the application of adjoint methods to storm surge modelling, with a number of conclusions drawn. The sensitivity of the skew surge at a given location with respect to the wind stress at previous times was found to behave as a shallow water wave which originates at the skew surge observation location and propagates backwards in time. This is consistent with the findings of previous work (Wilson et al., 2013), and has been additionally confirmed to first order within this thesis via an analytic approach. Chapter 4 has gone further than the existing literature, by applying the adjoint sensitivity analysis method to additional sources of model uncertainty, namely the bottom friction coefficient and bathymetry. An example of the physical insight which can be gained from this analysis is the effect of Dogger Bank, a sand bank off the UK North Sea coast, in reducing the skew surge impacting the south-east UK coast to storm surge; this effect is evident via the positive sensitivity of the modelled skew surge to water depth in the Dogger Bank region.

Further conclusions from the application of adjoint methods to surge modelling were drawn from the use of these sensitivity patterns to quantify the uncertainty contributed by each model input. Uncertainty in the wind stress depends strongly on the surge event and the forecast lead time, but the meteorological model inputs are in any case well known to dominate forecast uncertainty (Flowerdew et al., 2013). However, the uncertainty quantification of chapter 4 has instead been used to estimate skew surge uncertainties due to bathymetry and bottom friction, concluding that the use of a Manning coefficient for bottom friction with an uncertainty of $0.005 \text{ s m}^{-1/3}$ produces uncertainties in surge height of up to 20 cm for the case study event considered. This emphasises the importance

of model calibration in reducing this uncertainty, and was the motivation for the remainder of the work in this thesis.

Chapter 5 has compared approaches for estimating a spatially varying bottom friction parameter. One aspect of this work was the comparison of different input parameter spaces; while the estimation of a fully spatially varying Manning coefficient was found to produce significant improvements in model-observation misfit, the resulting spatial variation appeared not to be physically reasonable, motivating a different approach. Instead, sediment data was used to *a priori* constrain the input parameter space, such that three parameters were estimated, corresponding to the Manning coefficients for three different groups of sediment type. These resulting parameters were successfully estimated using both an adjoint gradient-based optimisation, and a Bayesian inversion approach via a Markov Chain Monte Carlo algorithm, where a Gaussian process emulator was used as a surrogate for the full numerical model. The parameter estimates from each of these methods, which were applied using two different data sets, were consistent within the estimated uncertainties. Furthermore, the estimated parameters were found to decrease model-observation misfit within an independent numerical model, indicating that the model calibration process avoided the influence of model-specific errors and therefore arrived at physically meaningful (and thus potentially generally applicable) friction parameters. It is noteworthy that the estimated uncertainty in the bottom friction parameter in the storm surge uncertainty quantification of chapter 4 was $0.005 \text{ s m}^{-1/3}$; this is consistent with the estimated uncertainties in the Manning coefficients inferred by the MCMC algorithm in chapter 5, which vary between 0.002 and $0.009 \text{ s m}^{-1/3}$.

The friction parameter estimation of chapter 5 relied on the availability of observation data; there were 16 locations within the selected model domain at which such data could be used. However, model validation and calibration is not possible in regions where observation infrastructure is lacking, yet many such regions could reap significant benefit from the use of well-calibrated numerical ocean models. An excellent example is given by the Maldives; the very existence of these islands is threatened by future sea level rise, while processes such as sediment and pollutant transport are pressing issues. This motivated the work of chapter 6, where new observations were proposed in order to provide the best constraints on unknown bottom friction parameters. In this work, possible combinations of observation locations were assigned measures of how well they are expected to perform when used within a parameter estimation problem. Two such measures were compared; one from the literature and the second proposed in this chapter to overcome shortcomings in the applicability of the first. In a preliminary application to the data-rich Bristol Channel case study, both measures were capable of identifying subsets of the available observation data which provide constraints on the friction parameters which are

almost indistinguishable from those obtained from the assimilation of all available data, thus demonstrating the redundancy within the dataset. The new method was then applied to the North Malé Atoll in the Maldives, where hypothetical observations of peak currents were proposed to constrain two unknown friction parameters. One of the main advantages of the new measure proposed here for selection of observation locations is its applicability to the selection of a greater number of observations than unknown model inputs, which proved particularly helpful in the Maldives application. These preliminary results therefore suggest that the framework can be used to inform future field work.

7.2 Potential for future work

Several possible avenues for future work have been discussed within the relevant chapters, and are summarised here.

7.2.1 Application of adjoint methods to storm surge modelling

While the work of chapter 4 represents an extension to the existing literature by applying adjoint methods to sensitivity analysis with respect to wind stress, bottom friction and bathymetry, the methods can be further applied to boundary condition and atmospheric pressure inputs. Additional model output locations can also be considered, to further explore the spatial pattern of uncertainty contributed by each input. Since only one storm surge case study was considered within this work, a comparison across multiple events may reveal further insight.

Chapter 4 tested the adjoint-based approximation of surge ensembles using wind stress perturbations which were proportional to the hindcast wind stress. This can be tested further using a variety of hindcast case studies, and testing the approximations using real meteorological ensemble data from the events. Similarly, the application to model-free hazard assessment can be tested for a variety of surge events, and at additional output locations. It was also suggested in chapter 4 that corrections to this leading order surge approximation could be introduced via a synthesised tide-surge interaction; this would require further work involving a variety of storm surge case studies.

7.2.2 Model calibration

The inference of sediment-based friction parameters in chapter 5 was not able to distinguish all three selected input parameters using available data (or even hypothetical new observations, as shown in chapter 6); the posterior probability density functions showed significant covariance between the Manning coefficients corresponding to rock and gravel sediment types. This suggests that the division of the sediment types into three groups, which within this work was fairly arbitrary, could be improved. The methods of chapter 6 could be used to identify the optimal grouping of sediment types, such that the parameters corresponding to all selected groups could be independently estimated using existing observation data.

Since the motivation of this work was the reduction of uncertainty introduced to surge models by an uncertain friction coefficient, an application to the North Sea domain of chapter 4 would be a natural extension. Furthermore, the second numerical model used within chapter 5 for further verification of estimated friction parameters, TELEMAC-2D, is somewhat similar in its discretisation to Thetis. The use of additional numerical models is therefore necessary for further validation, and to test the applicability of estimated parameters across different numerical models. The inference of friction parameters in a model domain which matches that of the UK operational surge model could be particularly impactful, if reductions in model-observation misfit achieved via these methods can be shown to be applicable across numerical models which differ more significantly.

Finally, chapter 5 considered the assimilation of observations of sea surface levels, but neglected tidal currents. The consideration of tidal currents is planned in future work. It is anticipated that, while currents may prove to be more sensitive to bottom friction than surface levels, observations (such as those made by ADCPs) are typically noisier, thus presenting a new challenge in the assimilation of such data.

7.2.3 Proposal of new observations

The framework used within chapter 6 for the proposal of observation locations requires an extension in order to be used to guide the deployment of a timeseries current-measuring device such as an ADCP. The volume-based measure introduced in this work for selecting optimal observation locations should handle this case naturally by considering each time-step of observation data as a distinct observation. In this case, a single observation location should be sufficient to constrain multiple input parameters, with the volume (in parameter sensitivity space) swept out by the sensitivity vector over time (e.g. over a

tidal cycle) a possible indicator for how well a given observation location would perform in constraining the unknown parameters.

References

- A. Aksoy, F. Zhang, and J. W. Nielsen-Gammon. Ensemble-Based Simultaneous State and Parameter Estimation in a Two-Dimensional Sea-Breeze Model. *Monthly Weather Review*, 134(2006):2951–2970, 2006.
- M. Alnæs, J. Blechta, J. Hake, A. Johansson, B. Kehlet, A. Logg, C. Richardson, J. Ring, M. E. Rognes, and G. N. Wells. The FEniCS project version 1.5. *Archive of Numerical Software*, 3(100), 2015.
- M. S. Alnæs, A. Logg, K. B. Ølgaard, M. E. Rognes, and G. N. Wells. Unified form language: A domain-specific language for weak formulations of partial differential equations. *ACM Transactions on Mathematical Software (TOMS)*, 40(2):1–37, 2014.
- J. L. Anderson. An Ensemble Adjustment Kalman Filter for Data Assimilation. *Monthly Weather Review*, 129:2884–2903, 2001.
- G. J. Arcement and V. R. Schneider. Guide for Selecting Manning’s Roughness Coefficients for Natural Channels and Flood Plains. Technical report, 1989.
- ASC. Managing climate risks to well-being and the economy. Adaptation Sub-Committee. Committee on Climate Change. Progress report. 2014.
- A. Avdis, A. S. Candy, J. Hill, S. C. Kramer, and M. D. Piggott. Efficient unstructured mesh generation for marine renewable energy applications. *Renewable Energy*, 116:842–856, 2018. ISSN 0960-1481. doi:<https://doi.org/10.1016/j.renene.2017.09.058>.
- A. Avdis, C. T. Jacobs, S. L. Mouradian, J. Hill, and M. D. Piggott. Meshing ocean domains for coastal engineering applications. *ECCOMAS Congress 2016 - Proceedings of the 7th European Congress on Computational Methods in Applied Sciences and Engineering*, 1(June):480–492, 2016. doi:10.7712/100016.1830.7712.
- C. B. Barber, D. P. Dobkin, and H. Huhdanpaa. The quickhull algorithm for convex hulls. *ACM Transactions on Mathematical Software (TOMS)*, 22(4):469–483, 1996.

- C. Bischof, A. Carle, G. Corliss, A. Griewank, and P. Hovland. ADIFOR-Generating Derivative Codes from Fortran Programs. *Scientific Programming*, 1:11–29, 1992.
- A. Bolle, P. Mercelis, D. Roelvink, P. Haerens, and K. Trouw. Application and validation of XBeach for three different field sites. ISSN 2156-1028. doi:10.9753/icce.v32.sediment.40.
- N. E. Bowler, A. Arribas, S. E. Beare, K. R. Mylne, and G. J. Shutts. The local ETKF and SKEB : Upgrades to the MOGREPS short-range ensemble prediction system. *Quarterly Journal of the Royal Meteorological Society*, 135(March):767–776, 2009. doi:10.1002/qj.
- J. Brown, L. Amoudry, F. Mercier, and A. Souza. Intercomparison of the Charnock and CORE bulk wind stress formulations for coastal ocean modelling. *Ocean Science*, 9(4):721–729, 2013.
- J. M. Brown, A. J. Souza, and J. Wolf. An 11-year validation of wave-surge modelling in the Irish Sea, using a nested POLCOMS-WAM modelling system. *Ocean Modelling*, 33:118–128, 2010. ISSN 14635003. doi:10.1016/j.ocemod.2009.12.006.
- J. M. Brown and J. Wolf. Coupled wave and surge modelling for the eastern Irish Sea and implications for model wind-stress. *Continental Shelf Research*, 29(10):1329–1342, 2009. ISSN 0278-4343. doi:10.1016/J.CSR.2009.03.004.
- R. Buizza, P. L. Houtekamer, Z. Toth, G. Pellerin, M. Wei, and Y. Zhu. A Comparison of the ECMWF, MSC, and NCEP Global Ensemble Prediction Systems. *Monthly Weather Review*, 133:1076–1097, 2005.
- T. Butler, L. Graham, D. Estep, C. Dawson, and J. J. Westerink. Definition and solution of a stochastic inverse problem for the Manning's n parameter field in hydrodynamic models. *Advances in Water Resources*, 78:60–79, 2015. ISSN 0309-1708. doi:10.1016/j.advwatres.2015.01.011.
- H. Charnock. Wind stress on a water surface. *Quarterly Journal of the Royal Meteorological Society*, 81(350):639–640, 1955. ISSN 00359009. doi:10.1002/qj.49708135027.
- C. Chen, H. Liu, and R. C. Beardsley. An Unstructured Grid, Finite-Volume, Three-Dimensional, Primitive Equations Ocean Model: Application to Coastal Ocean and Estuaries. *American Meteorological Society*, 20:159–186, 2003.
- H. Chen, A. Cao, J. Zhang, C. Miao, and X. Lv. Estimation of spatially varying open boundary conditions for a numerical internal tidal model with adjoint method. *Mathematics and Computers in Simulation*, 97:14–38, 2014. ISSN 0378-4754. doi:10.1016/J.MATCOM.2013.08.005.

- S. Danilov. Two finite-volume unstructured mesh models for large-scale ocean modeling. *Ocean Modelling*, 47:14–25, 2012. ISSN 14635003. doi:10.1016/j.ocemod.2012.01.004.
- S. Danilov. Ocean modeling on unstructured meshes. *Ocean Modelling*, 2013. ISSN 14635003. doi:10.1016/j.ocemod.2013.05.005.
- J. De Rouck, H. Verhaeghe, and J. Geeraerts. Crest level assessment of coastal structures - General overview. *Coastal Engineering*, 2009. ISSN 03783839. doi:10.1016/j.coastaleng.2008.03.014.
- H. de Vries. Probability Forecasts for Water Levels at the Coast of The Netherlands. *Marine Geodesy*, 32(2):100–107, 2009. doi:10.1080/01490410902869185.
- L. Debrou, P. Marchesiello, P. Penven, and G. Cambon. Two-way nesting in split-explicit ocean models: algorithms, implementation and validation. *Ocean Modelling*, 49:1–21, 2012.
- Delft Hydraulics. Delft3D-FLOW user manual, version 3.15. 2019.
- E. P. Diaconescu and R. Laprise. Singular vectors in atmospheric sciences: A review. *Earth-science reviews*, 113(3-4):161–175, 2012.
- Digimap. DiGSBS250K [SHAPE geospatial data], Scale 1:250000, Tiles: GB, Updated: 6 September 2011, BGS, Using: EDINA Geology Digimap Service, <https://digimap.edina.ac.uk>. 2011.
- Digimap. Marine Themes Digital Elevation Model 6 Arc Second [ASC geospatial data], Scale 1:250000, Tiles: 2062000000, 2060010060, 2060010040, 2060010020, 2060000000, 2058010080, 2058010060, 2058010040, 2058010020, 2058000000, 2056010080, 2056010060, 2056010040, 2056010020, 2056000020, 2056000000, 2054010080, 2054010060, 2054010040, 2054010020, 2054000020, 2054000000, 2052010080, 2052010060, 2052010040, 2052010020, 2052000020, 2052000000, 2050010080, 2050010060, 2050010040, 2050010020, 2050000020, 2050000000, 2048010080, 2048010060, 2048010040, Updated: 25 October 2013, OceanWise, Using: EDINA Marine Digimap Service, <https://digimap.edina.ac.uk>. 2013.
- Digimap. Marine Themes Digital Elevation Model 1 Arc Second [ASC geospatial data], Scale 1:50000, Tiles: 5050510045, 5050510050, 5051010030, 5051010035, 5051010040, 5051010045, 5051010050, 5051510025, 5051510030, 5051510035, 5051510040, 5051510045, 5051510050, Updated: 9 September 2016, OceanWise, Using: EDINA Marine Digimap Service, <https://digimap.edina.ac.uk>. 2016.

- A. T. Doodson. The harmonic development of the tide-generating potential. *Proceedings of the Royal Society of London. Series A, Containing Papers of a Mathematical and Physical Character*, 100(704):305–329, 1921.
- K. Döös, J. Nycander, and P. Sigray. Slope-dependent friction in a barotropic model. *Journal of Geophysical Research: Oceans*, 109(C1), 2004.
- G. D. Egbert and S. Y. Erofeeva. Efficient inverse modeling of barotropic ocean tides. *Journal of Atmospheric and Oceanic Technology*, 19(2):183–204, 2002. ISSN 07390572. doi:10.1175/1520-0426(2002)019<0183:EIMOBO>2.0.CO;2.
- G. Evensen. The Ensemble Kalman Filter for Combined State and Parameter Estimation. *IEEE Control Systems*, 29(3):83–104, 2009.
- P. E. Farrell, D. A. Ham, S. W. Funke, and M. E. Rognes. Automated derivation of the adjoint of high-level transient finite element programs. *SIAM Journal on Scientific Computing*, 35(4):C369–C393, 2013.
- J. Flowerdew, K. Horsburgh, C. Wilson, and K. Mylne. Development and evaluation of an ensemble forecasting system for coastal storm surges. *Quarterly Journal of the Royal Meteorological Society*, 136:1444–1456, 2010. ISSN 00359009. doi:10.1002/qj.648.
- J. Flowerdew, K. Mylne, C. Jones, and H. Titley. Extending the forecast range of the UK storm surge ensemble. *Quarterly Journal of the Royal Meteorological Society*, 139:184–197, 2013. doi:10.1002/qj.1950.
- S. W. Funke. *The automation of PDE-constrained optimisation and its applications*. Ph.D. thesis, Imperial College London, 2012.
- S. W. Funke, P. E. Farrell, and M. D. Piggott. Tidal turbine array optimisation using the adjoint approach. *Renewable Energy*, 63:658–673, 2014. ISSN 09601481. doi:10.1016/j.renene.2013.09.031.
- P. Gauthier, M. Tanguay, S. Laroche, and S. Pellerin. Extension of 3DVAR to 4DVAR: Implementation of 4DVAR at the Meteorological Service of Canada. *Monthly Weather Review*, 135:2339–2354, 2007. doi:10.1175/MWR3394.1.
- C. Geuzaine and J. F. Remacle. Gmsh: A 3-D finite element mesh generator with built-in pre- and post-processing facilities. *International Journal for Numerical Methods in Engineering*, 79(11):1309–1331, 2009. ISSN 00295981. doi:10.1002/nme.2579.
- R. Giering and T. Kaminski. Recipes for Adjoint Code Construction. *ACM Transactions on Mathematical Software*, 24(4):437–474, 1998. ISSN 00983500. doi:10.1145/293686.293695.

- A. E. Gill. *Atmosphere-ocean dynamics*. Academic Press, New York, 1982.
- GPy. GPy: A Gaussian process framework in python. <http://github.com/SheffieldML/GPy>, since 2012.
- L. Graham, T. Butler, S. Walsh, C. Dawson, and J. J. Westerink. A Measure-Theoretic Algorithm for Estimating Bottom Friction in a Coastal Inlet: Case Study of Bay St. Louis during Hurricane Gustav (2008). *Monthly Weather Review*, 145:929–954, 2017. ISSN 0027-0644. doi:10.1175/mwr-d-16-0149.1.
- L. Graham, S. A. Matthis, and T. Butler. BET package. 2013.
- L. C. Graham. *Adaptive measure-theoretic parameter estimation for coastal ocean modeling*. Ph.D. thesis, 2015.
- A. Griewank. Achieving logarithmic growth of temporal and spatial complexity in reverse automatic differentiation. *Optimization Methods and Software*, 1(1):35–54, 1992. doi:10.1080/10556789208805505.
- A. Griewank and A. Walther. *Evaluating derivatives: principles and techniques of algorithmic differentiation*. Society for Industrial and Applied Mathematics, 2nd edition, 2008.
- N. Guillou and J. Thiébot. The impact of seabed rock roughness on tidal stream power extraction. *Energy*, 112:762–773, 2016. ISSN 03605442. doi:10.1016/j.energy.2016.06.053.
- H. Haario, E. Saksman, and J. Tamminen. An adaptive Metropolis algorithm. *Bernoulli*, 7(2):223–242, 2001. ISSN 13507265. doi:10.2307/3318737.
- S. Hagelin, J. Son, R. Swinbank, A. Mccabe, and W. Tennant. The Met Office convective-scale ensemble, MOGREPS-UK. *Quarterly Journal of the Royal Meteorological Society*, 143(October):2846–2861, 2017. doi:10.1002/qj.3135.
- I. D. Haigh, M. P. Wadey, T. Wahl, O. Ozsoy, R. J. Nicholls, J. M. Brown, K. Horsburgh, and B. Gouldby. Spatial and temporal analysis of extreme sea level and storm surge events around the coastline of the UK. *Scientific Data*, 3:1–14, 2016. doi:doi:10.1038/sdata.2016.107.
- J. W. Hall, L. J. Manning, and R. K. Hankin. Bayesian calibration of a flood inundation model using spatial data. *Water Resources Research*, 47(5):1–14, 2011. ISSN 00431397. doi:10.1029/2009WR008541.

- S. Hallegatte, C. Green, R. J. Nicholls, and J. Corfee-Morlot. Future flood losses in major coastal cities. *Nature Climate Change*, 3(9):802–806, 2013. ISSN 1758678X. doi:10.1038/nclimate1979.
- Z.-H. Han, Y. Zhang, C.-X. Song, and K.-S. Zhang. Weighted gradient-enhanced kriging for high-dimensional surrogate modeling and design optimization. *Aiaa Journal*, pages 4330–4346, 2017.
- F. Harcourt, A. Angeloudis, and M. D. Piggott. Utilising the flexible generation potential of tidal range power plants to optimise economic value. *Applied energy*, 237:873–884, 2019.
- W. K. Hastings. Monte Carlo sampling methods using Markov chains and their applications. 1970.
- A. Heemink, E. Mouthaan, M. Roest, E. Vollebregt, K. Robaczewska, and M. Verlaan. Inverse 3D shallow water flow modelling of the continental shelf. *Continental Shelf Research*, 22(3):465–484, 2002. ISSN 0278-4343. doi:10.1016/S0278-4343(01)00071-1.
- J.-M. Hervouet. *Hydrodynamics of free surface flows: modelling with the finite element method*. Wiley, 2007.
- C. Hill, V. Bugnion, M. Follows, and J. Marshall. Evaluating carbon sequestration efficiency in an ocean circulation model by adjoint sensitivity analysis. *Journal of Geophysical Research: Oceans*, 109:1–12, 2004. doi:10.1029/2002JC001598.
- B. Hofmann. *Regularization for applied inverse and ill-posed problems: a numerical approach*. Springer, 1986.
- G. J. Holland. An Analytic Model of the Wind and Pressure Profiles in Hurricanes. *Monthly Weather Review*, 108:1212–1218, 1980.
- M. Homolya, L. Mitchell, F. Luporini, and D. A. Ham. TSFC: a structure-preserving form compiler. *SIAM Journal on Scientific Computing*, 40(3):C401–C428, 2018.
- K. J. Horsburgh and C. Wilson. Tide-surge interaction and its role in the distribution of surge residuals in the North Sea. *Journal of Geophysical Research*, 112(C8), 2007. ISSN 21699291. doi:10.1029/2006JC004033.
- P. L. Houtekamer and H. L. Mitchell. Data Assimilation Using an Ensemble Kalman Filter Technique. *Monthly Weather Review*, 126:796–811, 1998.

- P. Hristov, F. DiazDelaO, E. S. Flores, C. Guzmán, and U. Farooq. Probabilistic sensitivity analysis to understand the influence of micromechanical properties of wood on its macroscopic response. *Composite Structures*, 181:229–239, 2017.
- J. M. Janin, F. Lepeintre, and P. Pechon. Telemac-3D: A finite element code to solve 3D free surface flow problems. In *Computer modelling of seas and coastal regions*, pages 489–506. Springer, 1992.
- T. Kärnä, B. de Brye, O. Gourgue, J. Lambrechts, R. Comblen, V. Legat, and E. Deleersnijder. A fully implicit wetting-drying method for DG-FEM shallow water models, with an application to the Scheldt Estuary. *Computer Methods in Applied Mechanics and Engineering*, 200(5-8):509–524, 2011. ISSN 00457825. doi:10.1016/j.cma.2010.07.001.
- T. Kärnä, S. C. Kramer, L. Mitchell, D. A. Ham, M. D. Piggott, and A. M. Baptista. Thetis coastal ocean model: Discontinuous Galerkin discretization for the three-dimensional hydrostatic equations. *Geoscientific Model Development*, 11(11):4359–4382, 2018. ISSN 19919603. doi:10.5194/gmd-11-4359-2018.
- T. Kärnä, V. Legat, and E. Deleersnijder. A baroclinic discontinuous Galerkin finite element model for coastal flows. *Ocean Modelling*, 61:1–20, 2013. doi:10.1016/j.ocemod.2012.09.009.
- J. Kepler. *Astronomia nova*. 1609.
- K. O. Kim and T. Yamashita. Storm surge simulation using wind-wave-surge coupling model. *Journal of oceanography*, 64(4):621–630, 2008.
- S. Kramer, T. Kärnä, J. Hill, and S. W. Funke. stephankramer/uptide: First release of uptide v1.0. 2020. <http://doi.org/10.5281/zenodo.3909652>.
- P. Lang, J. Desombre, R. Ata, C. Goeury, and J. M. Hervouet. User manual of opensource software TELEMAC-2D. Report, EDF-R&D, www.opentelemac.org, 2014. V7.
- M. Lewis, S. Neill, and A. Elliott. Interannual variability of two offshore sand banks in a region of extreme tidal range. *Journal of Coastal Research*, 31(2):265–275, 2015.
- Y. Li, S. Peng, J. Yan, and L. Xie. On improving storm surge forecasting using an adjoint optimal technique. *Ocean Modelling*, 72:185–197, 2013. ISSN 1463-5003. doi:10.1016/J.OCEMOD.2013.08.009.
- N. Lin, K. Emanuel, M. Oppenheimer, and E. Vanmarcke. Physically based assessment of hurricane surge threat under climate change. *Nature Climate Change*, 2:462–467, 2012. ISSN 1758678X. doi:10.1038/nclimate1389.

- H. Liu, L. Xie, L. J. Pietrafesa, and M. Peng. Effect of ocean surface waves on storm surge and coastal flooding. In *27th Conference on Hurricanes and Tropical Meteorology*, pages 24–28. Citeseer, 2006.
- A. C. Lorenc. A global three-dimensional multivariate statistical interpolation scheme. *Monthly Weather Review*, 109(4):701–721, 1981.
- X. Lu and J. Zhang. Numerical study on spatially varying bottom friction coefficient of a 2D tidal model with adjoint method. *Continental Shelf Research*, 26(16):1905–1923, 2006. ISSN 0278-4343. doi:10.1016/J.CSR.2006.06.007.
- R. A. Luettich and J. J. Westerink. *Formulation and numerical implementation of the 2D/3D ADCIRC finite element model version 44. XX*. 2004.
- L. N. Ly and P. Luong. Numerical multi-block grids in coastal ocean circulation modeling. *Applied Mathematical Modelling*, 23(11):865–879, 1999.
- B. B. Mandelbrot. *The fractal geometry of nature*, volume 173. WH freeman New York, 1983.
- J. Marshall, A. Adcroft, C. Hill, L. Perelman, and C. Heisey. A finite-volume, incompressible Navier Stokes model for studies of the ocean on parallel computers. *Journal of Geophysical Research*, 102:5753–5766, 1997.
- S. Maßmann. Sensitivities of an adjoint, unstructured mesh, tidal model on the European Continental Shelf. *Ocean Dynamics*, 60(6):1463–1477, 2010a. ISSN 16167341. doi:10.1007/s10236-010-0347-6.
- S. Maßmann. *Tides on unstructured meshes*. Ph.D. thesis, Universitat Bremen, 2010b.
- T. Mayo, T. Butler, C. Dawson, and I. Hoteit. Data assimilation within the Advanced Circulation (ADCIRC) modeling framework for the estimation of Manning’s friction coefficient. *Ocean Modelling*, 76:43–58, 2014. ISSN 14635003. doi:10.1016/j.ocemod.2014.01.001.
- R. T. McCall, J. S. Van Thiel de Vries, N. G. Plant, A. R. Van Dongeren, J. A. Roelvink, D. M. Thompson, and A. J. Reniers. Two-dimensional time dependent hurricane overwash and erosion modeling at Santa Rosa Island. *Coastal Engineering*, 57:668–683, 2010. ISSN 03783839. doi:10.1016/j.coastaleng.2010.02.006.
- S. C. Medeiros and S. C. Hagen. Review of wetting and drying algorithms for numerical tidal flow models. *International Journal for Numerical Methods in Fluids*, 71:473–487, 2013. ISSN 02712091. doi:10.1002/fld.3668.

- S. K. Mitusch, S. W. Funke, and J. S. Dokken. dolfin-adjoint 2018.1: automated adjoints for FEniCS and Firedrake. *Journal of Open Source Software*, 4(38), 2019.
- B. Mourre, P. De Mey, F. Lyard, and C. Le Provost. Assimilation of sea level data over continental shelves: An ensemble method for the exploration of model errors due to uncertainties in bathymetry. *Dynamics of Atmospheres and Oceans*, 38:93–121, 2004. ISSN 03770265. doi:10.1016/j.dynatmoce.2004.09.001.
- R. Muir Wood and W. Bateman. Uncertainties and constraints on breaching and their implications for flood loss estimation. *Philosophical Transactions of the Royal Society A: Mathematical, Physical and Engineering Sciences*, 363(1831):1423–1430, 2005.
- P. Murty, A. Rao, K. S. Srinivas, E. P. R. Rao, and P. K. Bhaskaran. Effect of wave radiation stress in storm surge-induced inundation: A case study for the east coast of india. *Pure and Applied Geophysics*, pages 1–20, 2019.
- S. P. Neill, A. Angeloudis, P. E. Robins, I. Walkington, S. L. Ward, I. Masters, M. J. Lewis, M. Piano, A. Avdis, M. D. Piggott, G. Aggidis, P. Evans, T. A. A. Adcock, A. Židonis, R. Ahmadian, and R. Falconer. Tidal range energy resource and optimization Past perspectives and future challenges. *Renewable Energy*, 127:763–778, 2018. ISSN 18790682. doi:10.1016/j.renene.2018.05.007.
- W. Nowak. Using algorithmic differentiation for uncertainty analysis. In *22nd Telemac & Mascaret User Club*, pages 52–57. 2015. doi:10.5281/zenodo.165522.
- C. C. Pain, M. D. Piggott, A. J. Goddard, F. Fang, G. J. Gorman, D. P. Marshall, M. D. Eaton, P. W. Power, and C. R. de Oliveira. Three-dimensional unstructured mesh ocean modelling. *Ocean Modelling*, 10:5–33, 2005. ISSN 14635003. doi:10.1016/j.ocemod.2004.07.005.
- J. Pall, R. Chandra, D. Azam, T. Salles, J. M. Webster, R. Scalzo, and S. Cripps. BayesReef: A Bayesian inference framework for modelling reef growth in response to environmental change and biological dynamics. *Environmental Modelling & Software*, page 104610, 2020.
- D. F. Parrish and J. C. Derber. The National Meteorological Center’s spectral statistical-interpolation analysis system. *Monthly Weather Review*, 120(8):1747–1763, 1992.
- F. Pianosi, K. Beven, J. Freer, J. W. Hall, J. Rougier, D. B. Stephenson, and T. Wagener. Sensitivity analysis of environmental models: A systematic review with practical workflow. *Environmental Modelling and Software*, 79:214–232, 2016. ISSN 13648152. doi:10.1016/j.envsoft.2016.02.008.

- T. Pullen, N. W. H. Allsop, T. Bruce, A. Kortenhaus, H. Schüttrumpf, and J. W. der Meer. *EurOtop wave overtopping of sea defences and related structures: assessment manual*. 2007.
- S. Rasheed, S. C. Warder, Y. Plancherel, and M. D. Piggott. An improved gridded bathymetric dataset and tidal model for the maldives archipelago. *Submitted to Earth and Space Science*, 2020.
- C. E. Rasmussen. Gaussian processes in machine learning. In *Summer School on Machine Learning*, pages 63–71. Springer, 2003.
- F. Rathgeber, D. A. Ham, L. Mitchell, M. Lange, F. Luporini, A. T. McRae, G. T. Bercea, G. R. Markall, and P. H. Kelly. Firedrake: Automating the finite element method by composing abstractions. *ACM Transactions on Mathematical Software*, 43(3), 2016. ISSN 15577295. doi:10.1145/2998441.
- J. H. Rosman and J. L. Hench. A framework for understanding drag parameterizations for coral reefs. *Journal of Geophysical Research: Oceans*, 116(C8), 2011.
- A. Saltelli, M. Ratto, T. Andres, F. Campolongo, J. Cariboni, D. Gatelli, M. Saisana, and S. Tarantola. *Global sensitivity analysis: the primer*. John Wiley & Sons, 2008.
- A. Sandu, D. N. Daescu, G. R. Carmichael, and T. Chai. Adjoint sensitivity analysis of regional air quality models. *Journal of Computational Physics*, 204:222–252, 2005. ISSN 00219991. doi:10.1016/j.jcp.2004.10.011.
- A. F. Shchepetkin and J. C. McWilliams. The regional oceanic modeling system (ROMS): A split-explicit, free-surface, topography-following-coordinate oceanic model. *Ocean Modelling*, 2005. ISSN 14635003. doi:10.1016/j.ocemod.2004.08.002.
- SHOM. <https://data.shom.fr>. 2019.
- D. Sivia and J. Skilling. *Data analysis: a Bayesian tutorial*. OUP Oxford, 2006.
- S. D. Smith and E. G. Banke. Variation of the sea surface drag coefficient with wind speed. *Quarterly Journal of the Royal Meteorological Society*, 101(429):665–673, 1975. ISSN 00359009. doi:10.1002/qj.49710142920.
- T. Smith and P. Heimbach. Atmospheric Origins of Variability in the South Atlantic Meridional Overturning Circulation. *American Meteorological Society*, 32:1483–1500, 2019. doi:10.1175/JCLI-D-18-0311.1.
- I. M. Sobol. Global sensitivity indices for nonlinear mathematical models and their Monte Carlo estimates. *Mathematics and Computers in Simulation*, 55(1-3):271–280, 2001.

- P. Sochala, C. Chen, C. Dawson, and M. Iskandarani. A polynomial chaos framework for probabilistic predictions of storm surge events. *Computational Geosciences*, pages 1–20, 2019.
- T. Spencer, S. M. Brooks, B. R. Evans, J. A. Tempest, and I. Möller. Southern North Sea storm surge event of 5 December 2013: Water levels, waves and coastal impacts. *Earth-Science Reviews*, 146:120–145, 2015. ISSN 00128252. doi:10.1016/j.earscirev.2015.04.002.
- I. Sraj, M. Iskandarani, W. Carlisle Thacker, A. Srinivasan, and O. M. Knio. Drag parameter estimation using gradients and hessian from a polynomial chaos model surrogate. *Monthly Weather Review*, 142(2):933–941, 2014a. ISSN 00270644. doi: 10.1175/MWR-D-13-00087.1.
- I. Sraj, M. Iskandarani, A. Srinivasan, W. C. Thacker, J. Winokur, A. Alexanderian, C. Y. Lee, S. S. Chen, and O. M. Knio. Bayesian inference of drag parameters using AXBT data from typhoon fanapi. *Monthly Weather Review*, 141(7):2347–2367, 2013. ISSN 00270644. doi:10.1175/MWR-D-12-00228.1.
- I. Sraj, K. T. Mandli, O. M. Knio, C. N. Dawson, and I. Hoteit. Uncertainty quantification and inference of Manning’s friction coefficients using DART buoy data during the Thoku tsunami. *Ocean Modelling*, 83:82–97, 2014b. ISSN 14635003. doi:10.1016/j.ocemod.2014.09.001.
- P. Stansby, N. Chini, D. Apsley, A. Borthwick, L. Bricheno, J. Horrillo-Caraballo, M. McCabe, D. Reeve, B. D. Rogers, A. Saulter, A. Scott, C. Wilson, J. Wolf, and K. Yan. An integrated model system for coastal flood prediction with a case history for Walcott, UK, on 9 November 2007. *Journal of Flood Risk Management*, 6:229–252, 2013. ISSN 1753318X. doi:10.1111/jfr3.12001.
- T. Stocker, D. Qin, G.-K. Plattner, M. Tignor, S. Allen, J. Boschung, A. Nauels, Y. Xia, V. Bex, and P. M. (eds.). *IPCC, 2013: Climate Change 2013: The Physical Science Basis. Contribution of Working Group I to the Fifth Assessment Report of the Intergovernmental Panel on Climate Change*. Cambridge University Press, Cambridge, United Kingdom and New York, NY, USA, 2013.
- S. W. Suh, H. Y. Lee, H. J. Kim, and J. G. Fleming. An efficient early warning system for typhoon storm surge based on time-varying advisories by coupled ADCIRC and SWAN. *Ocean Dynamics*, 65:617–646, 2015. doi:10.1007/s10236-015-0820-3.

- J. F. Sykes, J. L. Wilson, and R. W. Andrews. Sensitivity Analysis for Steady State Groundwater Flow Using Adjoint Operators. *Water Resources Research*, 21(3):359–371, 1985.
- P. M. Tagade, B. M. Jeong, and H. L. Choi. A Gaussian process emulator approach for rapid contaminant characterization with an integrated multizone-CFD model. *Building and Environment*, 2013. ISSN 03601323. doi:10.1016/j.buildenv.2013.08.023.
- M. H. Tber, L. Hascoët, A. Vidard, and B. Dauvergne. Building the Tangent and Adjoint codes of the Ocean General Circulation Model OPA with the Automatic Differentiation tool TAPENADE. 2007.
- D. S. Ullman and R. E. Wilson. Model parameter estimation from data assimilation modeling: Temporal and spatial variability of the bottom drag coefficient. *Journal of Geophysical Research: Oceans*, 103(C3):5531–5549, 1998.
- C. Villaret, R. Kopmann, D. Wyncoll, J. Riehme, U. Merkel, and U. Naumann. First-order uncertainty analysis using Algorithmic Differentiation of morphodynamic models. *Computers & Geosciences*, 90:144–151, 2016. ISSN 0098-3004. doi:10.1016/J.CAGEO.2015.10.012.
- C. V. Vouriot, A. Angeloudis, S. C. Kramer, and M. D. Piggott. Fate of large-scale vortices in idealized tidal lagoons. *Environmental Fluid Mechanics*, 19(2):329–348, 2019. ISSN 15731510. doi:10.1007/s10652-018-9626-4.
- M. P. Wadey, I. D. Haigh, R. J. Nicholls, J. M. Brown, K. Horsburgh, B. Carroll, S. L. Gallop, T. Mason, and E. Bradshaw. A comparison of the 31 January1 February 1953 and 56 December 2013 coastal flood events around the UK. *Frontiers in Marine Science*, 2:84, 2015. ISSN 2296-7745. doi:10.3389/fmars.2015.00084.
- T. Wagener and F. Pianosi. What has Global Sensitivity Analysis ever done for us? A systematic review to support scientific advancement and to inform policy-making in earth system modelling. *Earth-Science Reviews*, 194(February 2018):1–18, 2019. ISSN 00128252. doi:10.1016/j.earscirev.2019.04.006.
- R. A. Walters, E. Lane, and R. Henry. Semi-lagrangian methods for a finite element coastal ocean model. *Ocean Modelling*, 19(3-4):112–124, 2007.
- D. Wang, Q. Liu, and X. Lv. A Study on Bottom Friction Coefficient in the Bohai, Yellow, and East China Sea. *Mathematical Problems in Engineering*, pages 2–9, 2014.

- S. C. Warder, A. Angeloudis, S. C. Kramer, C. J. Cotter, and M. D. Piggott. A comparison of Bayesian inference and gradient-based approaches for friction parameter estimation. *Submitted to Ocean Modelling*, 2020a.
- S. C. Warder, K. J. Horsburgh, and M. D. Piggott. Understanding the contribution of uncertain wind stress to storm surge predictions. In *4th IMA International Conference on Flood Risk, Swansea*. 2019.
- S. C. Warder, K. J. Horsburgh, and M. D. Piggott. Adjoint-based sensitivity analysis for a numerical storm surge model. *Submitted to Ocean Modelling*, 2020b.
- P. Wessel and W. H. F. Smith. A global, self-consistent, hierarchical, high-resolution shoreline database. *Journal of Geophysical Research: Solid Earth*, 101(B4):8741–8743, 1996. doi:10.1029/96JB00104.
- J. Williams, K. J. Horsburgh, J. A. Williams, and R. N. Proctor. Tide and skew surge independence: New insights for flood risk. *Geophysical Research Letters*, 43(12):6410–6417, 2016. ISSN 19448007. doi:10.1002/2016GL069522.
- C. Wilson, K. J. Horsburgh, J. Williams, J. Flowerdew, and L. Zanna. Tide-surge adjoint modeling: A new technique to understand forecast uncertainty. *Journal of Geophysical Research: Oceans*, 118(10):5092–5108, 2013. ISSN 21699291. doi:10.1002/jgrc.20364.
- G. Wu, F. Shi, J. T. Kirby, B. Liang, and J. Shi. Modeling wave effects on storm surge and coastal inundation. *Coastal Engineering*, 140:371–382, 2018. ISSN 03783839. doi:10.1016/j.coastaleng.2018.08.011.
- J. Wu. Wind-Stress Coefficients over Sea Surface near Neutral Conditions - A Revisit. *American Meteorological Society*, 10:727–740, 1980.
- J. Wu. Wind-Stress Over Sea Surface From Breeze to Hurricane. *Journal of Geophysical Research*, 87:9704–9706, 1982.
- D. Xie, Z. Wang, S. Gao, and H. J. De Vriend. Modeling the tidal channel morphodynamics in a macro-tidal embayment, Hangzhou Bay, China. *Continental Shelf Research*, 2009. ISSN 02784343. doi:10.1016/j.csr.2009.03.009.
- J. Zhang and H. Chen. Semi-Idealized Study on Estimation of Partly and Fully Space Varying Open Boundary Conditions for Tidal Models. *Abstract and Applied Analysis*, 2013.
- J. Zhang, X. Lu, P. Wang, and Y. P. Wang. Study on linear and nonlinear bottom friction parameterizations for regional tidal models using data assimilation. *Continental Shelf Research*, 31(6):555–573, 2011. ISSN 0278-4343. doi:10.1016/J.CSR.2010.12.011.

- C. Zhu, R. H. Byrd, P. Lu, and J. Nocedal. Algorithm 778: L-BFGS-B: Fortran subroutines for large-scale bound-constrained optimization. *ACM Transactions on Mathematical Software (TOMS)*, 23(4):550–560, 1997.